UNIVERSITY OF LIVERPOOL

School of Engineering

PhD. Thesis

Laser Surface Texturing of Titanium Alloy for Improved Wettability Properties

Thesis submitted in accordance with the requirements of The University of Liverpool for the degree of Doctor in Philosophy

by

David Rico Sierra

October 2020

Laser Group
School of Engineering
The University of Liverpool
Brownlow Street
Liverpool
L69 3GH
UK

Declaration

I hereby declare that all of the work contained within this dissertation has not been submitted for any other qualification.

Signed:

Date:

Abstract

Surface texturing of different types of materials has been explored through the years with the aim of modifying the intrinsic properties of such material surfaces. A wide range of surface texturing processes has been developed for the manufacturing industry, always looking to improve the quality of the final results while reducing the associated costs. Surface structuring processes for the modification of the wettability properties of the materials has been one of the most explored subjects in this area. This type of surface modification is mostly aimed at inducing high water repellence capabilities for different purposes such as self-cleaning and anti-icing. Development of this type of surfaces usually required the creation of micro and nanoscale feature in the material surface, however, surface micromachining processes have been always a challenging subject due to the scale of the required work, increasing the required manufacturing complexity and production costs.

Laser surface texturing has gained popularity in the micromachining surface processing due to being an accurate and highly controllable process capable of producing surface features in nano and micro scales. The use of ultra-short pulsed lasers with pulse durations in the range of femto and picoseconds have been capable of producing incredibly accurate results on the creation of surface features in these scales giving a significant advantage compared with traditional processes. On the other hand, the complexity of these types of laser systems and the low throughput capabilities have limited their use to mainly research purposes.

The introduction of robust nanosecond pulsed fibre lasers has opened a window of opportunity for the development of surface texturing processes with flexible and almost maintenance-free equipment suitable for the manufacturing industry. Due to the longer pulse duration, this type of laser systems are only capable of creating surface features in microscale producing significant thermal effects compared with ultra-short pulsed lasers.

The main aim of this thesis is to develop a surface structure capable of modifying the wettability properties of Ti-6Al-4V and thus develop a super-hydrophobic effect with the use of a nanosecond pulsed fibre laser.

A comprehensive study to understand the ablation mechanism of Ti-6Al-4V using the nanosecond pulsed fibre laser was carried out for a single pulse ablation process. The results reveal the effects of duration and temporal pulse shape in the ablated craters on the titanium alloy, showing a direct correlation between the amount of removed and molten material produced by the laser ablation process. These results provided a map of suitable parameters for the surface structuring process.

The creation of micro-pillar like surface structures through laser ablation showed to be beneficial for the development of a super-hydrophobic state of the titanium alloy surface. Molten material deposition due to the thermal component of the nanosecond pulsed laser was beneficial for the development of super-hydrophobic surfaces with static contact angle $\approx 163°$. A thermal post-processing was carried out for the improvement and stabilisation of the oxidation created on the surface by laser ablation developing the super-hydrophobic behaviour in the created micro-structure.

Surface nano-structures induced by a picosecond laser were produced on top of the micro-pillars showing improvements of the super-hydrophobicity state of the surface structure. Alternative single laser surface structures were created with different pulse durations (in the nanosecond regime) in order to emulate the induced nano-structures. These structures displayed super-hydrophobic effects increasing the static contact angle to $\approx 168°$ and contact angle hysteresis under $10°$ clearly displaying high water repellency capabilities.

Acknowledgements

I would like to express my most sincere gratitude to Dr. Stuart Edwardson that has been the main supervisor throughout the project, with Professor Geoff Dearden as my co-supervisor. I could never thank you enough for your patient, support and valuable guidance along my PhD research. I would also like to acknowledge Dr. Walter Pierre for the advice and knowledge provided. Without their advice and guidance this research project would not had been completed. I would like to extend my gratitude to Mr. Andy Snaylam and Ms. Andrea Jones for their help. Special thanks to the Consejo Nacional de Ciencia y Tecnologia de Mexico (CONACYT) for sponsoring my PhD. studies.

To my family back in Mexico, my mother, father and sister, for always provide me support and advice whenever I needed, especially on those difficult moments of doubt and fragility during this endeavour, you were, are and will always be the most important part of my life. I would like to also thank to my beautiful Mariana Garcia, who supported me through all my absences, my fits of pique and impatience, you will always be the owner of my heart.

Special appreciation to Dr Fiona McBride for her assistance and invaluable advice, with the surface chemistry analysis. Thanks must also go to Dr. Matt Bilton and the Imaging Centre at Liverpool for the help provided for imaging characterisation through SEM.

Last but not least, I would like to thank my colleagues and friends Jing Liu, Qianliang Li, Yue Tang, Tong Zhou and Guangyu Zhu members of the Laser Engineering group at the University of Liverpool for their advice and amazing memories throughout my research. Also, special thanks to my friends for their help and encouragement through these years away from home.

List of publications

- **Laser surface texturing of titanium with thermal post-processing for improved wettability properties** D. Rico Sierra, S.P. Edwardson, G.Dearden. Procedia CIRP (2018) Volume 74, 362-366.

Contents

List of Figures

List of Tables

List of Symbols

Symbol	Description
A_{LV}	Liquid-solid phase
A_{SL}	Solid-liquid phase
A_{SV}	Solid-vapour phase
B_e	Coefficient of electron heat capacity
C_i	Lattice heat capacity
D_L	Input beam size
D_{min}	Focussed spot diameter
E_{Pulse}	Laser pulse energy
f	Focal length focussing lens
F_0	Laser fluence
F_{th}	Ablation threshold
G_{rt}	Electron-lattice coupling at room temperature
k	Thermal conductivity
k_B	Boltzman constant
k_e	Electron thermal conductivity
l_s	Optical penetration skin depth
l_{th}	Thermal diffusion length

λ	Laser wavelength
M^2	Laser beam quality factor
r	Roughness ratio
Ra	Average roughness
r_f	Ratio of the total wetted area to the projected area
T_f	Fermi temperature
T_m	Melting point
T_v	Vaporisation temperature
v_f	Fermi velocity
α	Absorption coefficient
Ω_{vap}	Heat of evaporation
ω	Focussed spot laser radius
ϕ_s	Fraction of the area in contact with the liquid
ρ	Density
τ_e	Electron relaxation time
τ_i	electron lattice interaction time
τ_p	Pulse duration
θ	Contact angle
θ_{CB}	Cassie-Baxter contact angle
θ_y	Intrinsic contact angle
θ_w	Wenzel contact angle
z_F	Depth of focus

Chapter 1

Introduction

1.1 Research motivation

The research presented in this thesis is primarily concerned with laser surface texturing for the modification of wettability properties. The applications of laser surface texturing have been widely explored over several years. A number of advantages can be obtained with the use of lasers for modifying the surfaces of materials compared with traditional manufacturing methods such as mechanical machining and etching techniques. These include chemical cleanliness, controlled thermal penetration and distortion, non-contact processing, reduction in the number of required tools and ease of automation[1].

Due to the flexibility of lasers, most metallic materials are suitable for surface texturing. The accuracy and versatility of laser processing are highly valuable, especially with the use of high-value products. The flexibility of a laser process lends itself well to low volume high-value production such as in the aerospace industry (Figure 1.1).

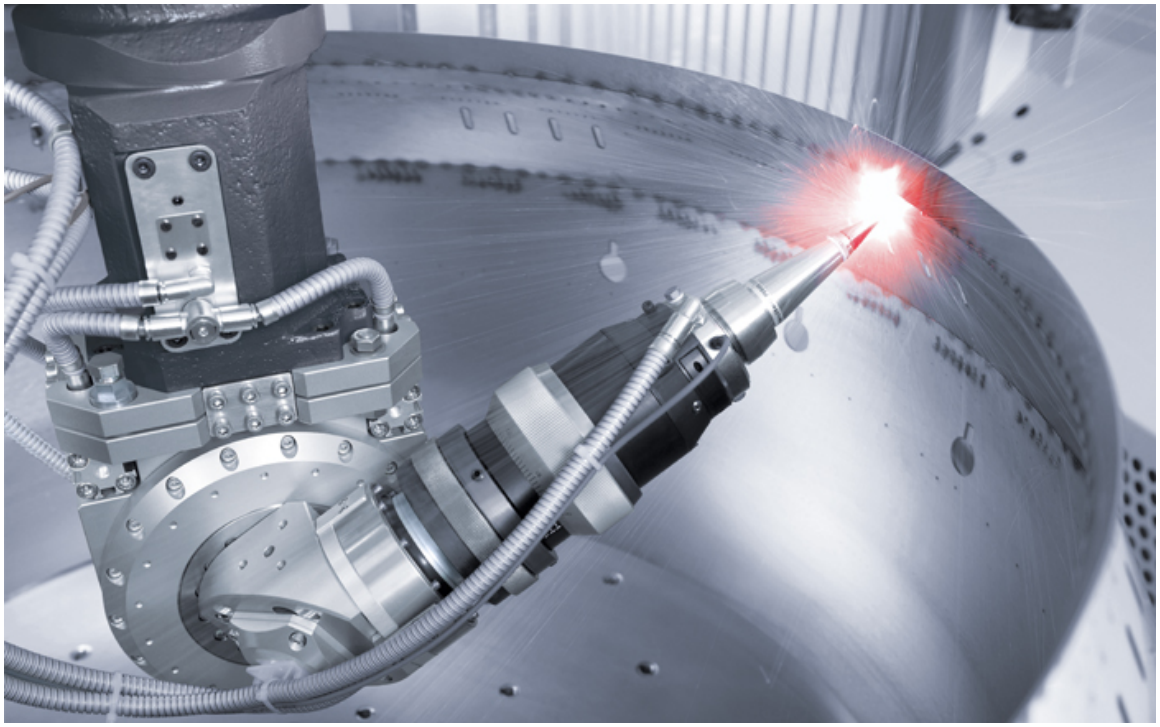

Figure 1.1: *Laser drilling of a combustion chamber LASERTEC*

Recently, laser surface texturing for the modification of wettability properties of metals has been the subject of numerous research studies due to its potential benefits and applications, such as self-cleaning surfaces, efficient catalysts and fluid transport[2–6].

Currently, continuous wave (CW) and long pulsed lasers (milli- and microsecond pulse duration) are widely used in different manufacturing industries; this is due to the cost-effectiveness of these systems and their use. Typical processes for these lasers include cutting, welding and additive manufacturing. For surface texturing, shorter pulsed lasers are typically required. Several laser systems are currently available on the market. Picosecond (ps) and femtosecond (fs) pulsed laser system have been proven reliable for the surface texturing of materials for the modification of wettability properties due to the high precision and low thermal input. However, the high cost and complexity of equipment and the environment required for the correct operation has limited these systems to purely research purposes to date. Besides this, the low manufacturing volume capabilities increases the limitation for the use of these systems in industry.

The use of fibre lasers has been increasing in the manufacturing industry in recent years. The power output of CW fibre lasers has been increased at a steady pace. This increase in power capabilities has made of fibre lasers one of the fastest-growing technologies due to the high demand of rapid growth industries such as additive manufacturing (Figure 1.2).

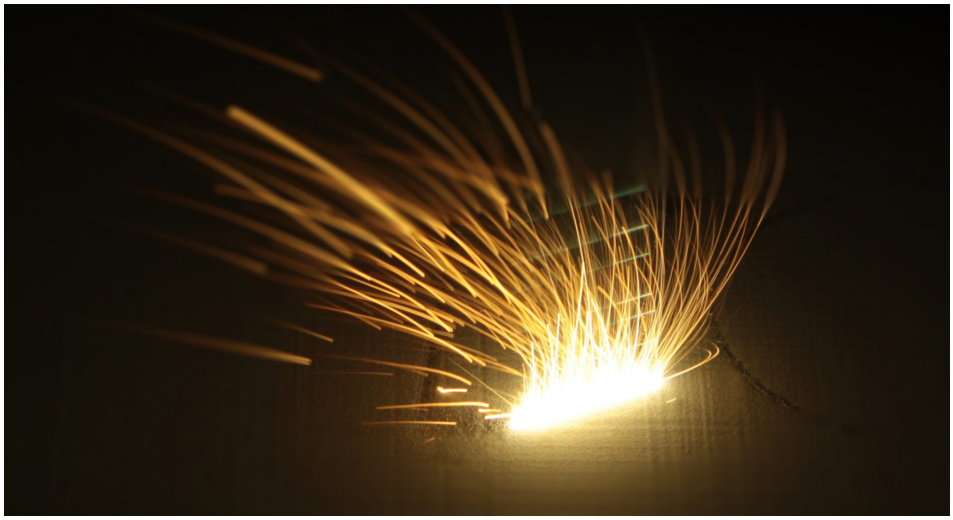

Figure 1.2: *Additive manufacturing process from Renishaw*

The introduction of high power fibre lasers in the manufacturing process has been a success due to a number of advantages over competing technologies such as gas-based and solid-state lasers. Maintenance-free, compact robust designs and minimal moving parts of fibre laser systems have made this technology a revolutionary tool for the industry. Furthermore, a relatively high wall-plug efficiency ($\sim$40%), compared with gas-based systems such as CO_2 lasers ($\sim$17%), makes these systems an important tool in manufacturing industries[7, 8].

Laser processing with pulsed lasers is well established, and although there are regular incremental improvements in laser source capabilities, step changes are few and far between. The majority of pulsed lasers rely on q-switching to generate the high peak power densities by using an external crystal to store and release energy in pulses. These devices are limited by q-switching technology that limits the flexibility of pulse frequency, pulse length and pulse energy.

A new range of pulsed fibre lasers that do not rely on q-switching to generate nanosecond pulses has been recently introduced; this gives significantly more flexibility in terms of pulse length, peak pulse power and frequency, giving users a broader range of processing parameters. The low cost and flexibility of these laser systems make them attractive for the manufacturing industry.

Fabrication of surfaces with modified wettability properties has been researched and developed through different manufacturing methods due to its different applications such as anti-icing, anti-corrosion, self-cleaning surfaces, etc. The ability to repel water from the surface due to the roll-off of the liquid without wetting it makes super-hydrophobic surfaces an interesting and high valued functionality of a product. A key unique aspect of laser technology is to be able to modify surface properties only where it is required[9].

There is an opportunity to develop laser surface texturing techniques capable of selectively modifying the wettability properties of materials and products. Ti-6Al-4V is one of the most used titanium alloys in various industries due to its corrosion resistance and high strength with relatively low weight[10]. Applications of interest are water repellence, self-cleaning and particularly de-icing of the materials. The de-icing effect is a particularly interesting property in the aerospace industry due to the ability to decrease the threat of ice accumulation on the aircraft surfaces. This can reduce the possibility of a dangerous change in the aerodynamic shape of the aircraft on icing conditions[9, 11].

1.2 Aim and objectives

The aim of this research is the laser surface texturing of Ti-6Al-4V with a nanosecond pulsed fibre laser for the controlled modification of wettability properties. The main goal is to create a super-hydrophobic state of the surface, meaning that it is extremely repellent to water. The requirements for this surface state are a low surface energy which is related to surface chemistry and topography. The focus of this thesis is to carry out a thorough investigation of the material ablation, the micro-structures created and the process conditions affecting surface chemistry. The main objectives of this research are:

- Identify the key parameters for the laser surface texturing with a nanosecond pulsed laser and the effects of pulse energy and pulse duration in the creation of surface micro-structures.
- To investigate different scanning techniques for the creation of stable super-hydrophobic surfaces on Ti-6Al-4V.
- To identify the necessary conditions for the stabilisation of a super-hydrophobic micro-surface over time.
- Identify the effects on wettability properties of adding laser-induced periodic surface structures (LIPSS), using ultra short pulsed lasers, on the created micro-structure and to develop an alternative surface structure with a single nanosecond pulsed laser.

1.3 Thesis structure

This thesis consists of six chapters. The current chapter provides an early introduction and insight into the motivation behind the research, including the main objectives of the project.

Chapter 2 contains a detailed review of the background and the current state of the art research on laser surface texturing for wettability modification. A detailed observation is given for the use of lasers and their effects on the surface texturing of metallic materials, in particular on Ti-6Al-4V.

Chapter 3 gives detailed information about the systems and equipment used for the presented research. Arrangements and research methods are explained and detailed through the research project. Information about the experimental procedures and material selection used throughout the thesis are explained. The market opportunities are highlighted and the possible application of the research is provided.

Chapter 4 presents a detailed study of the ablation process with a nanosecond pulsed fibre laser on Ti-6Al-4V. This analysis was carried out with single and multiple pulse ablation processes for a range of pulse durations from 65 to 200 ns. The influence of pulse duration in the ablation process is characterised in order to create a map of suitable processing parameters for laser surface texturing processes on the titanium alloy.

Chapter 5 presents the experimental results with the creation of micro-pillar surface structures on Ti-6Al-4V with varying pulse durations in order to explore the effects on the created surface structure. The optimisation of the surface texturing process is explored as well as the influence on the wettability properties of Ti-6Al-4V. The oxidation of the micro-structure is explored and the influence in the wettability modification is highlighted through the analysis of the oxidation state of different created surfaces.

Chapter 6 highlights the improvements in the wettability properties with the implementation of a hierarchical surface structure (micro and nano surface structure). The

use of LIPSS for the creation of nano-structures on the material as a viable method for the surface modification. Surface oxidation analysis of the hierarchical surface is explored in order to verify the modification in the material and how this impacts on the wettability behaviour. An alternative surface texturing technique with the use of a single nanosecond pulsed fibre laser is also explored for the development of super-hydrophobic surfaces on the titanium alloy.

Chapter 7 presents a discussion of the obtained results from chapter 4 to 6 including comparisons and references to previous investigations on laser surface texturing for super-hydrophobic behaviour.

Chapter 8 highlights the main findings through the research process presented in the current work and provides recommendations for possible future work for the creation of super-hydrophobic surfaces based on the research findings.

1.4 Summary

The main motivation for this research is based on the modification of the wettability properties of Ti-6Al-4V with laser surface structuring. The increasing use of laser systems in manufacturing processes and the wide application for materials with targeted modified wettability properties provide a high potential for industrial applications. This thesis focusses on the use of a state of the art robust nanosecond pulsed fibre laser suitable for industrial applications. Compared with complex femto and picosecond pulsed laser systems, the relatively low cost, flexibility and industrial robustness of the nanosecond pulsed fibre laser makes this research of significant interest for manufacturing processes.

Chapter 2

Literature review

2.1 Introduction

This chapter presents the background and a detailed overview of different surface texturing processes produced by conventional manufacturing techniques as well as with state of the art laser systems. Relevant information regarding laser technology and operation principles is also reviewed emphasizing advantages and disadvantages between the different types of laser systems. An overview of the material interaction mechanisms for surface texturing with short and ultra-short pulsed lasers is also explored in order to provide the background for this study.

The background theory and fundamental characteristics of super-hydrophobic surfaces are also explored in order to understand how the surface structure can modify the wettability properties of the materials. This provides the relevant information needed for the design of surface micro-structures for the wettability modification of Ti-6Al-4V to be explored in this study.

2.2 Surface texturing

Surface texturing processes are associated with the creation of tribological features, generally associated with the creation of grooves or dimples, in order to enhance different properties of the modified material or product. These types of features have been widely explored due to the benefits that an appropriate surface texture can provide, such as altering the flow of lubricants or even reducing the tool wear in materials machining[12, 13].

Tool quality and endurance are of significant importance on surface texturing of metallic materials. Slight surface scratch or defects on the finished product can result in complete rejection depending on the manufacturing requirements. Several investigations have been undertaken in order to improve different tribological effects on metallic surfaces, increasing of surface roughness for increasing friction values, wear and temperature between sliding textured surfaces[14–16].

Several surface texturing techniques have been developed through time in order to implement the desired surface topography for a wide range of applications. The implementation techniques can be divided into three main classifications, additive, formative and subtractive, a brief description will be presented in the next sections.

2.2.1 Additive techniques

Modification of surface structures can be achieved by the addition of thin films of substrates on the material surface. This process is generally based on material being deposited through physical or chemical methods. Chemical methods rely on chemical reactions between the adding material and the substrate, forming a strong bonding between both of them. Physical methods are usually based on the joining of the deposited material through solidification, aggregation and sputtering[17].

Chemical methods

- **Chemical conversion coating**: Is a passive method where the original surface is covered with a chemical component in order to generate a chemical or electrochemical reaction, producing a protective layer or even a surface texture. This method is widely used on corrosion resistance enhancement of different products in the automotive industry. However, due to industry competition, most of the specific details regarding several of these processes are closely protected[17, 18].

- **Chemical vapour deposition**: Is produced when the substrate is subjected to a thermal process inside a chamber containing one or more gases. A chemical reaction is then produced between the heated substrate and gases resulting in a thin layer of material being deposited on the substrate. This method can be used for tribological applications and protective coatings on metallic materials[19].

- **Electrochemical deposition**: With this technique, a metal coating is created on the substrate. In order to do this, the substrate is used as a conductor and submerged in a solution containing the desired metal ions or chemical elements. The materials within the solution are then deposited on the substrate by electrolysis[20].

Physical methods

- **Physical vapour deposition**: Is similar to the chemical vapour deposition (CVD) where a thin layer of vapour containing the desired elements is deposited in the substrate. The evaporation process is achieved inside a vacuum chamber activated by a physical process. The evaporated particles are then ejected and deposited on the material substrate forming a thin layer with the desired surface characteristics[21].

- **Patterned curing process**: Within this method, a thin layer of polymer or metallic material is applied to the substrate and cured with the use of chemical curing agents, UV radiation or heat. This creates a solid film adhered to the surface with good chemical and mechanical resistance, especially when metallic particles are applied. One of the bottlenecks for this method is the required time for the curing of the material deposited on the substrate[17].

- **Ink-jet material deposition**: In this process, the material is deposited into the substrate in a liquid form and then solidified in order to create the required surface structures. Within this method metals, polymers and ceramics can be deposited into the substrate. The required methods to transport the solid particles vary depending on the material, and can vary between the heating of the particles or their transport through a liquid solution[22, 23].

- **Laser cladding**: Similar to ink-jet printing laser cladding relies on material being deposited into the substrate. The material is usually in a powder form transported via gas flux and then melted into the substrate due to the heat provided by a controlled laser beam. Within this method, the molten material is adhered to the substrate and then solidified in order to create the desired surface features or producing complete parts into the substrate[24].

Figure 2.1: *Laser cladding process[25].*

2.2.2 Formative techniques

This process can be characterised by the plastic deformation of the substrate and subsequent deposition in a different location for the formation of surface structures[17].

- **Surface wrinkling**: This method consists in the use of different methods to modify the substrate, such as oxidation or coating processes on thermally expanding polymers. The film of the material is then subjected to stress due to the cooling of the polymer creating a buckling in the surface. This patterning process is often used for the modification of thin metal foils and can find applications on optical sensors[26].

- **Mechanical material displacement**: This type of surface texturing processing is commonly known as embossing. Within this method a plastic deformation is applied into the substrate in order to transfer the tool shape into the surface. This process usually requires the use of hardened and abrasive tools to be capable of producing the required shape into the material surface[17].

- **Laser shock peening**: This process is created when the material substrate is covered by a sacrificial layer. This layer is then processed with a high power pulsed laser providing energy output usually in the range of 10-500 J/pulse and pulse durations under 100 ns into the sacrificial layer. This process produces a shock wave that is then transmitted into the material substrate producing a plastic deformation and then modifying the surface. The use of the sacrificial layer can be beneficial in order to avoid the melting or even ablation of the substrate. This method has been shown to improve fatigue performances and mechanical properties of different alloys[27]. Figure 2.2 shows a schematic representation of laser shock peening.

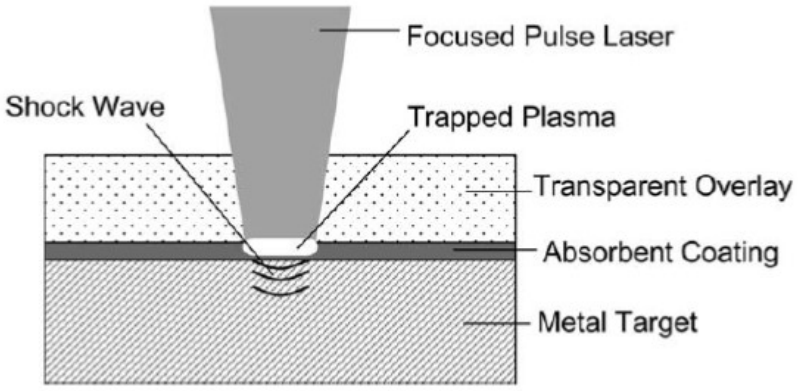

Figure 2.2: *Schematic image of laser shock peening process[27].*

2.2.3 Subtractive techniques

Chemical methods

Chemical etching is one of the most used methods for the modification of surface materials in the industry due to low cost and efficient material removal. The process is based on the removal of material from the surface due to the chemical reactions between reactive agents and the substrate[17].

- **Wet etching**: Is produced when the substrate is submerged on a chemical solution or sprayed with it. The chemical solution produces a reaction on the substrate capable of removing material due to a chemical reaction. In order to control the shape and features produced by this technique, a mask shield resistant to the chemical components is placed on the substrate avoiding the material removal on the surface covered by the mask[28].

- **Dry etching**: In this process, the material is removed from the substrate due to etchant gasses or plasma. However, these type of processes requires expensive equipment such as vacuum chambers in order to produce a suitable surface texturing. The most common methods for dry etching processes are plasma etching, where the substrate material is processed with the kinetic energy of particles delivered by ion beam, electron beam or photon beam, evaporating the material from the surface. Gas-phase etching, etchant is used to produce a gaseous reaction on the substrate thus removing material from the surface. Reactive ion etching

is a process where reactant gases are excited to ions using a strong electrical field directing them to the material substrate under low-pressure conditions[17, 28].

Mechanical methods

- **Grinding**: In this process, an abrasive material is used in a grinding tool or wheel in order to generate an intense local stress in the contact point of the substrate. This removes the material from the surface due to brittle fracture or plastic deformation of the substrate[29].

- **Honing process**: This method consists of a low-velocity abrasive process usually produced by a rotating tool with one or more abrasive stones in order to remove material from the substrate. This process is usually used for material finishing removing waviness and traces of grinding on the surface[30].

- **Patterned erosion process**: Under this method, an abrasive particle stream is applied into the substrate at high pressures. The particle size within the stream is selected according to the size of the required features. This method includes bead blasting, sandblasting, shot blasting and soda blasting[17].

- **Ultrasonic machining**: In this process a vertical tool transmits ultrasonic vibrations, usually with frequencies of $\geq$ 20 kHz, into an abrasive slurry between the tool and the substrate. The vibrations produced by the tool are transferred into the abrasive particles within the slurry, producing an interaction between the abrasive particles and the substrate in order to remove material due to microchipping[31].

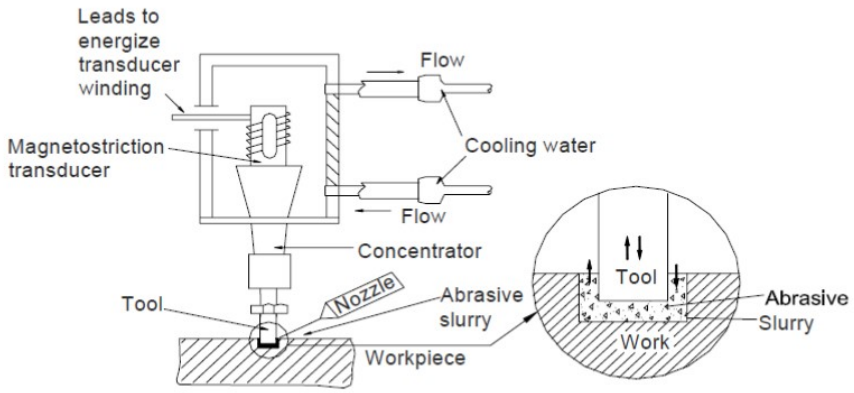

Figure 2.3: *Schematic for ultrasonic machining process[32].*

- **Vibro-mechanical texturing**: This process is based on a standard turning process. In the standard process, a cutting tool engages a rotating work-piece removing the material depending on the cutting tip geometry and depth of cutting parameters. The vibro-mechanical texturing process follows a similar approach but applies an ultrasonic vibration into the cutting tool in a perpendicular direction to the work-piece and thus creating the required surface texture due to the removal patterns produced by the ultrasonic vibrations[33].

Methods involving high temperatures

- **Electrical discharge texturing**: Is a variant of the Electrical Discharge Machining process(EDM). Within this process, the material is removed from the substrate due to the electrical discharge applied to the substrate by an electrode(tool). The substrate is submerged in a dielectric fluid and then an electrical discharge is applied through the electrode(tool), producing a spark and effectively removing material from the substrate due to a thermal vaporisation mechanism[34]. This process can be undertaken without the need for a dielectric fluid between the electrode (tool) and the substrate. In this case, the electrode is placed at a shorter distance from the substrate and a high voltage is induced in order to create an electric arc. This creates the required spark and high temperature in the substrate and thus, producing the removal of material[17, 35].

- **Focussed ion beam**: This process relies on a focussed ion beam in order to remove material from the substrate due to the high energy density and the small diameter of the beam. The material is then removed by physical sputtering, although, part of the material is re-deposited on the substrate. In this process, gas can be used within the chamber processing in order to increase the removal rate[36].

2.3 Laser surface texturing

This method is based on the interaction of a focussed laser beam with a substrate. This interaction can produce heating, melting, vaporisation or even ablation at very high intensities and short pulse durations. The ablation process triggers the material removal from the surface similar to the process achieved through Focussed Ion Beam (FIB) described in the previous section[17]. In order to fully understand the mechanics behind the process, laser ablation is described in the next section.

2.3.1 Laser ablation

The laser ablation mechanism can be described as the heat transfer into the substrate due to the excitation of molecules produced by the laser beam. The substrate is then heated causing the vaporisation of the material and the posterior ejection of the removed particles[37]. The ablation process is usually produced with pulsed laser systems in the range of nanoseconds to femtoseconds. The substrate removal mechanism can be divided into three stages:[38]

- **Absorption of energy**: In this stage, the substrate is irradiated with the laser beam usually at the focal point of the system in order to reduce the beam diameter and thus increase energy intensity within the surface. The substrate is then heated above the vaporisation point of the material initiating the ablation process[39]. The removed particles through the vaporisation process are then ejected from the substrate forming a plasma plume that can be continuously excited by the laser beam depending on the pulse duration used[40].

- **Transformation**: The ejected substrate particles are then suspended into the plasma plume. The suspended particles are then mixed with the ambient conditions inducing a chemical reaction of the particles due to the high-temperature conditions of the plasma plume. This can create new compounds on the debris from the laser ablation process[40].

- **Condensation**: The intense heat produced by the laser pulse and the plasma formation starts to diffuse into the surroundings. This last stage produces the solidification of ejected particles and molten material around the processed area of the substrate. The deposition of new elements particles is possible due to the possible chemical reactions within the plasma plume. [40, 41].

Figure 2.4 shows a schematic representation of the three stages of the substrate removal process through laser ablation.

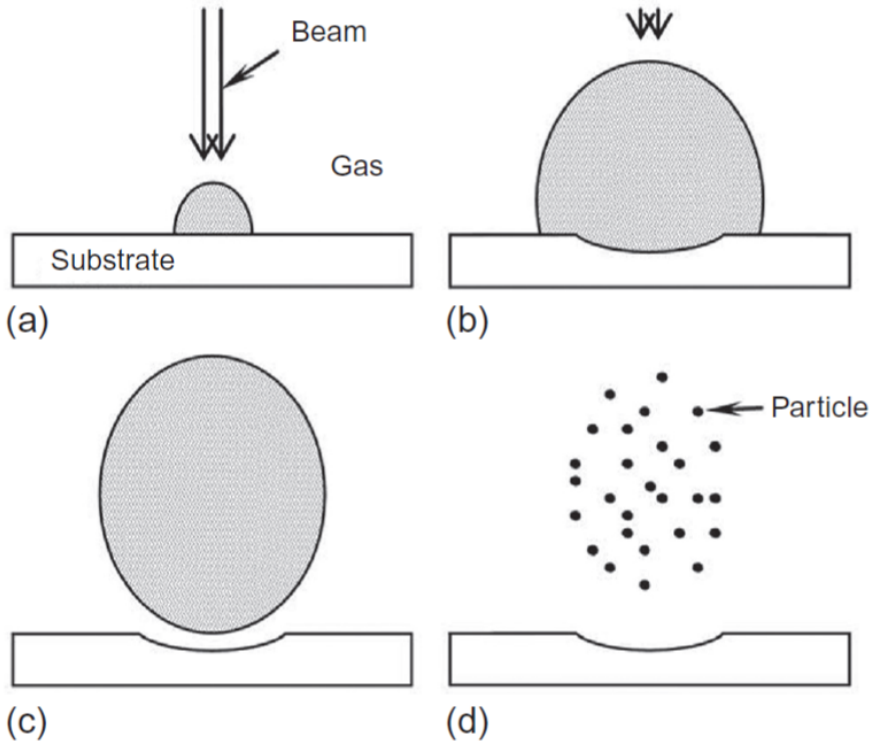

Figure 2.4: *Schematic diagram of the stages for material removal through laser ablation: a) initial beam interaction, b) continuous excitation due to laser irradiation, c) end of the laser pulse, and d) condensation of removed substrate particles[41].*

Laser ablation process can be achieved with both short (nanosecond) and ultra-short (pico and femtosecond) pulsed laser systems. Both of these systems transfer the energy into the surface layer, the penetration of this energy is indicated by the optical penetration depth given by Equation 2.1:

$$l_s = \frac{1}{\alpha} \tag{2.1}$$

Where:

- α is the material absorption coefficient for the laser wavelength used.

Laser surface processing relies on heating the substrate above the vaporisation point in order to remove material. In order to understand the heat interaction within the substrate the thermal diffusion length can be calculated by Equation 2.2:

$$l_{th} = \sqrt{D\tau_p} \tag{2.2}$$

Where:

- D is the heat diffusion coefficient of the material.
- τ_p pulse duration of the laser.

Equation 2.2 describes the diffusion length in correlation with the pulse duration of the processing laser beam. As can be observed if the pulse duration of the laser increases the thermal diffusion will increase as well. This means that an area bigger than the laser beam spot size is affected on the material substrate. This is typically observed in laser ablation processes with pulse durations in the range of nanoseconds and above. However, if the pulse duration decreases, typically with picosecond and femtosecond pulse durations, the area affected on the material substrate can be reduced enough to be confined within the laser beam spot size area[42].

The difference in the pulse duration has a great impact on the shape and quality of the surface structures produced. This differences can be observed in Figure 2.5.

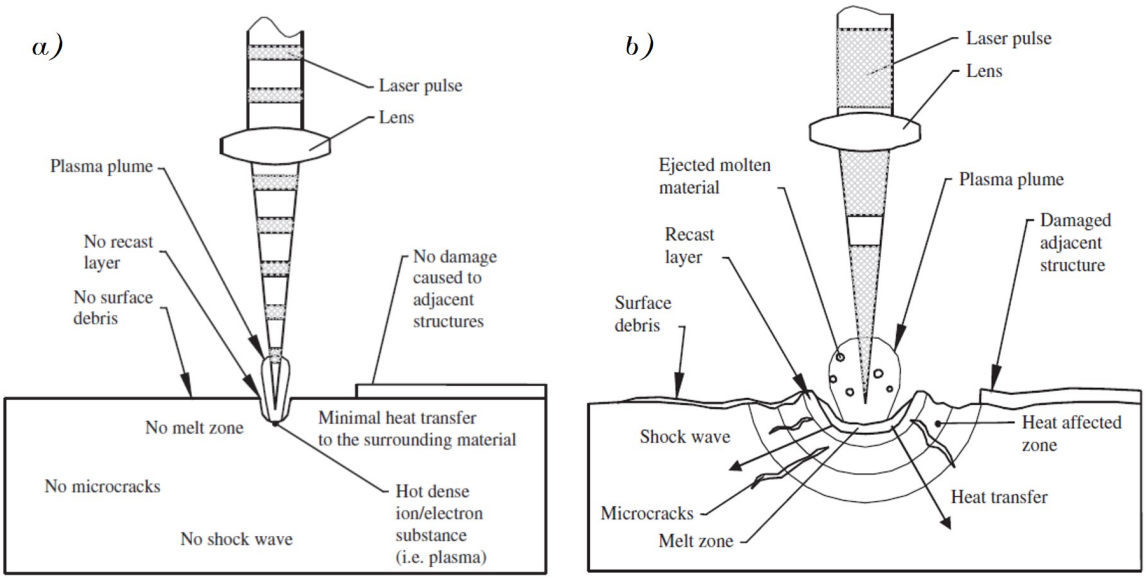

Figure 2.5: *Schematic diagram of laser ablation under different pulse durations, a) Laser ablation induced by ultra-short pulsed laser, b) Laser ablation induced by short pulsed laser[43].*

Figure 2.5 shows the main differences created on the substrate material by laser ablation under different pulse duration regimes. As can be observed a clear advantage can be observed for laser ablation with ultra-short pulsed lasers (picosecond and femtosecond pulse durations) over short pulsed laser ablation (nanosecond).

With ultra-short pulsed laser ablation the material is removed from the substrate due to a direct transition from the solid to vapour state. This reduces the thermal effects induced into the material substrate especially with laser ablation in the femtosecond regime[42, 44]. The picosecond laser ablation regime can create a small amount of molten material deposition on the surface, however, the ablation process still follows a direct material transition from solid to vapour[45].

The laser ablation with short pulsed lasers (nanosecond regime), produces a different transition state of the substrate. Due to the longer interaction time of the laser pulse, the material is melted and then heated until particles of the molten material are evaporated. Due to the vaporisation process being produced in the liquid form material, part of this is ejected from the substrate due to the plasma and vapour formation. This creates the surface debris accumulation shown in Figure 2.5 (b). Nevertheless, not all the molten material is ejected from the substrate, therefore, the remaining molten material is solidified after the laser pulse irradiation and a recast layer is formed on the material surface[43].

The short pulsed laser ablation (nanosecond regime), leads to a significant increase in the amount of material removed from the substrate with a single pulse compared with ultra-short pulsed ablation[46]. This also increases the molten material deposition on the material substrate increasing the overall roughness of the surface structure created. These effects can improve the surface structuring process, reducing the amount of time required for their generation. The generation of surface structures using a short pulsed laser ablation process is the main focus of this thesis and their results are explored in the following chapters.

2.3.2 Laser Induced Periodic Surface Structures (LIPSS)

Laser induced periodic surface structures or LIPSS are ripples-like surface structures induced by circular or linearly polarized lasers[47]. This type of structures can be produced in different types of materials such as metals, semiconductors and dielectrics[48]. Different theories behind the LIPSS formation have been proposed through time, including the interference of the laser beam radiation with the surface polaritons(a type of quasi-particle), proposed by Emmony *et al*[49]. Interaction of the laser radiation with the surface roughness of the material producing inhomogeneous absorption of the laser beam, to the effects of electromagnetic waves on the surface due to the laser radiation[50].

One of the main characteristics of the LIPSS is the separation between the induced ripples which is in correlation with the wavelength and polarisation of the laser beam due to the electromagnetic wave interaction at the surface of the material. This means that the separation between each one of the ripples is usually similar to the laser beam wavelength and with a ripple orientation perpendicular to the laser polarisation on strong absorbing materials such as metals and semiconductors. For polymers the ripple orientation is parallel to the laser beam polarisation[50].

LIPSS with periods similar to the wavelength of the incident laser beam used for their creation are called Low Spatial Frequency LIPSS (LSFL). The interaction of an electromagnetic wave scattered through the material surface due to the laser irradiation is generally accepted as the mechanics behind the generation of these type of LIPSS.[50]

However, LIPSS with a distance between the induced ripples significantly smaller in comparison with the wavelength of the laser beam used for their creation have been observed. These type of LIPSS are usually called as "non-classical" LIPSS or High Spatial Frequency LIPSS (HSFL). These type of ripple structures can be oriented perpendicular or parallel to the polarisation of the incident laser beam depending on the irradiated material[51–53]. The mechanics behind the creation of these type of LIPSS is still being discussed with several theories proposed such as, mechanisms of self-organisation, oxidation, the involvement of plasmonic effects and more[50]. Figure 2.6 shows the two types of laser induced surface structures (LSFL and HSFL).

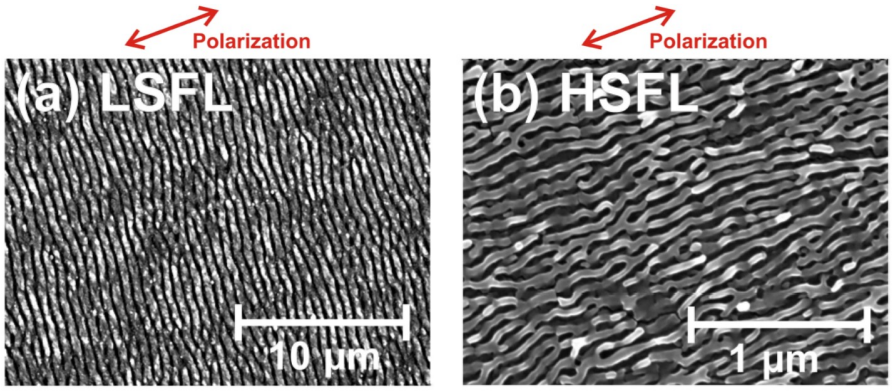

Figure 2.6: *SEM image of (a) Low Spatial Frequency LIPSS (LSFL) and (b) High Spatial Frequency LIPSS (HSFL) formed on Ti-6Al-4V surfaces and similar laser polarisation[50].*

2.4 Laser systems

2.4.1 Introduction

Light Amplification by Stimulated Emission of Radiation (LASER) is the main mechanism for the laser beam generation. Stimulated emission is a phenomenon postulated by Albert Einstein in 1917 as one of the three interaction processes between light and matter. Light produced by normal sources such as the sun or light bulbs produces radiation in all directions with various frequencies components. In contrast, the radiation produced by a laser is highly-collimated with a narrow spectral linewidth, focussing the radiation in a single direction. The radiation direction within a laser is determined by the axis of the optical resonator[54].

2.4.2 Operation principle

The basic principle for the generation of a laser beam is the stimulated emission due to light travelling down an optic axis confined between two mirrors. This makes the light to oscillate between the mirrors back and forth. An gain medium is placed on the optic axis between the mirrors. One of these mirrors must be partially transparent to the beam wavelength in order to transmit the rest of the light to produce the laser beam out of the system. The medium amplifies the oscillations of light due to the stimulated emission mechanism. This gain medium determines the wavelength of the laser beam and can be semi-conductor, solid-state, liquid, gas or relativistic electrons beam(free electron). This produces a photon from the gain medium to be stimulated at high energies by the light photon travelling within the optic axis(population inversion). The direction and phase from the stimulated photon will be equivalent to the incident photon, producing photon oscillation along the optic axis. In order to the activate the gain medium, a pumping system is required, this can be an electric current, a chemical reaction, a focused pulse of incoherent light, glow or radio frequency discharge[55–57].

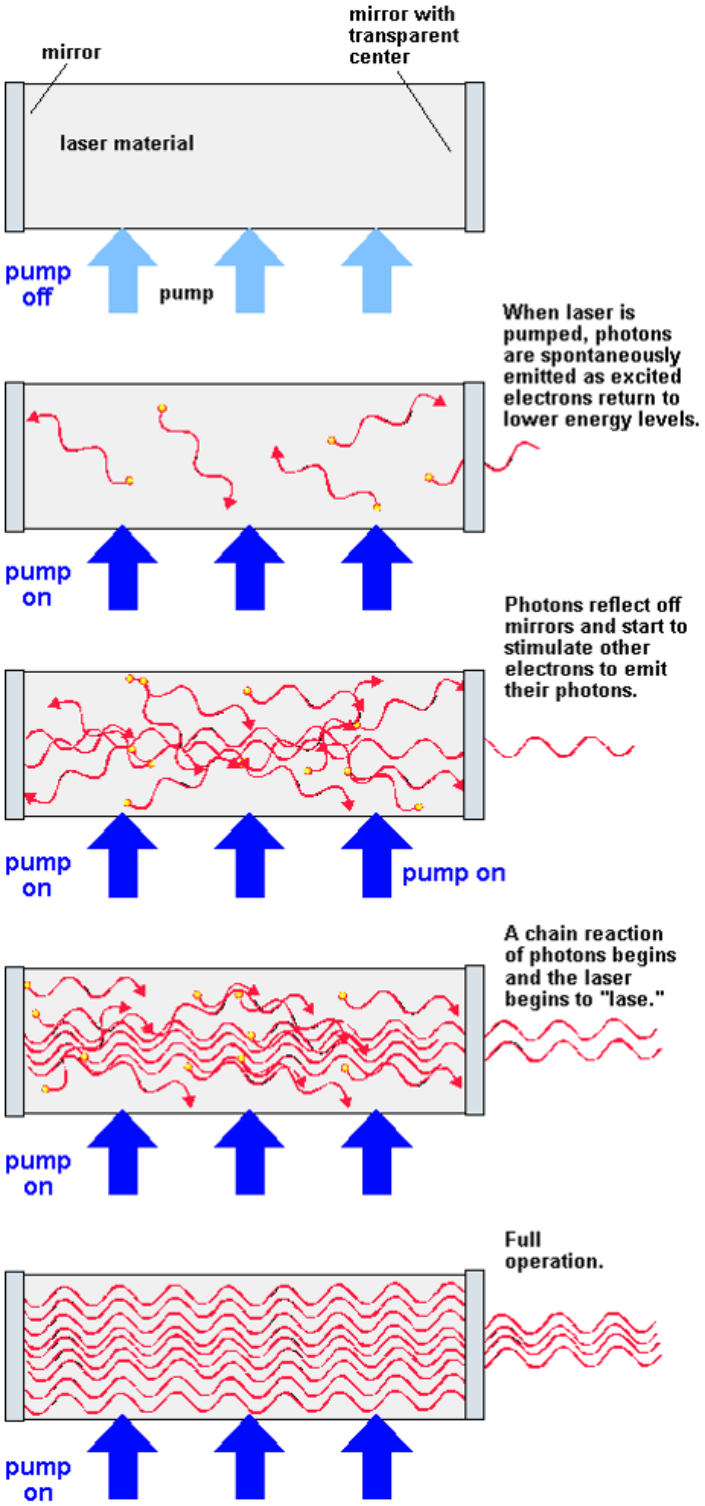

Figure 2.7: *Schematic diagram of the generation principle of lasers[56].*

Figure 2.7 presents an schematic representation of steps for the laser beam generation process according to the operation principles previously described.

2.4.3 Fibre lasers

Fibre laser operation is based on using an optical fibre as the active medium. This type of laser uses a double clad design confining the pump light in a multi-mode optical waveguide. The double clad is around the rare earth doped central core(gain medium), enabling the use of low brightness high power diodes as a pump. The confinement produced by the double clad force the pump light to repeatedly interact with the central core (gain medium) along the fibre length. Low maintenance requirements and robustness against thermal effects are two of the main advantages over other types of laser sources.[58]. Figure 2.8 shows a representation of the fibre laser.

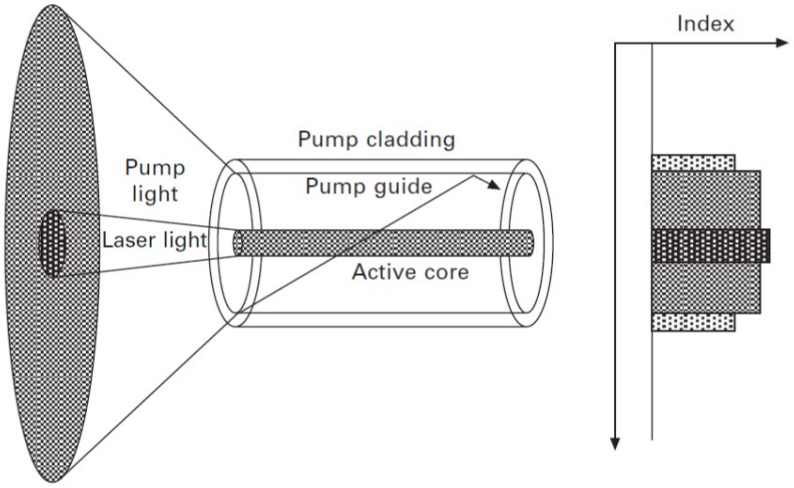

Figure 2.8: *Schematic representation of a double clad optical fibre[58].*

Due to the long geometry of the optical fibre, this type of laser has a superior thermal load handling. This thermal handling capability allows the use of fibre lasers in manufacturing environments with minimum maintenance requirements. However, this type of lasers usually requires a power amplifying method in order to obtain energy levels suitable for laser processing[58].

2.4.4 Operation modes

Laser systems can be operated in two basic modes, continuous wave (CW) and pulsed mode. Continuous wave laser delivers a constant, uninterrupted laser beam, usually with a stable output power. In a pulsed mode lasers, the beam power is delivered in short period of time. This mode usually emits a high energy in the period of time defined by the pulse duration producing a high laser peak power as shown in Figure 2.9.

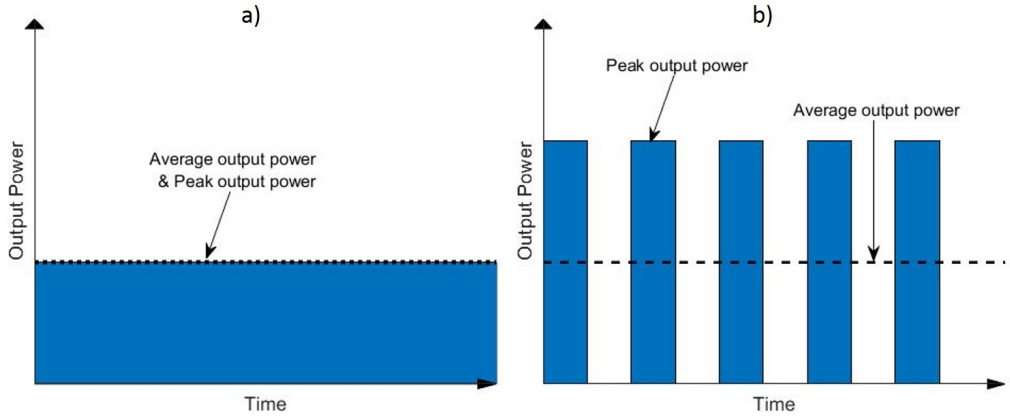

Figure 2.9: *Schematic representation of laser operation modes, a) Continuous wave mode, b) Pulsed mode.*

In this thesis, the pulsed mode of the laser is used for the surface texturing of the titanium alloy. Several technologies are available for the generation of short and ultra-short pulsed lasers, a brief description is presented in the next section.

2.4.5 Generation techniques for short and ultra-short pulsed lasers

Q-switching

Laser pulses through Q-switching technique are generated by stopping the laser generation accumulating the population inversion within the gain medium. In order to stop the laser generation, an increase in the resonator losses are produced through an electro-optic modulator or switch, thus blocking the resonator. The increase in the resonator losses are produced by changing the Q factor of the resonator. If the Q factor (or resonator quality) increases, the resonator losses are decreased. The low Q factor on the resonator is then maintained until the gain medium has the maximum energy

stored. After this, the resonator losses are decreased by increasing the Q factor and the laser pulse is produced. This technique allows high pulse peak power levels generation in the range of kilo-Watts (kW), mega-watts (MW) or even giga-watts (GW)[59]. Figure 2.10 presents the temporal pulse generation with a Q-switching technique.

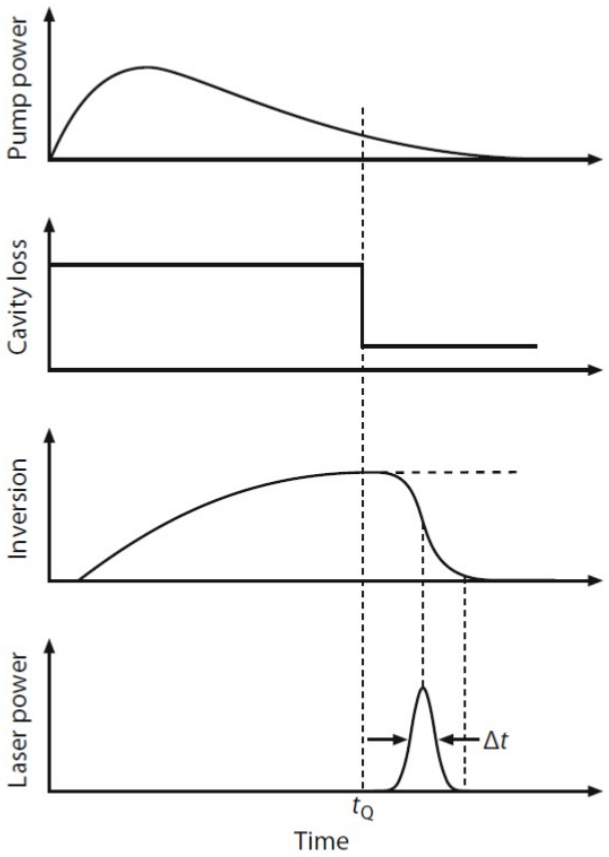

Figure 2.10: *Temporal development of a laser pulse through Q-switching technique. Pump power or lamp output, resonator or cavity loss, inversion or population difference of the upper and lower laser level, and laser power output[59].*

Mode locking

Within a normal laser, the beam light is reflected between the two mirrors back and forth. Due to this light oscillation within the cavity, standing waves are produced due to the light interference. These standing waves produce longitudinal modes within the laser cavity. These modes oscillate independently from each other almost like an independent laser within the laser cavity[60, 61].

In order to create a laser pulse with these longitudinal modes, the oscillation must be modified in order to create a fixed phase between the individual modes. When a fixed phase is induced in the different longitudinal modes, a constructive interference between these modes will occur producing a localized radiation in space forming a single laser pulse with high intensity[60, 61]. This method can be seen in Figure 2.11.

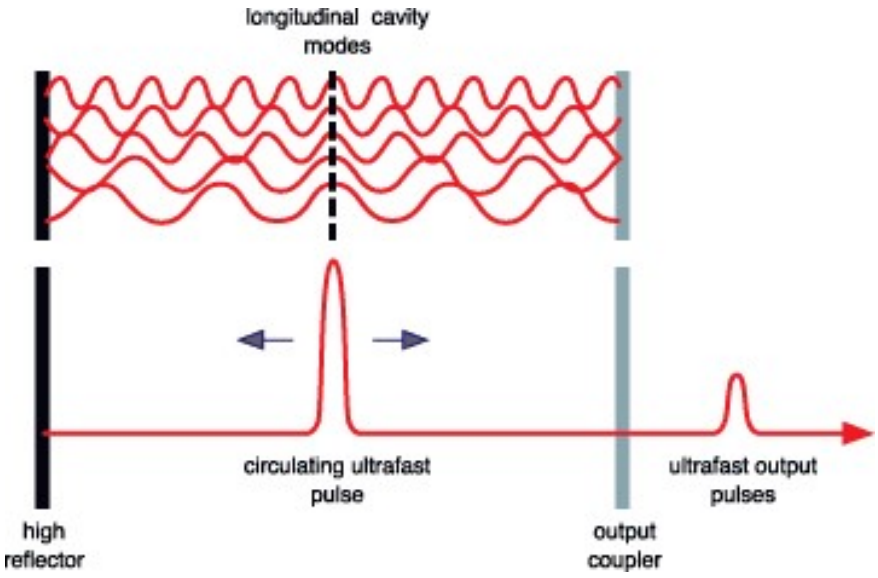

Figure 2.11: *Mode locking laser pulse generation[62].*

The mode locking pulse generation technique can be divided into active mode locking and passive locking. Active mode locking relies on an external signal in order to induce the fixed phase of the different longitudinal modes. This signal is usually induced by an electro-optic or acousto-optic modulator modifying the resonator losses in order to modulate the phase of the longitudinal modes[60].

In a passive mode locking, the modulation is achieved through the adding of a saturable absorber generating the periodic modulation required for the fixed phase of the longitudinal modes. Nowadays most of the passive mode locked lasers use semiconductor saturable absorber mirror(SESAM). This device basically replaces the rear mirror in the laser resonator[60].

In order to amplify the power of the laser pulse a Master Oscillator Power Amplifier(MOPA), is used as one of the most common methods. This method is composed by a Master Oscillator generating the seed laser and supplying a small signal pulse train in the range of mW. This can be a diode laser or a q-switched fibre laser. An optical amplifier is then used to increase the laser power of the seed laser through the gain medium. An advantage of a laser diode seed MOPA is the ability to change the duration and the temporal shape of the pulse[63]. An schematic of the MOPA structure is shown in Figure 2.12.

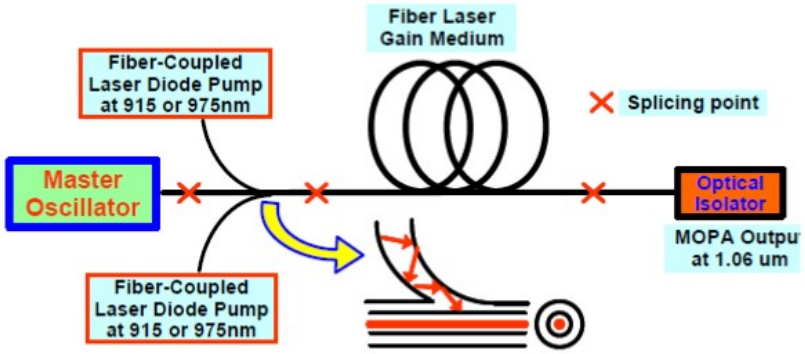

Figure 2.12: *Schematic of MOPA for a pulsed fibre laser[63].*

As a modification to the fibre laser, an oscillator or cavity can be created with the addition of a fibre Bragg grating to create a Master Oscillator. This type of modification allows the increase of the power up to tens of m, whereby a set pulse train can be subsequently amplified[64]. A schematic representation of the Bragg grating based fibre oscillator is shown in Figure 2.13.

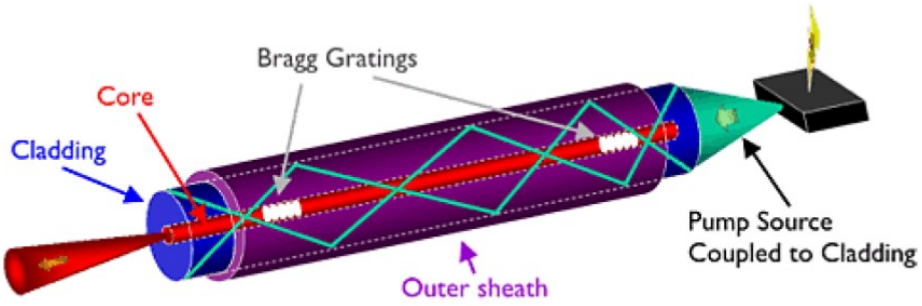

Figure 2.13: *Schematic representation of Bragg gratings in a fibre laser core. (Image courtesy of SPI Lasers, UK)*

Chirped pulse amplification

Power amplification of ultra-short pulses is generally required due to the low power generated due to the small pulse duration. The energy of the pulse can be amplified by cavity dumping, or a longer cavity design, however, the increase of femtosecond laser pulses to μJ regime will increase the peak power into levels that would damage or destroy most of the optical equipment required for the laser generation. In order to avoid this, the pulse is stretched before the power amplification. After the power amplification the pulse is compressed to its original pulse duration. This method allows the amplification of ultra-short pulse lasers (usually in the femtosecond regime), avoiding the damage to the laser cavity and its optical components[65]. A schematic of a typical chirped pulse amplification set-up is shown in Figure 2.14.

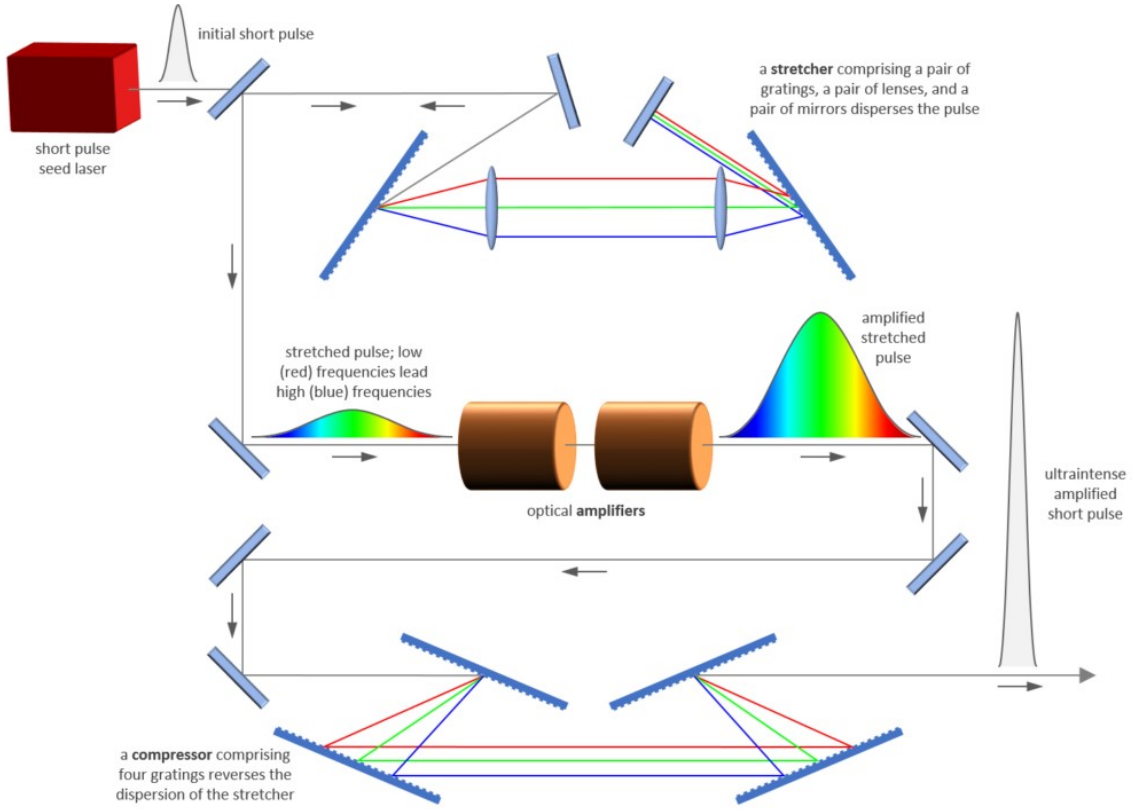

Figure 2.14: *Schematic of set-up for a chirped pulse amplification [66].*

2.5 Super-hydrophobic surfaces

2.5.1 Super-hydrophobic surfaces in nature

Super-hydrophobic surfaces can be observed in nature exhibiting micro and nanoscale surface features that influence the water repellency properties. The creation of micro and nanoscale protrusions on the surface induces a decrease in the contact area between liquid and surface[67]. This is due to the contact between the two elements being constrained only with the tips of the created protrusions, allowing the creation of air bubbles between the surface and the liquid[68–71].

Different types of super-hydrophobic structures have been studied over the years with most of these investigations trying to emulate diverse characteristics observed in natural super-hydrophobic surfaces such as the lotus flower and taro leaf surfaces[67, 72]. Several studies have demonstrated that this super-hydrophobic behaviour is due to the combination between a hierarchical surface structure (micro and nano scale), and the combination of hydrophobic waxes in the case of the lotus flower. This wax layer works as an hydrophobic coating of the surface allowing the formation of pockets of air within the surface structure and decreasing the contact area between the liquid and the surface[73, 74]. Figure 2.15 shows the wettability properties of the Lotus leaf.

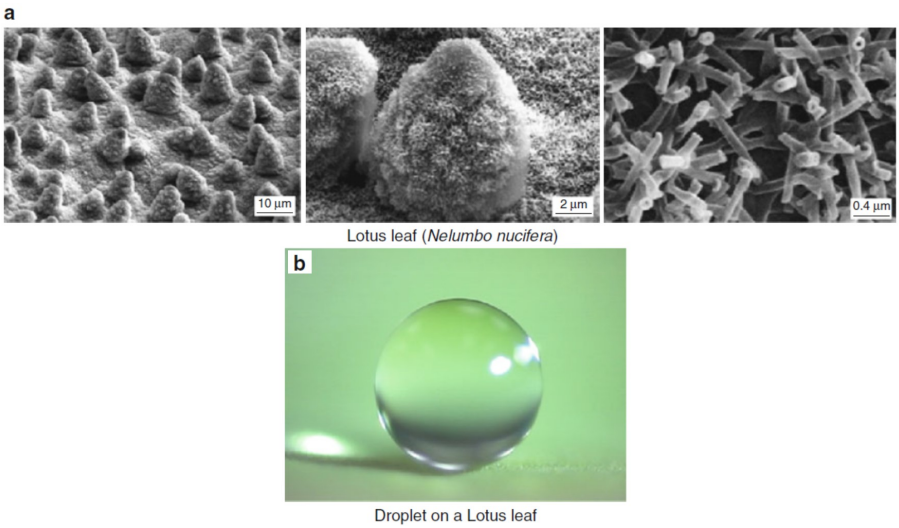

Figure 2.15: *a) SEM images of a Lotus leafs micro-structure with different magnifications, b) water droplet in contact with the Lotus leaf surface [75].*

2.5.2 Theoretical models

The interaction between a liquid droplet and a surface can be defined by the Young equation as starting point. This equation is used to predict the contact angle between a liquid and a flat surface considering the equilibrium state of the three phases of the system. These three phases are the solid-vapour(γ_{SV}), solid-liquid(γ_{SL}) and liquid-vapour(γ_{LV}) interfaces[76]. The Young equation predicts the contact angle of the flat surface through Equation 3.2:

$$\cos\theta = \frac{\gamma_{SV} - \gamma_{SL}}{\gamma_{LV}} \tag{2.3}$$

Within Young equation γ represents the surface energy, hence the resulting angle from the Young equation relates to the intrinsic contact angle of the surface material. A schematic representation of the three phases is given in Figure 2.16.

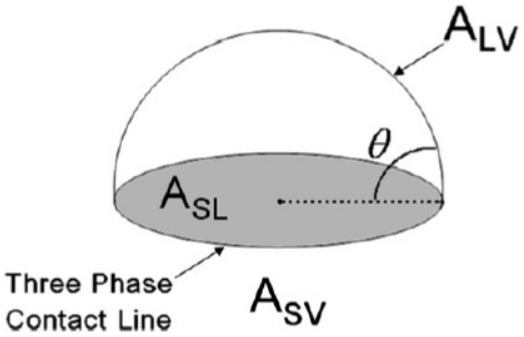

Figure 2.16: *Droplet of liquid contact angle in a balanced position showing the three phases. A_{LV} liquid-vapour interface, A_{SL} solid-liquid interface and A_{SV} solid-liquid interface[76].*

Figure 2.16 displays the equilibrium state of the contact angle between the three phases in a completely flat surface. However, surfaces are not completely flat in normal conditions and the contact angle of rough surfaces cannot be explained by Young's equation. In order to resolve this, two wettability states are proposed by Wenzel and Cassie-Baxter. These wettability states are dependant on the roughness conditions and surface energies[77–79]. Figure 2.17 shows a schematic representation of the Wenzel (a) and the Cassie-Baxter (b) models.

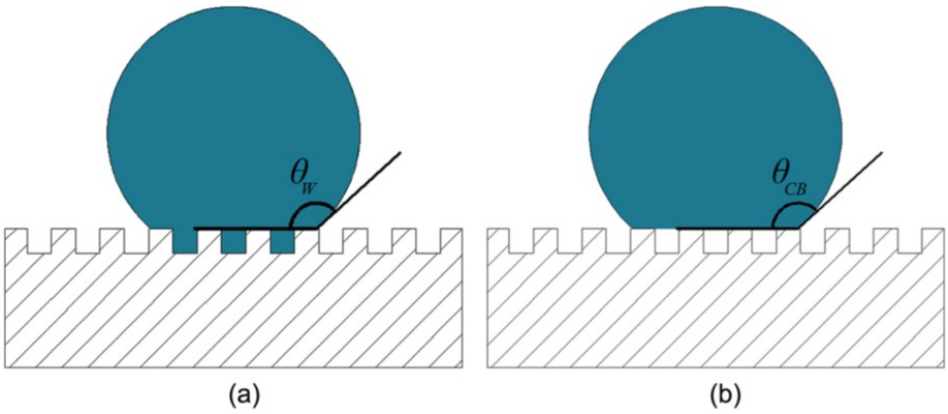

Figure 2.17: *Schematic representation of a) Wenzel wettability model, b) Cassie-Baxter model[80].*

Wenzel model describes the wettability capabilities of the surface as a homogeneous wetting regime, where the liquid is completely in contact with the substrate regardless of the surface roughness. The contact angle behaviour can then be calculated with Equation 2.4:

$$\cos\theta_w = r \cdot \cos\theta_y \tag{2.4}$$

Where:

- θ_w is the contact angle of the rough surface under Wenzel model
- r is the roughness ratio (roughness ratio is the area of the rough surface divided by the area of an ideal flat surface)
- θ_y is the intrinsic contact angle.

As can be seen from equation 2.4 the contact angle in the Wenzel state relies on the intrinsic contact angle and the surface roughness. If the intrinsic contact angle is below 90° the contact angle of the surface will decrease as the surface roughness increases. However, if the intrinsic contact angle is above 90° the contact angle will increase as the roughness is increased[77, 78]. This means that in the Wenzel state the contact angle will follow the natural wettability tendency of the material due to the liquid being completely in contact with the surface.

The Cassie-Baxter model describes a heterogeneous interaction between the liquid and the rough surface. As can be observed from Figure 2.17 the liquid droplet is not in contact with the entire surface, in this case the contact angle can be calculated with Equation 2.5:

$$\cos\theta_{CB} = r_f \cdot \phi_s \cdot \cos\theta_y + \phi_s - 1 \tag{2.5}$$

Where:

- θ_{CB} is the contact angle of the rough surface under Cassie-Baxter model
- r_f is the ratio of the total wetted area to the projected area
- θ_y is the intrinsic contact angle.
- ϕ_s is the fraction of the area in contact with the liquid

From the equation 2.5 it can be observed that the contact angle on the Cassie-Baxter model relies on the intrinsic contact angle of the material that is in contact with the liquid. However, due to the liquid being in contact only with a fraction (r_f) of the total surface this needs to be taken into account for the calculation of the contact angle due to the heterogeneous model[79].

The two theoretical models can create a mathematical approximation for the static contact angle measurement and can be used for the characterisation of the super-hydrophobic surfaces when high contact angles are measured (generally $> 150°$)[81]. However, a high static contact angle not always implies a super-hydrophobic behaviour, thus, an additional measurement is required for the correct wetting classification. For this, the contact angle hysteresis(CAH) is typically measured in conjunction with the static contact angle, in this case a low contact angle hysteresis($<$ 5-10°) is commonly associated with super-hydrophobic surfaces[82, 83].

2.5.3 Super-hydrophobic surfaces produced with laser systems

Modification of wettability properties of metals through surface texturing has been widely explored due to the possible applications for a metallic surface with a high water repellency or super-hydrophobic behaviour. Corrosion resistance, self-cleaning, micro-fluid control, and functional surfaces for medical and aerospace industries are some of the possible applications for surfaces with super-hydrophobic behaviour. This behaviour can be useful for improving the life span and reducing the corrosion of high valued products[76, 80].

Several investigations for the modification of the wettability properties through laser processing have been made over time, mainly focussing on the use of short and ultra-short pulse durations[84, 85]. A review of different laser process for achieving super-hydrophobic surface is described below.

Combination of laser surface texturing and chemical post-treatments have proven beneficial for the creation of super-hydrophobic surfaces. The creation of micro-cone size surface structures on an AISI 316L stainless steel coated with a functionalised silane has produced near super-hydrophobic surfaces with static contact angles close to 150°. However, the lack of the chemical coating reduced the contact angle of the surface to less than 120°[86]. Titanium with 99.99% purity was treated with a femtosecond laser and a post-chemical treatment using NaOH solution created a hierarchical surface structure, samples with the chemical treatment showed a significant decrease in the contact angle in comparison with samples without the chemical treatment. However, a super-hydrophobic state of the surface was not achieved with any of the samples[87].

High contact angle measurements have been produced with the use of femtosecond lasers for the creation of LIPSS structures on different materials such as Ti-6Al-4V, Titanium with 99.99 % of purity, different types of stainless steel. The contact angle usually increases with time with no post-treatment after the laser surface texturing process[88–90]. However, the creation of LIPSS does not always lead to a super-

hydrophobic state of the surface due to the surface chemistry and the type of alloy treated as demonstrated by P.Bizi-bandoki *et al*[91].

Creation of micro-pillar like surface structures with picosecond laser has proven to improve the wettability properties of the aluminium reaching contact angles $\approx 150°$[92, 93]. However, this laser texturing process usually requires a high number of laser pulses in a single place for the creation of the required features(more than 300 pulses); contact angle evolves over time presenting a hydrophilic behaviour after the laser treatment and transitioning to a super-hydrophobic behaviour after 31 days of ambient air storage.

Creation of micro-pillar like surface structures on stainless steel with picosecond laser and a chemical post-treatment showed a super-hydrophobic behaviour with contact angles $\approx 163°$[94].

Comparison between surface structures created on stainless steel using picosecond or nanosecond lasers have proven that the picosecond has an advantage in the creation of super-hydrophobic surfaces. Surface structures processed with the picosecond laser in ambient air shown a static contact angle $\approx 160°$ in comparison with the structures created with nanosecond pulsed laser showing 150° of contact angle. However, if the material is processed in water the contact angle decreases below the super-hydrophobic behaviour for both laser systems[95]

The creation of a micro-pillar like surface structure on stainless steel with a nanosecond pulsed laser and electro-deposition have used for the generation of super-hydrophobic contact angles in the range of $\approx 153°$. However, this process requires a high number of steps after the laser surface texturing in order to protect the created surface from damage due to the electro deposition process[96].

Near super-hydrophobic surface structures on Ti-6Al-4V have been created with nanosecond pulsed lasers, using line patterns and micro-pillar like surface structures, reaching static contact angles of 137° and 142° respectively[97, 98].

Nanosecond laser systems capable of producing high laser fluence in pulse durations below 25 ns have been capable of producing super-hydrophobic surfaces on brass[98] and pure titanium (TA2)[99]. These laser systems rely on their high laser fluence capabilities and slow processing speed in order to create a surface structure capable of creating pockets of air and thus a super-hydrophobic surface.

Table 2.1: *Super-hydrophobic laser surface structures with different laser pulse duration regimes, images and data for the Femtosecond laser from S. Shaikh et al. [90], for Picosecond laser from R. Jagdheesh [92] and for Nanosecond laser from C. Yang et al. [99].*

Femtosecond pulsed laser		
Surface structure	**Fluence(J/cm^2)**	**Static CA (°)**
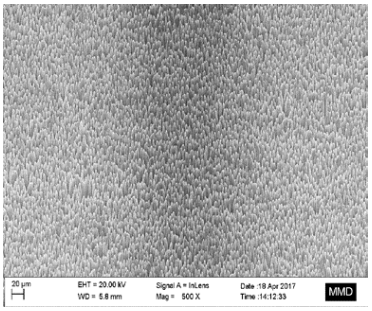	0.6	160° after 12 days
Picosecond pulsed laser		
Surface structure	**Fluence(J/cm^2)**	**Static CA (°)**
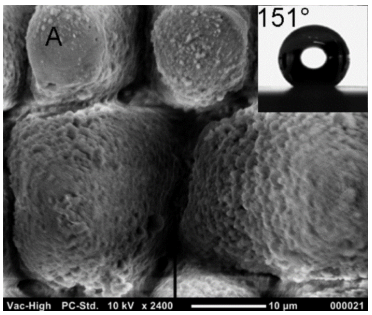	2.82	151° after 4 days
Nanosecond pulsed laser		
Surface structure	**Fluence(J/cm^2)**	**Static CA (°)**
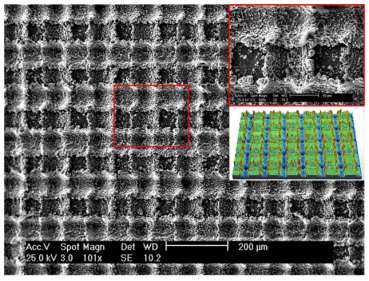	152.79	153° after 30 days

Table 2.1 shows a summary of super-hydrophobic surface structures created via laser surface texturing with different pulse regimes. As can be seen surface structures created on Ti-6Al-4V with a femtosecond pulsed laser can reach static contact angles above 150°, a micro-pillar like structure can be observed from the image and a low laser fluence is employed for the creation of this surface. However, due to the low repetition frequency of the femtosecond laser employed(3 kHz), a scanning speed of 800 μm increases significantly the processing time. Relatively high static contact angles are achieved after only 12 days with no post-treatment required and ambient condition storage[90].

Super-hydrophobic surface structures created with picosecond laser follows a similar approach to the one used by the femtosecond laser as can be observed from Table 2.1. In this case Al_2O_3 is processed with a 6.7 ps pulsed laser to create a micro-pillar like structure, a high number of pulses per spot is applied to the surface(375 - 750), which creates the required surface. As can be seen from the image presented a nano-scale structure can be observed on top of the micro-pillars specifically with 375 pulses per spot resulting in a super-hydrophobic surface with a static contact angle of 151° after 4 days with no additional treatment after the laser processing[92].

Surface structures created with nanosecond pulsed laser depend on the accumulation of molten material on the surface to create pockets of air thus, producing a super-hydrophobic behaviour based on the Cassie-Baxter interaction model between the liquid and the surface. As can be observed from the surface presented on Table 2.1(Nanosecond pulsed laser), the grid scanning technique creates a molten material deposition in the edges of the ablated channels. This molten material creates a surface structure capable of creating pockets of air between on the untreated surface. However, a constant material deposition through all the surface is required in order to ensure the creation of such pockets of air within the structure and in this case a high level of laser fluence is required for the molten material deposition on TA2[99].

2.6 Summary

A number of different laser systems and types have explored the development of super-hydrophobic surfaces, most of the time relying on the creation of a hierarchical surface structure with micro-scale features and nano-scale features(LIPSS). Combinations of both types of structures have been proven beneficial for the development of super-hydrophobic surfaces on metallic materials. These type of surfaces are usually created by ultra-short pulsed lasers such as pico and femtosecond pulsed lasers. However, due to the high cost and limitations on the manufacturing scale and throughput, these systems are usually constrained to purely research purposes.

Nanosecond pulsed lasers has been shown to be able to create super-hydrophobic surfaces, however, high levels of laser fluence and highly specialised laser equipments are usually used for the manufacturing of this type of surfaces. As discussed in this chapter, robust fibre lasers are a suitable option for manufacturing environments. However, due to power constraints of this type of laser, the creation of the same topography for super-hydrophobic surfaces has been difficult to achieve to date. This presents an opportunity for the development of scanning techniques capable of producing super-hydrophobic surfaces on titanium alloys. Ease of manufacture and the reduction of manufacturing steps are some of the desired characteristics for the manufacturing process. This thesis will explore different scanning techniques for the development of super-hydrophobic surfaces on Ti-6Al-4V using a nanosecond pulsed fibre laser for this purpose.

Chapter 3

Equipment and experimental procedure

3.1 Introduction

This chapter describes the general equipment and experimental procedures used throughout the research presented in this thesis. The contents of the chapter are split up into three main sections, the equipment used, materials and experimental procedures. Any experiment specific equipment or procedure will be given in the results chapters.

3.2 Equipment

3.2.1 Laser systems

SPI G4 nanosecond pulsed fibre laser

The main laser source for this work was the SP-020P-A-HS-L-A-Y. This nanosecond pulsed fibre laser, shown in Figure 3.1, is a class 4 system supplied by SPI Lasers. The system is part of the redENERGY G4 air-cooled pulsed fibre laser family of SPI, capable of working with a near-infrared wavelength (1064 nm). This laser has a Master Oscillator Power Amplifier(MOPA) architecture, based on a dual-stage fibre amplifier with an optical seed pulse generated by a single-mode doped fibre with integrated Bragg gratings (See Chapter 2 "Laser systems" section for more details). The fibre amplifiers are pumped by multi-mode laser diodes, and the beam is delivered by a fibre-optic beam delivery cable terminated in a beam delivery optic(BDO) incorporating a Faraday isolator and beam expander collimator to provide a collimated output beam.

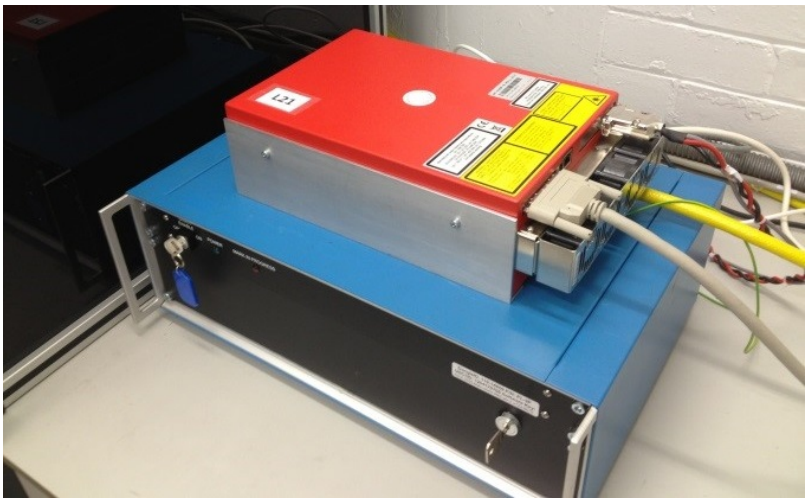

Figure 3.1: *SPI G4 020P-A-HS-L-A-Y nanosecond pulsed laser system and Pipeline-1 USB controller*

The beam expander collimator attached at the end of the fibre (PT-P00554) provides a nominal beam diameter of 8 mm allowing the integration of the system with galvanometer scanning systems for final focusing and delivery of the laser beam.

The nanosecond pulsed laser is capable of working in both CW and pulsed mode, with a maximum average power of 20 W and maximum pulse energy of 0.8 mJ at 200 ns of pulse duration and a repetition rate of 25 kHz. A beam quality of $M^2 = 1.83$ is delivered by the system due to the low mode configuration.(Appendix A)

In pulsed mode, the laser can provide different pulse durations in the range from 9 to 200 ns. To modify the pulse duration, the supplier provides a range of selectable parameters called waveforms. The waveform defines the default "switching frequency" (PRF_0) for maximum peak power. The system can be operated with any pulse repetition rate, from 1 to 1,000 kHz regardless of the selected waveform; however, a table with default values of PRF_0 for each waveform is provided by the manufacturer, this is due to safety measures included within the system(Appendix B). The safety measures decrease the average power linearly when the system works below the PRF_0 in order to prevent damage to the laser diodes. If the system is used in repetition frequencies above PRF_0 the average power is maintained whilst peak power and pulse energy are decreased (See Figure 3.2)[100]. Due to the flexibility of pulse durations, the temporal shape varies in relation with the pulse duration. This pulse temporal shape is given in Appendix C.

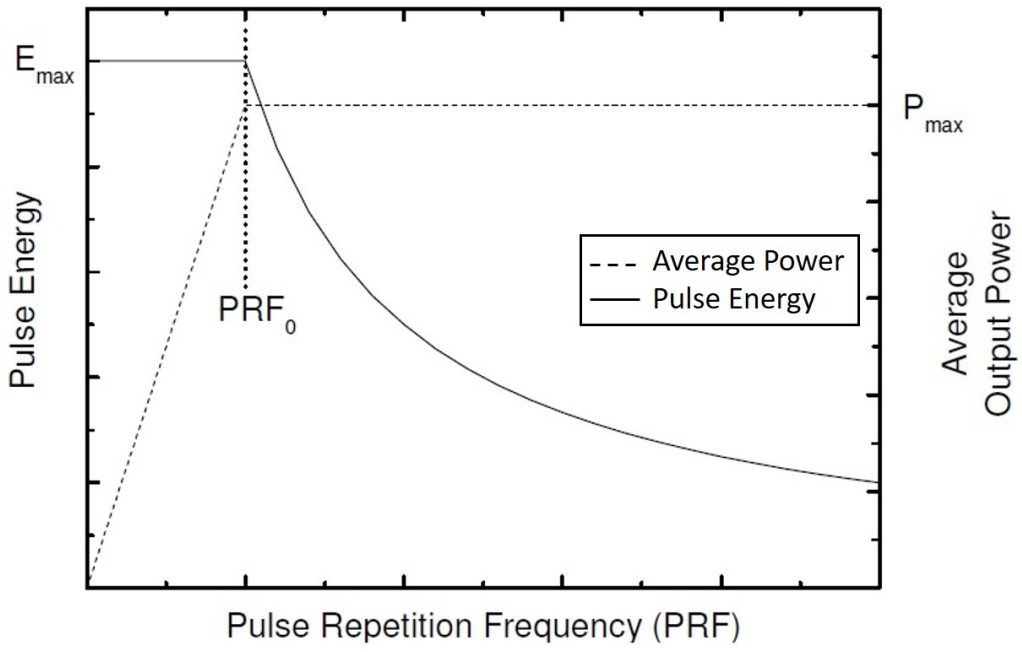

Figure 3.2: *Average power and Pulse Energy vs Pulse Repetition Frequency*

The laser is combined with a Nutfield Pipeline-1 USB controller which includes a SCAPS USC-1 scan controller. The arrangement of the controller system is provided with a safety interlock loop. The system works in analog channels for controlling the nanosecond pulsed fibre laser and a XY2-100 digital interface for the galvo scan head in order to enable mark on the fly process. With this process, the user is able to modify different parameters of the fibre laser without interrupting the marking process. Power, pulse duration, frequency and even laser mode (CW or pulsed mode) can be controlled on the fly [101, 102].

A galvo scan head system is used as a final delivered system of the laser beam. The system is a Nutfield XLR8-10 scan head with a resolution of 16 μrad (see Figure 3.3)[103]. A 160 mm focal length f-theta lens is attached to the scan head in order to focus the laser beam. The XLR8 scan head consists of two galvanometer scanners (one for each direction, vertical and horizontal). The use of the scan head provides the capability of deflecting the incident optical beam to specific locations on the target within a scan field area of 120 x 120 mm with a resolution of <8 μm[104].

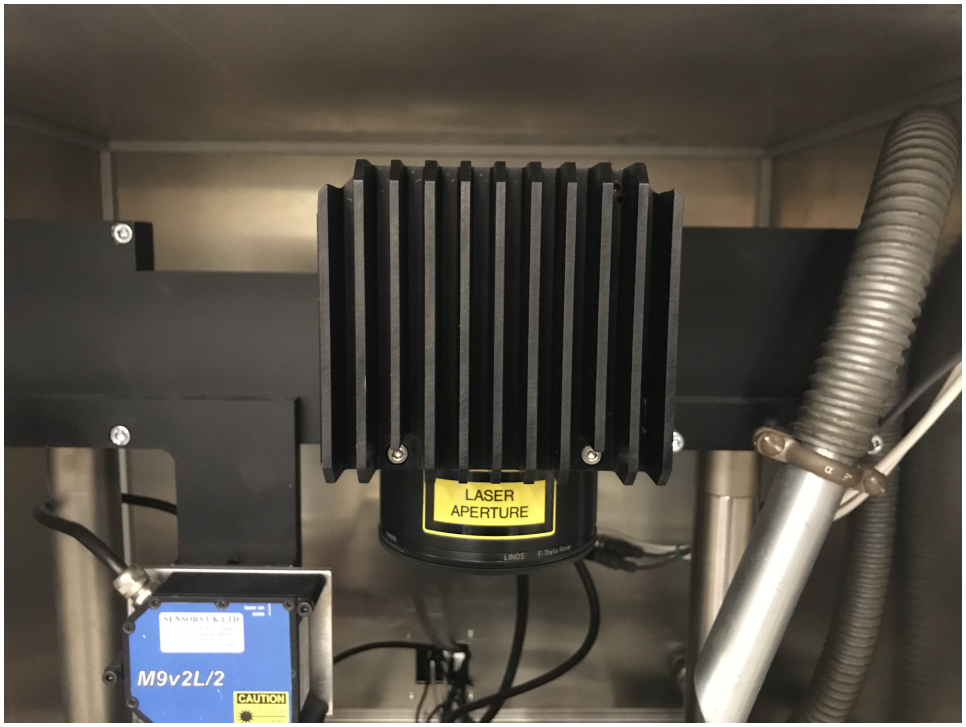

Figure 3.3: *XLR8-10 Scan head with 160 mm f-theta lens attached*

The use of the laser system is controlled through the software package Nutfield Waverunner, which is based on SCAPS SAMLight, providing user-friendly control over different functions for the development of different shapes and scanning techniques (see figure 3.4). Parameters of the nanosecond pulsed laser are controlled by the software, power, pulse duration, frequency and laser mode (CW or pulsed mode) are easily modified on the fly. These parameters are then communicated to the laser via the pipeline interface using a transistor-transistor (TTL) 5V logic.

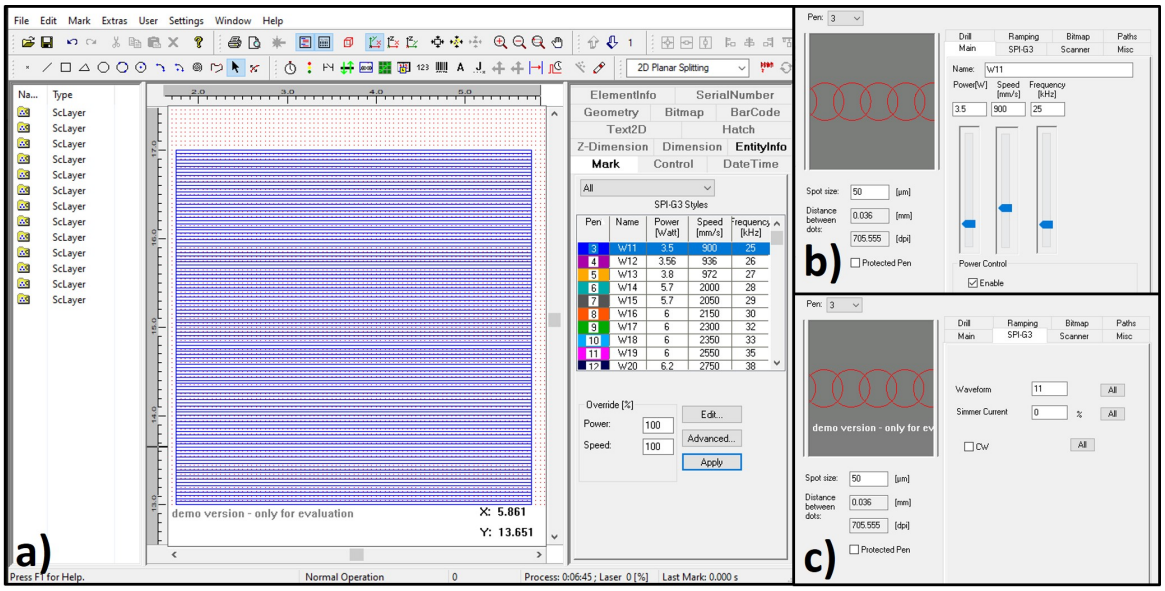

Figure 3.4: *Nutfield Waverunner software control for the nanosecond pulsed fibre laser a) Main window layout, b) Laser parameters editor, c) Laser waveform and mode selection (CW or pulsed mode)*

Several tools are provided for the design and control of the required laser path. Basic shapes and text can be defined and modified according to design requirements. The versatility of the software allows the user to create a completely customized scanning technique according to user requirements. The ability to modify the required parameters of the nanosecond pulsed fibre laser creates a versatile interface where the whole system can be managed with the exception of the distance between the galvo scan head and the material[105, 106].

In order to verify the correct power input from the laser system, a calibration process was carried out during this work. The calibration process followed the instructions provided by the software manual for the Power Map function(seen on Figure 3.5). For this, the average laser power delivered by the laser when a 8-bit value of 255 is requested by the laser controller; this is measured through a power meter(Thorlabs PM200 with thermal sensor), the measured power is then typed in the Max-Watts field and the corresponding Watt-Bit list is updated according to this value. The corresponding 8-bit values for each one of the updated Watt data on the table is then verified by the corresponding 8-bit values for each given Watt values[107].

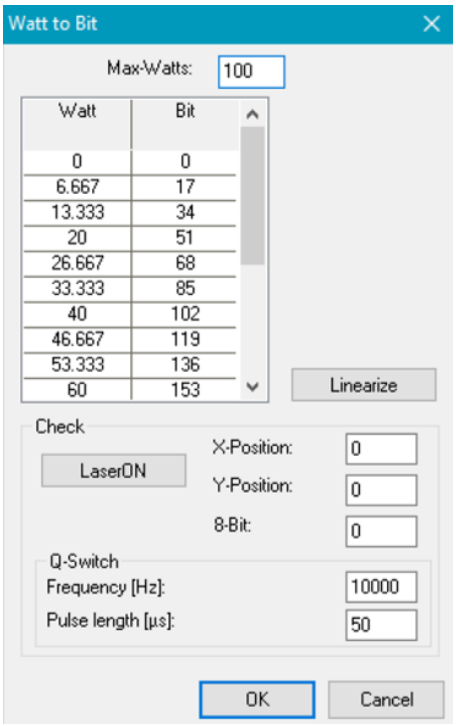

Figure 3.5: *Power Map function on Waverunner software [107]*

The calibration process in the laser system revealed a loss of 0.6 W of the maximum power reaching a maximum level of 19.4 Watts compared with the 20 W from product specification. The calibration process ensures that the power delivered by the system meets the requested levels by the software and controller equipment.

Three precision stages provided by Thorlabs are used as the positioning system for the Ti-6Al-4V samples. Two Thorlabs LTS150 with integrated controllers are used for the linear positioning (X and Y direction). These stages provide 150 mm of linear travel with a load capacity of up to 15 kg and 5.0 μm of accuracy[108]. The two linear stages are mounted in a stepper motor driven lab jack (Thorlabs L490MZ) with a load capacity of 15 kgs providing vertical movement for modifying the distance between the material and the galvo scan head (see Figure 3.6). The L490MZ lab jack provides a vertical travel range of 52 mm with $<$ 20nm of resolution[109]. Control over the positioning of the three stages is through the Thorlabs APT software; the software includes a wide range of drivers for different and configuration options for different stages. Each one of the stages can be configured with a different set of parameters for the correct integration of the system.

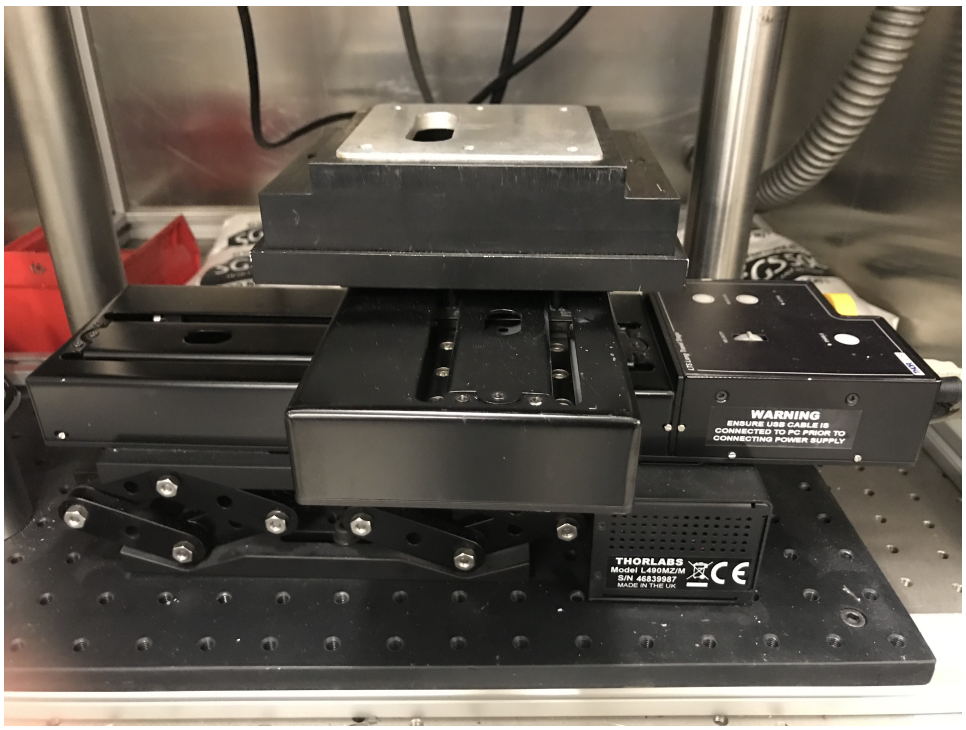

Figure 3.6: *3 axis Thorlabs positioning stage*

The full integration of the nanosecond pulsed laser with the stage system provides a highly controllable environment for the use of the laser and the research process. Flexibility in the configuration of each one of the systems provides a wide range of parameters to explore for the development of this thesis.

10ps High-Q laser system

A second laser source for this thesis is a 10 ps pulsed laser system supplied by High-Q (see Figure 3.7). The system is capable of providing pulses of 10 picoseconds in pulse duration with a maximum pulse frequency of 50 kHz. The system has a fundamental wavelength of 1064 nm with a diode pumped seeded Nd:VAN regenerative amplifier. The control of the system is provided through a dedicated software package where the repetition rate can be controlled. The laser source is capable of delivering a maximum average power of 2 W at a repetition rate of 20 kHz. The beam quality delivered by this system has an M^2 of 1.3.

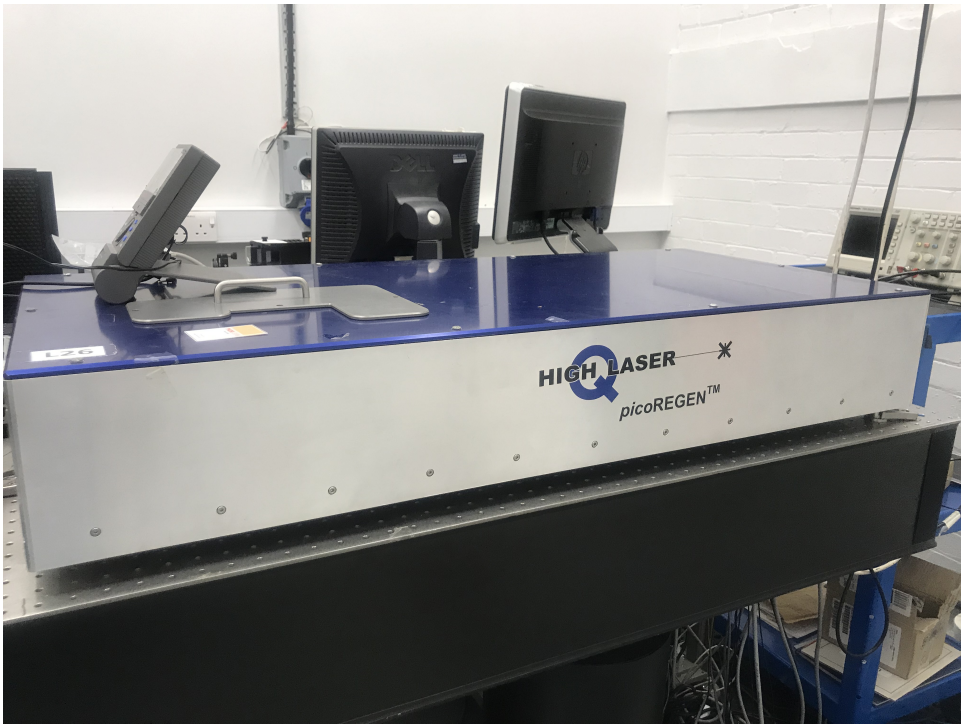

Figure 3.7: *High-Q laser system*

An arrangement of optics is required in order to optimise the laser beam for the experimental set-up. In figure 3.7, a schematic of the used experimental set-up is presented.

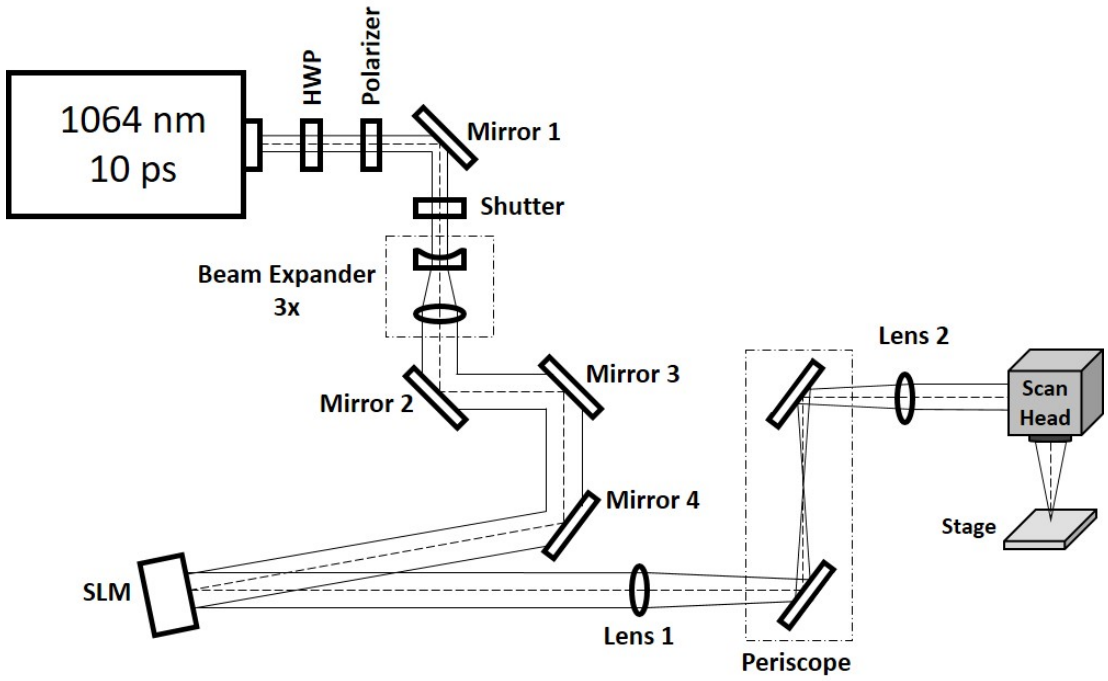

Figure 3.8: *Schematic of the optical layout used for the High-Q laser system*

The schematic in figure 3.8 shows a linear polarized beam passing through a half wave plate and a Glan-laser polarizer which forms an attenuator and sets the polarization direction. A beam expander (M $\approx$ 3) is used to optimise the size of the beam. After the beam expander, three plane mirrors (Mirrors 2, 3 and 4) control the beam path before the reflective phase-only Spatial Light Modulator (SLM). A Hamamatsu X10468-03 liquid crystal on silicon (LCoS) SLM dielectric coated for a 1064 nm wavelength (reflectivity $\approx$ 95 %, fill factor 98 %) is used as a mirror applying a correction field. A 4f imaging system with two lenses (Lenses 1 and 2), is used to reconstruct the beam from the SLM to the input aperture of the galvo scanner system (Nutfield XLR8-10) with the use of periscope mirrors. The SLM has the ability to modify the phase and polarisation state of the reflected beam. For this study the SLM is used only in a passive mode as a mirror.

A galvo scanning system (Nutfield XLR8-10) is used as a final delivery method for the laser beam. Attached to the galvo scan head a F-theta lens of 100 mm of focal length focusses the beam into the material. In Figures 3.9 and 3.10 the optics set-up and galvo scanning system can be observed.

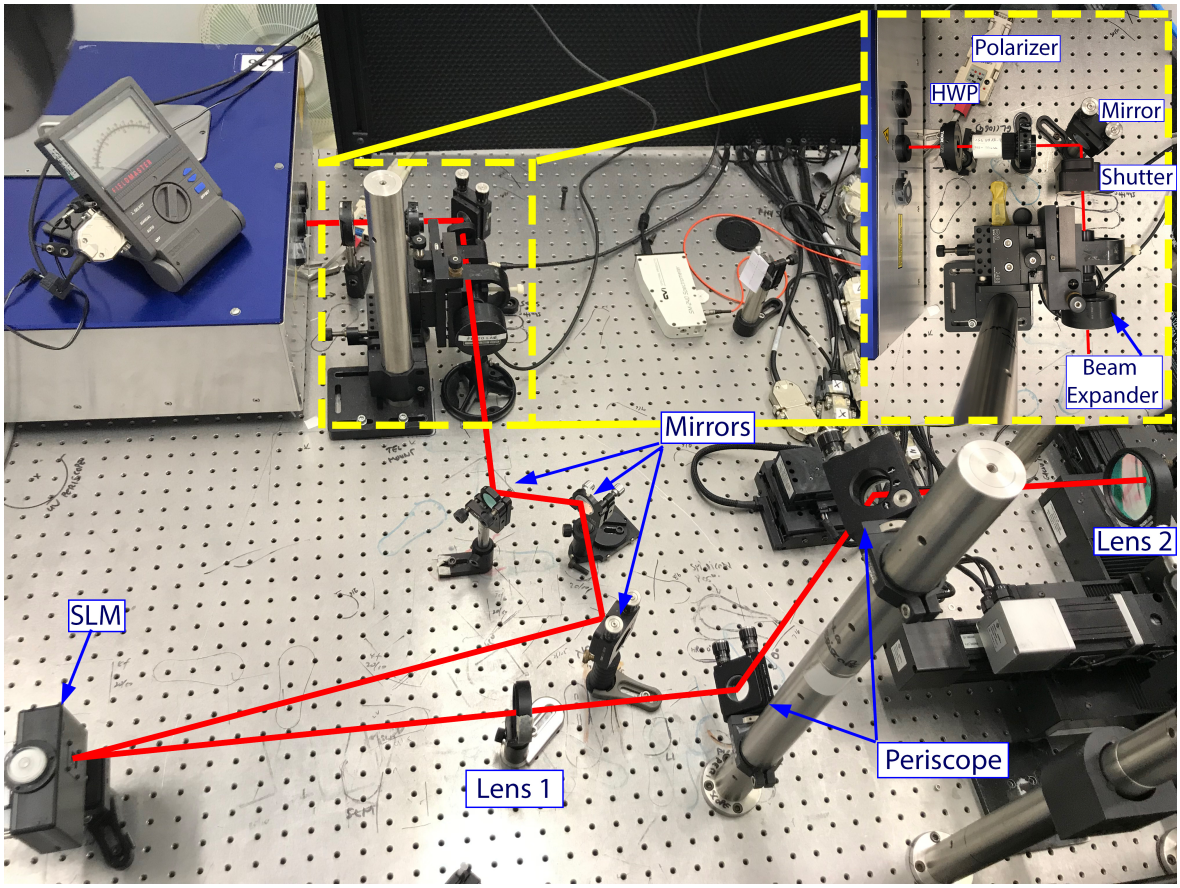

Figure 3.9: *Optical set-up for the High-Q picosecond laser and laser path*

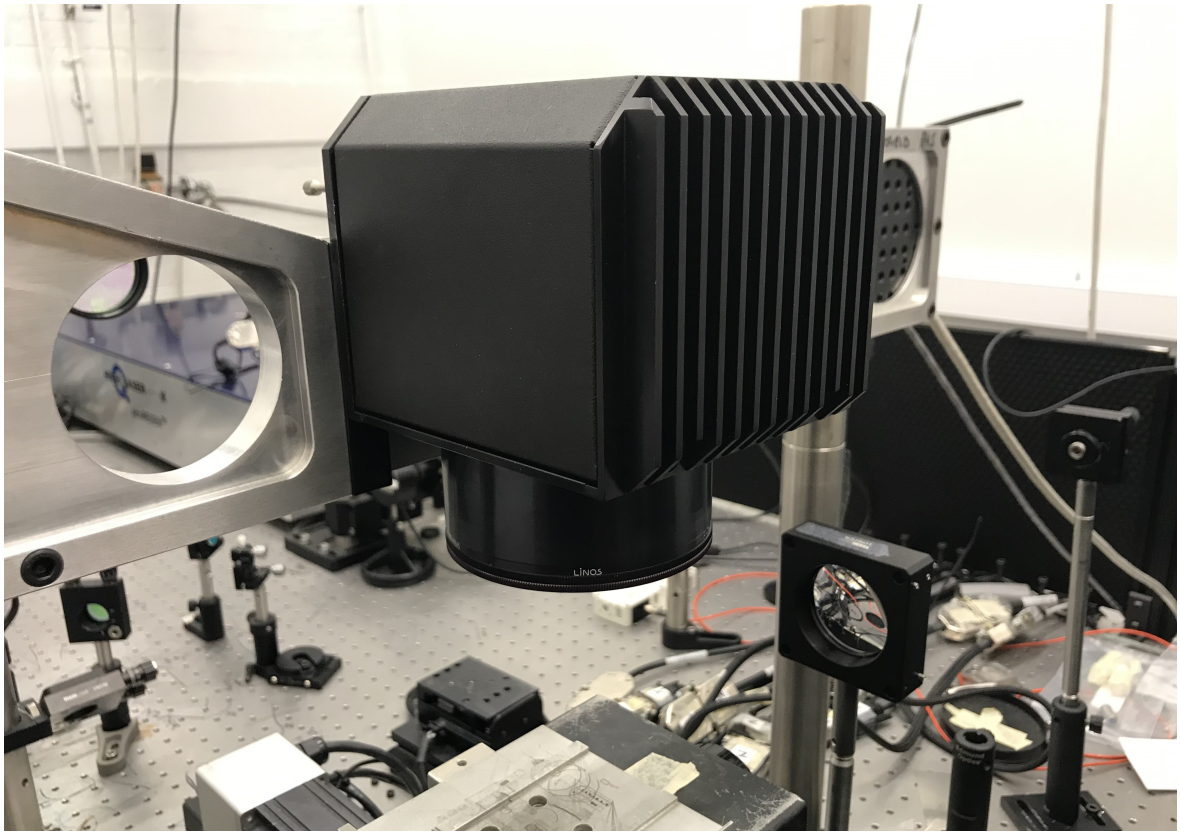

Figure 3.10: *Galvo scanning system Nutfield XLR8-10 with 100 mm F-theta lens*

3.2.2 Essential equipment

Optical microscope

An optical microscope (Nikon Eclipse LV150NL) combined with a USB CMOS camera (Thorlabs DCC164c) was used for the optical examination of the samples produced through this research. The microscope is provided with integrated LED illumination for sample examination, allowing the observation of surface features without requiring an external source of light. The system includes several standard objective lenses with magnifications of 5x/10x/20x/50x/100x, allowing the imaging of micro and nano-scale features. A maximum sample size of 150 x 150 mm allows the imaging of relatively large sample areas[110]. The camera is connected to a PC for imaging processing as can be observed in Figure 3.11.

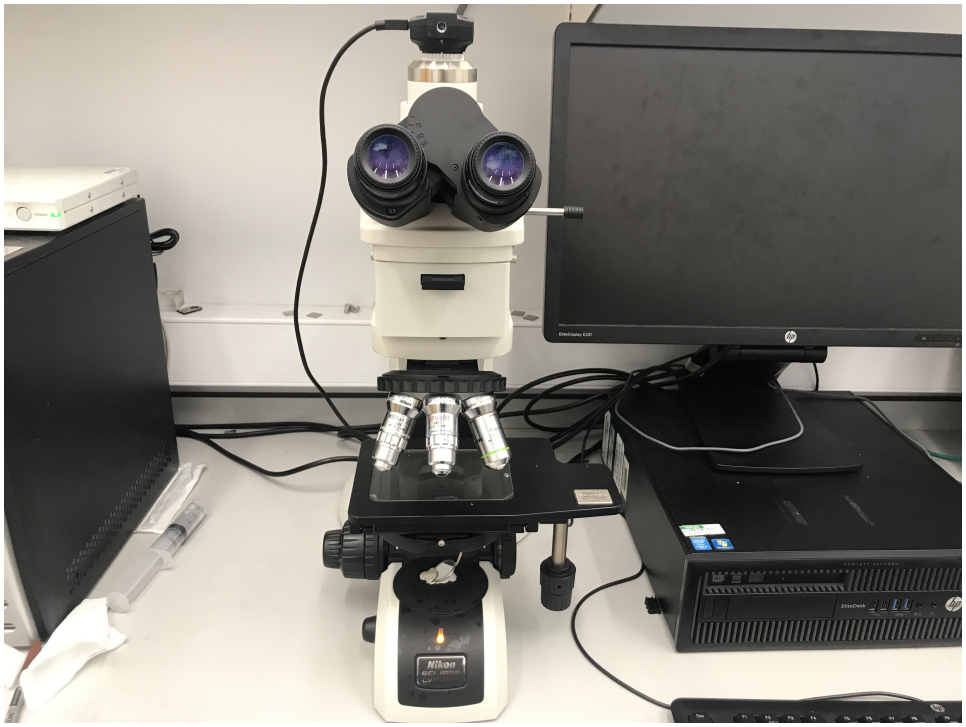

Figure 3.11: *Nikon Eclipse LV150NL optical microscope*

The PC is configured with the Thorlabs DCx camera software for image processing. This software provides a wide range of tools and drivers for different types of CMOS cameras creating a package of different tools for sample imaging. The software provides additional tools for the management and improvement of the images obtained by the microscope, as well as the ability to record video. One of these tools provides capabilities for measuring distances within the field of view of the image. In order to obtain reliable measures from the software, a calibration is required. The calibration process defines the ratio between the pixels in the image and the real distance through the imaging of a standard scale bar of 1 mm with 10 μm divisions. Different types of image files can be obtained from this software for further processing of additional analysis. Figure 3.12 shows an example of the software interface with the image of the 1 mm scale for calibration[111].

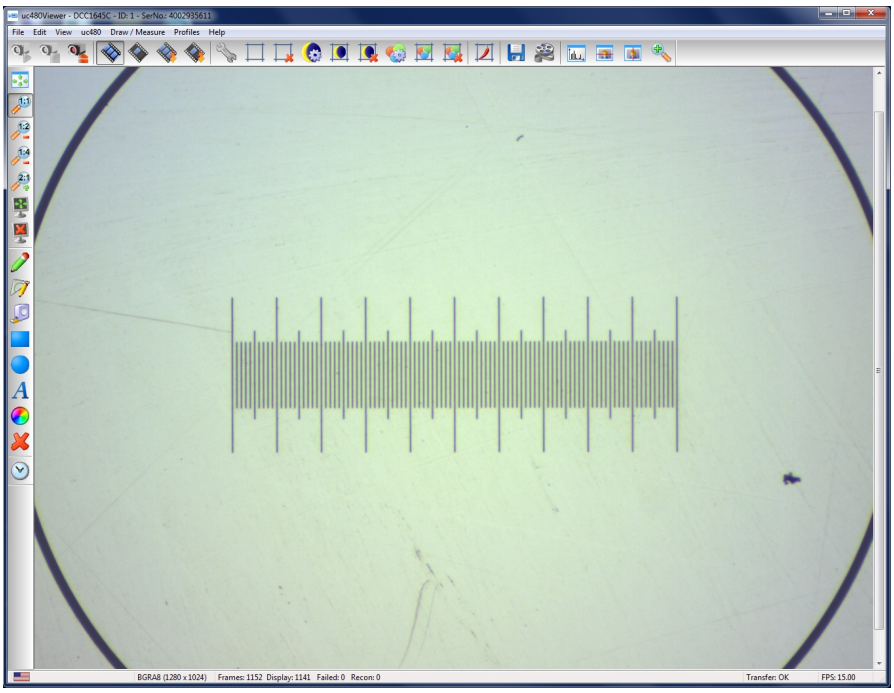

Figure 3.12: *Thorlabs DCx cameras software with standard scale bar of 1 mm and 10 μm divisions*

The integration of the microscope with the software provides a reliable tool for imaging examination of the samples produced during this research. Equipment and software flexibility contribute to the in-depth analysis of the material and laser-produced surface features.

Optical profiling system

To obtain three-dimensional surface profiles of the created features, an optical profiler system (WYKO NT1100) is used. The equipment is capable of obtaining a surface profile of most materials. The system uses a vertical shift interference (VSI) method; this method is based on white light vertical interferometry to obtain the necessary measurements from the surface topography. This non-contact method allows the collection of surface topography measurements with high resolution. With a resolution of 0.1 nm in the vertical direction, plus an x-y resolution of 0.81 μm this equipment is an excellent tool for the characterization of the created features on the material through laser processing. The equipment is complemented with an illuminator capable of controlling the light intensity used by the profiler in order to obtain a clear and reliable measurement of the surface profile. Figure 3.13 shows the profiling system and illuminator arrangement for surface profiling of the created samples. A dedicated software package (Vision32) is used for the control and setup parameters of the equipment for the measurement techniques and calibration [112].

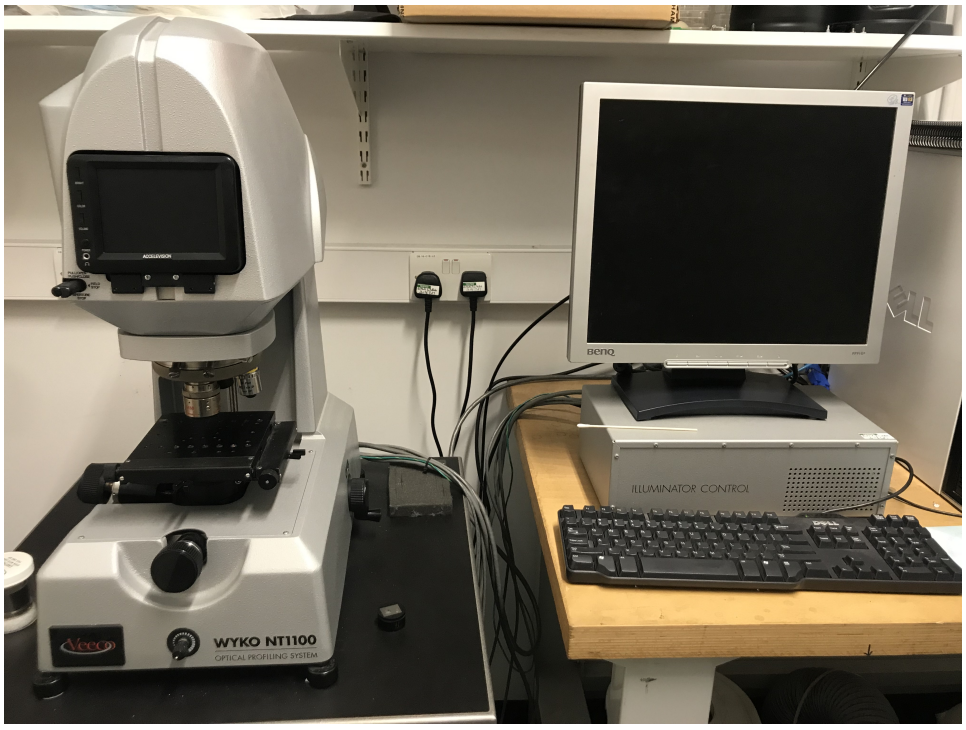

Figure 3.13: *WYKO NT1100 optical profiler*

The Vision32 software provides the necessary tools for the correct configuration and operation of the optical profiling system. Different parameters can be defined for an adequate measurement technique of each sample, depending on the particular characteristics of the surface. The range, magnification and threshold of measurements can be defined for a reliable analysis of the surface profile. Representation of results through the software can be explored in different modes, the 2D representation of the surface is one of the most helpful capabilities of the software (see Figure 3.14) in order to obtain cross-section measurements of the surface features. 3D representations of the surface and general data of the area can be obtained through the different surface analysis tools. Capabilities for exporting the obtained data into different formats for their interpretation with different software packages, such as MATLAB or Excel, is fully available in the software package. Images, such as the 3D graph of the analysed area can be exported for the correct representation of the surface profile[112]. The integration of the software and equipment provides a reliable tool for the analysis of the modified material surfaces created with laser processing through this research.

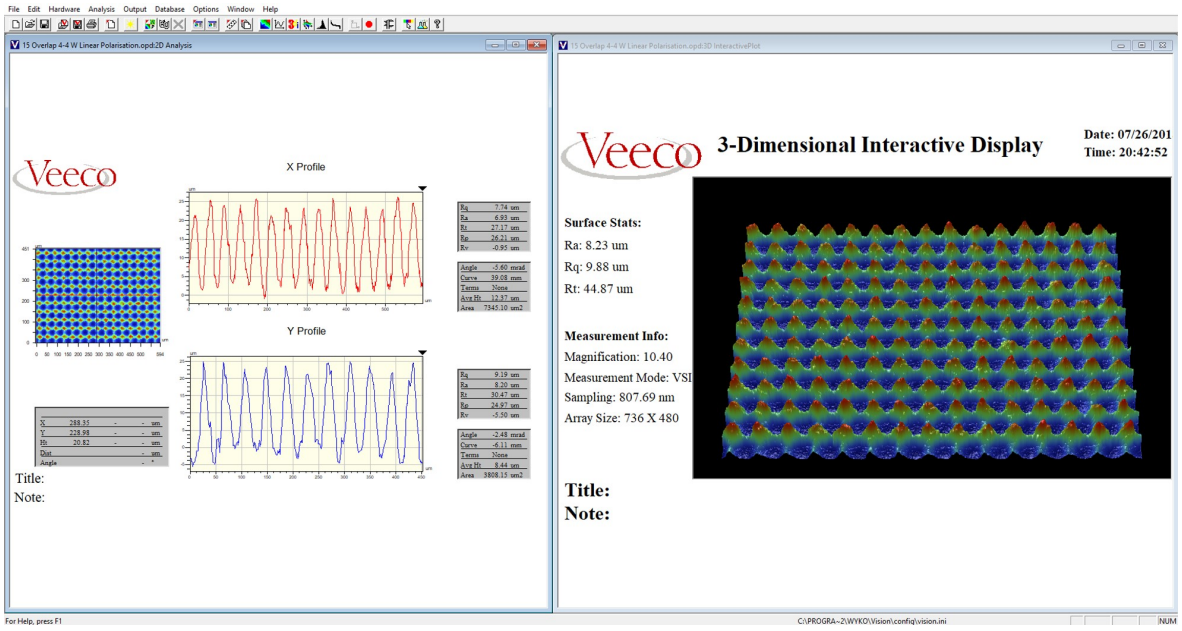

Figure 3.14: *Vision 32 software displaying 2D Analysis and 3-D representation of a structured surface*

Contact angle analysis equipment

The Kruss EasyDrop analysis system observed in Figure 3.15 is the equipment used for the calculation of surface tension and surface energy through evaluating the shape of liquid drops and the interaction with the surface. For this research, the main interest is to analyse how the surface structuring through laser processing can modify the wettability of the materials. The system consists of manual dosing through a rotating mechanism syringe, releasing a drop of liquid of ≈ 10 μl into the surface of the sample. The sample is positioned in a height-adjustable table illuminated from one side; a USB CMOS camera attached to a zoom and focussing device in the opposite side is used to record an image of the drop and the surface interaction. The design of the equipment provides a simple but reliable tool for contact angle measurement[113].

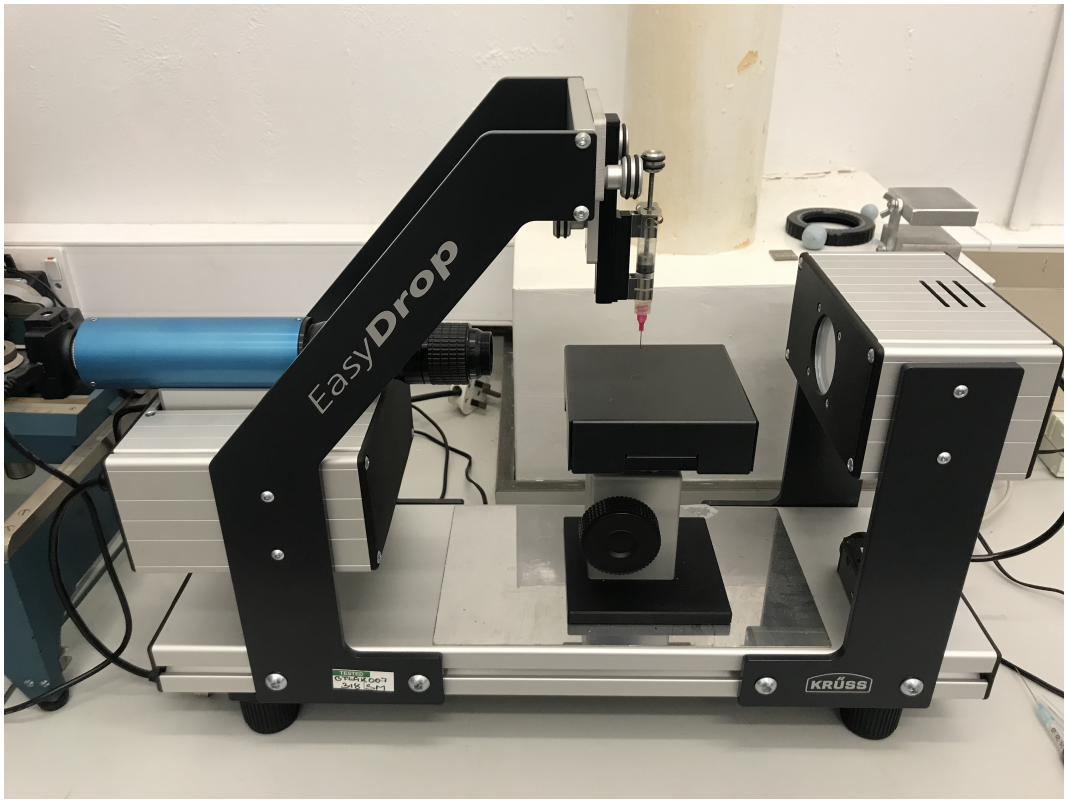

Figure 3.15: *Kruss EasyDrop analysis system*

Dedicated software (DSA1) is provided with the equipment for the analysis of the obtained images through the EasyDrop system. The software provides a set of different evaluation methods for the contact angle calculation, surface energies and surface tensions. Tools for the correct analysis of the images are provided within the software; the determination of the surface line and the contact analysis method can be defined for the measuring process. In Figure 3.16 a typical analysis of contact angle through the DSA1 software is displayed.

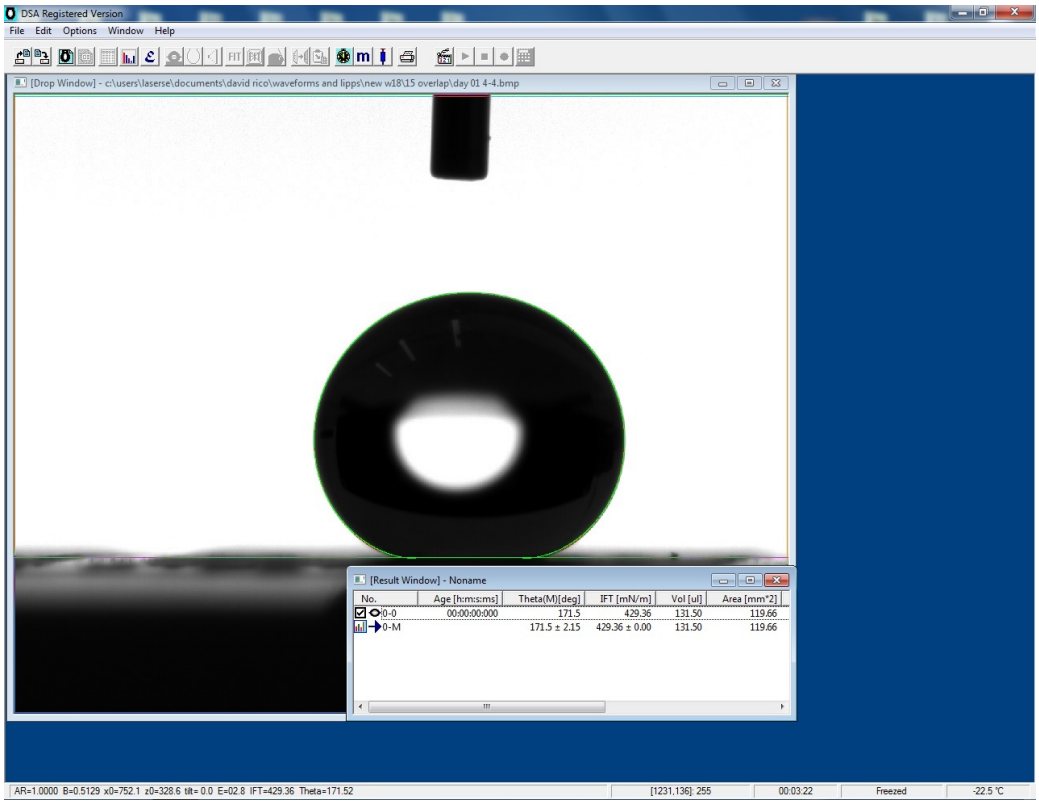

Figure 3.16: *Drop Shape Analysis software package (DSA1)*

EasyDrop equipment and DSA1 software provide accurate measurements for the analysis of the produced samples in this thesis and a comparison point for the improvements of wettability properties of the processed surfaces.

Scanning electron microscope

For detailed surface imaging a scanning electron microscope tungsten filament, Oxford INCA X-act EDX detector (SEM JEOL 6610) was used (Figure 3.17). The equipment is capable of providing detailed images of the modified material at high levels of magnification. The system has a resolution up to 3.0 nm with an accelerating voltage of 30 kV. Several tools for the sample positioning and imaging are provided with the instrument, this allows sample imaging with high flexibility. The main requirement for the imaging is the conductivity of the material to observe, in this case the use of Ti-6Al-4V and their conductivity properties are suitable for the correct imaging. Measurement tools are provided within the software of the system for the characterisation of the images. Implementation of the EDX detector for element characterisation of the sample provides a tool for preliminary element analysis of the surface. This is an ideal instrument for obtaining images of the surface structures developed by the laser scanning used in this thesis. The use of the electron microscope is in collaboration with the Imaging Centre at Liverpool University (iCal).

Figure 3.17: *SEM JEOL 6610*

X-ray photoelectron spectrometer

In order to fully understand the modification of the wettability properties on Ti-6Al-4V, surface chemistry analysis was carried out using X-ray photoelectron spectroscopy equipment (Axis-SUPRA equipment from Kratos Analytical) seen in Figure 3.18. The system provides quantitative elemental and chemical information on the first 10 nm of the material surface. A fully automated sample loading, helps to avoid the contamination of the material surface for a proper chemistry characterisation[114]. The equipment includes an optical microscopes for sample identification and processing software for data acquisition. The obtained data is analysed with the CasaXPS software package for their correct interpretation. The equipment is required for the analysis of the oxidation state of the surface laser processing. The characterisation of the chemistry of Ti-6Al-4V is fundamental for the modification of the wettability properties as stated in Chapter 2.

Figure 3.18: *Axis-Supra instrument (Kratos Analytical)*

3.3 Material selection

The main objective of this thesis is to modify the wettability properties for the Ti-6Al-4V through laser surface texturing for potential industrial applications. Chemical and temperature resistance makes this material suitable for products with high added value. Due to the high strength to weight ratio this titanium alloy is suitable for a wide range of applications in different industries, such as biomedical and aerospace. For these reasons, this material is identified as one of the most common titanium alloys in the market.

Ti-6Al-4V has excellent corrosion resistance and outstanding fatigue and crack resistance compared to steel. However, one of the biggest problems in using this type of titanium alloy is the difficult manufacturing process of such material. Titanium alloys are particularly difficult to machine due to the strength of the material and the wear of the required tools for the manufacturing process. In this area, laser manufacturing provides a better tool for the machining of these alloys avoiding the need for contact tools with the material. Through this research a commercially available Ti-6Al-4V Grade 5 was used for the productions of samples for wettability modification. The chemical composition of the material is shown in Table 3.1.

Table 3.1: *Typical material properties of Titanium Alloy Ti-6Al-4V Grade 5*

Element	**Content in %**	**Physical properties**	**Typical value**
Aluminium, *Al*	6	**Density**	$4.42 g/cm^3$
Vanadium, *V*	4	**Melting range**	$1649°C$
Carbon, *C*	< 0.1	**Specific heat**	$560 J/kg.°C$
Iron, *Fe*	< 0.25	**Resistivity**	$170 ohm.cm$
Oxygen, *O*	< 0.2	**Thermal conductivity**	$7.2 W/m.K$
Nitrogen, *N*	< 0.05	**Thermal expansion 0-100°*C***	$8.6x10^{-6}$
Hydrogen *H*	< 0.015	**Thermal expansion 0-300°*C***	$9.2x10^{-6}$
Titanium *Ti*	Balance	**Beta Transus**	$999 \pm 15°C$

3.4 Sample preparation

Two types of samples were used for this thesis, the first one with Ti-6Al-4V polished with mirror finishing and the second type as-received material in order to explore the capabilities of laser processing not only in laboratory conditions but also in a manufacturing environment.

The first type of samples had to be cut in a size of 15 x 15 mm approximately in order to be mounted in a non-conductive resin for the polishing treatment. After this the titanium samples were polished achieving a mirror finishing surface with an average roughness of $Ra \sim 30$ nm. The second type of samples is as received material cut into 20 x 20 mm with 2.05 mm of thickness and an average roughness of $Ra \sim 600$ nm. In Figure 3.19 the roughness profile of both samples is shown.

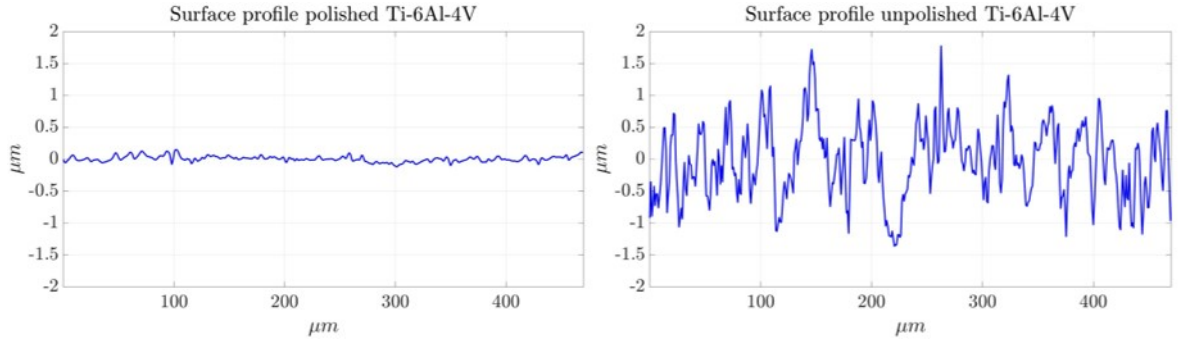

Figure 3.19: *To the left Ti-6Al-4V polished sample with average roughness of Ra ∼ 30 nm, To the right, as received Ti-6Al-4V sample with average roughness of Ra ∼ 600 nm*

Both types of samples were cleaned with acetone previous to the laser treatment in order to reduce the amount of contamination in the surface and the possible effects in the laser surface texturing.

3.5 Experimental procedure

3.5.1 Focal position

The use of galvanometer scan head systems is widely used in different applications; it provides a common solution for an optical scanning technique in the marking field. The scan head used in this thesis is an arrangement of two mirrors attached to galvanometers in order to provide the laser positioning in X and Y direction. Figure 3.20 shows a typical arrangement for a 2D scan head system.

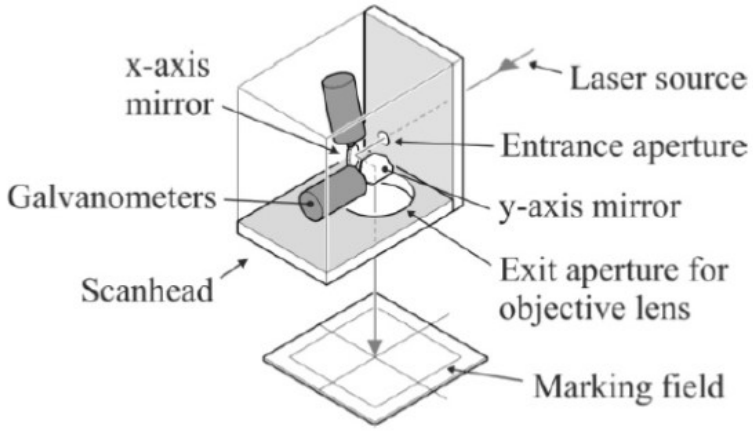

Figure 3.20: *Arrangement principle for 2D galvanometer scanning system[115]*

A focusing lens is attached to the scan head system focussing the laser beam into the sample. In the used arrangement in this thesis, a F-theta lens of 160 mm focal length (LINOS F-Theta-Ronar 160 mm) is used as the objective lens. The lens is designed in an optical-glass material with a transmission $\geq 96\%$ and a damage threshold for the coating of the lens is up to 40 J/cm^2 for a 1064 nm wavelength. One of the most useful characteristics of F-theta lenses is the ability to keep the focus position in the same plane over the entire scan field[116].

The next step for the use of the scanning head is to identify the required distance between the system and the material in order to work in the focal position of the lens. Figure 3.21 shows the schematic diagram of the F-theta 160 mm lens and the working distances for the focus point.

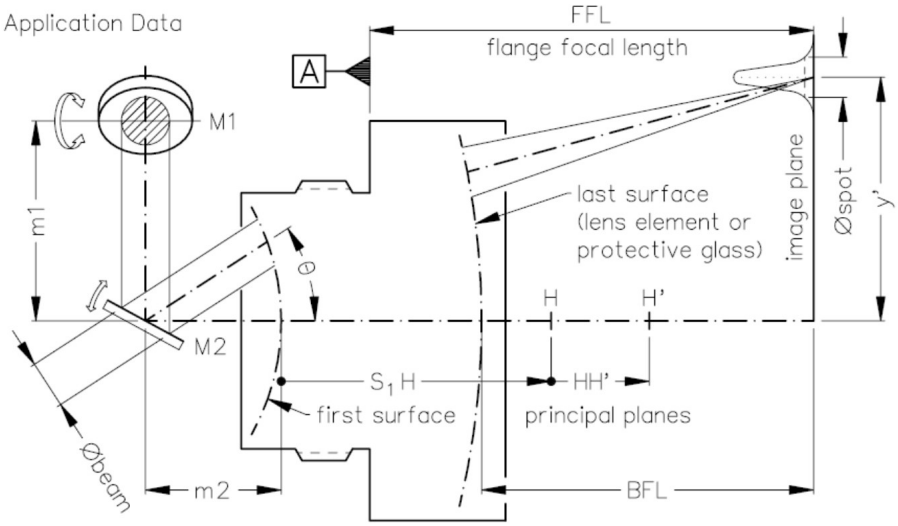

Figure 3.21: *Schematic drawing of the LINOS F-Theta-Ronar 160 mm lens, 1064 nm wavelength[117]*

Within the parameters provided by the lens manufacturer, the distance between the material and the lens is shown as flange focal length (FFL). With the use of the 160 mm focal length this FFL distance is 184.4 mm. Measurements between the scan head and 3-axis table were measured in order to find the correct position for the image plane. Figure 3.22 shows the 3-axis stage at a nominal position of 22.6 mm where a 184.4 mm distance is achieved as suggested by the lens manufacturer.

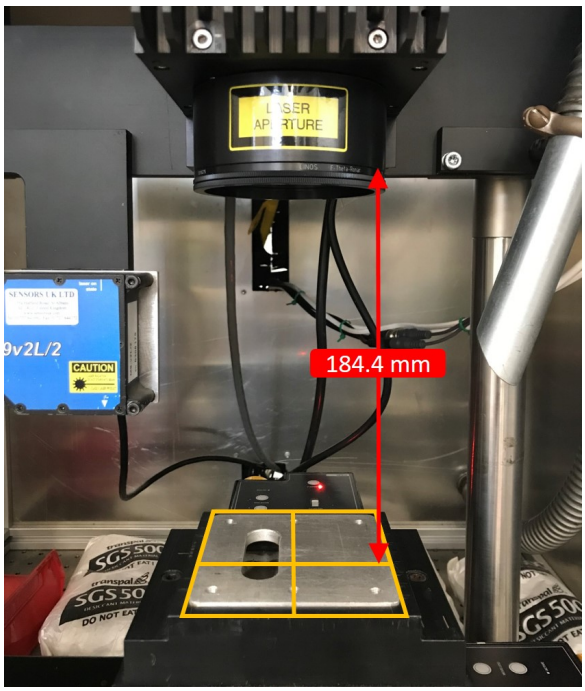

Figure 3.22: *Distance between 3-axis Thorlabs stage and the XLR8 scanning system at a 22.6 mm position in the stepper motor driven lab jack*

The focal position should give the smallest possible beam size. By reducing the area processed by the laser to a minimum, the intensity increases and the required energy to process the material decreases. In Figure 3.23 the distribution of a focussed laser is shown.

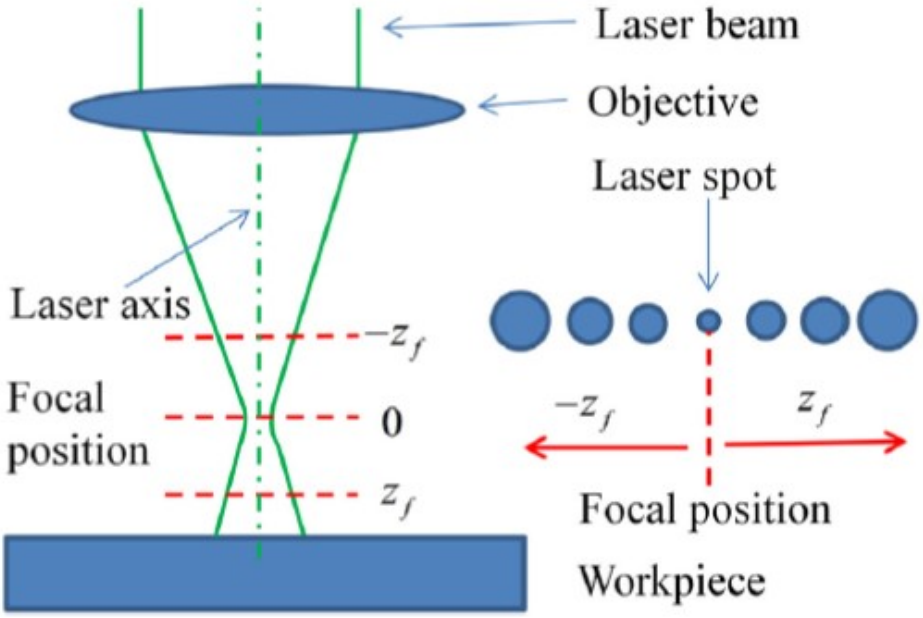

Figure 3.23: *Energy distribution of a focussed laser beam[118]*

Stage position was modified according to the measured material thickness of each sample in order to keep the correct distance between the galvo scanning system and the material. This is to ensure the laser processing of each one of the samples in the focal plane.

This process is replicated in the High-Q picosecond pulsed laser. The Nutfield XLR8-10 scan head used with this system includes a F-theta lens with a focal length of 100 mm (LINOS F-Theta-Ronar 100 mm). This difference in the lens modifies the distance from the scanning system to the material in order to obtain the focal plane. This working distance (WD) is measured from the edge of the equipment to the focal plane (WD = 126 mm) as shown in Figure 3.24.

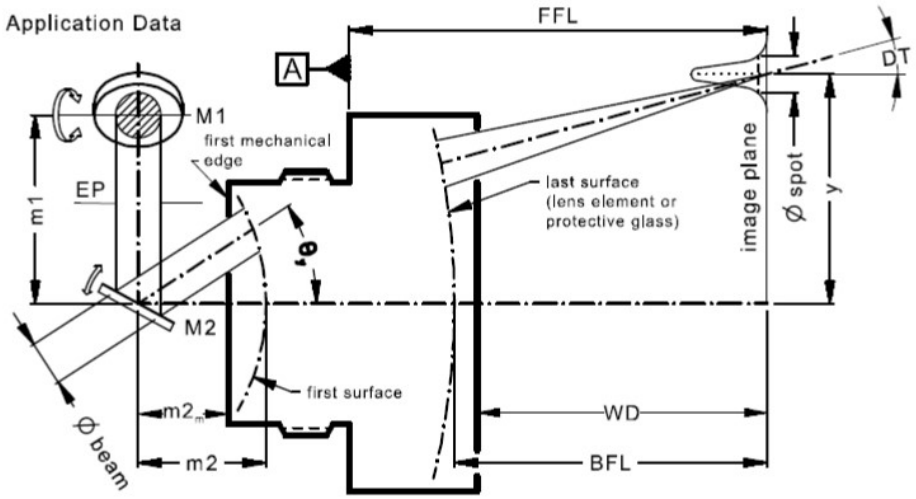

Figure 3.24: *Schematic drawing of the LINOS F-theta-Ronar 100 mm lens, 1064 nm design wavelength [119]*

3.5.2 Thermal post-processing

The creation of superhydrophobic surfaces is highly related to the micro and nano structures created on the surface of a material, however, a coating on top of these structures is commonly used to improve the wettability properties. In the case of metallic materials, this coating is an oxide of the material. This oxidation is created during the laser surface texturing process and it requires a certain amount of time in order to fully stabilise the layer. The required time is mostly determined by the type of material and the storage conditions, typically more than 2 weeks are required. In order to reduce this time, the implementation of a low-temperature annealing process has been previously reported with mixed results in the wettability behaviour[120–124].

To investigate the effect of thermal post-processing in the wettability properties on the laser textured material the use of a conventional electric oven was required. The equipment used was an electrical oven Memmert SM 100, capable of reaching temperatures up to 220°C (Figure 3.25). The samples were placed inside the oven at different temperatures from 100 to 200 °C in the pre-heated oven for the low temperature annealing. The time for this thermal post-process was varied in order to find the most suitable parameters for an effective wettability modification.

Figure 3.25: *Memmert SM 100 oven with sample placement*

3.5.3 Sample storage conditions

Due to the duration of measurement tests of the contact angle, the samples had to be stored. To minimize the introduction of new elements in the storage conditions, these were placed in small plastic boxes to avoid contamination with external agents, but still maintaining normal ambient conditions (Figure 3.26).

Figure 3.26: *Sample box for storage conditions*

3.6 Summary

This chapter highlights the equipment employed in this research. The two main pulsed laser sources during this thesis (SPI Laser and High-Q Laser) were described. The illustration of the required equipment for the correct operation of both laser systems such as galvanometer scan head systems and positioning stage was explained. Measurement equipment used through the development of this research was explained, white light interferometer, SEM and contact angle measurement equipment are fundamental for the correct characterisation of the created surface structures with the laser systems. Material selection for the research is explained and their main properties discussed. Fundamentals for the experimental set-up and the sample positioning due to the galvanometer scan head operation requirements are explained. Finally, sample post-processing methods and storage conditions are reviewed for the correct parameter analysis of the samples.

Chapter 4

Nanosecond pulsed laser ablation of Ti-6Al-4V

4.1 Introduction

To create a structured surface capable of modifying the wettability properties of Ti-6Al-4V, a window of suitable parameters needs to be defined. Numerous pulsed laser types have been investigated in recent years for this application, all with different operating parameters. The difference discovered between these operating parameters makes it necessary for the exploration of suitable parameters for the surface texturing of a given material and laser type. In this chapter, the effects of individual parameters on a surface are presented. One of the main results to analyse is the ablation threshold of the material with different pulse durations. Ablation threshold is defined as the minimum amount of energy required for ablation to occur. In this chapter, the ablation threshold of Ti-6Al-4V is calculated with different pulse durations to have a complete understanding of the effects on the material with the varying parameters. The ablation threshold parameters are analysed through an optical microscope and white light interferometer, showing the effects of varying the pulse duration and laser energy on the material.

Surface topography of the ablated material surface is analysed with a white light interferometer(WYKO NT1100) in order to observe the effects on the amount of material removed by laser ablation as well as the deposition of molten material on the surface.

Tests were undertaken on the main laser system of this research, the nanosecond pulsed laser described in Chapter 3, in order to explore a more robust industrial method for the creation of superhydrophobic surfaces. The thermal component of the nanosecond pulse regime can improve the creation of beneficial surface structures due to the deposition of molten material created by the pulse.

4.2 Experimental procedure ablation threshold

Initial tests were aimed to understand the production of ablated craters in the surface of the material under different nanosecond pulse durations. For this, two different sets of Ti-6Al-4V samples (polished and as-received samples), were placed in the focal plane of the nanosecond pulsed laser system. Before laser processing, all the samples were cleaned with acetone and dried under ambient conditions. For the ablation technique, a set of lines with the parameters showed in Table 4.1 were produced in both sets of samples with increasing laser energy.

Table 4.1: *Processing parameters for ablation threshold calculation on polished and as-received Ti-6Al-4V*

Variable	Range of values	Units
Average power	$2.50 - 7.20$	$Watts$
Frequency	$25 - 65$	kHz
Pulse duration	$65 - 200$	ns
Scanning speed	$Varied$	mm/s
Number of lines per pulse duration	31	
Average power step	0.10	$Watts$

Thirty-one different average power levels, with a step of 0.10 Watts, were used in order to obtain a meaningful amount of data for the calculation of the ablation threshold for each pulse duration. To produce individual ablated craters, the scanning speed was varied to have enough separation between the individual laser pulses according to the repetition frequency used (Figure 4.1). As the focused beam size was approximately 50 μm, a 75 μm spacing was chosen and maintained. Due to the beam quality and divergence, the created spot in the surface is not perfectly circular, the shape of the ablated craters is elliptical under lower laser fluence. For these conditions, the crater diameter was measured as the smallest elliptical diameter. Three craters were measured at each parameter to obtain a statistical value of the crater size with the specific set of parameters.

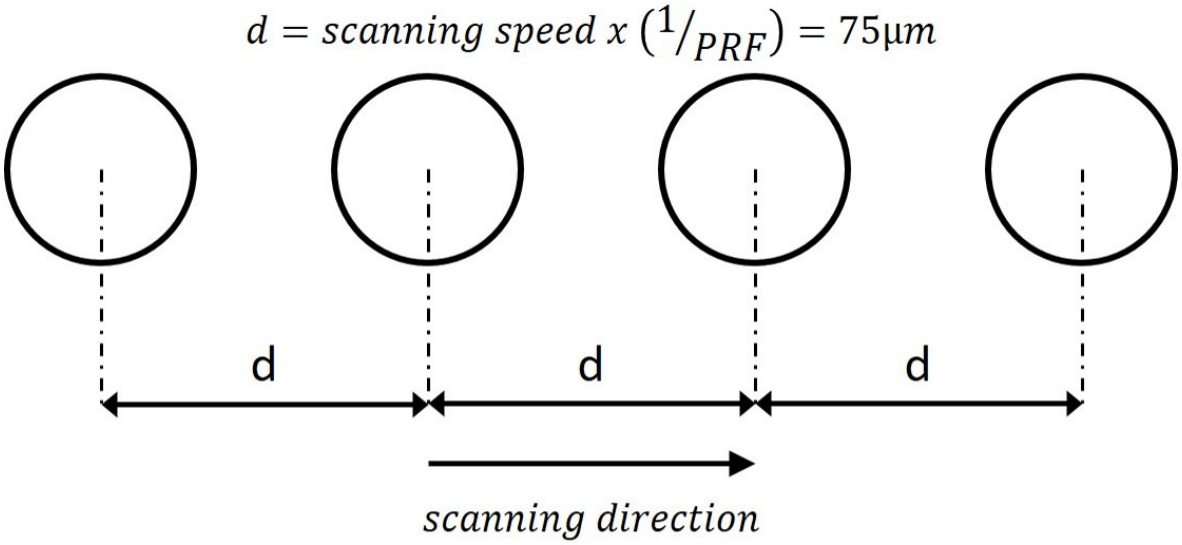

Figure 4.1: *Schematic of nanosecond laser pulse separation for ablation threshold*

The depth of ablation for each one of the parameters was measured with a white light interferometer (WYKO NT1100). A comparison between the pulse duration and the amount of material removed from the material surface was then made. The characterisation of the effects of these parameters in the material surface provides the required knowledge for the creation of surface structures with the nanosecond pulsed laser.

4.3 Experimental results

4.3.1 Ablation threshold

The ablation threshold calculation is based on the comparison between the ablated diameter and the energy used by the laser system. For this the peak fluence needs to be calculated with Equation 4.1[125]:

$$F_0 = \frac{2}{\pi w_0^2} E_{pulse} \tag{4.1}$$

Where:

- w_0^2 is the radius of laser spot size
- *Epulse* is the energy per pulse

For obtaining w_0^2, the laser spot size can be calculated through Equation 4.2 and the equipment parameters for the nanosecond pulsed laser and galvo scanning system given in Table 4.2[1]:

$$D_{min} = \frac{4M^2\lambda f}{\pi D_L} \tag{4.2}$$

Table 4.2: *Nanosecond pulsed laser and galvo scanning system specifications*

Parameter	Specification	Units
Input beam size (D_L)	8.00	mm
Beam quality (M^2)	1.83	
Wavelength (λ)	1064	nm
Focal length of focussing lens (f)	160.3	mm

From the system specifications in Table 4.2, D_{min} can be calculated as $49.68\mu m$. This value is only valid at the focal plane of the galvo scanning system.

The relation between the ablated crater size and the peak fluence of the laser system can be analysed for the calculation of the ablation threshold. This is given by Equation 4.3 due to the quasi-Gaussian distribution of the laser beam of the system[126].

$$D^2 = 2w_0^2 \ln \frac{F_0}{F_{th}} \tag{4.3}$$

Where:

- D^2 is the square diameter of the ablated crater
- w_0^2 is the beam spot radius
- F_0 is the peak fluence
- F_{th} is the ablation threshold

A plot between D^2 (square diameter of the ablated crater) against the peak fluence can be produced in order to obtain a trend line for the crater size. The trend line of the plotted data is obtained through MATLAB software as shown in Figure 4.2.

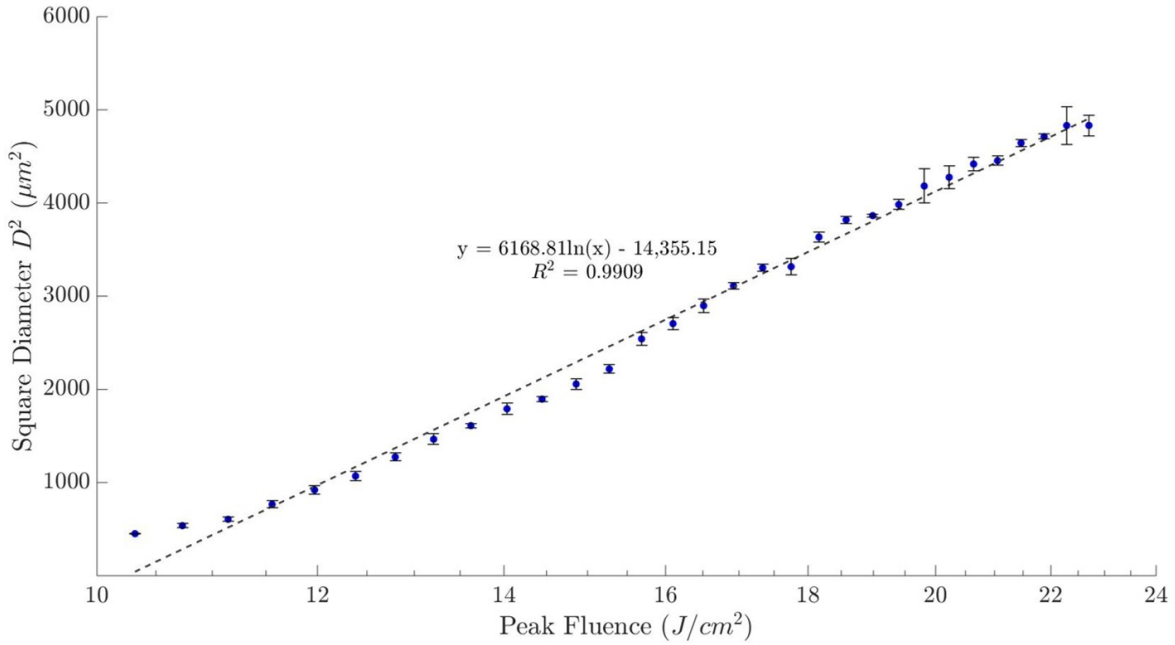

Figure 4.2: *Graph of square ablated crater diameter of polished Ti-6Al-4V against the peak fluence with 200 ns pulse duration. The dotted line represents the fitting equation presented on the graph and R^2 as the variance proportion of the trend line against the measured data.*

After determining the trend line, the extrapolation of D^2 back to zero is calculated for obtaining the ablation threshold of Ti-6Al-4V. With the obtained data the calculated ablation threshold for a single 200 ns pulse duration is $10.25 \pm 0.0933 J/cm^2$ according to variance (R^2).

The process is repeated for different pulse durations with the nanosecond pulsed laser from 65 to 200 ns. The calculation of the ablation threshold with different pulse duration was necessary for the creation of a surface structure in the titanium alloy. With the crater size measurements for each one of the pulse duration, the corresponding trending lines were obtained. Figure 4.3 shows a graph delimiting the ablation of polished Ti-6Al-4V with different pulse durations (65 to 200 ns).

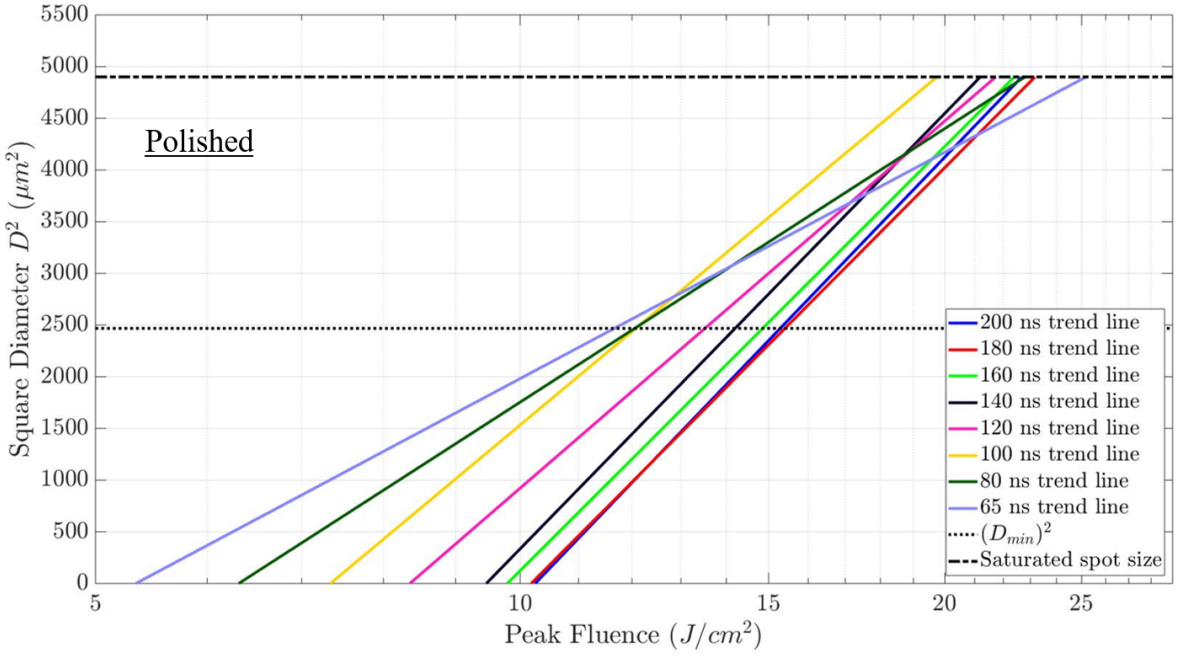

Figure 4.3: *Graph of trend lines for 200 ns to 65 ns pulse duration of square ablated crater diameter of polished Ti-6Al-4V against peak fluence. The dotted line represents the calculated minimum spot size of the focussed laser beam (D_{min}). The dash-doted line represents the saturated crater size for a single spot ablation.*

From the graph in Figure 4.3 the calculated trend lines of different pulse durations for the ablated crater size against peak fluence can be observed. The graph is divided with two horizontal lines representing the calculated minimum spot size (D_{min}) and the saturated ablated crater size for the system configuration ($\approx 70\ \mu m$ of diameter). These lines divide the graph into two zones; the first zone shows at what peak fluence (J/cm^2) the ablated crater size is inferior to the calculated laser spot beam (D_{min}) for different pulse durations. The second zone in the graph (between the two horizontal lines) represents peak fluence required for an ablated crater size superior to D_{min}.

The slope of the different trend lines is close to constant between 200 and 100 ns pulse durations, however, for pulse durations inferior to 100 ns the slope changes as can be observed in the trend lines for 80 and 65 ns pulse duration. The change in the slope of the trend lines is due to the decrease in the interaction time between the laser beam and the surface for the material ablation. Calculation and plotting of the corresponding trend lines allows the prediction of the ablated crater size with different pulse durations at a given pulse energy (E_{Pulse}).

The same procedure was performed on as-received Ti-6Al-4V in order to observe possible differences between the ablated crater size and peak fluence required for different pulse durations.

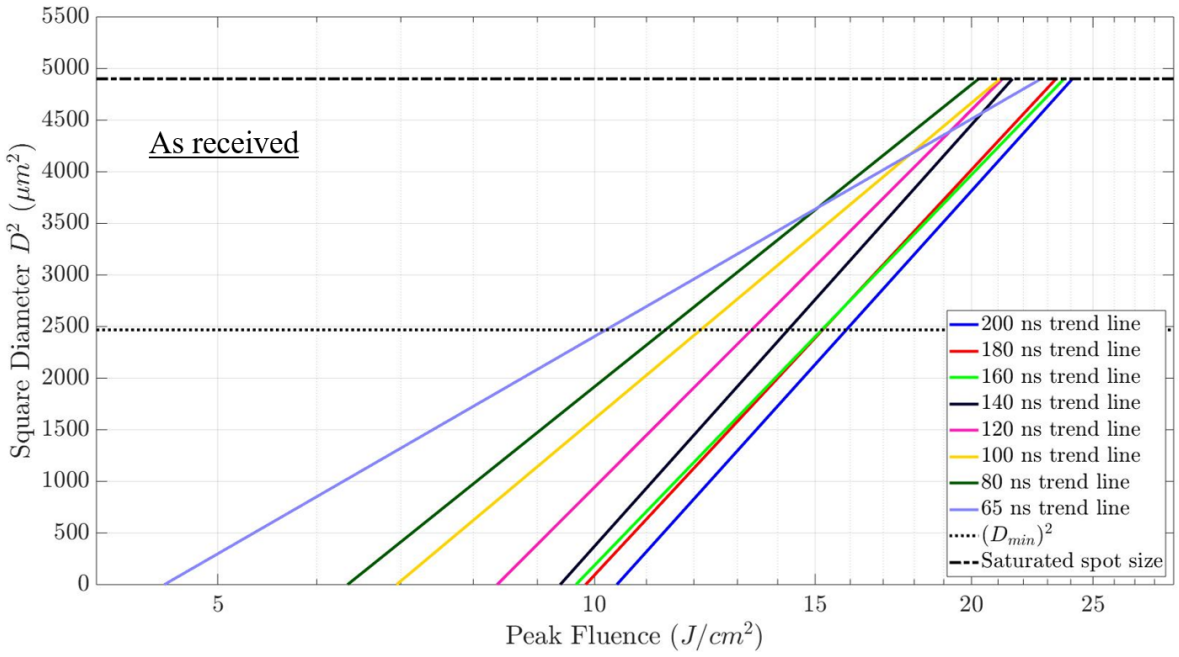

Figure 4.4: *Graph of trend lines for 200 ns to 65 ns pulse duration of square ablated crater diameter of as-received Ti-6Al-4V against peak fluence. The dotted line represents the calculated minimum spot size of the focussed laser beam (D_{min}). The dash-doted line represents the saturated crater size for a single spot ablation.*

Figure 4.4 shows the calculated trend lines for the ablated crater size with different pulse duration on the surface of as-received Ti-6Al-4V. From this graph it can be observed that the tendency on the trend lines is similar to those calculated for polished Ti-6Al-4V. The only significant difference is on the required peak fluence (F_0) for the ablation to occur at 65 ns of pulse duration. This F_0 is reduced in comparison with the F_0 required for ablation to occur on polished samples as shown on Figures 4.3 and 4.4.

The two horizontal lines divide the graph into two zones in the same way as in Figure 4.3, since the material is placed in the focal plane, the same as the polished sample, keeping the calculated D_{min} and saturated spot size in the same values. The slope of the trend line is constant for different pulse durations other than the slope for the 65 ns pulse duration trend line, similar to the one shown in Figure 4.3.

In order to observe the specific conditions for each of the pulse durations, the ablation threshold was calculated for a pulse duration range between 65 and 200 ns. The calculation of these values is fundamental for the determination of the minimum F_0 required for the removal of material from the surface through laser ablation.

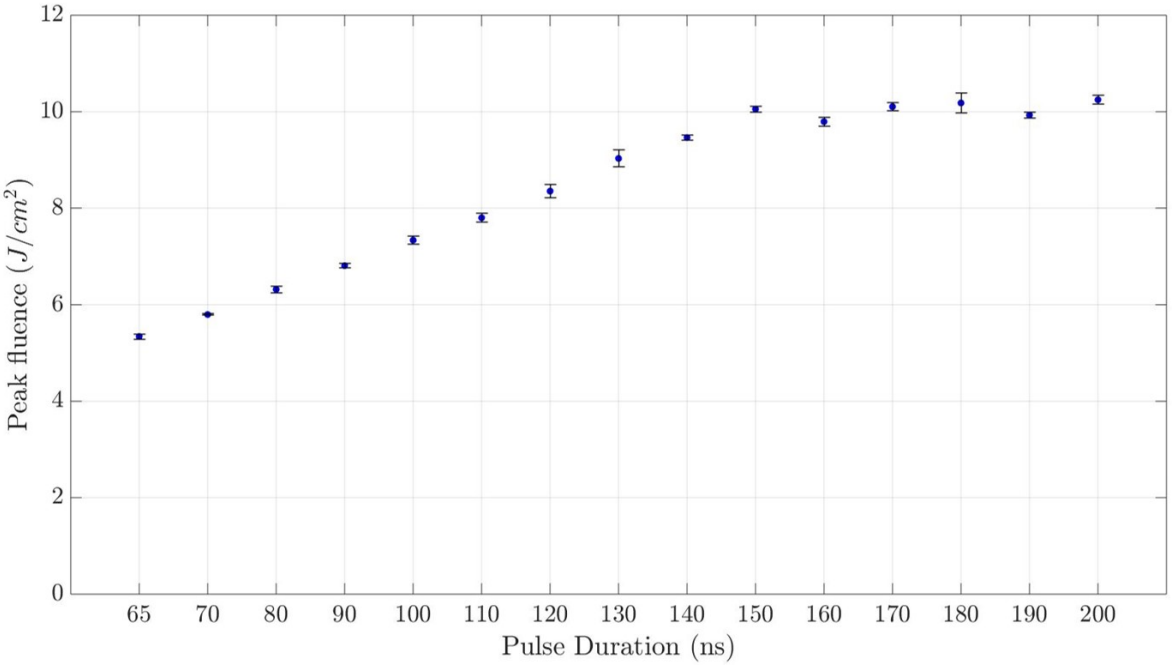

Figure 4.5: *Graph of ablation threshold of polished Ti-6Al-4V with a nanosecond pulsed laser and different pulse durations.*

The ablation threshold of the titanium alloy reduces as the pulse duration decreases, as it can be observed from Figure 4.5. As shown in this graph, the required F_0 for ablation is almost constant for pulse durations between 150 and 200 ns. As the pulse duration decreases below 150 ns, the ablation threshold steadily decreases as the pulse duration is reduced.

The nanosecond fibre laser system uses a set of pre-defined repetition frequencies in order to obtain a reliable pulse energy with different pulse duration as described in Chapter 3 Section 3.2.1 "SPI G4 nanosecond pulsed fibre laser". However, the user manual provided by the manufacturer clearly states that the change on pulse duration of the system has an effect on the temporal pulse shape.

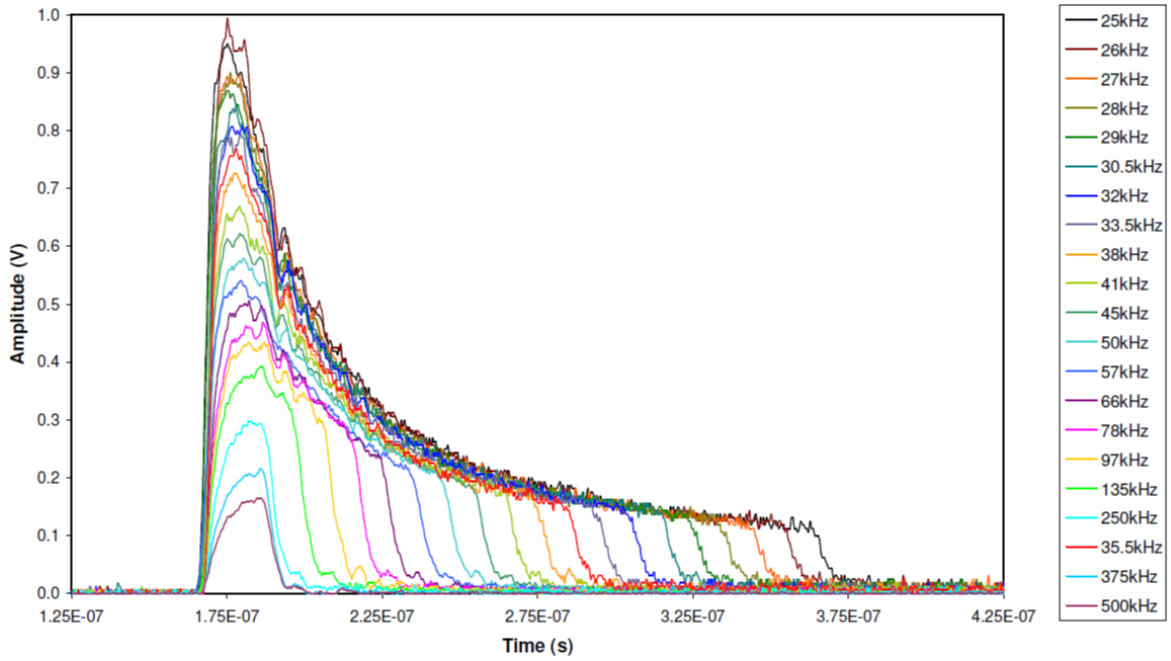

Figure 4.6: *Example of pulse shapes for a 20W pulsed laser module provided by SPI Lasers [100])*

Figure 4.6 shows the temporal pulse shape of different pulse durations for the SPI G4 nanosecond fibre laser system. To the right a list of the pre-defined repetition rate for each pulse duration is displayed, starting from 25 kHz(200 ns pulse duration), and increasing up to 500 kHz(9 ns pulse duration). As can be noticed from the graph the pulse rapidly increases on intensity at the beginning of the pulse until reaching a maximum pulse energy and then decreases almost with the same rate, however, this is followed by a long low-intensity tail until the end of the pulse. This is specially noticeable in long pulse durations (100 to 200 ns), nevertheless as the pulse duration is reduced below 100 ns(45 kHz of repetition frequency), this low-power tail of the pulse is decreased and the shape of the pulse approaches a Gaussian shape.

As the temporal shape of the nanosecond pulse approaches to the Gaussian shape, the energy is more efficiently deposited on the material and the ablation threshold is reduced [127]. However, even when the required E_{Pulse} for ablation is reduced, the average power is increased due to the operation principles of the laser system.

The decrease in pulse duration requires an increase in the repetition frequency, thus an increase in average power is required to maintain the pulse energy. In this case, the average power required for the ablation threshold with a 65 ns pulse duration is $\approx 3.36W$, which is higher than the $\approx 2.48W$ of average power required for the ablation threshold with a 200 ns pulse duration.

The calculation of the ablation threshold for as-received Ti-6Al-4V with different pulse durations was carried out with the same procedure as with polished samples in order to compare the effects of sample roughness on ablation of the material. Comparison between the calculated values are shown in Figure 4.7.

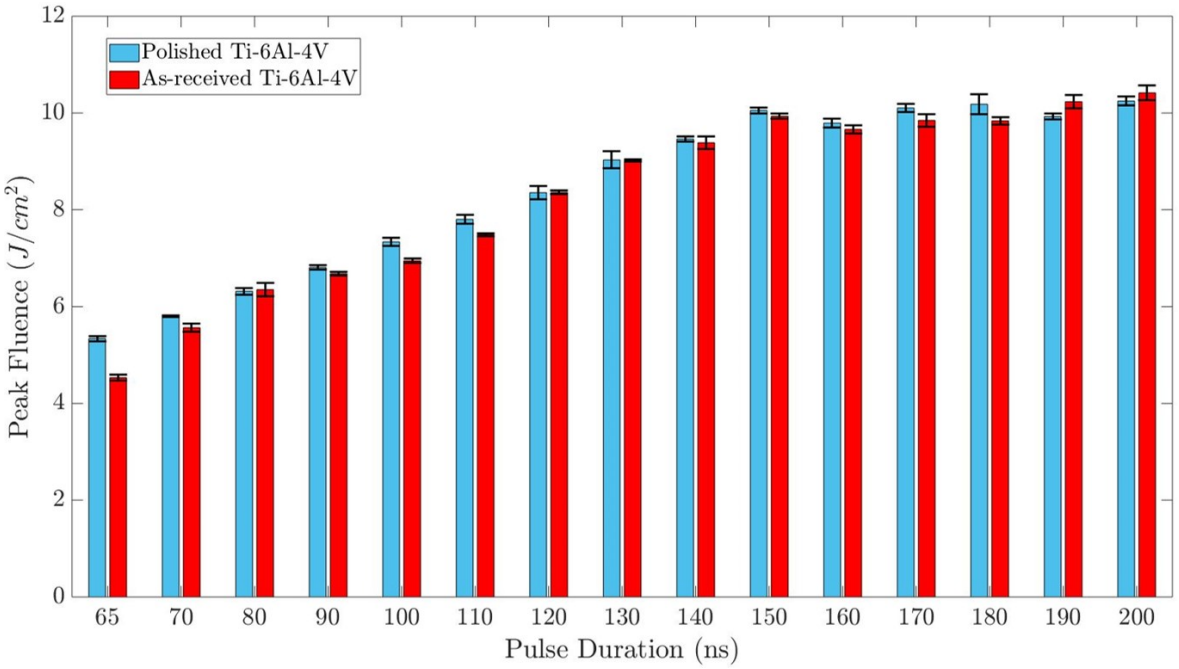

Figure 4.7: *Graph of Peak Fluence required for ablation threshold of polished Ti-6Al-4V (Blue) and as-received Ti-6Al-4V (Red)*

The comparison between ablation threshold values obtained on polished and as-received Ti-6Al-4V showed a similar trend of decreasing the required F_0 for ablation as the pulse duration decreases. The ablation threshold of as-received Ti-6Al-4V is similar to the polished sample in most of the different pulse durations with the exception of the 65 ns pulse duration.

The difference found with the 65 ns pulse duration for the two types of samples is approximately a Peak Fluence (F_0) of 0.81 J/cm^2 inferior for the ablation threshold of as-received Ti-6Al-4V to the required F_0 for the polished sample(5.34 J/cm^2 for polished and 4.53 J/cm^2 for as-received samples).

Obtained measurements showed that the nanosecond pulsed laser is fully capable of ablating the surface of both types of samples within the operational parameters of the system. The pulse duration reduction has effects on the shape of the ablated crater due to the reduced interaction time between the beam of the laser and the material surface as it can be observed in Figure 4.8.

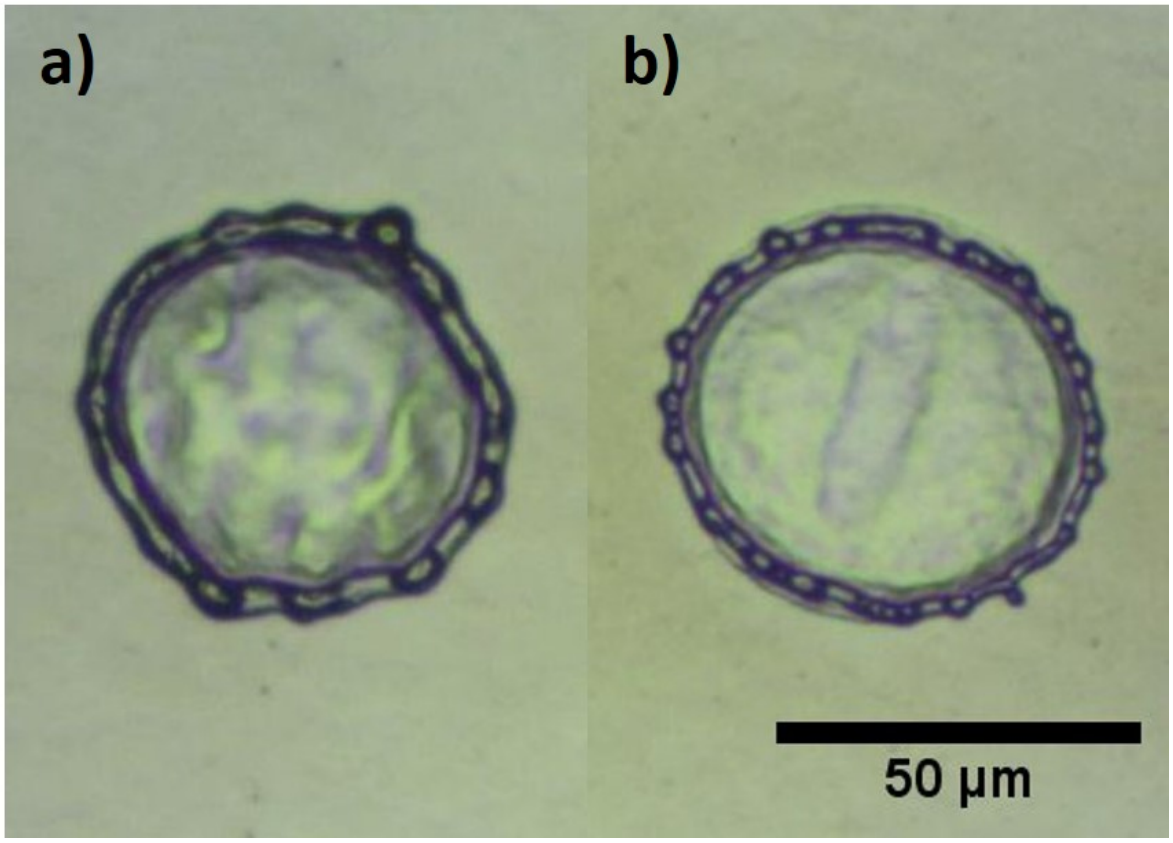

Figure 4.8: *Ablated craters created with single pulse nanosecond ablation, a) 200 ns pulse duration with $E_{Pulse} \approx 148\ \mu J$ b) 65 ns pulse duration with $E_{Pulse} \approx 113\ \mu J$. E_{Pulse} is calculated for a crater size $\approx D_{min}$ for both pulse durations.*

These effects will be explored in the next section of the current chapter for a detailed analysis. Differences between the required levels of energy for the ablation and the shape of the ablated craters need to be taken into consideration for the creation of surface micro-structures in the following chapters.

4.3.2 Surface topography

To evaluate the amount of material removed by ablation with different levels of energy and pulse duration, the samples were measured with a white light interferometer (WYKO NT1100). Samples used for the calculation of the ablation threshold were analysed in order to compare the effects of energy level, for this the depth of ablation was measured. A typical cross-sectional view of three ablated craters on the surface of polished Ti-6Al-4V is shown in Figure 4.9.

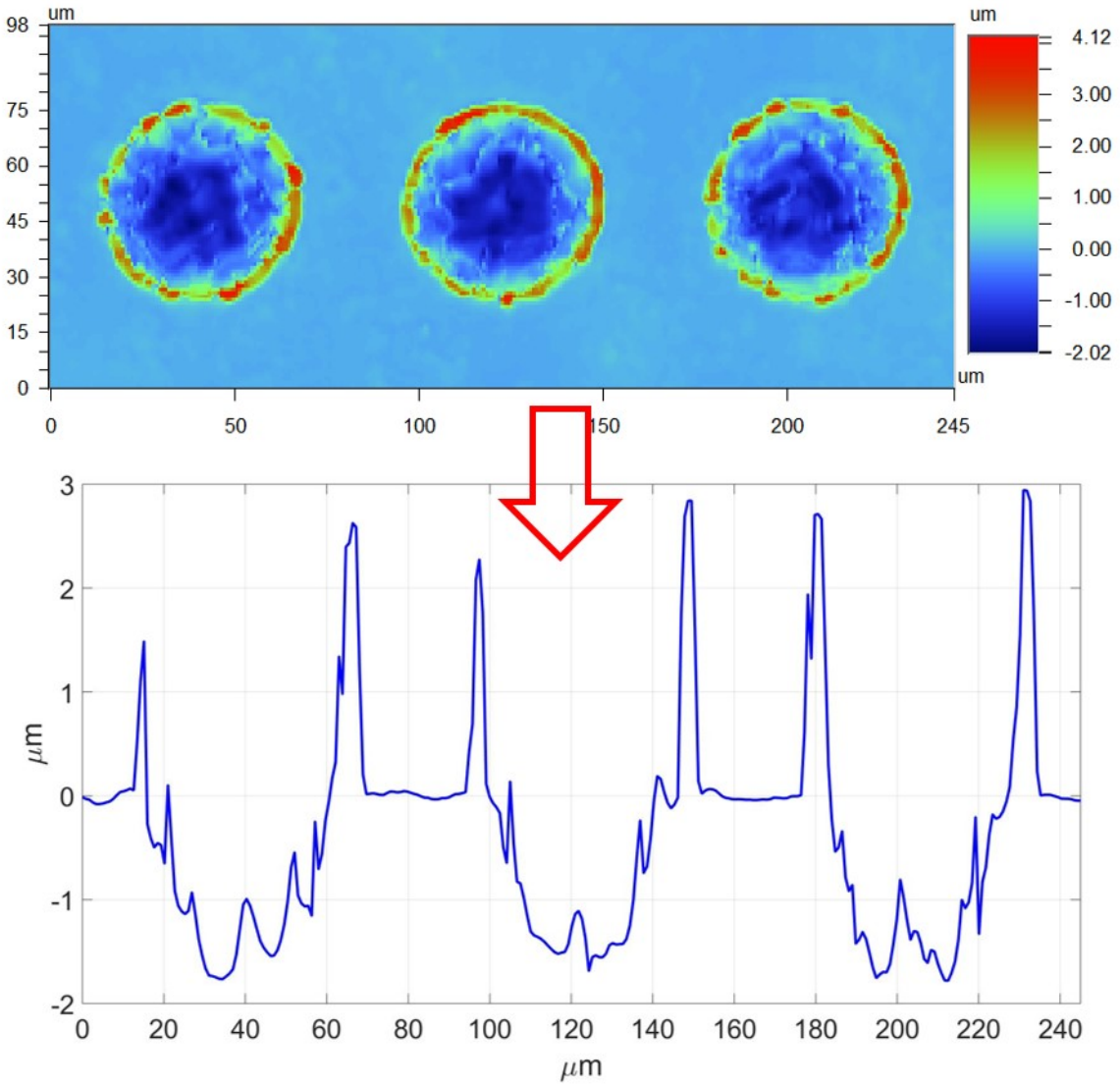

Figure 4.9: *Cross-sectional surface profile analysis of ablated polished Ti-6Al-4V with nanosecond pulsed laser ($E_{Pulse} \approx 148\ \mu J$ and 25 kHz of repetition rate) for ablation depth measurements*

Measurements of the ablation depth are carried out through the method shown in Figure 4.8 for each one of the parameters produced in the ablation threshold section. This is to be able to compare the effects of energy and pulse duration in the amount of material removed by the laser. A typical graph for the ablation depth is shown in Figure 4.10.

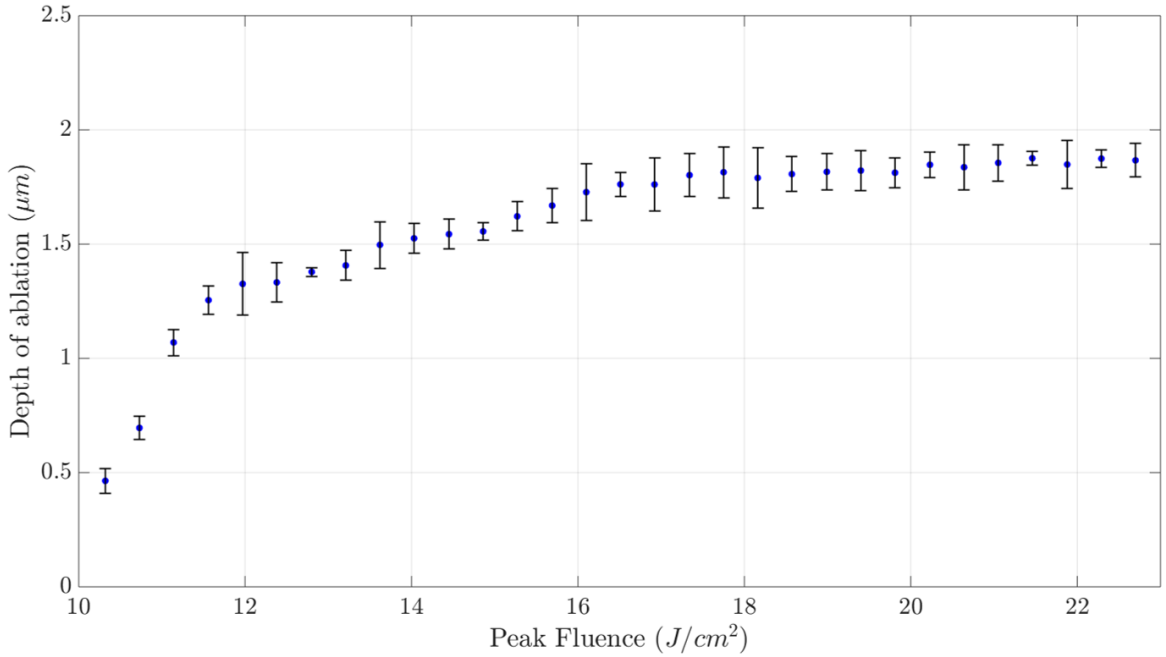

Figure 4.10: *Ablated depth vs pulse energy for a single pulse ablation with 200 ns of pulse duration and a repetition rate of 25 kHz on polished Ti-6Al-4V*

The ablation depth is small with low energy values, however, it increases as the E_{Pulse} of the laser energy increases, as can be observed from Figure 4.10. The relatively large error bars presented on the graph are result of the quality beam mode of the laser system, further highlighted in the next pages of this section. An increase in E_{Pulse}, therefore, modifies the amount of material removed as well as the ablated crater size. This increase occurs until the E_{Pulse} reaches a level where the laser pulse cannot remove more material through a single spot ablation process. After this point, the laser keeps increasing the intensity on the surface of the material causing undesirable results due to the high thermal component applied. These types of effects are not suitable for the production of a functional surface on the material since they can affect the material condition, decreasing the final quality and reliability of a component.

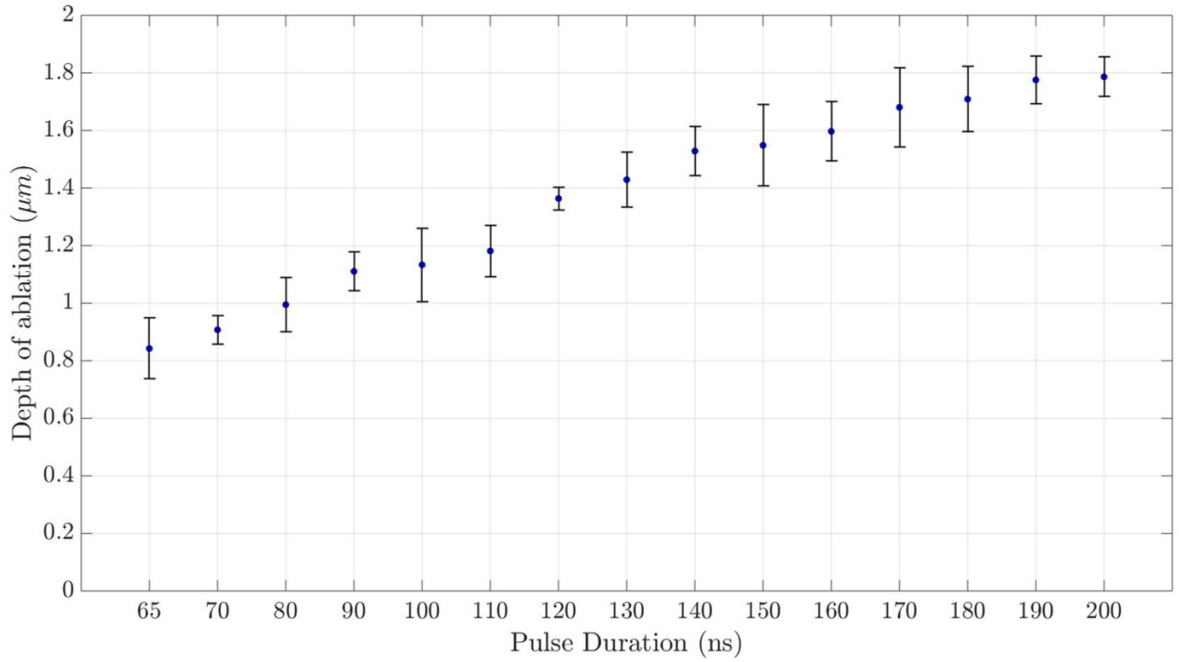

Figure 4.11: *Depth of ablation of different pulse duration. The used E_{Pulse} is the required for a crater size $\approx D_{min}$*

Figure 4.11 shows the depth of ablation created with different pulse durations in a range of 65 to 200 ns. The E_{Pulse} used for the ablated craters was calculated through the obtained trend line functions for the ablation threshold mentioned in the previous section of this chapter. The E_{Pulse} was calculated for an ablated crater size $\approx D_{min}$ for a correct comparison between the removed material.

As can be seen from Figure 4.11, the amount of removed material is reduced as the pulse duration is reduced, this is due to the pulse shape delivered by the G4 nanosecond fibre laser(see Figure 4.6). The pulse shape of the laser system is characterised as a relatively fast peak pulse (of around 40 ns), followed by a low energy pulse trail to complete required pulse duration; this shape is valid especially for pulse durations between 100 and 200 ns. This particular pulse shape is more efficient for the removal of material from the surface due to the extended pulse trail as discussed by Ali Gokhan Demir *et al* [127].

As the pulse duration decreases below 100 ns, the pulse shape is closer to a Gaussian-shape pulse, however, the decrease in pulse duration and the configuration of the SPI G4 system decreases the amount of material removed by a single spot ablation. The operation parameters of the SPI nanosecond pulsed laser, average power and pulse repetition frequency are increased for the correct operation of the laser system, thus, the required energy consumption is increased with shorter pulse durations.

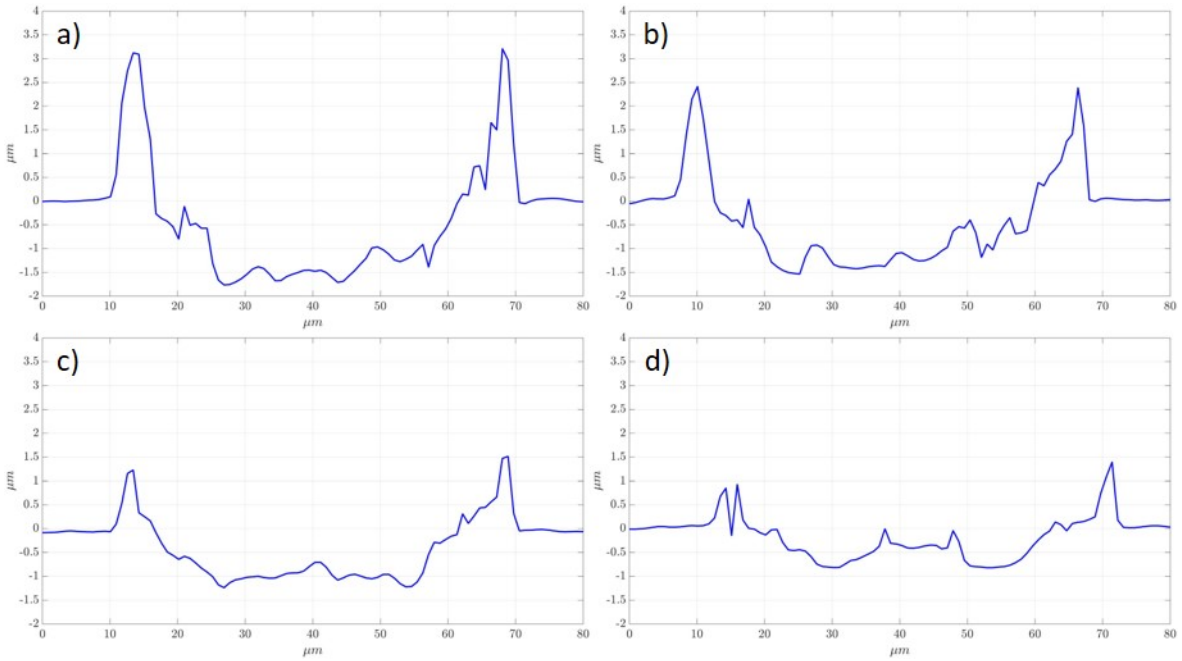

Figure 4.12: *Profile section of single spot ablation polished Ti-6Al-4V, with the nanosecond laser pulse, a) 200 ns pulse duration, b) 160 ns pulse duration, c) 110 ns pulse duration, d) 65 ns pulse duration*

Figure 4.12 shows the surface profile of the material ablated with a single spot and different pulse durations. From these profiles, the amount of material removed with the different pulse durations can be observed, as well as the re-deposition of the molten material on the edges of the ablated crater. The four graphs show how the depth of ablation is reduced as the pulse duration reduces, starting from a 200 ns pulse duration and reducing to 65 ns. The depth of the ablated crater reduces by more than half between these two pulse durations, starting with a 1.78 μm of average depth with a 200 ns, and reducing to 0.84 μm with a 65 ns pulse.

Another important effect can be observed from these profile graphs, the quality or mode of the laser beam delivered by the system. As can be observed, reducing the pulse duration for ablation of the surface, displays how the mode of the laser has an effect on the ablated crater. Profiles of the ablated crater with 110 and 65 ns pulse durations, show the effect of laser beam quality in the system, ($M^2 \approx 1.83$). The centre of the ablated crater shows an area where the material has not been removed as efficiently as in the surrounding areas of the crater.

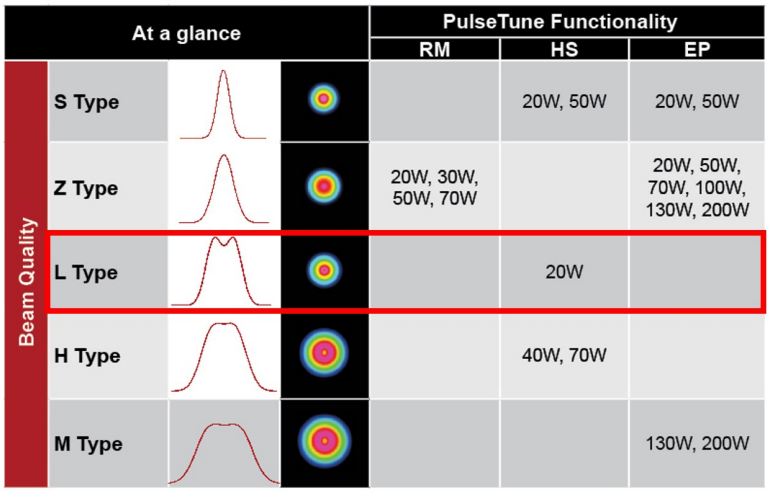

Figure 4.13: *Beam quality option and combinations provided by SPI Laser for the redENERGY G4 Nanosecond Pulsed Lasers*

The laser beam quality factor the system is defined by the manufacturer as seen in Figure 4.13. The table shows the beam quality factor or mode for different G4 nanosecond pulsed laser variants. In this case, the L type corresponds to the system used in this investigation. The cross-section of the L type laser beam shape is shown.

As seen in Figures 4.12 and 4.13, the beam quality has an effect on the energy distribution of the laser through the spot beam applied in the surface, affecting the ablated crater shape. This is particularly noticeable with short pulse durations(65 - 100 ns). Due to the amount of interaction time between the beam and the material, this effect is reduced with larger pulse duration, such as the 200 ns pulse.

The laser beam is near Gaussian with a slight dip in intensity at its peak. Figure 4.13 shows the effect of this in the ablated crater shape, where the centre of the crater is generally the deepest point, and the depth is reduced as it approaches the ablated crater edges. This is due to most of the energy delivered by the laser being concentrated in the centroid of the laser beam, and this energy is reduced as it moves away from this point. The slight dip intensity is only apparent in Figure 4.12 (c) and (d), i.e. shortest pulse duration.

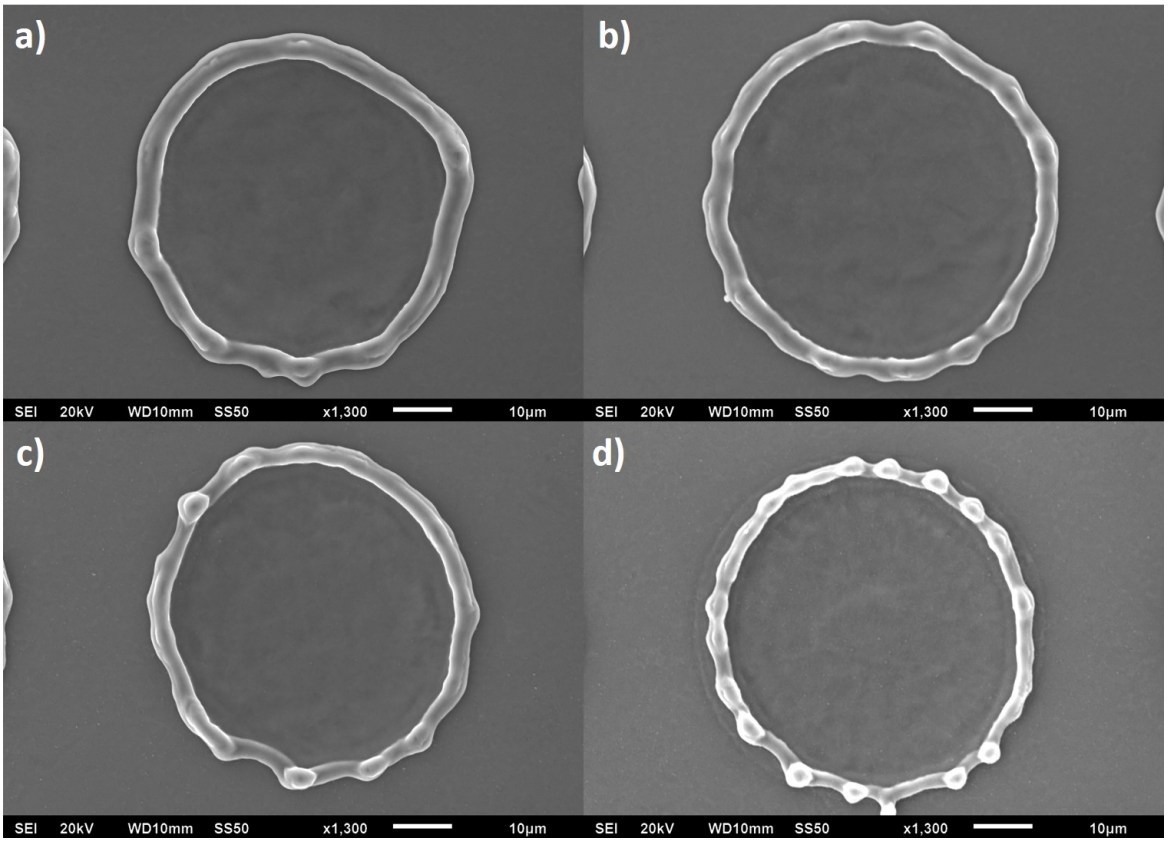

Figure 4.14: *Ablated craters created with single pulse nanosecond ablation, with different pulse duration and required E_{Pulse} for a crater size $\approx D_{min}$, a) 200 ns pulse duration, b) 160 ns pulse duration, c) 110 ns pulse duration, d) 65 ns pulse duration*

Figure 4.14 shows the difference in the amount of molten material in the outer ring of the ablated crater. The molten material is apparently reduced as the pulse duration is decreased. The reduction of molten material in the outer ring of the ablated crater is due to the temporal pulse shape of the nanosecond laser. The pulse rise followed by a low energy coupling time increases the interaction between the laser radiation and the heated substrate increasing the formation of molten material on the surface as previously reported[127–129].

One of the main differences of short-pulsed lasers compared with ultra-short pulsed lasers is the thermal component deposited into the material. Ultra-short pulsed lasers such as femto and picosecond pulsed lasers are capable of ablating the material without the significant generation of a thermal component in the surface, this is called cold ablation, thus avoiding re-deposition of molten material on the surface. The thermal component of the nanosecond pulse melts part of the material in the ablation process, as discussed in Chapter 2 Section 2.3 "Laser Surface Texturing".

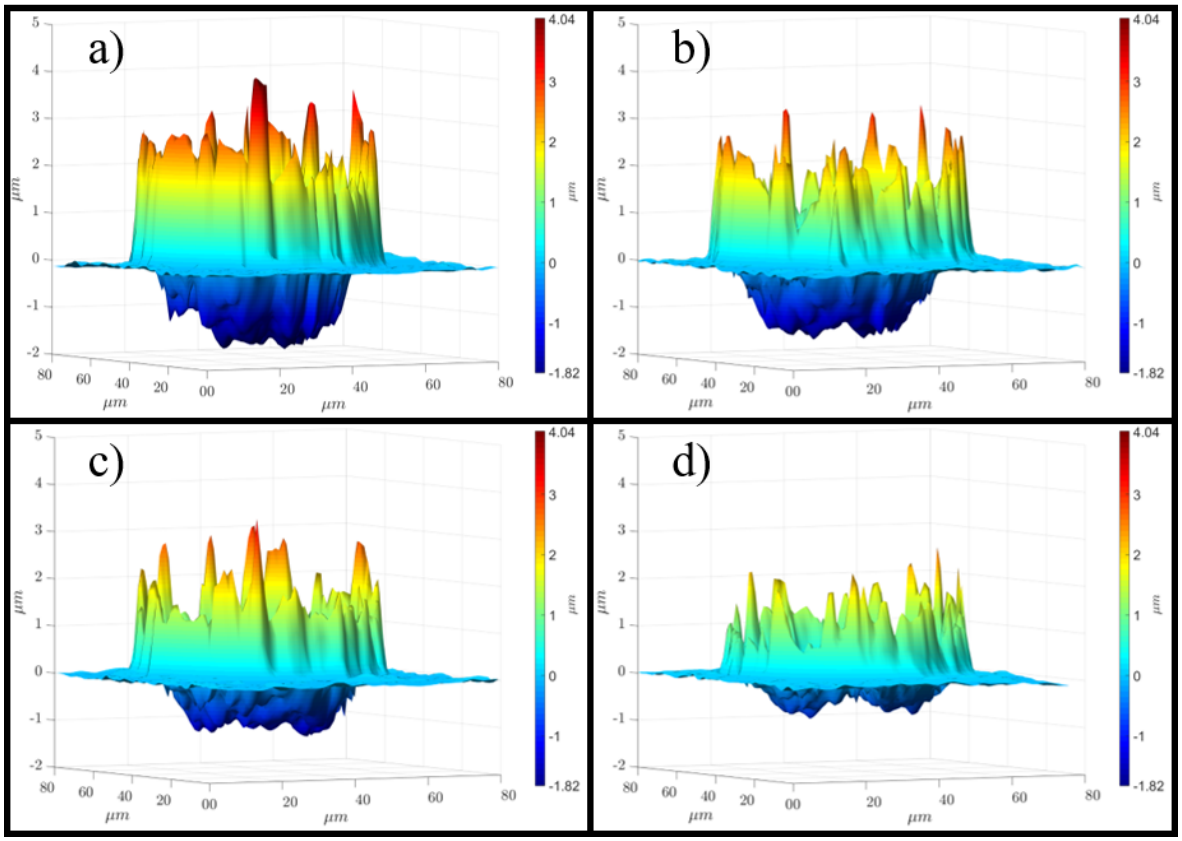

Figure 4.15: *3D representation of ablated crater and molten material with a single pulse of the nanosecond pulsed laser on Ti-6Al-4V polished surface, a) 200 ns pulse duration* $E_{Pulse} \approx 148\,\mu J$*, b) 160 ns pulse duration* $E_{Pulse} \approx 144\,\mu J$*, c) 110 ns pulse duration* $E_{Pulse} \approx 121\,\mu J$*, d) 65 ns pulse duration* $E_{Pulse} \approx 113\,\mu J$*.*

The effect of pulse duration during the ablation process with a nanosecond pulsed laser can be observed in Figure 4.15. The amount of re-deposited molten material on the surface is decreased as the pulse duration decreases.

The height of molten material in the surface reaches a maximum of 4.04 μm with the 200 ns pulse duration, and decreases as the pulse duration decreases, reaching a height of 2.85 μm with a 65 ns pulse duration. The uniformity of the molten material on the surface is affected by the reduction of the pulse duration as can be observed. With the use of 65 ns pulse duration for ablation, a smaller volume quantity of molten material is deposited in the outer ring of the ablated crater. In comparison, the quantity of molten material deposited in the outer ring is significantly increased with 200 ns pulse duration.

From Figures 4.12 and 4.14 it can be observed how the ablation and the surface topography is affected with the modification of the pulse duration. Due to the quality of the nanosecond pulsed laser ($M^2 \approx 1.83$), reducing the interaction time of the laser beam with the material can affect the shape of the ablated crater. Reduction of pulse duration has the effect of reducing the depth of ablation and the height of the molten material re-deposited on the outer ring of the ablated crater as observed by Ali Gokhan *et al* [127]. A processing map for a single pulse ablation of Ti-6Al-4V could, therefore, be defined for different pulse durations and their effects on the surface material. The amount of removed material from the surface of Ti-6Al-4V is measured for a single spot ablation, with the depth of ablation reducing as the pulse duration reduces. However, the use of multiple pulse ablation is typically employed for surface texturing of different materials[46, 86–88]. For this, the depth of the ablation is measured for a different number of pulses (1, 2, 4, 8, 16 and 32)with parameters shown in Table. 4.3:

Table 4.3: *Nanosecond pulsed laser parameters for ablation with different number of pulses*

Pulse duration	E_{Pulse}	**Frequency**
200 ns	$148\mu J$	$25kHz$
160 ns	$144\mu J$	$29kHz$
110 ns	$121\mu J$	$38kHz$
65 ns	$113\mu J$	$65kHz$

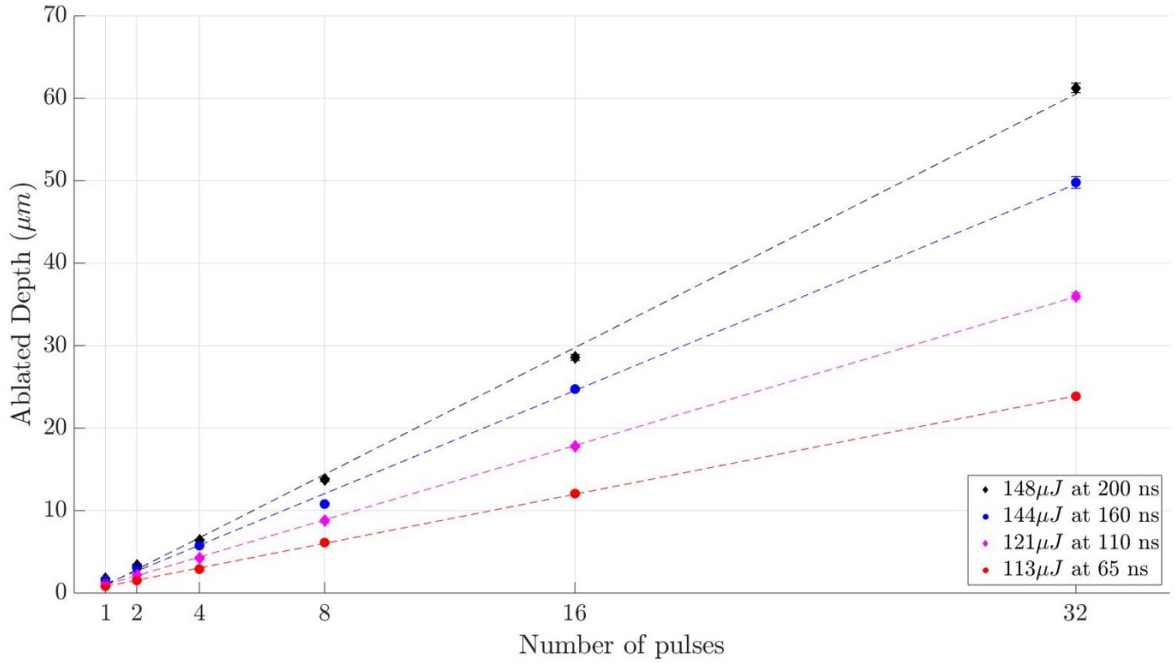

Figure 4.16: *Ablated depth against a different number of pulses in a single spot with different pulse duration and pulse energy.*

Figure 4.16 and Table 4.4 shows how the ablation depth for each of the different pulse durations is modified almost in a linear trend. If the ablation depth is divided between the number of pulses, the results are close to the original ablation depth for a single pulse as would be expected due to a calculated depth of focus of $\approx \pm 1.99\, mm$ given by Equation 4.4[130]:

$$z_F = \pm 2.56 \frac{M^2 \lambda f^2}{D_L^2} \tag{4.4}$$

Where:

- M^2 is the beam quality
- λ is the wavelength of the laser system
- f is the focal length of focusing lens
- D_L is the input beam size

The depth of focus is defined as the distance where the focussed laser beam has approximately the same intensity, defining the working distance where the laser is able to produce the same effect on the material surface[130].

Depth of focus calculation means that the laser system has a window of almost 2 mm where the amount of material removed by each pulse should be similar due to the same beam intensity applied to the material surface.

Table 4.4: *Depth of ablation on Ti-6Al-4V with different pulse durations and a different number of pulses. The displayed values are the average of 7 different crater measures with their corresponding standard deviation.*

Pulse duration	**Ablated Depth (μm)**					
	1 Pulse	**2 Pulses**	**4 Pulses**	**8 Pulses**	**16 Pulses**	**32 Pulses**
200 ns	1.77 ± 0.07	3.38 ± 0.10	6.42 ± 0.13	13.74 ± 0.20	28.59 ± 0.37	61.24 ± 0.57
160 ns	1.60 ± 0.10	3.10 ± 0.11	5.75 ± 0.09	10.79 ± 0.13	24.73 ± 0.19	49.79 ± 0.71
110 ns	1.18 ± 0.09	2.17 ± 0.10	4.23 ± 0.18	8.76 ± 0.20	17.79 ± 0.16	36.02 ± 0.41
65 ns	0.84 ± 0.11	1.53 ± 0.09	2.90 ± 0.17	6.12 ± 0.14	12.06 ± 0.18	23.86 ± 0.09

The creation of a deeper crater increases the amount of molten material deposited on the edges of the ablated crater due to the thermal component of the nanosecond pulsed laser as can be seen in Figure 4.17.

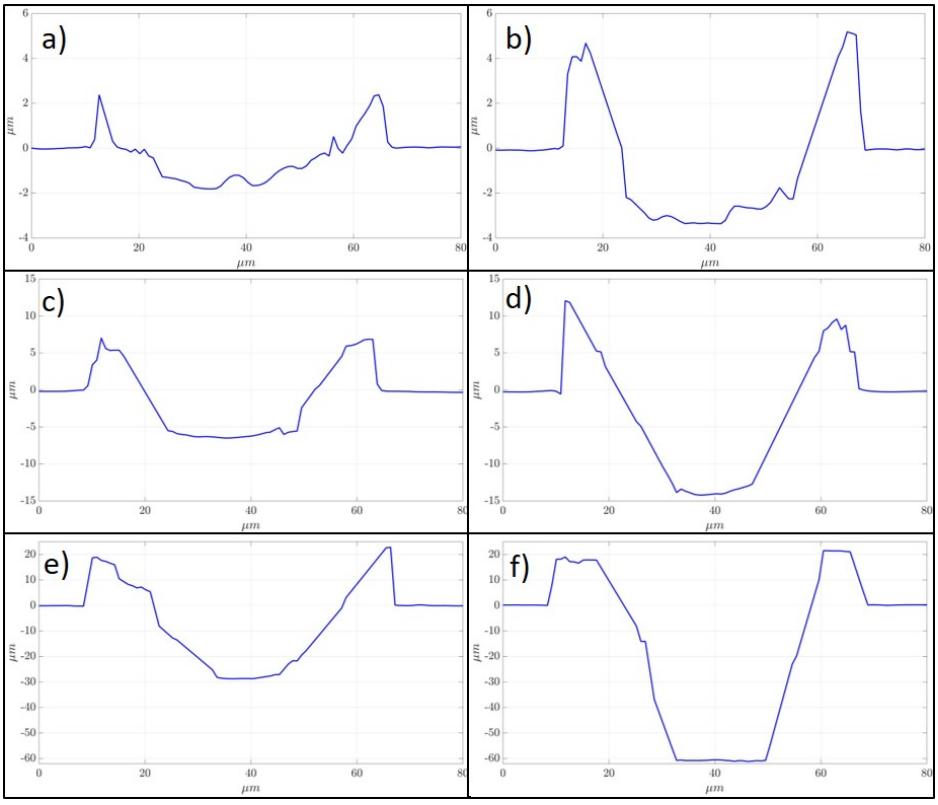

Figure 4.17: *Surface profile of the ablated crater with pulses of 200 ns of pulse duration, a) 1 pulse, b) 2 pulses, c) 4 pulses, d) 8 pulses, e) 16 pulses and f) 32 pulses.*

Figure 4.17 shows how the depth of ablation increases with the number of used pulses in the same spot, however, due to the long pulse duration (200 ns) the accumulation of molten material on the crater edges is increased due to the interaction time of the laser with the material surface. Reducing the pulse duration reduces this interaction time, reducing the ablated depth and the molten material deposited on the crater edge as can be observed in Figure 4.18 below.

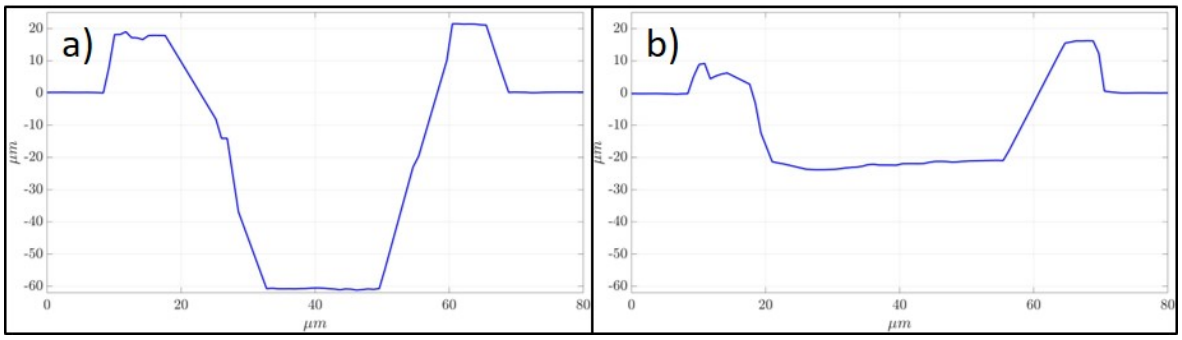

Figure 4.18: *Surface profile of ablated crater with 32 pulses with different pulse durations, a) 200 ns of pulse duration, b) 65 ns of pulse duration*

Figure 4.18 shows the comparison between the ablated depth with 32 pulses with 200 and 65 ns of pulse duration. As can be observed not only the ablated depth is reduced but also the amount of molten material deposited in the crater edge is reduced. This confirms the observations made about the difference in the pulse shape of the G4 SPI Laser between long pulse duration (100 to 200 ns) and shorter pulse duration (below 100 ns) where a long pulse duration increases the generation on molten material.

Another difference that can be observed in Figure 4.17 is the shape of the ablated crater. The ablated crater with a 65 ns pulse duration appears to be wider than the crater created with 200 ns pulse duration. This is due to the accumulation of molten material in the edges of the crater and the observation limitations of the white light interferometer, which is unable to clearly measure the edges features, especially when the ablated depth is increased. As the depth is increased the molten is unable to reach the top of the surface and thus is deposited in the inside crater edges as can be observed from Figure 4.18.

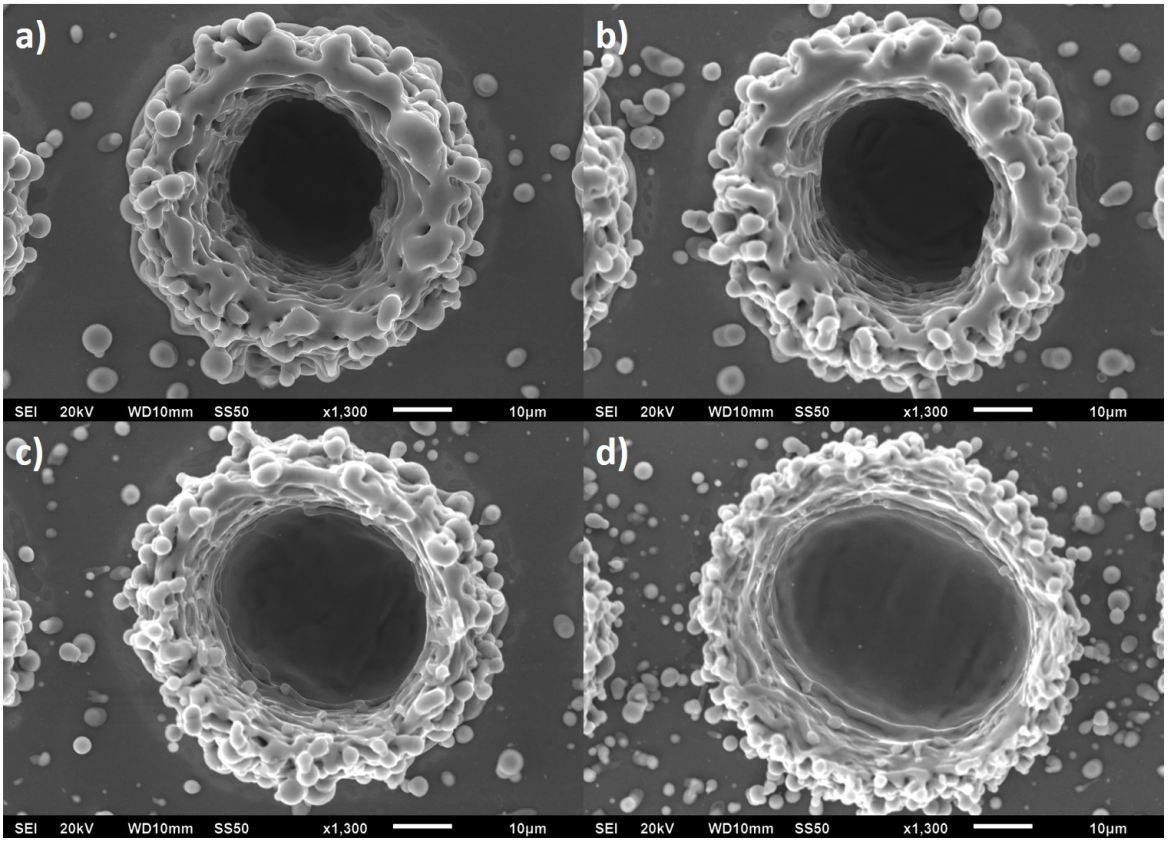

Figure 4.19: *Ablated crater with 32 pulses and different pulse durations, a) 200 ns pulse duration $E_{Pulse} \approx 148\,\mu J$, b) 160 ns pulse duration $E_{Pulse} \approx 144\,\mu J$, c) 110 ns pulse duration $E_{Pulse} \approx 121\,\mu J$, d) 65 ns pulse duration $E_{Pulse} \approx 113\,\mu J$.*

Figure 4.19 shows how the molten material is trapped inside the ablated crater with 200 and 150 ns of pulse duration, reducing the size of the crater due to the molten material accumulated within the crater. With pulse duration of 110 ns and 65 ns the crater size is increased due to less ablated depth and the molten material being expelled to the surface. The 65 ns pulse duration creates a more defined crater, however, the amount of molten material expelled from the crater spot is increased and more molten material can be observed on not processed areas away from the crater spot. A hypothesis for this effect is the relation between the produced shockwave through laser ablation and the molten material produced. As the pulse duration decreases the molten material volume produced by ablation and the thermal component of the nanosecond pulsed laser decreases as well, thus the produced shock wave is able to push the material further away due to the reduced molten material volume[127].

In order to obtain a more accurate representation of the difference of ablated and molten material with different pulse durations, material volume calculations were carried out with the acquired data from the white light interferometer. Volumes of the ablated material and the deposited molten material on the crater edge are presented in Figures 4.20 and 4.21.

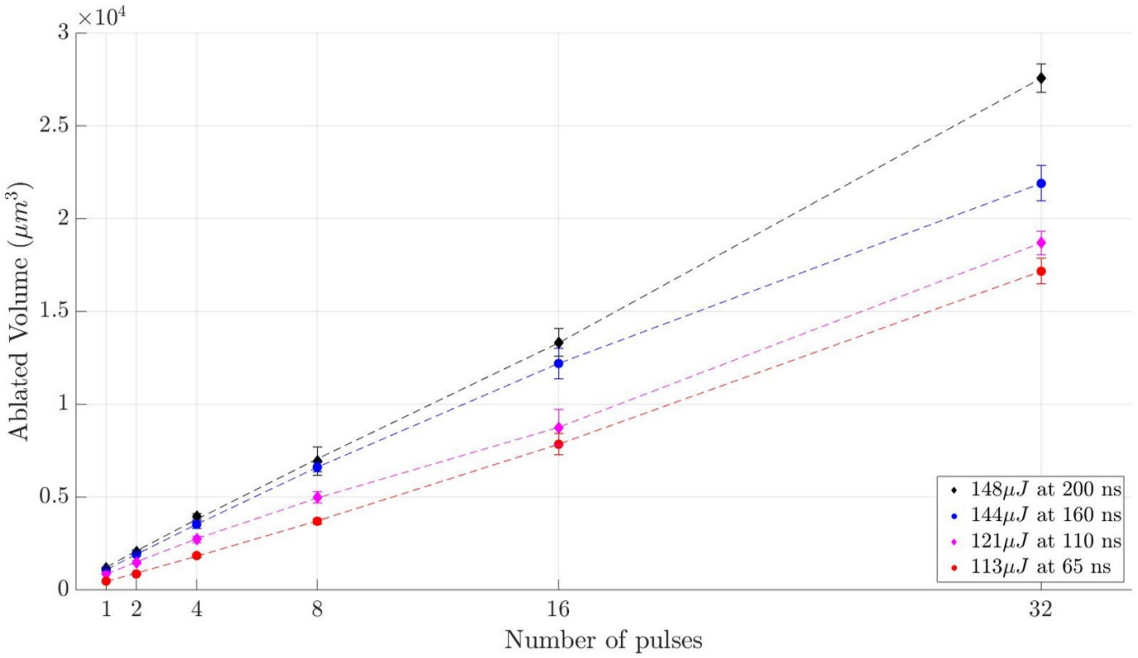

Figure 4.20: *Ablated volume against different number of pulses in a single spot with different pulse duration and pulse energy.*

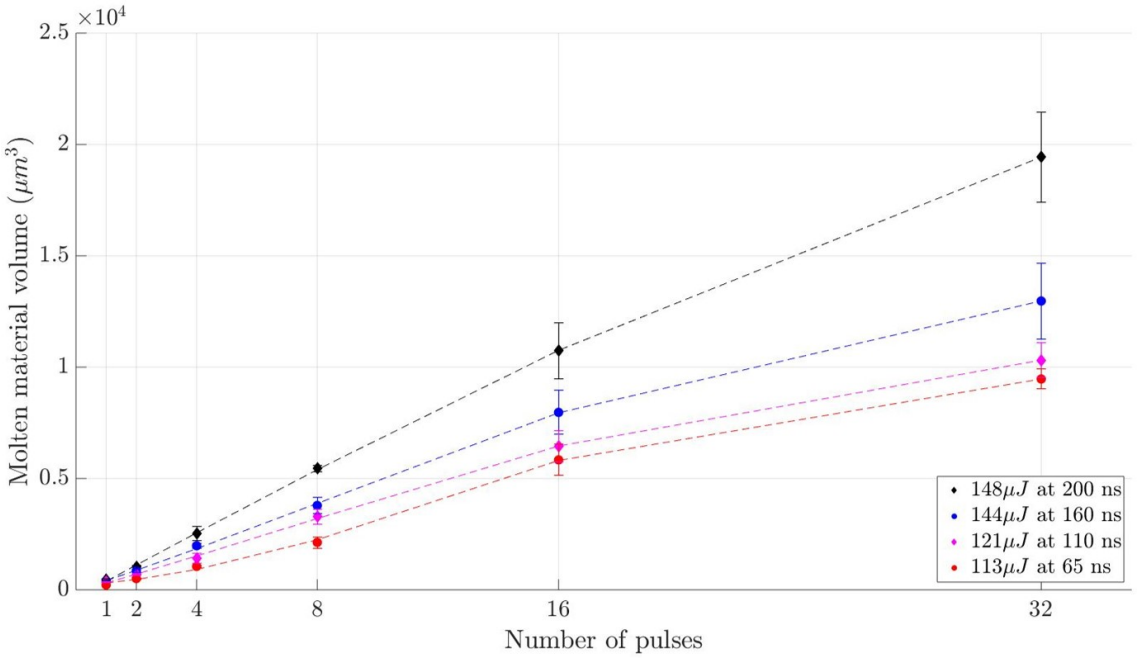

Figure 4.21: *Molten material volume against different number of pulses in a single spot with different pulse duration and pulse energy.*

Figures 4.20 and 4.21 show how the ablated and molten material volume increases as the number of pulses increases. However, ablation with shorter pulse duration, such as 65 ns, removes a lower volume from the surface and thus the volume of molten material deposited on the surface is also reduced in comparison with 200 ns pulse duration.

It is important to clarify that the obtained volumes for ablated and molten material are an estimation. This is due to the operation principle of the white light interferometer, which is based on light reflection from the material to acquire the required data. Besides, the ablated volume can be underestimated on the ablated craters with 16 and 32 pulses, due to the molten material accumulation inside of the crater. The high thermal accumulation for high pulse numbers not only creates the molten material deposition on the surface material and inside of the ablated crater, but also changes the colour of the material. This creates a black molten material, which is difficult to observe with the white light interferometer especially with the uneven deposition of the material as can be observed in Figure 4.22 below.

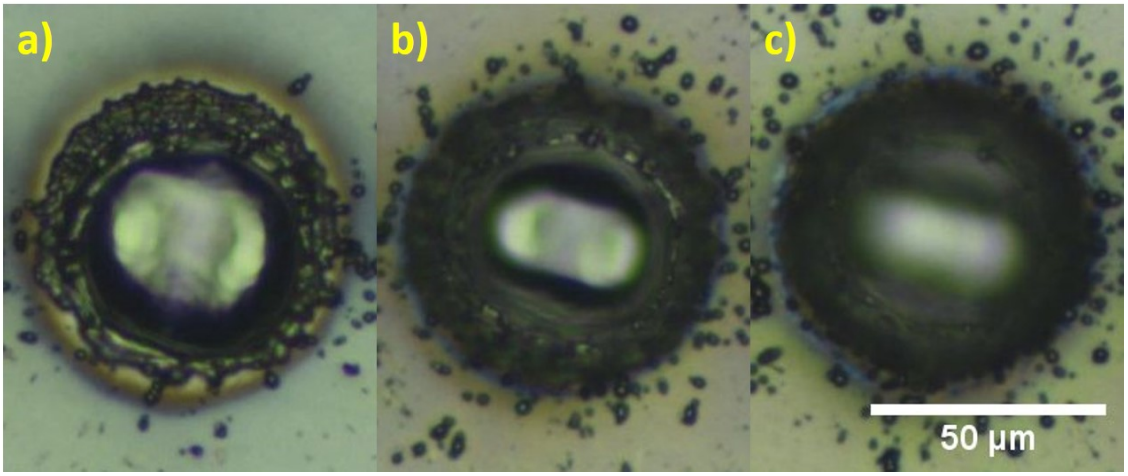

Figure 4.22: *Ablated craters created with* $E_{Pulse} \approx 113\,\mu J$ *and pulse duration of 65 ns. a) 8 pulses, b) 16 pulses, c) 32 pulses ablated craters.*

As can be observed from Figure 4.22, the molten material deposited on the surface is darkened in comparison with the polished surface of Ti-6Al-4V. This creates limitations on the required light reflection for the operation of the white light interferometer. These limitations have an impact on the material volume calculation of ablated craters with a high number of pulses.

The increase in the number of pulses used for ablation of Ti-6Al-4V was shown to be efficient for the removal of a greater amount of material from the surface thus increasing the ablated depth. However, the increment in the number of pulses can have a negative effect on the surface topography, especially with high numbers of pulses as seen in Figure 4.23.

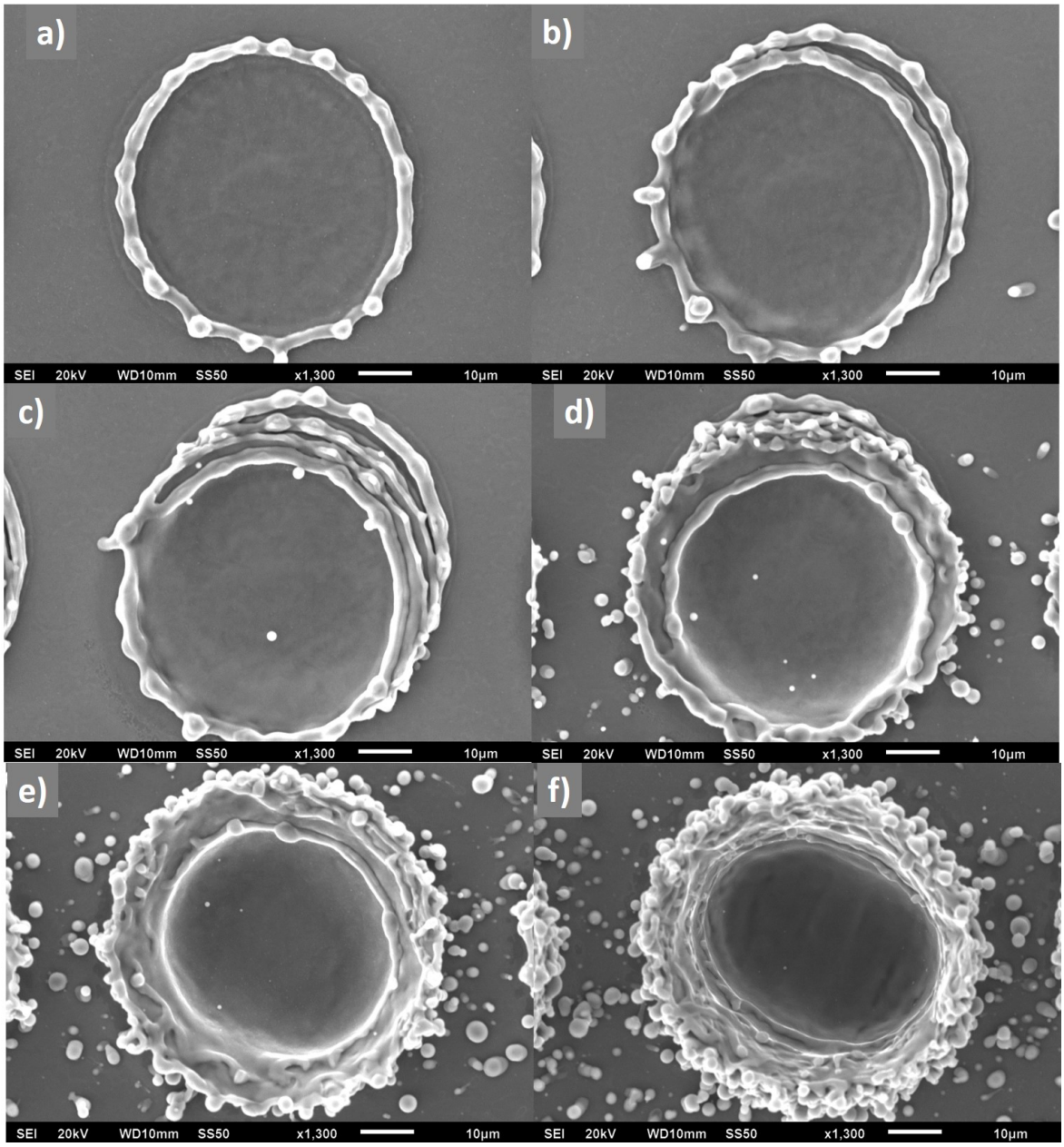

Figure 4.23: *Ablated craters created with $E_{Pulse} \approx 113\mu J$ and pulse duration of 65 ns. a) Single pulse, b) 2 pulses, c) 4 pulses, d) 8 pulses, e) 16 pulses and f) 32 pulses ablated craters.*

Figure 4.23 shows how the increase in the pulse number for the ablation of the material surface has a detrimental effect on the quality of the ablated surface. An increasing amount of molten material can be seen to accumulate on the surface. A significant amount of molten material was expelled out of the laser beam ablation area for ablated craters with 8, 16 and 32 pulses. It can also be seen the slight misalignment of the ablated craters and molten material deposition, especially with a low number of pulses.

The increased amount of molten material away from the ablated surface and crater edge represents a potential complication for the creation of micro-structure on the material. One of the main advantages of the laser system in comparison with traditional manufacturing methods is the processing accuracy and the highly controllable features created. In this case, using a high number of pulses for ablation of the material can create uncertain features in the microstructure, due to the high amount of molten material deposited on the surface. In order to create a functional microstructure on the surface, it is important to control and reduce these types of uncertainties as much as possible.

Further exploration of the possible surface features generated by these laser types will be given in Chapter 5.

4.4 Summary

Analysis of the ablation process with a nanosecond pulsed laser on Ti-6Al-4V was carried out using different E_{Pulse} and pulse duration to characterise the effects on the material surface. The ablation threshold was calculated by the measurement of the crater size with different E_{Pulse} for a range of different pulse durations (65 to 200 ns) to create a process window for the ablation of the material and thus, the creation of micro-structured surfaces in subsequent chapters.

A study into the ablated surface topography of the Ti-6Al-4V was carried out. Measurements of the depth of ablation with different pulse duration showed that as the pulse duration is reduced the amount of material removed reduces as well. This is the case even when the E_{Pulse} is calculated for obtaining an ablated crater diameter similar to the theoretical D_{min} for each one of the pulse durations. The amount of molten material re-deposited on the ablated crater edges decreases as the pulse duration decreases, following a similar pattern as with the removed material. Effects of the laser quality on the ablated crater shape were characterised for decreasing pulse durations, showing that a smaller pulse duration magnifies the pulse shape of the laser beam.

The use of different numbers of pulses for material surface ablation showed that the depth of ablation obtained can be multiplied by the number of pulses used in the same spot on the surface. The depth of ablation decreases in the same way as with the decrease of pulse duration. However, the adverse effects of using a high amount of pulses for surface ablation are also explored, especially with regards to the amount of material re-deposited on the surface. Ablated and molten material volumes were estimated through the white light interferometer in order to confirm the obtained results from the ablation depth with a different number of pulses and pulse durations. The molten material accumulation inside of the ablated crater, especially with longer pulse durations (100 - 200 ns) and a high number of pulses makes these results only an estimate of the real ablated and molten material volumes.

The observations made in this chapter for the ablation of the Ti-6Al-4V with a nanosecond pulsed laser and the effect of using different pulse durations highlights the capabilities of the laser system for the modification of the material surface topography. The obtained results of these effects create a suitable process map of parameters for the creation of functional microstructures on the surface of the material such as the modification of wettability properties. This will be presented in Chapter 5.

Chapter 5

Surface structuring for wettability modification

5.1 Introduction

The use of super-hydrophobic surfaces is being widely investigated for several applications such as corrosion resistance, self-cleaning, micro-fluid control, and functional surfaces for medical and aerospace industries. Different types of super-hydrophobic structures have been studied over the years, several of these studies have tried to emulate diverse properties observed in nature. Most of these structures found in nature depend on a coating or texture that helps increase water repellency[69, 72, 131].

Laser texturing for the creation of super-hydrophobic material surfaces has been investigated previously, largely with the use of pulsed lasers in the femto and picosecond regime. The use of next generation robust fibre based nanosecond pulsed lasers can potentially reduce the cost and complexity of this application significantly.

Improvements in wettability can take several days and even weeks after laser treatment, depending on the processed metal system. A surface will initially present a hydrophilic effect typically and the contact angle will evolve over a number of days. Several studies have been made to understand this process and have concluded that the chemistry in the surface plays a fundamental role in the improvement and stability of the effect. An initial oxidation is induced by laser processing on the surface and this oxidation layer is enhanced with time due to the ambient conditions improving the contact angle on the surface[91].

In this chapter the use of a nanosecond pulsed laser to create a micro-structure on the surface of Ti-6Al-4V is investigated. The thermal component of the nanosecond pulse regime can improve the creation of beneficial surface structures due to the deposition of molten material created by the pulse, improving not only the amount of ablated material but also deposition of material on the top of the surface. In addition, a thermal post-process is investigated in order to explore the effects on the oxidation layer created by laser processing and the required time for stabilisation of the contact angle[120]

5.2 Preliminary scanning technique

In order to compare the capabilities of the nanosecond pulsed fibre laser with previous investigations, polished Ti-6Al-4V samples were processed with a square-grid based laser ablation technique[98, 99, 120, 121]. This technique involves the creation of micro-channels in both horizontal and vertical directions on the material surface. This type of surface structuring technique has been widely explored for wettability properties modification on ultra-short pulsed lasers (femto and picosecond pulse regime)[89, 92–94, 96]. The scanning head system (Nutfield XLR8-10) allows the deflection of the laser beam into a stationary sample maintaining focusing conditions as long as the sample is positioned in the focal plane as discussed in Chapter 3 of this thesis. A schematic diagram of the scanning technique surface texturing of Ti-6Al-4V is shown in Figure 5.1 below.

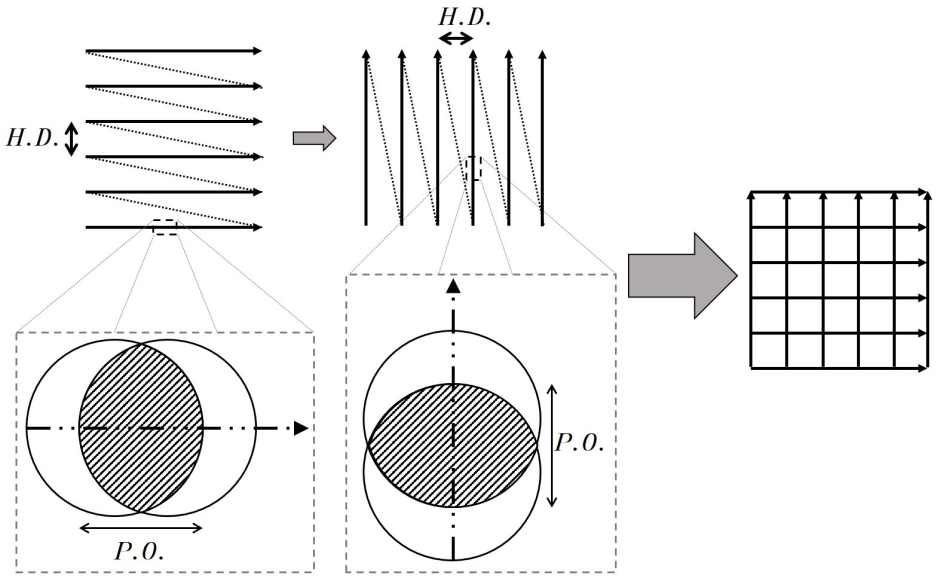

Figure 5.1: *Scanning technique schematic for nanosecond pulsed laser surface structuring of Ti-6Al-4V for a given Hatch Distance (H.D.) and Pulse Overlap (P.O.)*

Figure 5.1 shows the scan technique divided into two steps. The first step creates an arrangement of horizontal lines with a constant Hatch Distance (H.D.) and a Pulse Overlap (P.O.). The same parameters are used for the second step, where vertical lines are created on top of the structured surface to form a square-grid surface texturing on the material.

Pulse overlap of the created lines is defined by Equation 5.1 below[132]:

$$P.O. = 1 - \frac{v_s}{D_{min} f_p} \tag{5.1}$$

Where:

- v_s is scan speed
- f_p is repetition frequency of laser system
- D_{min} is the calculated spot size defined on Chapter 4 of this thesis $\approx 49.68\ \mu m$.

With the scanning technique described in the schematic presented in Figure 5.1, a high pulse overlap is required for the complete line ablation on the material surface. The laser parameters used for this technique are presented in Table 5.1 below.

Table 5.1: *Laser processing parameters for Ti-6Al-4V surface texturing for the square-grid based scanning technique*

Laser parameter	**Value**
Laser fluence, [J/cm²]	4.13, 5.16, 6.19, 7.22, 8.26, 9.29
Repetition frequency, [kHz]	65
Pulse duration, [ns]	65
Scan speed, [mm/s]	260
Hatch Distance, [H.D. (μm)]	50, 100, 150, 200
Pulse Overlap, [P.O. (%)]	91.95

After laser surface texturing, the samples were placed in a conventional electric oven (MEMMERT SM 100) for 24 hours at a temperature of 120 °C for a low-temperature annealing treatment, this treatment has been previously explored with other materials in order to decrease the time necessary for the stabilization of the contact angle on laser surface textured metallic surfaces[120, 121].

5.3 Experimental results preliminary scanning technique

5.3.1 Surface topography

The fabrication of the microstructure was analysed using a white light interferometer(WYKO) in order to characterise the effects of laser fluence and hatch distance between scanned lines on the material surface. Figure 5.2 shows four created surface structures with the same laser fluence ($6.11\ J/cm^2$) and four different hatch distances. As can be observed, the ablated channels created a hierarchical surface structure where part of the material is removed due to laser ablation and the other part is redeposited as molten material on the edges of the ablated channels due to the thermal component of the nanosecond pulsed laser and high pulse overlap.

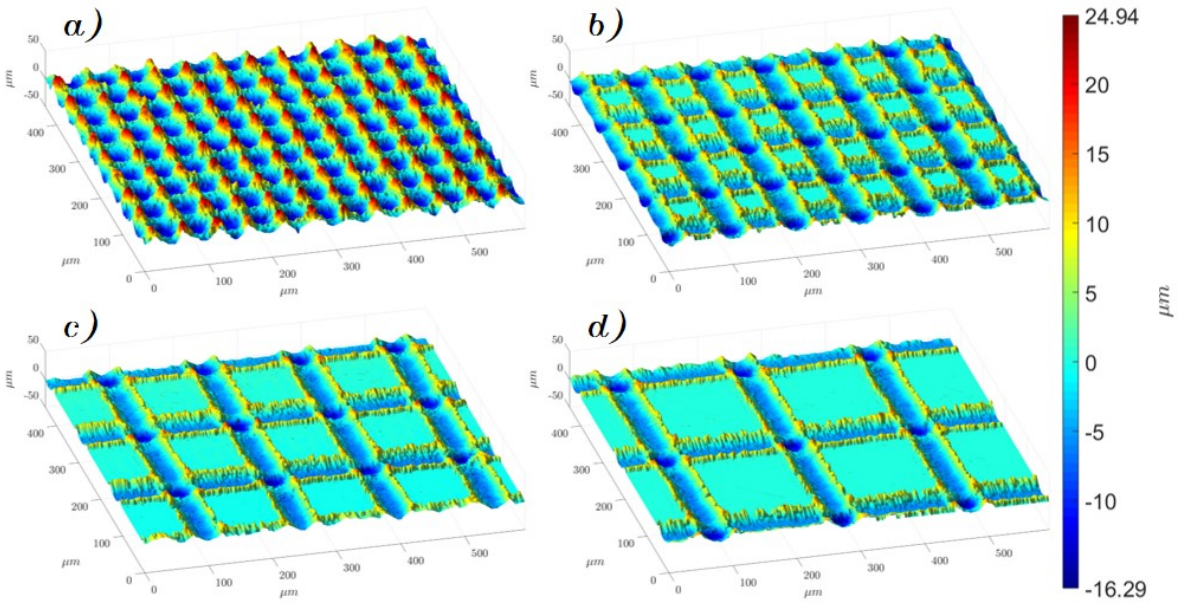

Figure 5.2: *Laser textured surfaces on Ti-6Al-4V with* $6.11\ J/cm^2$ *and different Hatch Distance (H.D.), a)* $50\ \mu m$*, b)* $100\ \mu m$*, c)* $150\ \mu m$ *and d)* $200\ \mu m$

Figure 5.2 shows that with increasing hatch distance, above $50\ \mu m$, surface areas are left untreated by the laser beam, leaving a polished surface behind. The creation of two fundamental types of surface structures can be observed from this figure. With $50\ \mu m$ hatch distance a micro-pillar surface structure type is created on the surface due to $D_{min} \approx 49.68\,\mu m$. Creating a surface were $D_{min} \approx Hatch\ Distance$ means that there is virtually no area left without laser ablation on the material surface.

The zero distance between the ablated channels means that effectively the intersection areas are ablated twice and the deposited molten material forms a micro-pillar like surface structure. With a hatch distance $> 50\ \mu m$ the creation of channels on the material surface is clearly defined, and only the intersection points are ablated twice by the laser, creating a larger molten material around these particular points.

To characterise the effects of increasing laser fluence on the creation of this type of microstructures, six different fluences were investigated. The micro-channels were analysed and characterised for a comparison of the ablated depth(A.D.), molten material height(M.M.H.) and ablated width(A.W.), with the increasing laser fluence as shown in Figure 5.3.

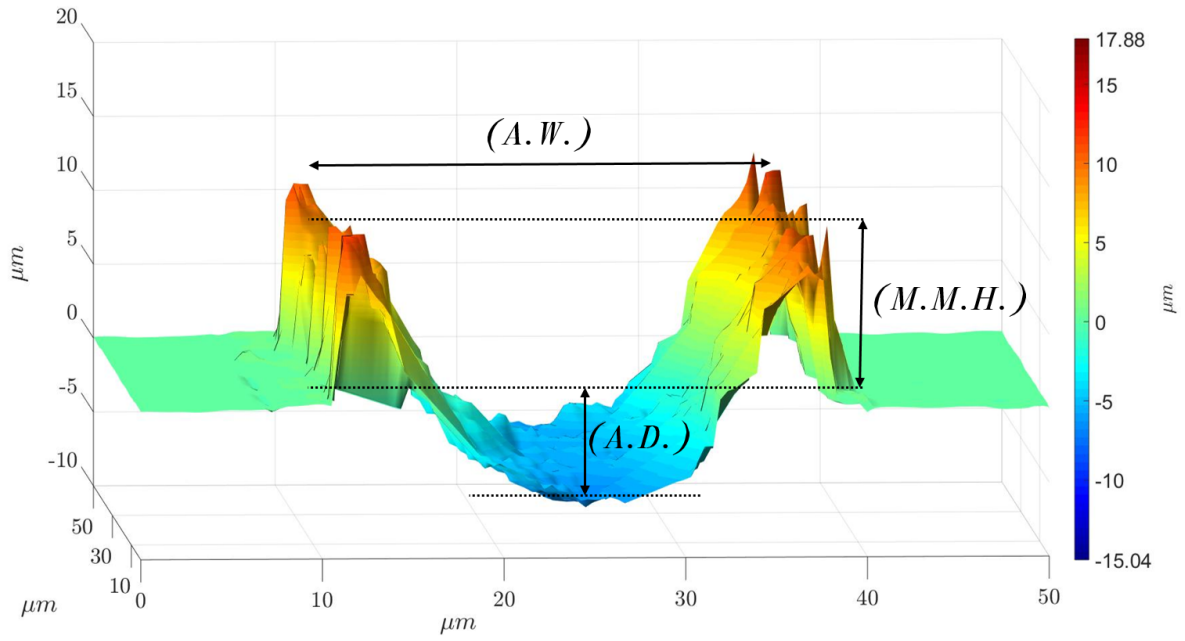

Figure 5.3: *Schematic diagram of ablated channel with 6.19 J/cm^2 of fluence and distance measurements*

Figure 5.3 displays a cross-section diagram of a typical ablated channel with the nanosecond pulsed laser, in this case, created with 6.19 J/cm^2 of laser fluence. Measurements for the six different laser fluences were undertaken on surfaces created with H.D. of $100\mu m$ to compare features measurements with the untreated portion of the surface.

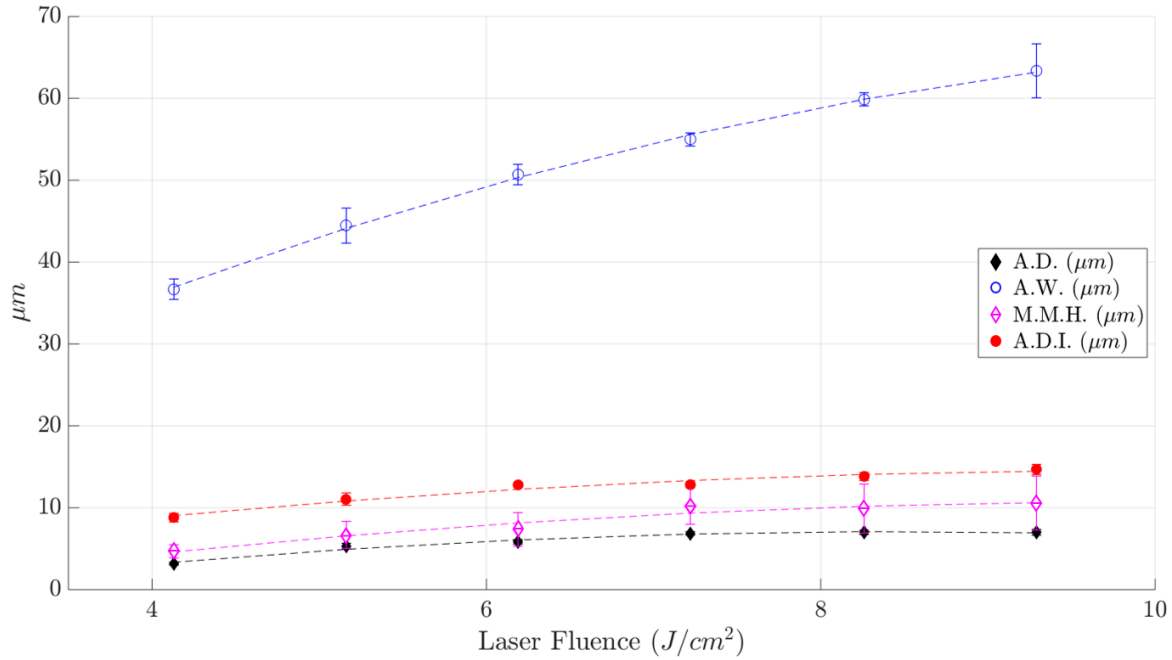

Figure 5.4: *Measurements of channel characteristics vs laser fluence [A.D. = Ablated Depth, A.W. = Ablated Width, M.M.H. = Molten Material Height and A.D.I. = Ablated Depth on Intersecting Points]*

Figure 5.4 shows how the increasing laser fluence increases the Ablated Width (A.W.) and Ablated Depth (A.D.) of the channels created on the material surface. The increase of these measurements means that a higher amount of molten material is deposited on the ablated channel edges, increasing the Molten Material Height (M.M.H.). However, it is important to notice that A.D. remains virtually the same for laser fluences from 7.22 to 9.29 J/cm^2, following the same trend presented on Chapter 4 "Surface Topography" section of this thesis, indicating that in order to increase the A.D. a higher number of laser pulses are required instead of increasing E_{Pulse}.

The scanning technique means that a double ablation process is produced on the intersecting channel points and this measurement is presented in Figure 5.4 as Ablated Depth on Intersecting points (A.D.I.). As can be observed, the ablated depth in these areas is double that of a single ablated channel, as expected according to the depth of focus of the system discussed in the previous chapter of this thesis.

With increasing laser fluence the amount of molten material deposited on the channel edges is increased as well. However, the amount of molten material deposited on the surface is increasingly uneven with laser fluence above 7.80 J/cm^2, creating variations in the molten material height through the ablated channel as shown on the Molten Material Height measurement variations presented in Figure 5.4.

These variations have a detrimental effect on the microstructures created on the material surface. With higher laser fluence, the thermal component into the material increases affecting the deposition of molten material and the overall quality of the ablated channels. The width of the ablated channels increases pushing a larger amount of material into the edges and ejecting drops of molten material outside the laser beam path. It has been observed from previous investigation with nanosecond pulsed lasers that the shockwave expansion of a single nanosecond pulse ablation is increased as the laser fluence increases[127, 133]. As observed in Chapter 4 section 4.3.1 "Ablation threshold" on this thesis, with an increase in the laser fluence, the size of the ablated crater increases, however the ablated depth for a single pulse ablation follow a slightly different trend, with a quick rise in the ablated depth as the laser fluence increases followed by a rapid stabilisation of the ablated depth with the a particular pulse duration as can be observed in the section 4.3.2 "Surface topography" of this work. this two observation can explain how with an increased laser fluence the A.W. measurement increases, however the A.D. rapidly stabilises, and also with the increase of the fluence the shockwave created by the ablation plume increases pushing the molten material further away from the laser path.

The creation of suitable super-hydrophobic surface with lasers mainly relies on the creation of air pockets within the surface and water droplet interaction. An uneven surface structure creates a problem for the formation of these air pockets, together with and increase in the size of the ablated channels(A.W.), produces a surface structure with increasable uncontrollable effects on features definitions and the molten material deposition as can be observed in Figure 5.5.

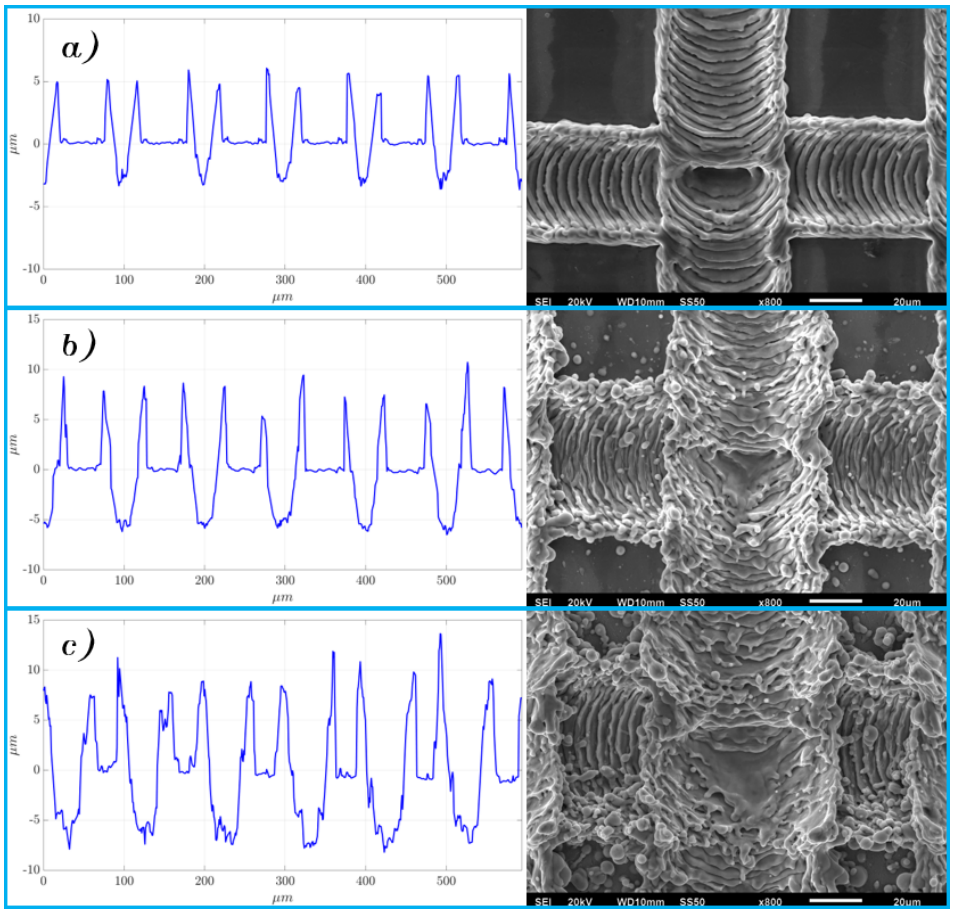

Figure 5.5: *Surface profile and SEM image of ablated micro-channels with* 100 μm *of separation and increasing laser fluence, a)* 4.13 J/cm^2 *laser fluence, b)* 6.19 J/cm^2 *laser fluence, and c)* 9.29 J/cm^2 *laser fluence*

Figure 5.5 shows the comparison of surface profiles with 100 μm of hatch distance created with three different laser fluence. As can be observed the overall quality of the microstructure decreases as the energy input of the laser system is increased. With a laser fluence of 9.29 J/cm^2, Figure 5.5 (c), the amount of molten material randomly deposited on top of the ablated and untreated area increases significantly, decreasing the overall definition of the ablated channel shape. In comparison, the microstructure created with 4.13 J/cm^2, Figure 5.5 (a), displays a clearly defined laser path with lack of molten material outside of the ablated channel.

These effects are magnified in the surface microstructures created with 50 μm of hatch distance due to the theoretical lack of separation between the ablated channels as can be observed in Figure 5.6.

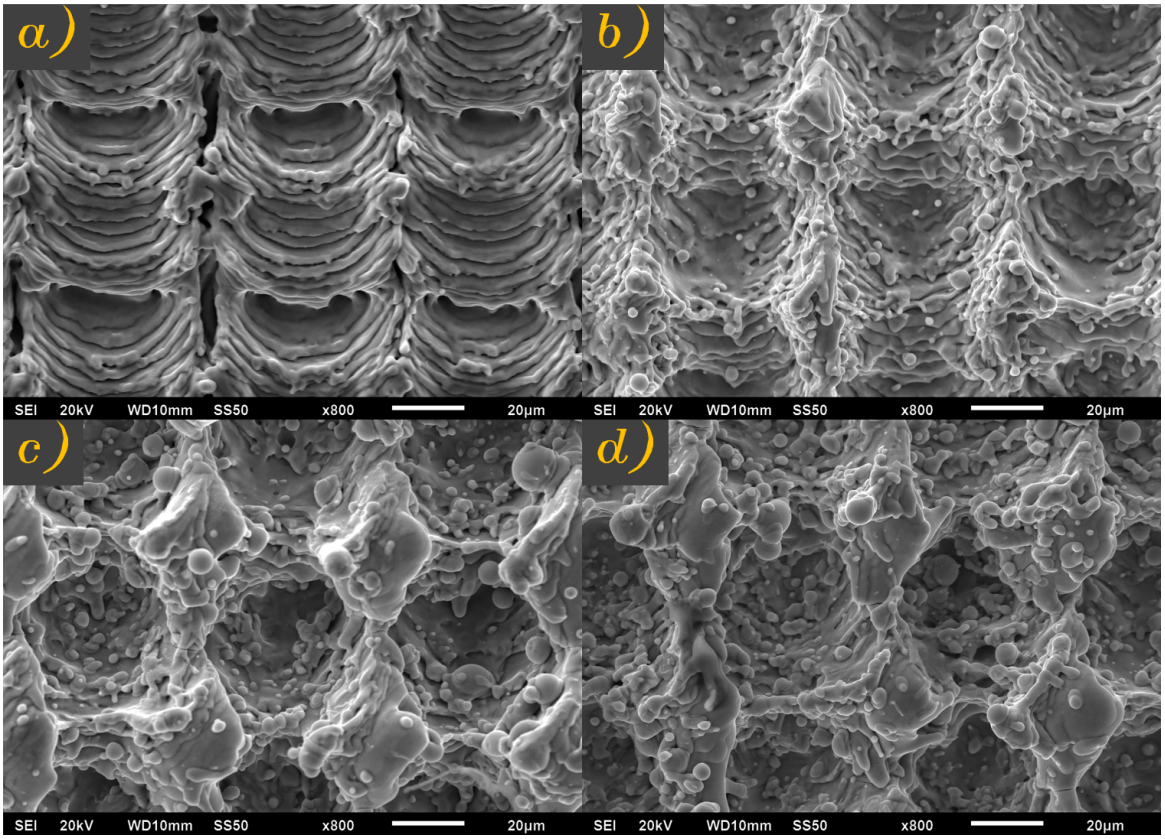

Figure 5.6: *Surface profile and SEM image of ablated micro-channels with* $500\,\mu m$ *of hatch distance and increasing laser fluence, a)* $4.13\,J/cm^2$ *laser fluence, b)* $6.19\,J/cm^2$ *laser fluence, c)* $8.26\ J/cm^2$ *laser fluence and d)* $9.29\ J/cm^2$ *laser fluence*

Figure 5.6 shows how the increasing laser fluence has a detrimental quality effect on the microstructures created with $50\ \mu m$ of hatch distance. The created channels and the molten material are uniformly defined on the created microstructures with 4.13 and 6.19 J/cm^2 of laser fluence, as shown in (a) and (b). However, with the increase of laser fluence, these surface definitions are lost, creating a large amount of molten material randomly deposited on the surface, as can be observed on (c) and (d). The high accumulation of molten material deposition even produces unions of the created micro-pillars by laser ablation as observed on (d). This effect creates an uncontrollable surface microstructure with the use of high laser fluence due to the random nature of the molten material deposition.

These type of effects on the creation of surface microstructures for wettability modification can have a detrimental effect on the hydrophobicity of the material, due to the lack of constant surface features.

Surface topography analysis highlights one of the main differences in the creation of micro-structures with the SPI G4 laser system and previous investigations for the creation of super-hydrophobic surfaces on metallic materials[97, 120, 123]. A fundamental difference with the majority of previous investigations is on the type of laser used. Ultra-short pulsed lasers such as femto and picosecond pulsed lasers are often used for the creation of super-hydrophobic surface structures. These laser systems have the ability to create features on the micro-scale regime, due to laser ablation, and nanoscale surface structures called LIPSS. Laser-Induced Periodic Surface Structures (LIPSS) tend to be created on metallic materials, generating perpendicular ripples to the polarisation of the laser beam[48, 134–136].

Previous investigations have used this capabilities for the creation of surface micro-structure through laser ablation of a material with ultra-short pulsed laser. This creates a low-energy surface allowing the formation of air pockets between the micro-structured surface, causing a water droplet to just touch the top of the micro-structure, thus creating a super-hydrophobic surface[137–139].

The creation of super-hydrophobic surfaces with nanosecond pulsed lasers is of significant interest currently. A number of studies published during the course of this work have used a similar concept to that proposed here for surface modification[84, 99, 140]. These systems rely on a significantly smaller laser beam size in order to reduce the width of the ablated channels, this allows the creation of micro walls due to the molten material deposition allowing pockets of air to be formed within the created micro-structure. However, the creation of this type of micro-structures means that areas of untreated material have been left behind which can have a detrimental effect for the super-hydrophobic behaviour with the possibility of the water droplet touching these untreated areas and changing the wettability state of the surface structure as described in the next sections[120, 121].

5.3.2 Contact angle development

Contact angle measurements of samples were analysed for the increasing laser fluence and hatch distance in order to characterise the effects of the created micro-structure on the surface of the material. Three different contact angle measurements were undertaken in the centre of the structured area surface in order to obtain a statistical sample of the measurements. Two sets of samples were produced with the same laser parameters, one set of samples was put through thermal post-processing and stored under normal ambient conditions after this process. The second set of samples were not subjected to the thermal post-processing and simply stored under normal ambient conditions in order to verify the effects of thermal post-processing on the contact angle development.

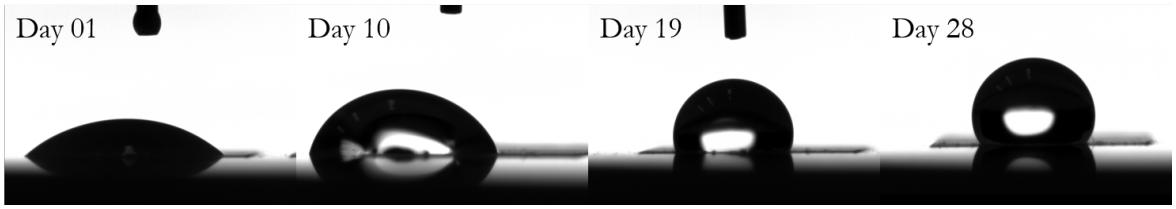

Figure 5.7: *Static contact angle development through time of Ti-6Al-4V with nanosecond ablated surface without thermal post-process,* $4.13 J/cm^2$ *of laser fluence and a hatch distance of* $50\ \mu m$

Figure 5.7 shows how surface micro-structures created through laser ablation on metallic materials without thermal treatment show a hydrophilic behaviour after the laser process. It takes several days before the contact angle acquires a hydrophobic (contact angle $> 90°$) or even super-hydrophobic(contact angle $> 150°$) effect. This effect has been previously investigated and it has been concluded that the oxidation state of the surface plays a fundamental role on the development of metallic super-hydrophobic surfaces[92, 98, 99]. This oxidation layer is normally activated through the laser ablation process and stabilised through time under ambient conditions[90, 91, 120].

This effect was observed on the samples with no thermal post-processing with the static contact angle measurements presented in Figure 5.8.

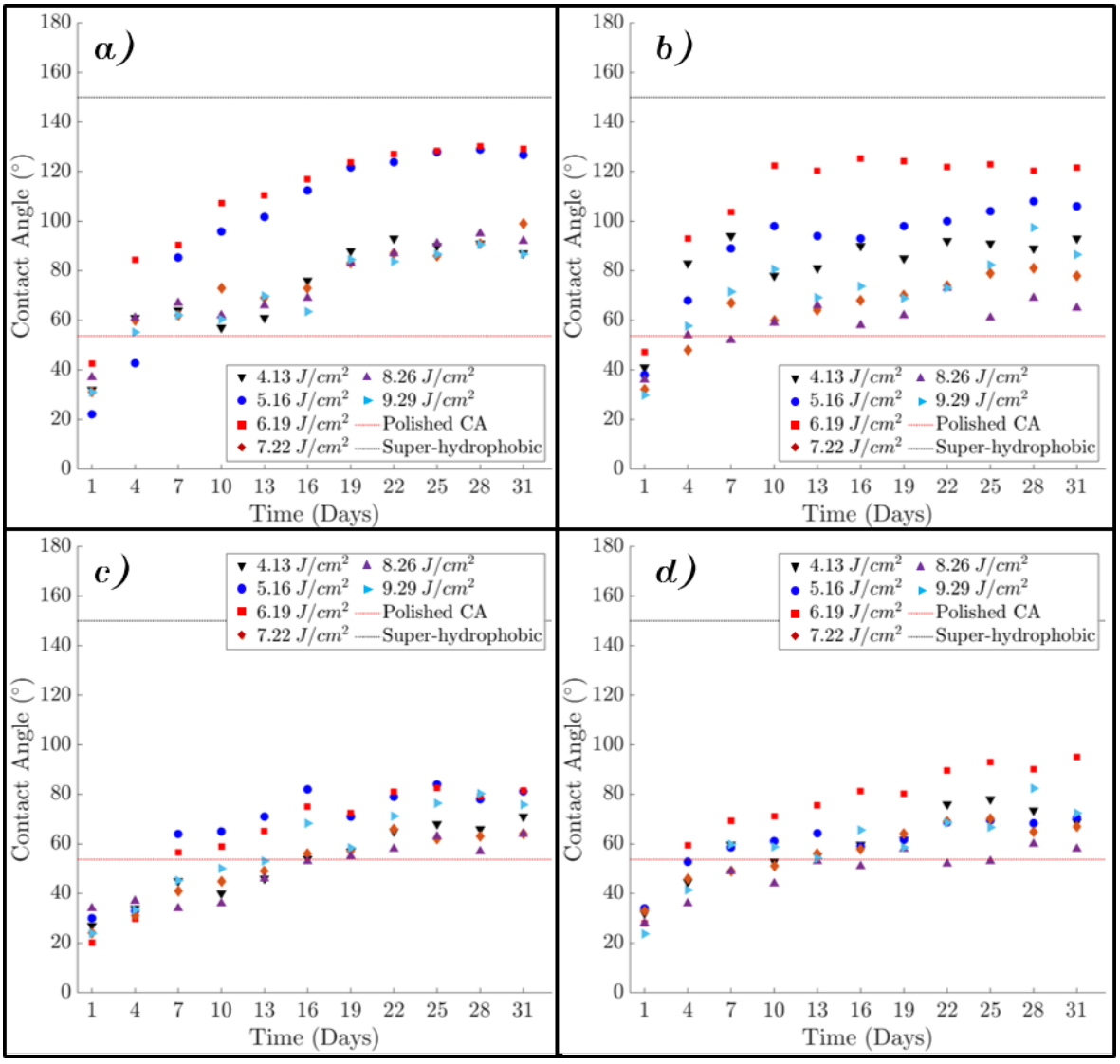

Figure 5.8: *Static contact angle values for square-grid shaped nanosecond laser structured surface on Ti-6Al-4V,* ***No Thermal post-processing****, four different Hatch Distance (H.D.) a) 50 µm of H.D., b) 100 µm of H.D., c) 150 µm of H.D. and d) 200 µm of H.D.*

As can be observed in Figure 5.8, samples with no thermal post-processing present a hydrophilic behaviour in the first days after the laser surface texturing process, as the static contact angle decreases in comparison with samples with no surface texturing(polished Ti-6Al-4V). However, after a few storage days, the static contact angle steadily rises to reach hydrophobic or even near super-hydrophobic levels, depending on the structure created by the laser processing. All the processed samples exhibited a static contact angle superior to the polished CA after 31 days.

Samples with $50\,\mu m$ of H.D., processed with laser fluence of $5.16\,J/cm^2$ and $6.19\,J/cm^2$ seen in Figure 5.8(a), exhibit a higher static contact angle in comparison with samples of H.D. $> 50\,\mu m$, reaching 126° and 129° respectively after 31 days. However, not a single sample reached super-hydrophobic levels($> 150°$ of static contact angle). The same behaviour is observed in samples with $100\,\mu m$ of H.D. and laser fluences of $5.16\,J/cm^2$ and $6.19\,J/cm^2$(Figure 5.8 (b)) reaching similar measurements of static contact angle after 31 days.

Samples with $150\,\mu m$ and $200\,\mu m$ of H.D., seen in Figure 5.8(c) and (d), displayed reduced static contact angle measurements. After 31 days these samples exhibit a hydrophobic behaviour with measurements below 100° of static contact angle. As can be observed from the measurements presented in Figure 5.8, the samples followed the Wenzel state model, due to the increase of the roughness ratio and the intrinsic contact angle of the polished Ti-6Al-4V $\approx 54°$.

However, as shown in Figure 5.8, the contact angle improves with time and after several days it reaches a hydrophobic state (after 7 days), even reaching near-super-hydrophobic contact angle after 31 days. This follows the same observed wettability behaviour previously discussed by *Bizi et al* where the surface chemistry plays a fundamental role for the contact angle improvement over time[91].

Another characteristic of the Wenzel state, is the lack of liquid displacement or rolling. This means that even when the contact angle is almost in the super-hydrophobic regime, the liquid droplet will stay on the same surface area even when the material is tilted at high angles. This was observed for all the samples after 31 days.

In order to observe the effects of micro-structured surfaces with thermal post-process, the static contact angle of each surface with thermal post-processing was measured on different days during a one month period as shown in Figure 5.9.

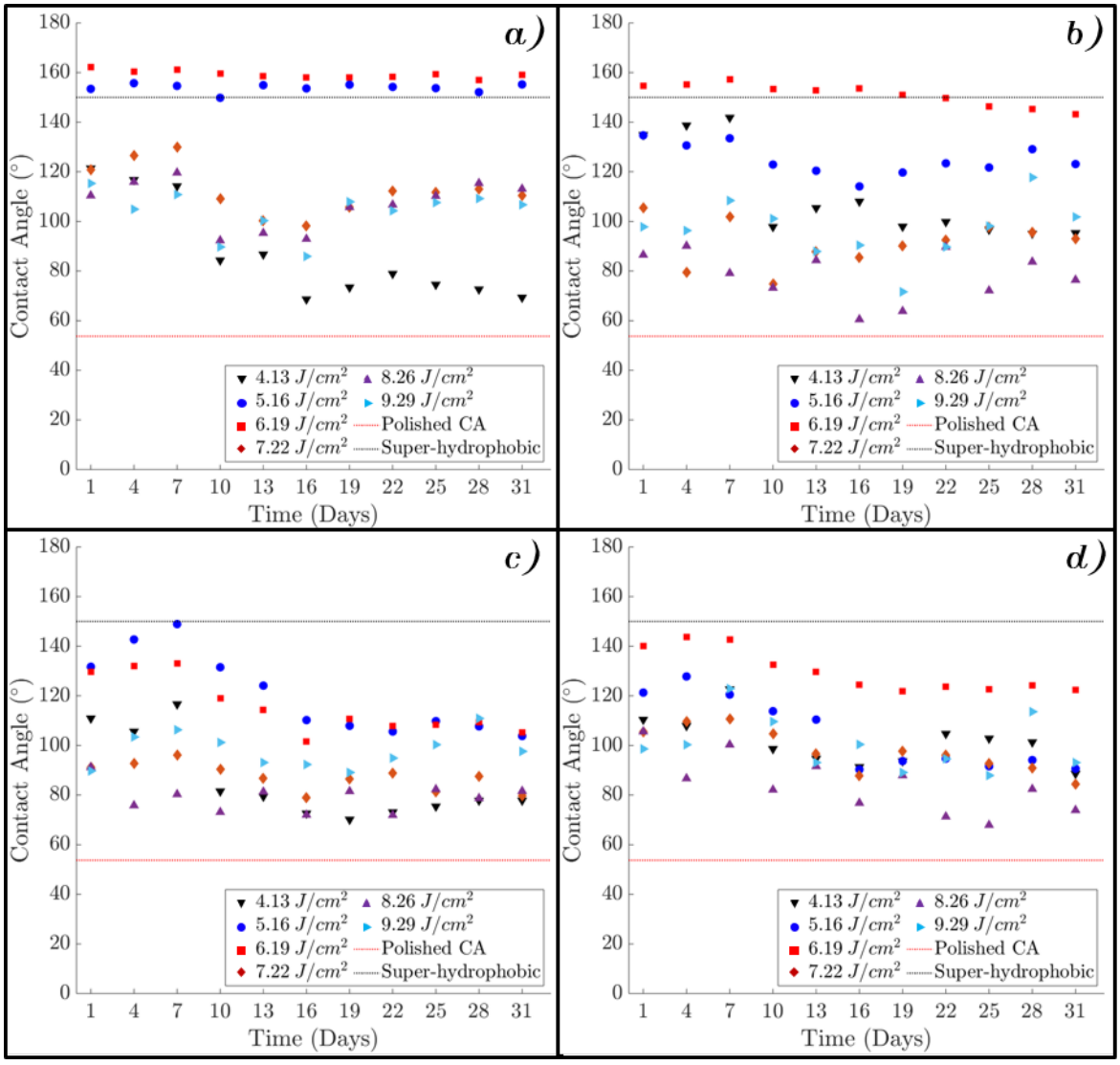

Figure 5.9: *Static contact angle values for square-grid shaped nanosecond laser structured surface on Ti-6Al-4V,* ***Thermal post-processing****, four different Hatch Distance (H.D.), a)* 50 μm *of H.D., b)* 100 μm *of H.D., c)* 150 μm *of H.D. and d)* 200 μm *of H.D.*

As can be observed from Figure 5.9, all the samples show a contact angle superior to the contact angle of a polished surface (Polished CA) since the first day, this is due to the thermal post-process applied to the sample right after the laser surface texturing. However, only a few samples present a super-hydrophobic contact angle ($> 150°$). Two of these surfaces are with a hatch distance(H.D.) of 50 μm and laser fluence of 5.16 and 6.19 J/cm^2. The third surface showing a super-hydrophobic behaviour is with a H.D. of 100 μm and 6.19 J/cm^2 of laser fluence.

The increase of laser fluence has an effect on the contact angle development. When the used energy reaches a point where the molten material is chaotically deposited on the surface, the contact angle presents only a hydrophobic behaviour. This can also be explained by the changes of molten material height and ablated width of the ablated channels on the surface. With the increase of these values the ablated path works as a water channel, spreading the liquid across the material surface via capillary effect due to the pressure applied by the liquid droplet onto the material and constrained only by the created microstructures.

Wetting behaviour of micro-structured surfaces is commonly characterised by two models, Wenzel state model and the Cassie-Baxter state as previously discussed in section 2.5 "Super-hydrophobic surfaces" of this thesis. These two models base their contact angle characterisation as the relation between the intrinsic contact angle and the roughness of the surface structure given by equations 5.2 (Wenzel state) and 5.3 (Cassie-Baxter state):

$$\cos\theta_w = r \cdot \cos\theta_y \tag{5.2}$$

$$\cos\theta_{CB} = r_f \cdot \phi_s \cdot \cos\theta_y + \phi_s - 1 \tag{5.3}$$

As can be observed from Equation 5.2, for the Wenzel state, the wetting capabilities of the material are increased as the roughness ratio (r) of the material is increased, thus reducing the hydrophobicity of the material with the increasing roughness when the intrinsic contact angle of the surface (θ_y) is $< 90°$. However, if the intrinsic contact angle is $> 90°$, the contact angle should increase as the surface roughness is increased[9, 68, 72, 76].

For the Cassie-Baxter state, the contact angle is dependent on the intrinsic contact angle of the material as well, however, for the Cassie-Baxter model, the liquid is in contact only with the protrusions on the surface due to the pockets of air created by the surface structure, this fraction of the total area is defined as ϕ_s. If there are no pockets of air within the surface microstructure, ϕ_s becomes 1 and the equation is converted to the Wenzel state equation[68, 72].

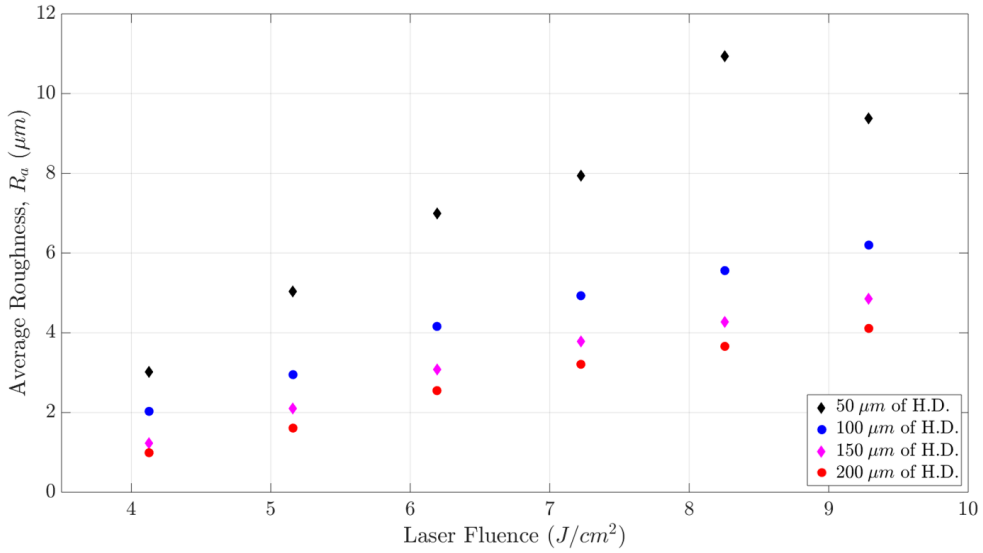

Figure 5.10: *Average roughness (R_a) of surface structured samples with increasing laser fluence and hatch distance (H.D.) measured with white light interferometer (WYKO).*

Figure 5.10 shows how with increasing laser fluence the average roughness on the surface micro-structure is increased for different hatch distance with the exception of the sample created with 9.29 J/cm^2 and 50 μm of hatch distance. This is likely due to the relatively high fluence increasing the size of the ablated crater above the hatch distance ($50\mu m$), thus affecting the surface structure due to overlap of the ablated craters.

The main observed difference is between the average roughness of processed samples with a hatch distance of $50\,\mu m$ compared with the other hatch distance values. This is due to the increasing untreated surface area with hatch distance $=>$ $100\,\mu m$, leaving untreated polished material and thus reducing the average roughness of the sample in comparison with samples processed with $50\,\mu m$ hatch distance where the full area is treated by laser ablation.

The intrinsic or polished contact angle of Ti-6Al-4V is below 90° which means that with the increase of R_a on the structured surface, the resulting contact angle should decrease. This is the case for samples without the thermal post-process after laser surface texturing process as previously observed in Figure 5.8 of the current chapter.

In order to better characterise the wettability behaviour of the samples, the contact angle hysteresis and sliding angle was measured for samples with static contact angle => 150°. Contact Angle Hysteresis (CAH) is defined as the difference between advancing and receding contact angle [141]. For this investigation a tilted surface method for the measurement of the contact angle hysteresis (shown in Figure 5.11) was carried out.

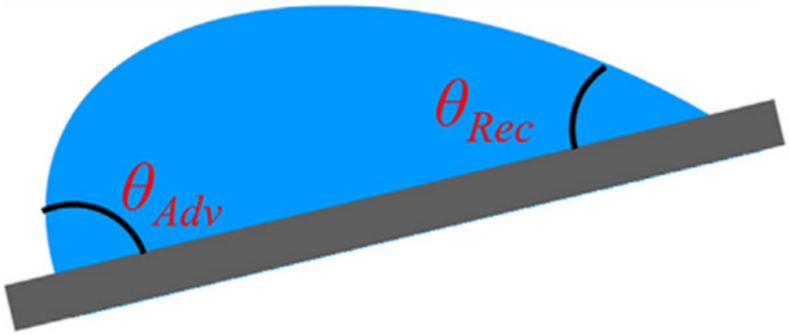

Figure 5.11: *Schematic for contact angle hysteresis calculation through tilted surface method for advancing (θ_{Adv}) and receding (θ_{Rec}) contact angle[142]*

Sliding angle is typically measured using the tilted plate method(similar to the CAH), this method consists in placing the liquid drop onto the surface, which is slowly inclined until the liquid drop slides away from the surface [143]. This method is presented on Figure 5.12(c).

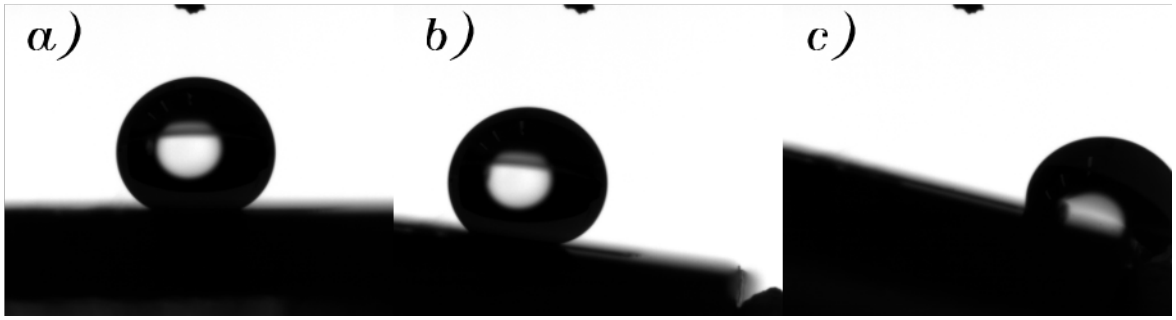

Figure 5.12: *Water droplet on the surface of laser textured Ti-6Al-4V with* $6.19\,J/cm^2$ *and* $50\,\mu m$ *H.D., a) Static contact angle with no surface tilt, b) Surface tilting at* $8°$ *for contact angle hysteresis (CAH), c) Sliding angle of the water droplet at* $\approx 14°$ *of tilt.*

Figure 5.12 shows an example of the super-hydrophobic behaviour achieved on surface structure processed with 6.16 J/cm^2 and 50 μm of H.D. A high static contact angle($> 150°$) can be observed on (a), tilting plane for contact angle hysteresis on (b) and the slide of the water droplet for the sliding angle measurement on (c). Table 5.2 below shows the exact measurements for samples with 50 μm of H.D. and two different laser fluence.

Table 5.2: *Contact angle and surface roughness after 31 days on Ti-6Al-4V surface structured with* 50 μm *hatch distance*

Laser Fluence J/cm^2	**Measurements**			
	Static CA	**CAH**	**Sliding angle**	R_a
5.16 J/cm^2	155.20°	23.45°	24°	5.04 μm
6.19 J/cm^2	159.10°	15.79°	14°	7.00 μm

As shown on Figure 5.12 and Table 5.2, surface structures with 50 μm hatch distance and 6.19 J/cm^2 displays the best contact angle and hydrophobic behaviour of the created samples. The measurements for contact angle hysteresis(CAH) of the two samples displayed levels above the 10°, displaying a near super-hydrophobic behaviour of the surface structure. In order to fully characterise a surface with a super-hydrophobic behaviour, the static contact angle requires levels superior to 150° and a contact angle hysteresis(CAH) below 10°[82, 83]. Table 5.2 shows a how as the CAH increases, the sliding angle increases in consequence.

As seen on Figure 5.9 and Table 5.2, the only two samples with static contact angle values superior to 150° through the 31 days of measurement, were the ones processed with 5.16 and 6.19 J/cm^2 of laser fluence. Samples created with the same hatch distance but increased laser fluence (above 6.19 J/cm^2) have a detrimental effect on the hydrophobic behaviour, decreasing the contact angle and returning to the Wenzel wetting state.

The loss of super-hydrophobic behaviour on the samples can be attributed to the micro-structure generated on the surface of the material, as the features of the structure can be affected due to the high molten material accumulation as shown on Figure 5.13 below.

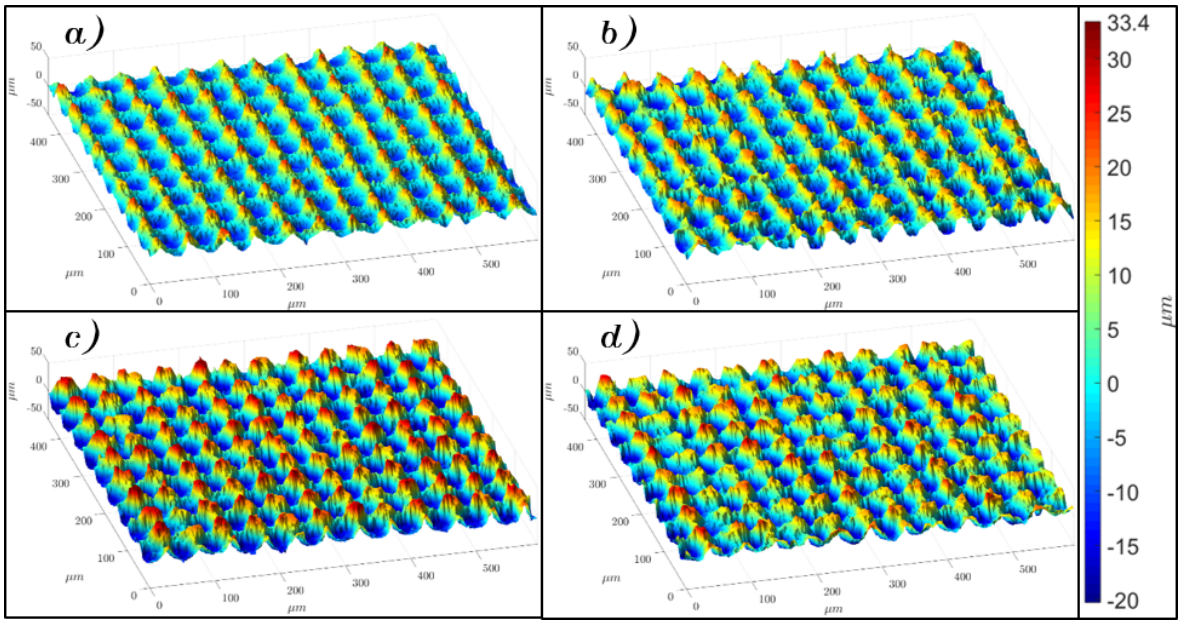

Figure 5.13: *Laser textured surfaces on Ti-6Al-4V with* 50 μm *of hatch distance and increasing laser fluence, a)* 6.19 J/cm^2*, b)* 7.22 J/cm^2*, c)* 8.26 J/cm^2 *and d)* 9.29 J/cm^2

Figure 5.13 shows how the increase in laser fluence has a negative effect on the quality of the surface micro-structure, especially on the molten material deposition. Figure 5.13 (b, c and d) display the problem with the molten material deposited on the structure and effectively joining several of the created micro-pillars. This surface structure effect has a detrimental effect on the contact angle, avoiding the creation of the necessary pockets of air within the surface for a super-hydrophobic behaviour under the Cassie-Baxter state[79]. Without these pockets of air a Wenzel state of the surface describes the contact angle development due to the liquid penetration within the micro-structure wetting the surface as a whole and keeping the droplet position on the same area[77, 78].

Contact angle measurements and surface characterisation provides a general understanding of the micro-structures required for a super-hydrophobic behaviour of the material. Several investigations have presented different types of micro-structures on metallic surfaces with a wide range of pulsed laser systems (femto, pico and nanosecond pulsed lasers) as mentioned on Chapter 2 Section 2.5.3 "Super-hydrophobic surfaces produced with laser systems" on this thesis.

Femto and pico-second pulsed laser surface processing for super-hydrophobic behaviour manly rely on the creation of multi scale structures on the material (micro and nanoscale structures). Due to the ability of femto-second pulsed lasers for inducing nano-structures on top of ablated micro-structures,this presents a fundamental advantage for the creation of super-hydrophobic surfaces[88–90]. However, these high valued systems are mostly confined to research purposes due to the low flexibility and low volume manufacturing capabilities.

Nanosecond lasers have been investigated for the creation of super-hydrophobic surfaces, however, most of the investigated systems rely on high energy density capabilities,high beam quality laser beam and a small spot size capabilities[98, 99]. In order to obtain these system characteristics the required equipment often increases the system value and decreases the manufacturing flexibility.

Super-hydrophobic surfaces created with nanosecond pulsed lasers, mostly rely on the molten material deposition, enough molten material height is required for the creation of pockets of air within the surface structure and thus avoiding the complete wetting of the surface by the liquid droplet[98, 99]. This laser surface texturing process relies on high Pulse Overlap (P.O.) for the accumulation of molten material on the edges of the ablated path thus decreasing the manufacturing speed. As observed in the obtained results in this section, the SPI G4 nanosecond pulsed laser has limitations for the creation of super-hydrophobic surfaces with these type of techniques. A low pulse overlap technique for super-hydrophobic surfaces is therefore proposed in the next section.

5.4 Improved scanning technique

Section 5.3 of the current chapter presented wettability modification properties of Ti-6Al-4V with laser ablation and a square-grid scanning technique. As the previous results showed, a micro-pillar like surface structure is the most effective for the improvement of static contact angle allowing a super-hydrophobic behaviour on the material surface. an alternative, low pulse overlap method with a number of overscans is presented in Figure 5.14 below.

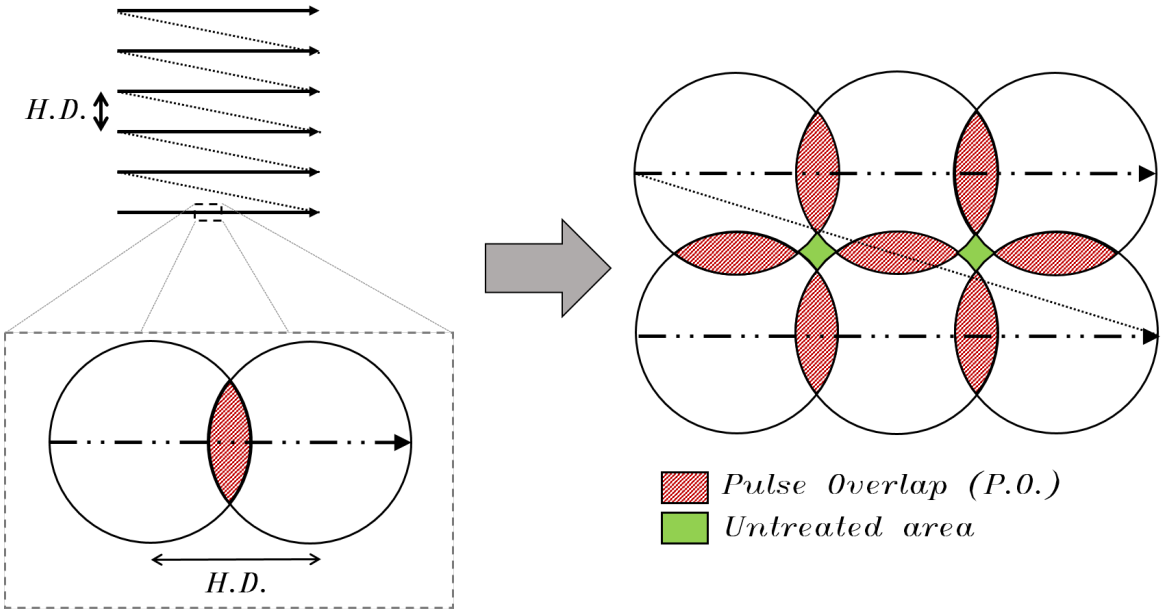

Figure 5.14: *Improved scanning technique schematic for low pulse overlap nanosecond pulsed laser surface structuring of Ti-6Al-4V*

Figure 5.14 shows how the pulse overlap employed by a modified scanning technique is significantly reduced. In this case the pulse overlap (red) is applied not only to the scanning direction of the laser beam, but also through the separation between each scanned line or the hatch distance (H.D.).

With the selected pulse separation a untreated surface area (green) is created in order to allow for molten material deposition, resulting from the ablation crater and thermal component of the nanosecond laser, for the micro-pillar surface creation.

To produce the desired scanning technique described in Figure 5.14 a relatively high scanning speed is required for the pulse separation. For the increase of ablated depth and molten material deposition on the untreated areas, the scanning technique was also repeated 10 times, effectively over-scanning each one of the ablated craters. Different pulse durations have been explored in order to verify the capabilities in order to create a suitable surface micro-structure for the modification of the wettability properties. The parameters are shown in Table 5.3 below.

Table 5.3: *Laser processing parameters for Ti-6Al-4V surface texturing for the creation of micro-pillar with low pulse overlap*

Laser parameter	**Value**
Laser fluence, [J/cm²]	6.71
Repetition frequency, [kHz]	25 - 45
Pulse duration, [ns]	200 - 90
Scan speed, [mm/s]	Variable
Hatch distance, [H.D. (μm)]	36
Pulse overlap, [P.O. (%)]	23.37
Surface overscan	10

Table 5.3 shows the parameters used for the creation of micro-pillar surface structures. A laser fluence of 6.71 J/cm^2 with decreasing pulse durations from 200 to 90 ns was chosen in order to explore the effects of pulse duration on the creation of a defined micro-structure and fixed laser fluence. Repeatability and accuracy provided by the scan head (XLR8-10), allows an accurate spot ablation position in order to produce a multiple spot ablation on the same area. After the laser surface texturing process, samples were placed into an electric oven (MEMMERT SM 100) for 20 hours at a pre-heated temperature of 200 °C for thermal post-processing, in order to stabilise and improve the oxide layer induced by laser ablation on the material surface.

5.5 Experimental results of improved scanning technique

5.5.1 Surface topography

Laser texturing of Ti-6Al-4V with low pulse overlap and using 10 overscans creates a micro-pillar shaped surface structure. However, the use of different pulse durations has an effect on the created surfaces. As the pulse duration decreases the amount of material removed by the laser decreases as discussed in Chapter 4 section 4.3.2 "Surface topography" of this thesis.

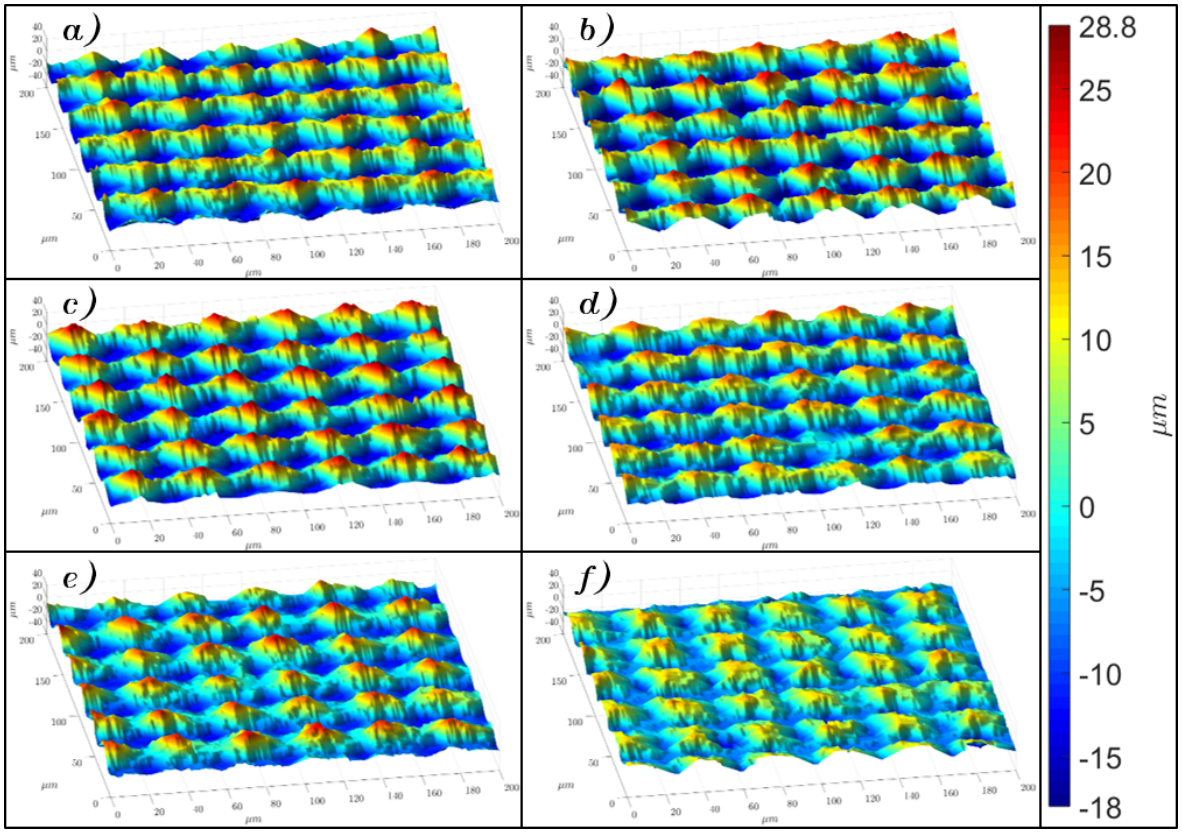

Figure 5.15: *Laser textured surfaces on Ti-6Al-4V with* 6.71 J/cm^2 *low pulse overlap, 10 overscans and decreasing pulse duration, a) 190 ns pulse duration, b) 170 ns pulse duration, c) 150 ns pulse duration, d) 130 ns pulse duration, e) 110 ns pulse duration and f) 90 ns pulse duration.*

Figure 5.15 shows the differences between the created surfaces with a constant laser fluence and scanning technique but with a decreasing pulse duration. The basic shape of the created micro-structures is constant across all the different pulse durations. However, as can be observed the ablated depth and height of molten material is reduced with reducing pulse duration.

Figure 5.15 (a), (b) and (c) displays a relatively similar micro-structure with similar distances between the ablated surface and the top of the molten material comparing the surface micro-structures with a pulse duration of 130 ns and below (c), (d) and (e), shows a decreasing distance between the ablated surface and the molten material deposited within the untreated area of the surface. This is expected and is consistent with to the obtained results of ablated depth and molten material height measurements presented in Chapter 4.

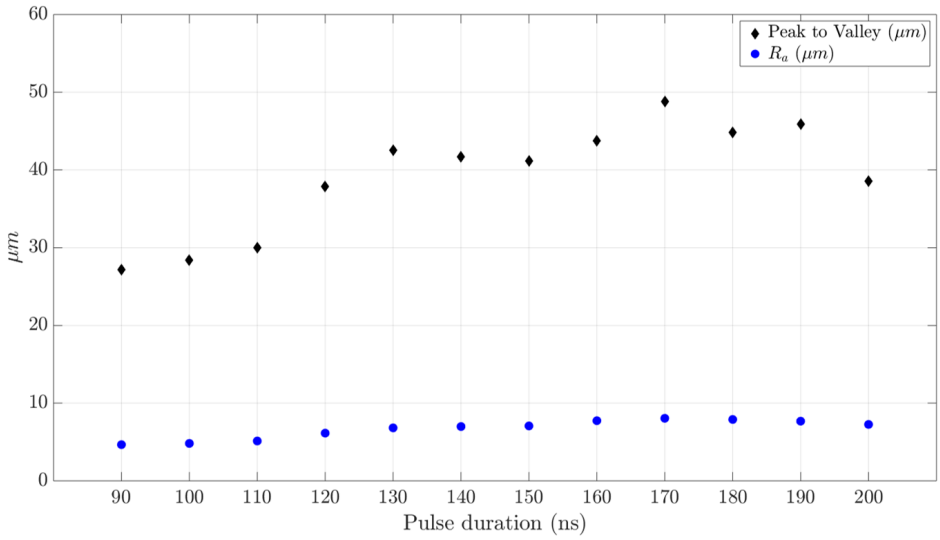

Figure 5.16: *Peak to valley and average roughness R_a measured of the created surface micro-pillar structures with 6.71 J/cm^2 and different pulse durations(WYKO data).*

Figure 5.16 shows the measurements obtained using a white light interferometer of the created micro-structures with different pulse durations. Peak to valley measurement refers to the distance between the bottom ablated surface and the top of the molten material that forms the micro-pillar. As can be seen, this measurement decreases steadily from 130 ns of pulse duration and below as would be expected due to the decrease of ablated depth with these pulse durations. However, the increasing trend of peak to valley distance can be observed to decrease again for pulse durations above 170 ns. This is due to the effects of the pulse duration on the ablation explored on the previous chapter. It was demonstrated that E_{pulse} for ablation increases as the pulse duration increases. In this case, E_{pulse} is kept constant and the pulse duration is increasing thus, decreasing the capabilities of the laser pulse for removing material from the surface.

Another effect observed on the created surface micro-structure is the shape of the deposited molten material. With longer pulse durations the molten material is deposited along the scanning direction forming a channel-like micro-structure.

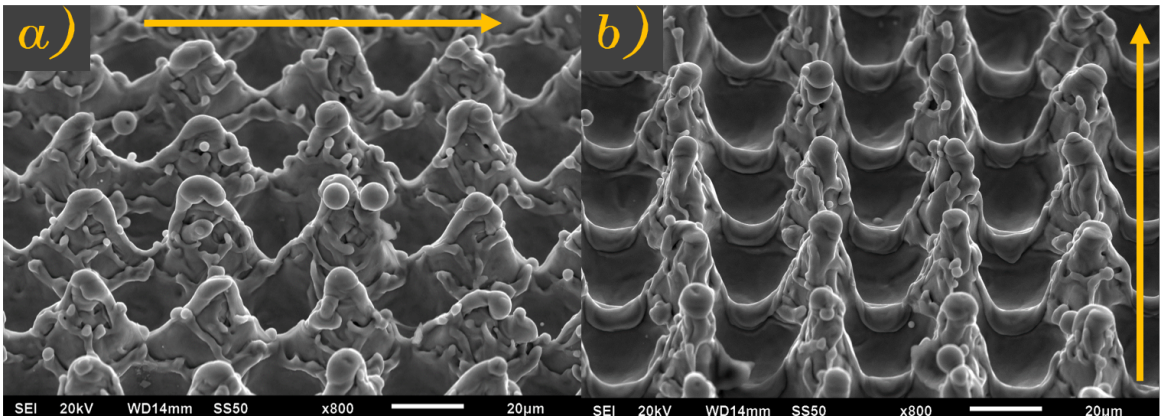

Figure 5.17: *Surface micro-structure created with* 6.71 J/cm^2 *laser fluence and 200 ns of pulse duration at 25 kHz, yellow line displays the scanning direction, a) Perpendicular view to scanning direction, b) Parallel view to scanning direction.*

Figure 5.17 shows the created micro-structure with perpendicular (a), and parallel (b), views relative to the scanning direction used for the material ablation with 200 ns pulse duration. As can be observed the perpendicular view shows how the molten material is deposited along the scanning direction, in comparison the parallel view(b), which shows a clean micro-pillar formation. This is likely due to the quality or mode of the laser system ($M^2 = 1.83$) which indicates that the laser spot is not a perfect circular shape.

This effect is increased due to the fact that the E_{pulse} used for the creation of the micro-structure is inferior to the required E_{pulse} for the creation of an ablated crater $\approx D_{min}$.

This effect is repeated on the created micro-structures with long pulse durations, however, this decreases as the pulse duration decreases due to the increased ablated crater size with the same E_{pulse} but smaller pulse duration. These effects are presented in Figure 5.18.

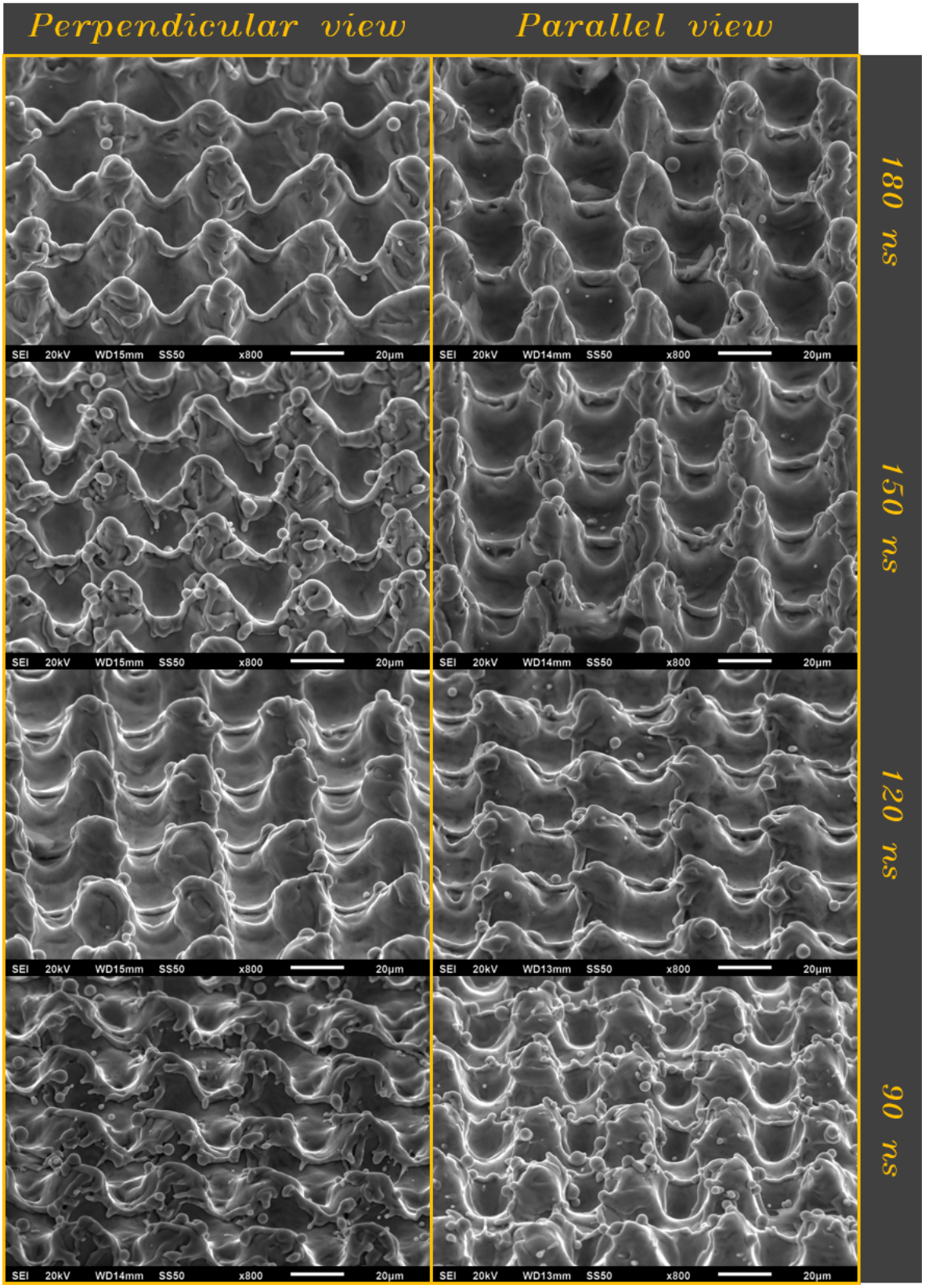

Figure 5.18: *Surface micro-structure created with* 6.71 J/cm^2 *laser fluence and different pulse durations, perpendicular and parallel view to scanning direction are presented for each pulse duration.*

5.5.2 Contact angle

The static contact angle of the samples was measured every three days, starting one day after laser surface texturing due to the post-thermal process method. Each data point presented in Figure 5.19 represents the average of three different static contact angle measurements on the central area of the processed surface.

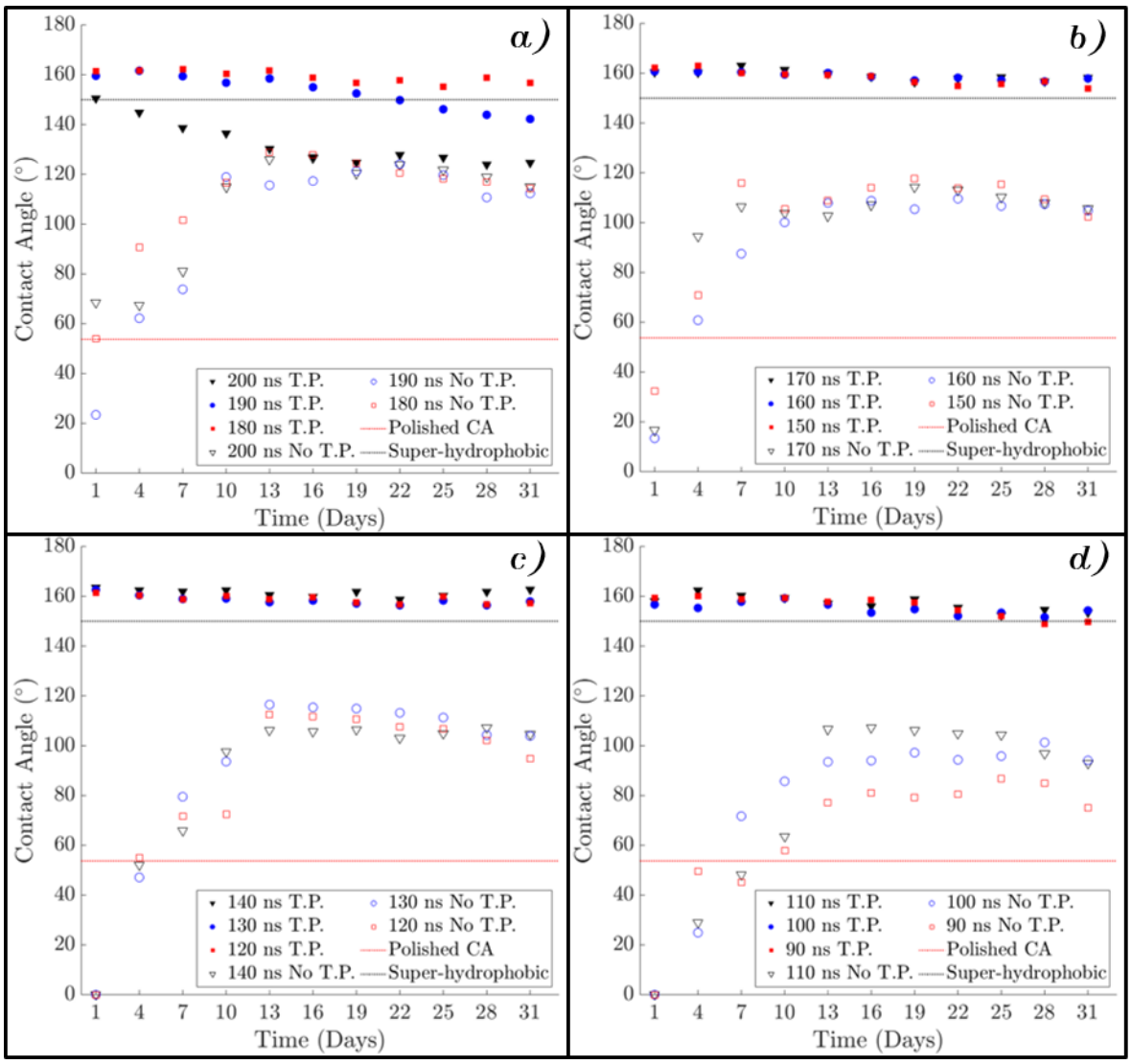

Figure 5.19: *Static contact angle of micro-pillars surface structures created with the improved scanning technique, 6.71 J/cm^2 and decreasing pulse duration. Two different type of samples are plotted, samples with* ***Thermal Post-process (T.P.)*** *and* ***without Thermal Post-process (No T.P.)****, a) 200 to 170 ns pulse duration, b) 170 to 150 ns pulse duration, c) 140 to 120 ns pulse duration, d) 110 to 90 ns pulse duration.*

Figure 5.19 shows the static contact angle development through time for the improved scanning technique for the creation of the micro-pillar shaped surface structures. A clear difference in the wettability behaviour can be seen between samples with the thermal post-processing(T.P.) and samples without the post-processing treatment(No T.P.).

The static contact angle reaches super-hydrophobic levels with almost all the samples processed with the scanning technique, even when the pulse duration is decreasing as long when the thermal post-process is used for the stabilisation of the oxide layer on the material surface. However, as shown in Figure 5.19 (a), surfaces created with 200 and 190 ns pulse durations display a super-hydrophobic behaviour in the first few days, but this effect is lost over time, returning to a hydrophobic behaviour where a high contact angle is exhibited, but no real liquid repellency. This type of effect is attributed to the surface structure shape, with longer pulse durations the material is deposited to the edges of the scanning direction creating a channel-like surface micro-structure. This is likely related to the laser spot not being completely circular in shape as previously discussed in Chapter 3 of this thesis.

However, reducing the pulse duration provides a more circular shape of the ablated crater, improving the structure and thus the wettability properties of the surface micro-structure. Figure 5.19 (b), (c) and (d) show how the contact angle displays a super-hydrophobic behaviour from day 1 after the thermal post-process with a good stabilisation over the 31 days of measurement.

In comparison, samples with laser surface texturing under the same scanning technique but with no thermal post-processing(No T.P.) display a reduced static contact angle directly after the texturing process and slowly improving over time. This behaviour is typically observed in previous investigations when a metallic material is subjected to a laser surface texturing process[88–93].

However, as the pulse duration decreases, the static contact angle on the first day decreases on samples without the thermal post-processing(No T.P.). This effect is amplified with pulse durations below 150 ns where the contact angle is displayed as zero (Figure 5.18 (c) and (d)) on the first day after the laser surface texturing procedure. This is due to the liquid droplet extending outside of the field of view of the DropShape analysis system, effectively displaying a hydrophilic effect on the surface.

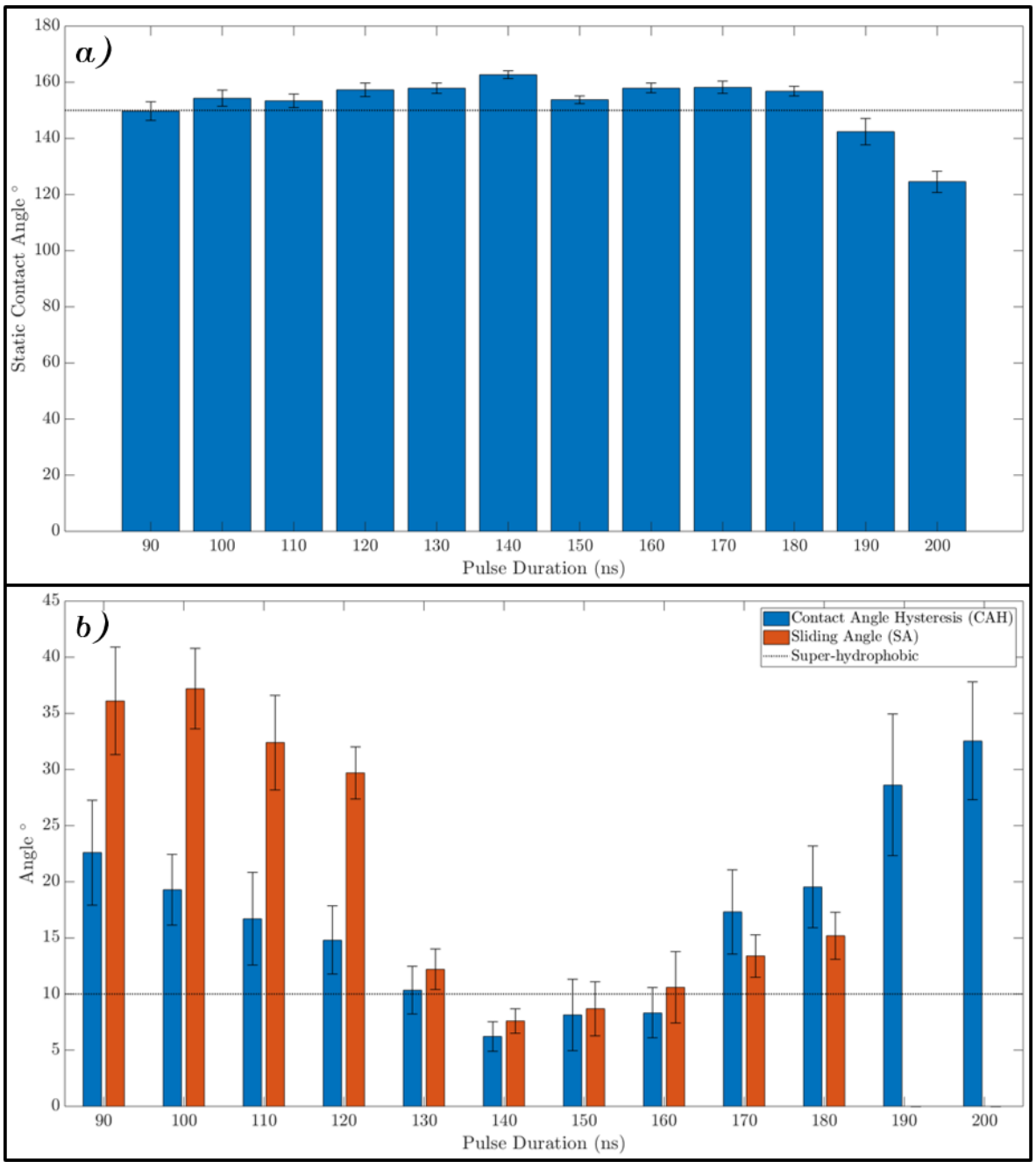

Figure 5.20: *Contact angle angle measurements after 31 days on Ti-6Al-4V surface structured with 6.71 J/cm^2 laser fluence, thermal post-process and different pulse durations. a) Static contact angle after 31 days, b) Contact angle hysteresis (CAH) and Sliding angle (SA) after 31 days, the dotted line represents the required value for super-hydrophobicity behaviour.*

In order to completely characterise the super-hydrophobicity of the created micro structures, the static contact angle, Contact Angle Hysteresis (CAH) and Sliding Angle (SA) were measured after 31 days as shown in Figure 5.20. Figure 5.20(a) shows how the static contact angle is $> 150°$ for the majority of the pulse durations used for surface structuring of Ti-6Al-4V after 31 days with the exception of surfaces created with 190 and 200 ns pulse duration where the contact angle after 31 days is $< 150°$.

To properly classify a super-hydrophobic surface, the contact angle hysteresis(CAH) is measured after 31 days. As shown in Figure 5.20(b) the highest values for CAH are presented on the surfaces created with 200 and 190 ns. There is no sliding angle measurement for these two surfaces, which means that no surface tilting angle is able to move the droplet from the contact position on the surface.

However, as the pulse duration is reduced, the contact angle hysteresis decreases until reaching $6.23° \pm 1.33$ on the surface created with a pulse duration of 140 ns. With pulse durations below 140 ns the CAH increases again as the pulse duration decreases. The same trend is observed on the sliding angle measurements with different pulse durations, however, there is a big increase on the SA for surfaces created with pulse durations below 130 ns reaching a maximum level of $37.2° \pm 3.6$ for the surface created with 100 ns of pulse duration.

As can be observed, the micro-structure shape has a fundamental role on the wettability of the surface. Surfaces created with 200 and 190 ns pulse duration display a channel-like shape with most of the molten material deposited along the scanning direction. However, as the pulse duration decreases the created micro-structures display a more defined micro-pillar structure, with the deposition of the molten material on the untreated areas (Figure 5.15). A side-effect With the decrease of the pulse duration is the decrease of the distance between the tips of the micro pillars and the ablated valleys due to the decreasing removal capabilities as described in Chapter 4 of this thesis.

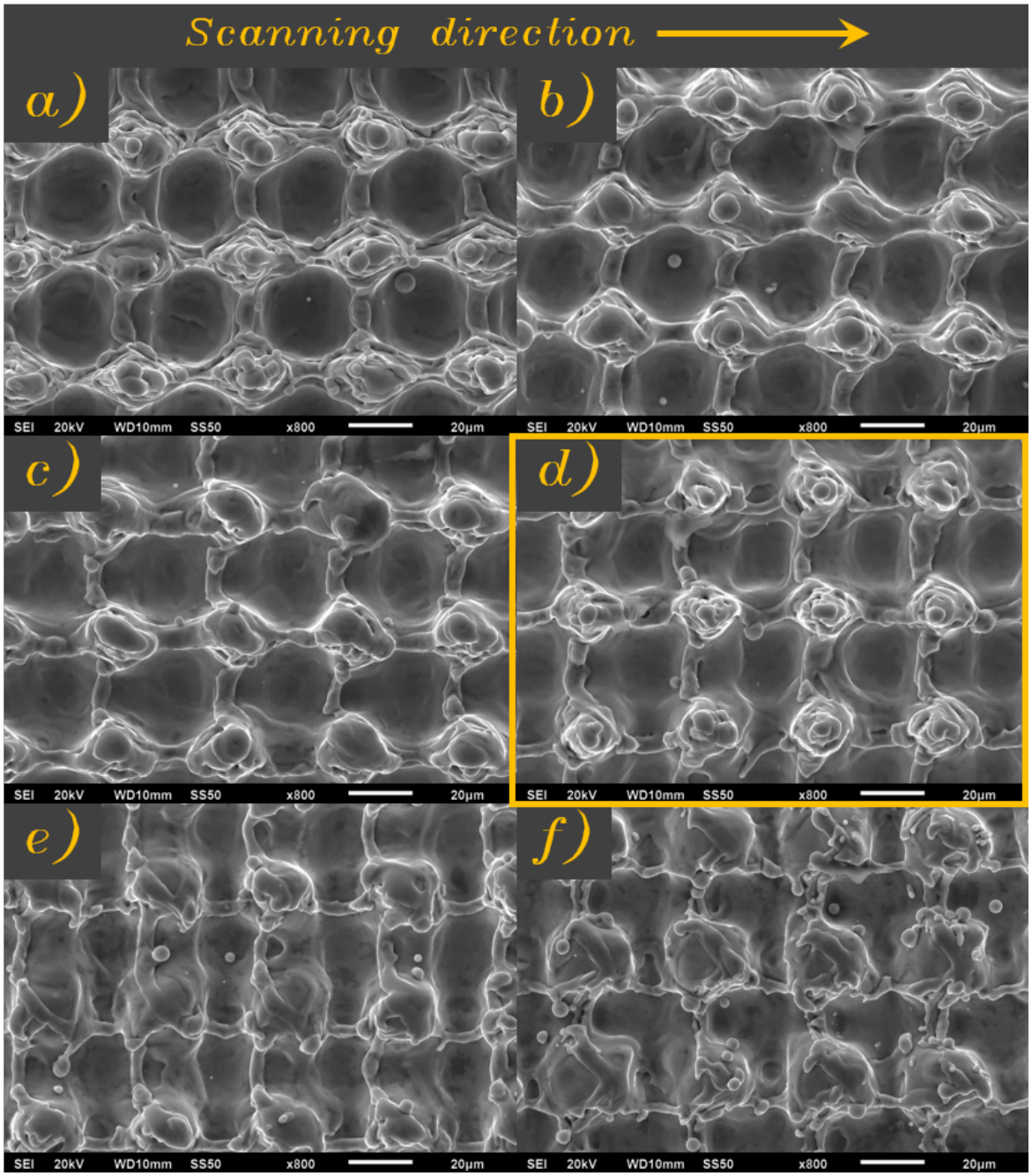

Figure 5.21: *Scanning Electron Microscope (SEM) images of created micro-pillar structures with different pulse duration, a) 200 ns pulse duration, b) 180 ns pulse duration, c) 160 ns pulse duration, d) 140 ns pulse duration, e) 120 ns pulse duration and f) 100 ns pulse duration. (6.71 J/cm^2 laser fluence and scanning speed range of 900 to 1,620 mm/s)*

The Figure 5.21 shows how with a pulse duration of 140 ns a clearly defined micro-pillar structure is created. Micro-structures created with a longer pulse duration tend to form a channel in the scanning direction. In comparison, shorter pulse durations create a structure where the micro-pillars are seemingly less defined (Figure 5.21 (e) and (f)).

These effects can be explained by the change in the ablated craters with a constant E_{pulsed} and a decreasing pulse duration. Chapter 4 of this thesis described how the ablation threshold decreases as the pulse duration decreases, effectively reducing the required E_{pulse} for the ablation of the material.

With this characterisation it can be assumed that using a constant E_{pulse} will increase the size of the ablated crater as the pulse duration decreases. At the same time the ablation depth will be decreasing as the pulse duration decreases.

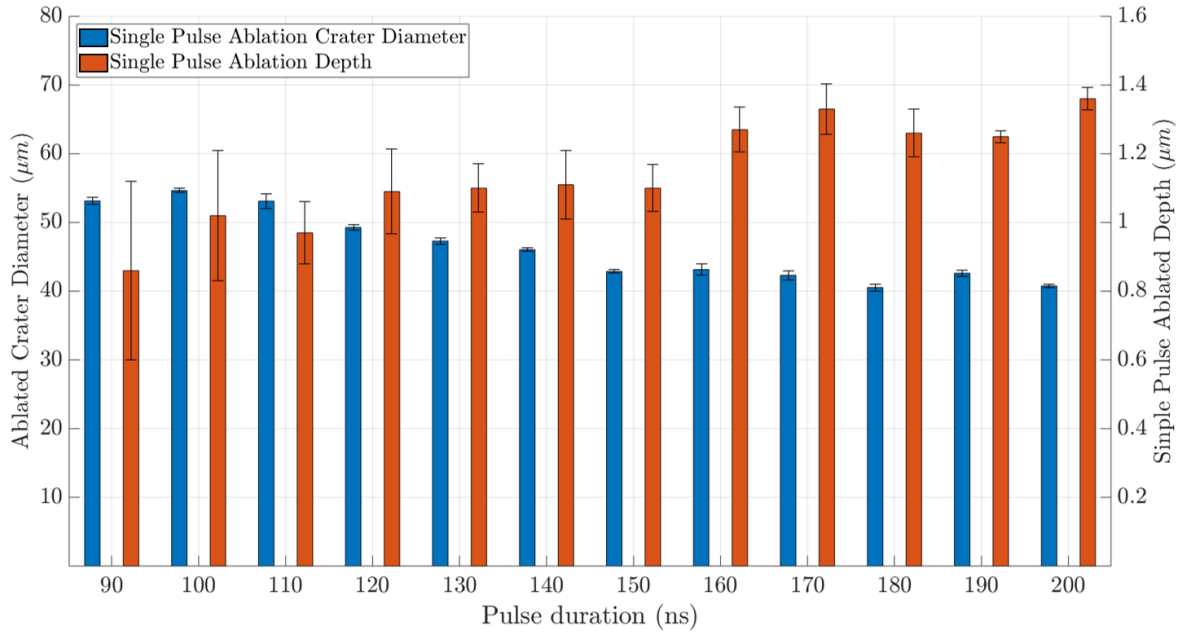

Figure 5.22: *Calculated ablated diameter with 130 μJ of E_{pulse} and decreasing pulse duration in blue, measured ablation depth for a single pulse ablation displayed on red*

Figure 5.22 shows how the ablated crater diameter increases as the pulse duration decrease according to the calculated ablation threshold trends described in Chapter 4 of this thesis. The increase in the ablated crater diameter means that the Pulse Overlap (P.O.) between the ablated craters is increased with shorter pulse durations reducing the space for the molten material deposition, thus, reducing the height of the micro-pillars as shown in Figure 5.16. In comparison, depth of ablation er pulse decreases as the pulse duration decreases which coupled with the quality mode of the SPI G4 laser system ($M^2 \approx 1.83$) explains the reduction in the size of the micro-pillars features.

5.5.3 Surface chemistry

In order to characterise the surface chemistry generated by the thermal post-process, the created surfaces were analysed through XPS. The XPS analysis was carried out on an Axis-Supra instrument from Kratos Analytical using monochromatic Al $k\alpha$ radiation (225 W) and a low-energy electron flood source for charge compensation. Survey scan spectra were acquired using a pass energy of 160 eV and a 1 eV step size. Narrow region scans were acquired using a pass energy of 20 eV and a 0.1 eV step size. The hybrid lens mode was used in both cases. The data was converted into the VAMAS file format (*.vms) and imported into the CasaXPS software package for analysis.

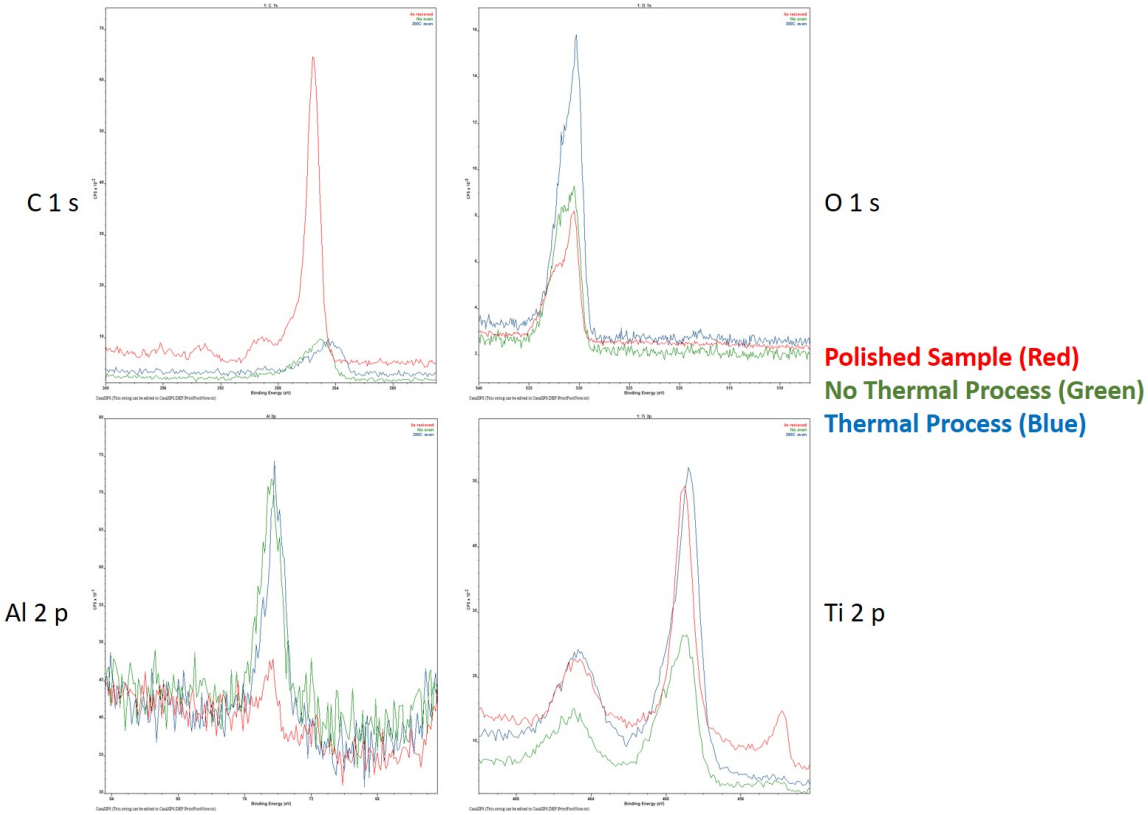

Figure 5.23: *XPS Spectra for Ti-6Al-4V structured samples 6.71 J/cm^2 and 130 ns pulse duration, red spectra corresponds to as received sample (polished without laser surface structuring), green spectra is for laser surface structure without thermal post-processing, and blue spectra indicates the sample with laser surface structuring and thermal post-processing.*

For the analysis an average of six samples was selected in order to verify the change in the surface oxidation with laser surface texturing and the difference between samples without or without thermal post-processing.

From the XPS analysis presented in Figure 5.23 a lower carbon concentration (C 1s) on both samples with laser surface texturing (with and without thermal post-processing) can be observed in comparison with the untreated sample (polished). This is due to the amount of surface contamination that can be transferred onto the material surface under ambient conditions. A second point is the significant increase in oxygen concentration (O 1s) on the samples with laser surface texturing and thermal post-processing in comparison with samples without thermal post-processing and polished, indicating a higher titanium oxide accumulation on the surface.

Aluminium levels were similar (Al 2p) between samples treated with laser surface texturing, however, for the polished sample, only a small amount of aluminium concentration was detected, this could be due to the relatively high levels of contaminants on the surface (carbon).

The titanium oxide analysis (Ti 2p) shows that the proportion of titanium oxide (Ti(IV)) increases on the samples with laser surface texturing whilst the amount of titanium metal (Ti(o)) decreases as shown in Figure 5.24.

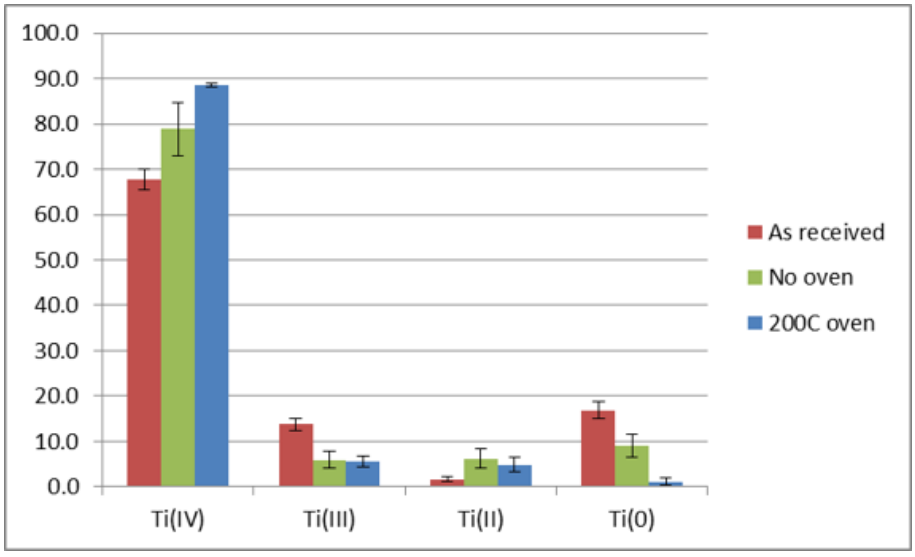

Figure 5.24: *Averaged percentage area of each titanium oxidation state*

As can be observed from Figures 5.23 and 5.24, the oxidation state on the surface does appear to play a fundamental role in the wettability of the structured surface. The increasing accumulation of stable TiO_2 (Ti(IV) oxide) benefits the creation of super-hydrophobic surfaces on titanium alloys due to their natural water repellency properties. This has been demonstrated in previous investigations that shown that a higher accumulation of TiO_2 increases the hydrophobicity of the titanium alloy[90, 99, 140, 144].

With the XPS analysis it can be observed that the thermal post-processing plays a fundamental role for the stabilisation and increase of titanium oxides on the surface, thus, decreasing the amount of time required to reaching a super-hydrophobic state of the surface through laser surface texturing.

While a comparison of specific laser parameters did not show a large enough difference, the influence of the topography combined with the surface chemistry is undeniable.

5.6 Summary

The use of lasers to create micro-structures on metal surfaces in order to change the wettability properties of a material has been widely explored to date, however this has been mainly confined to ultra-short pulsed lasers working in the femto and picosecond regime. In order to explore a more robust industrial method for the creation of super-hydrophobic surfaces, a fibre based nanosecond pulsed laser has been used to process polished Ti-6Al-4V samples to produce customised topography. The samples have then received a low temperature annealing post-treatment. This decreased the required time for reaching the super-hydrophobic point considerably. The nanosecond pulsed laser provides a thermal component in the surface, helping with the creation of micro pillars in the surface morphology. The use of scanning electron microscopy (SEM), white light optical profiling, XPS analysis, and contact angle measurements were used to characterize and quantify the effects of the surface modification on the wetting properties of the material.

Several investigations have been developing surface micro-structures capable of the creation of pockets of air within the surface structure for the improvement of the contact angle and super-hydrophobicity of the metallic material, most of them rely on ultra-short pulsed lasers and their ability to create not only a hierarchical surface structure with micro and nano scale levels of structures thanks to the creation of LIPSS[88–91].

The use of nanosecond pulsed lasers for the development of super-hydrophobic surfaces have been previously addressed. However most of these investigations rely on the creation of high amounts of molten material on the surface through slow ablation and smaller spot sizes for the creation of micro walls capable of creating pockets or air within the surface. In the case of the SPI G4 laser used in this work, several limitations for the creation of these types of walls are presented, a bigger spot size, over beam quality (M^2) and variable pulse shape make the creation of these previously investigated micro-structures difficult to achieve.

This chapter presented an alternative scanning technique for the creation of micro-pillar like structures. These structures are capable of producing the necessary pockets of air within the surface for the development of super-hydrophobic surfaces. The use of thermal post-processing has proved helpful for the decrease of the typical required time for metallic laser structured surfaces to achieve high levels of hydrophobicity. The development of an improved scanning technique with low pulse overlap takes advantage of the thermal component of the nanosecond pulsed laser and the molten material deposition for the creation of these types of micro-structures.

Characterisation of the oxidation state of the surface through XPS analysis showed that a simple thermal post-process treatment can improve the stabilisation of the oxidation state of the surface after laser texturing, increasing the hydrophobicity nature of the surface through the oxide layer.

The creation of a suitable micro-structure through the nanosecond pulsed laser and different pulse durations was successful. However, it is important to note that due to the laser beam quality and the parameters specification of the SPI G4 system, a detailed analysis of ablated craters and shape is required for parameter selection for the surface texturing process to creation of a suitable micro-structure.

The lack of a nanoscale structure on the surface presented in previous investigation can have detrimental effects on the hydrophobic levels[88, 90, 92]. This can decrease the static contact angle as observed in several of the created micro-structures, especially with long pulse duration such as 200 and 190 ns. A replacement for these type of nanoscale structures with the nanosecond pulsed laser and their effects on the wettability properties of the titanium alloy will be addressed in Chapter 6.

Chapter 6

Hierarchical surface structures

6.1 Introduction

Super-hydrophobic surfaces are widely observed in nature, a combination of hierarchical structures, nano and micro scale surface structures are often identified on natural super-hydrophobic surfaces such as the Lotus leaf. These structures are capable of creating the required pockets of air for a decreasing surface contact area between the liquid droplet and the surface[69, 71, 72]. Creation of these types of surface structures is possible through laser surface texturing techniques with the use of ultra-short pulsed lasers, working in the femto or picosecond regimes. The micro-scale surface structure can be created through laser ablation of the material and the nano-scale structure through the creation of Laser Induced Periodic Surface Structures (LIPSS)[88–91]. These are ripple-like surface nano-structures induced by ultra-short pulsed lasers as described in Chapter 3.

The use of these types of laser can be beneficial for a cleaner and more accurate creation of microstructures due the to cold ablation process. However, the creation of the micro-surface structures required for a super-hydrophobic behaviour is commonly a slow process using femto and picosecond pulsed lasers due to limitations in the amount of removed material per pulse[145, 146]. Usually requiring a multi-pulse ablation process to achieve the appropriate features size increasing the required processing time.

This creates a potential advantage for a nanosecond pulsed laser over ultra-short pulsed lasers for manufacturing surface microstructures. However, there is a limitation for the creation of nanoscale surface structures and thus hierarchical surface structures (nano and micro scale) with a nanosecond pulsed laser[140].

This chapter presents a hierarchical structure created through the use of two types of lasers, a nanosecond pulsed laser for the rapid creation of microstructures and a picosecond pulsed laser for inducing nanoscale surface structures (LIPSS). The influence of this type of hierarchical surface structure on the wettability properties of Ti-6Al-4V is analysed and an alternative structure is proposed for the creation of super-hydrophobic surfaces using only a nanosecond pulsed fibre laser.

6.2 Scanning technique for hierarchical surface structures

In order to generate the required hierarchical surface structure, a nanosecond pulsed fibre laser (SPI G4) is used for the creation of the microstructure on Ti-6Al-4V and followed by a nanoscale structure on top of this surface with a picosecond pulsed laser. The two scanning techniques used are presented in the next sections.

6.2.1 Scanning technique for the nanosecond pulsed laser

The scanning technique used for the creation of the microstructure surface follows the approach described in Chapter 5 **"Improved scanning technique"** section as shown in Figure 6.1 below.

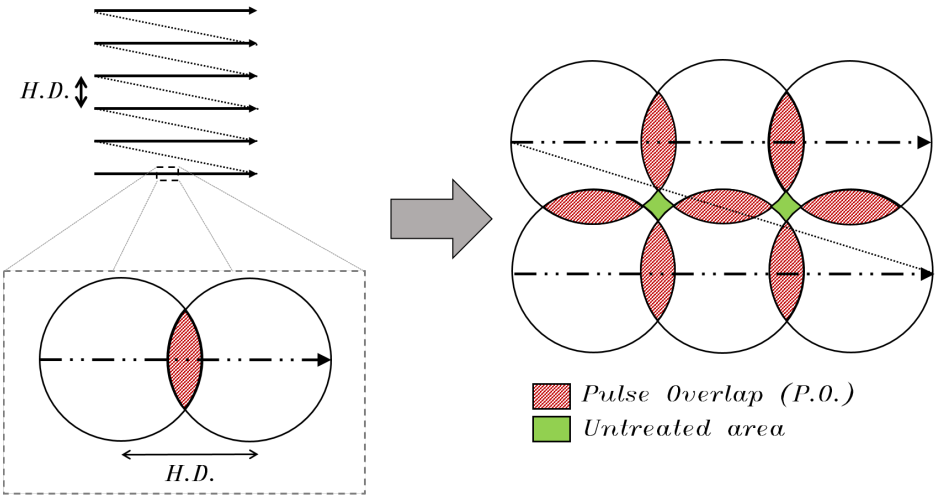

Figure 6.1: *Scanning technique schematic for creation of microstructure on Ti-6Al-4V surface with a nanosecond pulsed laser*

Samples were processed with a low percentage Pulse Overlap (P.O.) between the theoretical spot size (D_{min}), a suitable Hatch Distance (H.D.) in order to have a similar pulse overlap on horizontal and vertical direction. Finally, the surface was processed 10 times (10 overscans) in order to follow the exact same approach for a micro-pillar surface structure as described in Chapter 5. A pulse duration of 130 ns was chosen for the ablation of polished Ti-6Al-4V with the parameters presented in Table 6.1. These parameters were found to produce the best results on static contact angle and contact angle hysteresis in Chapter 5 of this thesis.

Table 6.1: *Laser processing parameters for Ti-6Al-4V surface texturing for the creation of microstructure with a nanosecond pulsed fibre laser*

Laser parameter	Value
Laser fluence, [J/cm²]	6.71
Repetition frequency, [kHz]	33
Pulse duration, [ns]	130
Scan speed, [mm/s]	1,188
Hatch distance, [H.D. (μm)]	36
Pulse overlap, [P.O. (%)]	23.37
Surface overscan	10

After the nanosecond laser processing of polished Ti-6Al-4V the sample was processed on the picosecond pulsed laser for the generation of a nanostructure surface on top of the created micro-stucture.

6.2.2 Scanning technique picosecond pulsed laser

For the creation of the nano-structure the High-Q picosecond pulse laser described in Chapter 3 was used with a similar scanning technique as presented in Figure 6.1. In this case a high pulse overlap was required in order to fully cover the surface with a nano-structure.

A similar procedure was employed for sample preparation for the picosecond laser. The structured Ti-6Al-4V was placed at the focal plane of the galvo-scanning system with a theoretical $D_{min} \approx 25\,\mu m$ calculated with the equation previously used for the theoretical spot calculation presented in Chapter 4.

Parameters used for the creation of Laser Induced Periodic Surface Structures are presented in Figure 6.2 and Table 6.2.

Table 6.2: *Laser processing parameters for Ti-6Al-4V Laser Induced Periodic Surface Structures (LIPSS), with High-Q picosecond pulsed laser.*

Laser parameter	Value
Laser fluence, [J/cm²]	0.20
Repetition frequency, [kHz]	10
Pulse duration, [ps]	10
Scan speed, [mm/s]	20
Hatch distance, [H.D. (μm)]	10
Pulse overlap, [P.O. (%)]	92

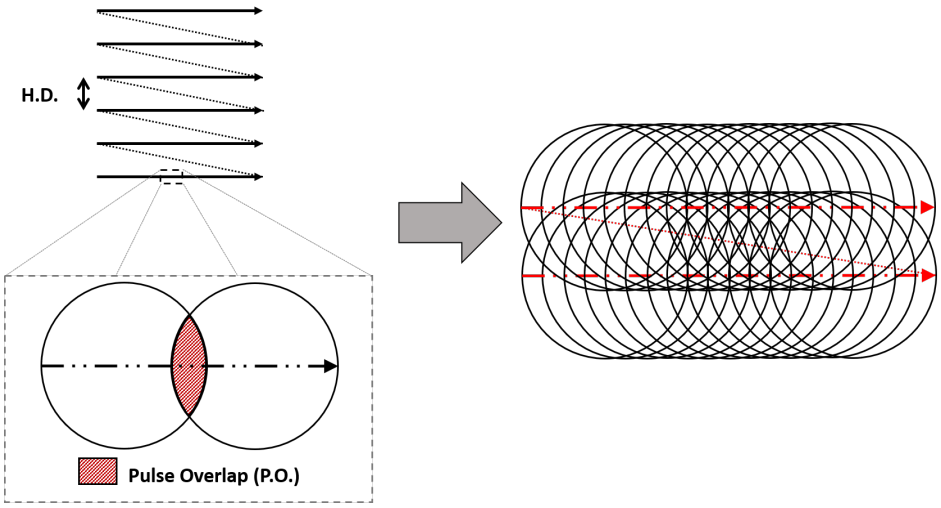

Figure 6.2: *Scanning technique schematic for generating Laser Induced Periodic Surface Structure (LIPSS) or nano-structures surfaces on top of micro-structured Ti-6Al-4V with a picosecond pulsed laser*

The scanning technique for the creation of LIPSS only requires a single scan of the surface texture. Samples were placed in the electric oven (MEMMERT SM 100) after the dual laser surface texturing for 20 hours thermal process at a pre-heated temperature of 200 °C to stabilise the oxide formation as discussed in Chapter 5.

6.3 Experimental results hierarchical surface structure

6.3.1 Surface topography

The surface texturing of the Ti-6Al-4V polished sample was analysed using the white light interferometer (WYKO) in order to assess and compare the differences between a micro-structured surface and the hierarchical surface structure (nano and micro scale surface texture). Figure 6.3 shows both of the created surfaces.

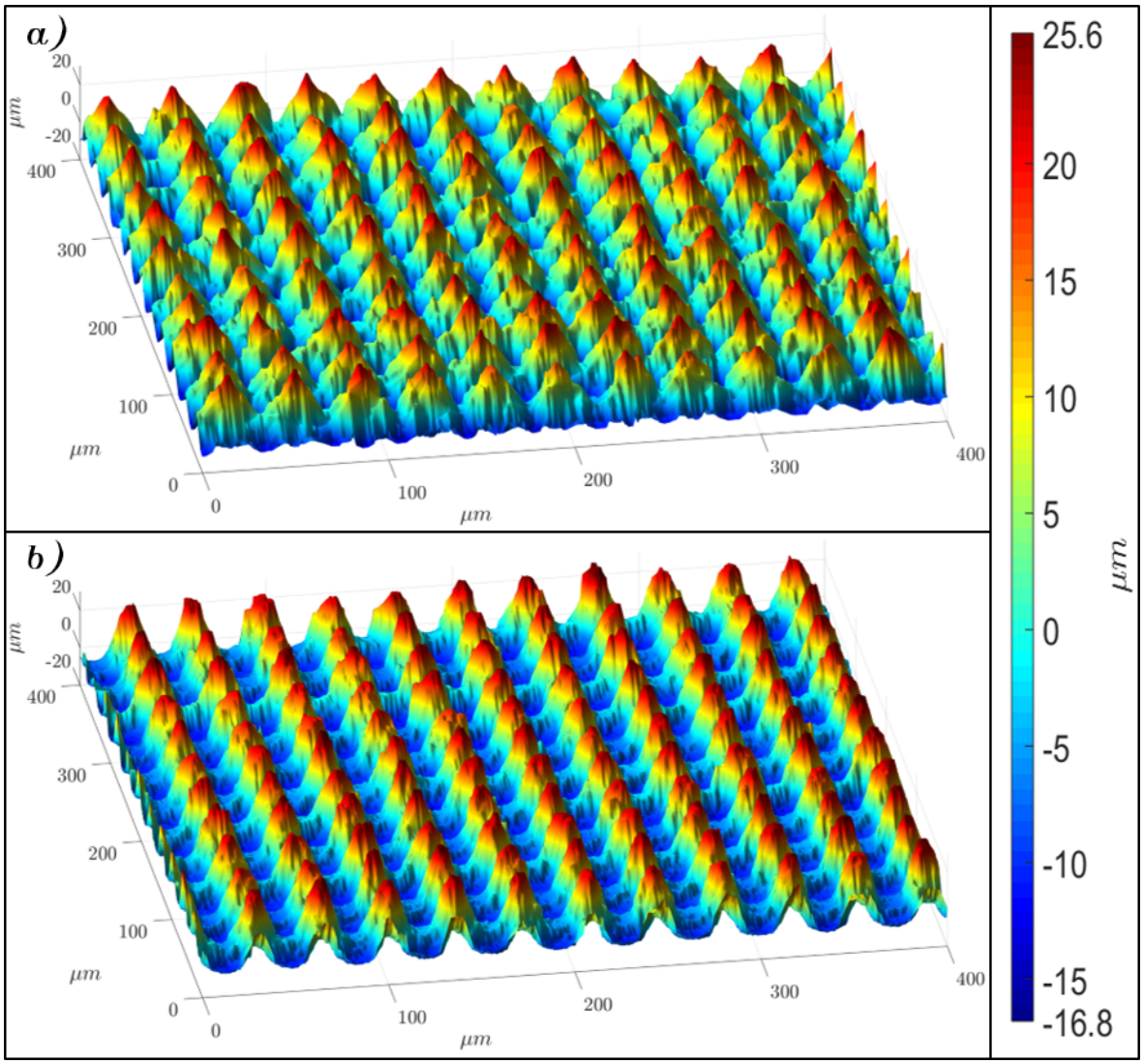

Figure 6.3: *Laser textured surfaces on Ti-6Al-4V, a) Microstructure with nanosecond pulsed laser 6.71 J/cm^2 fluence, 130 ns pulse duration, 30 kHz of pulse frequency, b) Hierarchical surface structure created with nanosecond pulsed laser at 6.71 J/cm^2 fluence and picosecond laser with 0.20 J/cm^2 laser fluence, 10 ps pulse duration, 10 kHz pulse frequency.*

As observed in Figure 6.3 a more defined micro-pillar structure can be seen in the hierarchical surface. This is likely due to the LIPSS formation of the surface allowing a better light reflection for the white light interferometer(WYKO) analysis. However, the most important difference between the two structures is the creation of a nanoscale surface shown in Figure 6.4 below.

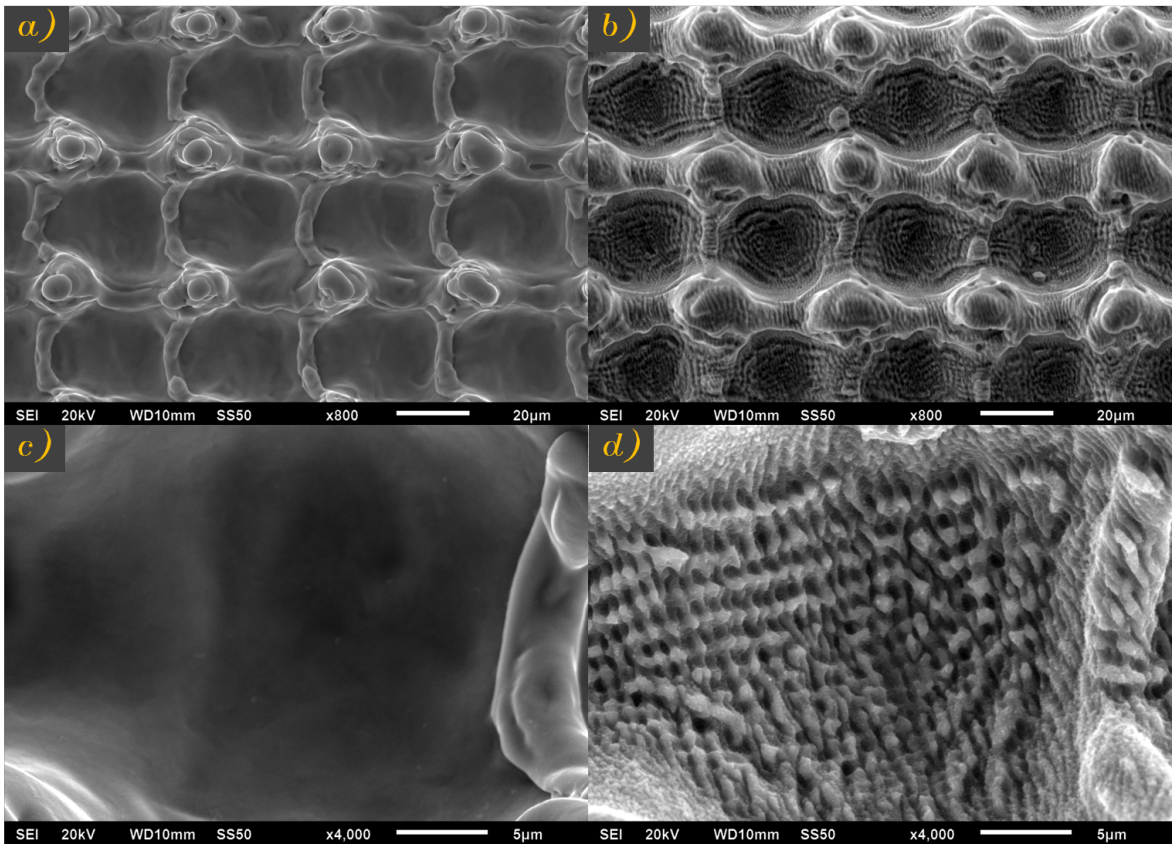

Figure 6.4: *SEM images of laser textured surfaces on Ti-6Al-4V, a) Micro-structure with nanosecond pulsed laser 6.71 J/cm^2 fluence, 130 ns pulse duration, 30 kHz of pulse frequency, b) Hierarchical surface structure created with nanosecond pulsed laser at 6.71 J/cm^2 fluence and picosecond laser with 0.20 J/cm^2 laser fluence, 10 ps pulse duration, 10 kHz pulse frequency, c) Ablated crater centre without nanoscale features, d) Nanoscale structure created inside the ablated crater.*

Figure 6.4 shows how the micro-structure is fully covered with laser induced periodic surface structures (LIPSS) created by the picosecond laser without modifying the fundamental characteristics of the micro-pillars. As can be observed, the centre of the nanosecond ablated craters of the micro-structure appear to be smooth and polished(Figure 6.4 (a)). In comparison, the surface structure processed with both laser systems (nano and picosecond laser) displays a clear nanostructure at the centre of the ablated craters and across all the features of the surface (Figure 6.4 (b) and (d)).

The use of the picosecond laser to induce LIPSS on the surface micro-structure created with the nanosecond laser only modifies the surface with nanoscale features without modifying the fundamental micro-pillar structure. In order to achieve this the E_{pulse} used by the picosecond laser needs to be kept as low as possible to avoid significant ablation of the material and thus modifying the created micro-pillar structure.

The nanoscale features created on the surface have a vertical orientation in comparison with the scanning direction of the laser system due to the induced polarisation of the Spatial Light Modulator (SLM) described in Chapter 3. The orientation and nanoscale features can be observed in figure 6.5 below.

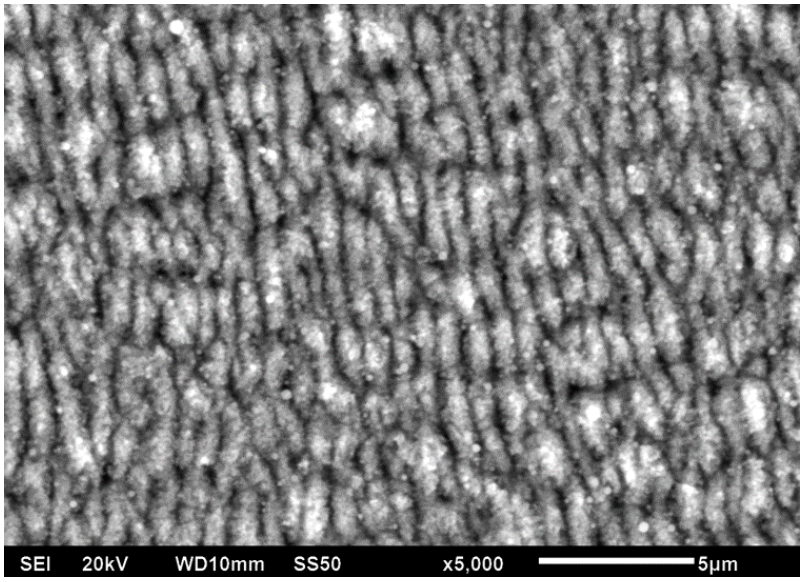

Figure 6.5: *SEM image of Induced Laser Periodic Surface Structure (LIPSS) created on polished Ti-6Al-4V using a picosecond laser with 0.20 J/cm^2 fluence and 10 kHz.*

Figure 6.5 shows the nanoscale surface structure induced on polished Ti-6Al-4V with a periodicity of approximately 1 μm. The separation between the nano-structures is defined by the wavelength of the laser source, 1064 nm in the case of the High-Q Picosecond laser described in Chapter 3. One of the theories behind the generation of these type of nano-structures is the laser beam interaction with the electromagnetic wave of the surface [50, 134].

In order to verify the created nano-structures and any impact on the micro-structure, a comparison between the features was performed with the white light interferometer (WYKO) and presented in Figure 6.6 below.

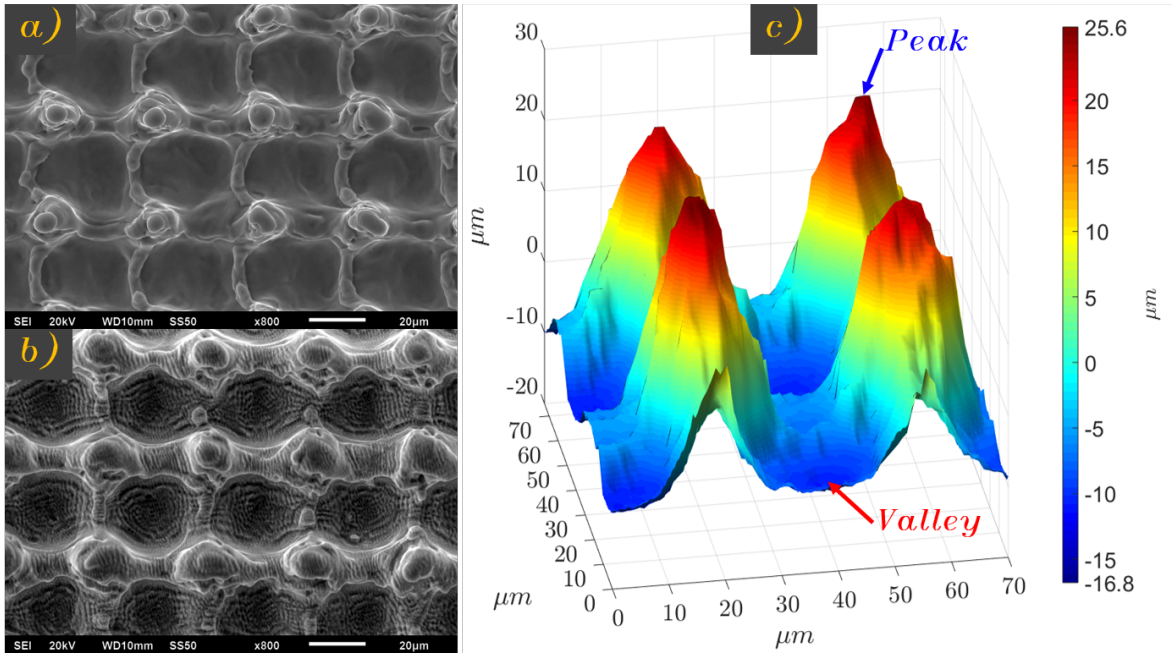

Figure 6.6: *SEM images and 3D surface interpretation of micro-pillar structure created with nanosecond and picosecond pulsed laser a) SEM image of surface micro-structure with nanosecond pulsed laser processing, b) SEM image of hierarchical surface structure created with nanosecond and picosecond pulsed laser, c) 3D representation of micro-pillar surface created.*

Figure 6.6 shows the two types of surface structures, a purely micro-structure surface (a) and the hierarchical structure (b). Measurements of the main characteristics of both surfaces are displayed in Table 6.3 below for comparison.

Table 6.3: *Surface measurements of the micro-pillar surface structure created with the nanosecond pulsed laser and the hierarchical micro-structure processed with the nanosecond and picosecond pulsed laser systems.*

Surface Structure	**Peak to Valley** (μm)	**Average Roughness Ra** (μm)
Micro-pillars	42.46 ± 0.98	6.67 ± 0.09
Hierarchical structure	41.68 ± 1.08	7.39 ± 0.15

Table 6.3 shows how the basic micro-pillar structure presents only a small change in the distance between the deepest part of the surface and the top of the micro-pillar (Peak to Valley) of less than 1 μm from measurements taken through the white light interferometer(WYKO).

A more significant difference between the average roughness measurements (Ra) can be observed between the two types of surface structures. This measurement was increased by 0.72 μm for the hierarchical structure compared with the purely micro-pillar structure. This is due to the induced nano roughness across the entire surface structure. The creation of the laser induced periodic surface structure (LIPSS) is particularly noticeable in the centre of the ablated craters as observed in Figure 6.4 (c) and (d), this has the effect of increasing the average roughness (Ra) across the surface modifying a seemingly polished ablated crater to a surface with a visible roughness.

The creation of these type of structures has been widely observed on natural surfaces increasing the ability to repel water. The hierarchical surface structures reduce the surface energy, decreasing the ability of a liquid to adhere to the surface and allowing the creation of the necessary pockets of air between the surface and the droplet creating a super-hydrophobic surface. These effects will be presented in the next section with the measurement comparison between the two types of surface for their wettability properties[72, 74, 76].

6.3.2 Contact angle

The static contact angle of the samples was measured in order to compare the difference in the wettability properties between the two types of surface structures. Figure 6.7 shows the contact angle measurements for both types of structures, each data point represents the average of three different measurements in the centre of the surface structure.

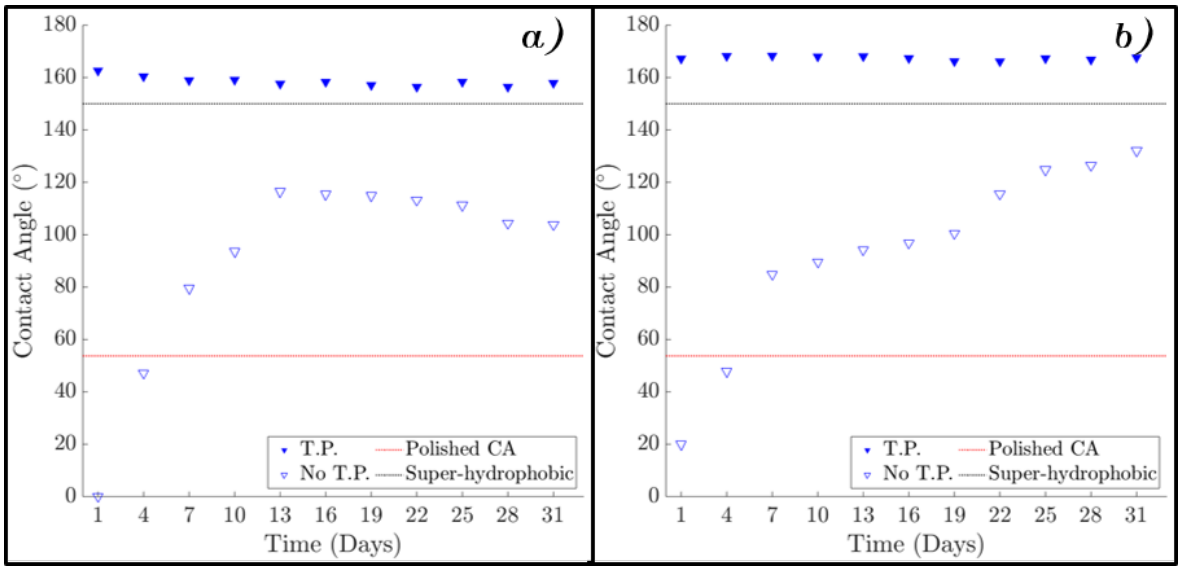

Figure 6.7: *Static contact angle of surface structures created with improved scanning technique and laser induced periodic surface structures produced by the picosecond pulsed laser with* ***Thermal Post-processing*** *(**T.P.**) and with* ***No Thermal Post-processing*** *(**No T.P.**), a) Static contact angle of micro-structured surface with nanosecond pulsed laser and 6.71 J/cm^2, b) Static contact angle of hierarchical surface structure processed with nanosecond and picosecond pulsed laser*

Figure 6.7 shows how the static contact angle of the hierarchical surface structure (b) is slightly improved compared with the micro-pillar structure. Static contact angle stability over time is similar for samples processed with thermal post-processing. In comparison, samples with no thermal post-processing show a typical behaviour for laser surface structures, starting with a hydrophilic behaviour for the first few days and slowly improving over time. However, the hierarchical surface structure (Figure 6.7 (b)) with no thermal post-processing displays a clear improvement of wettability behaviour in comparison with the micro-structure processed with only a nanosecond pulsed laser and without thermal post-processing (Figure 6.7 (a)).

Static contact angle measurements showed a similar behaviour between the two types of surface structures with thermal post-processing. Hierarchical surface structure created with both laser systems showed a slight improvement in the static contact angle measurements, however the big difference between both samples is shown on Contact Angle Hysteresis (CAH) and Sliding Angle (SA) measurements as shown in Table 6.4 below.

Table 6.4: *Static contact angle measurements after 31 days on Ti-6Al-4V surface structured with nanosecond pulsed laser and picosecond pulsed laser*

Surface Structure	**Measurements**		
	Static CA	**CAH**	**Sliding angle**
Micro-pillars	157.90° ± 1.81	10.34° ± 2.12	12.20° ± 1.80
Hierarchical structure	167.60° ± 1.21	5.18° ± 2.1	8.20° ± 1.50

As observed in Table 6.4 a clear improvement of the super-hydrophobicity behaviour is achieved with the hierarchical surface structure. The reduction on contact angle hysteresis (CAH) and sliding angle (SA) displays an improvement over the surface structure created with only the nanosecond pulsed laser as both of the measurement exhibit super-hydrophobic levels($< 10°$).

Inducing a nanoscale structure on top of the created micro-structure reduces the surface energy of the material, increasing the hydrophobicity of the structure. These nanoscale features are especially important in the centre of the ablated craters in order to increase the surface roughness ensuring the liquid is unable to adhere to the surface creating a more reliable water hydrophobic behaviour. These types of surface structures have been widely explored with ultra-short pulsed lasers looking to emulate hydrophobic surfaces found in nature such as the Lotus flower[74, 92, 140]. This work is demonstrating that these structures can be made with nanosecond and picosecond lasers to improve throughput and surface stability.

6.3.3 Surface chemistry of hierarchical surface structure

In order to compare the effects of the two types of surface structures on the chemical composition of the Ti-6Al-4V a XPS analysis was carried out. Six different samples were analysed under the same conditions as presented in Chapter 5 through the Axis-Supra instrument. Three different surface structures were analysed, purely nano-structured surface (LIPSS), purely micro-structured surface (micro-pillars) and combination of both surface structures (LIPSS on top of micro-pillars). For each one of these type of surface structures two samples were analysed, with and without thermal post-processing for a correct comparison. The goal of the analysis was to obtain atomic concentrations of elements on the surface and presented in Figure 6.8 below.

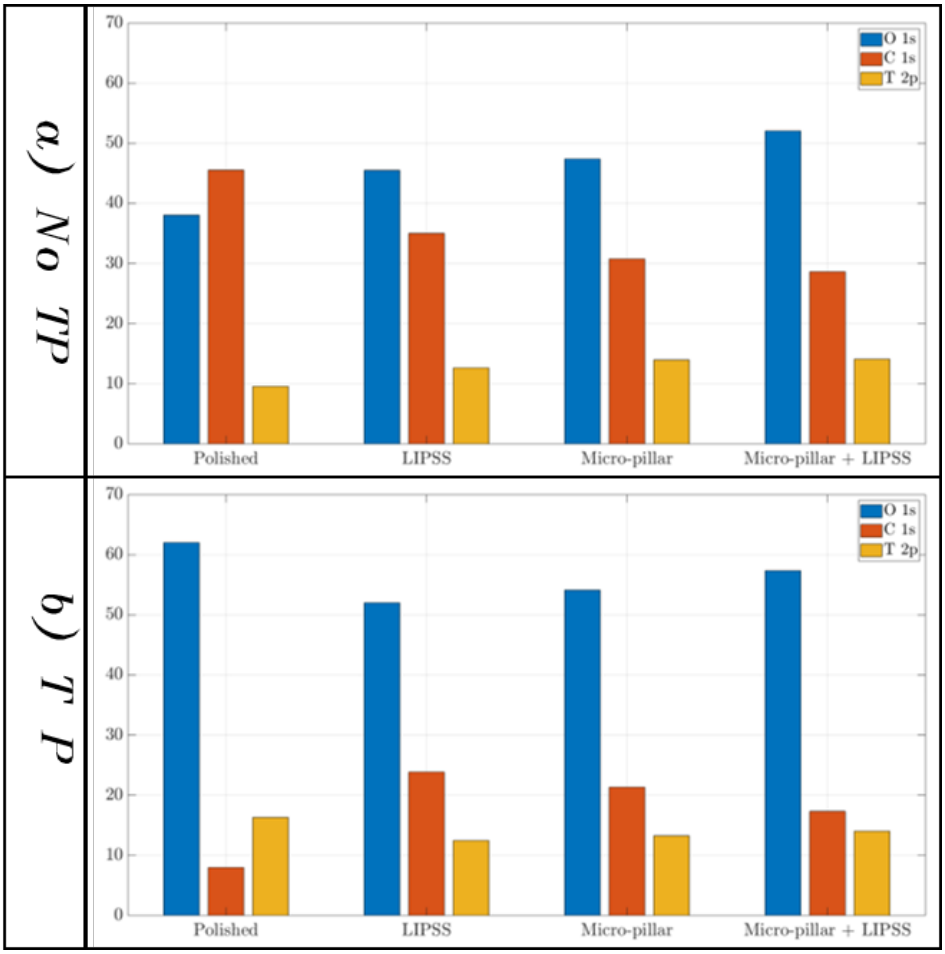

Figure 6.8: *Atomic % concentration of Oxygen (O 1s (Blue)), Carbon (C 1s (Orange)) and Titanium (Ti 2p (Yellow)), on Ti-6Al-4V surface with different structures one day after laser surface processing, a) Sample without thermal post-processing, b) Sample with thermal post-processing. Both samples were analysed 1 day after the laser surface texturing process.*

Figure 6.8 shows the main difference between samples with and without thermal post-processing. A decrease in the carbon concentration (C 1s) is observed in all of the four different surface structures with thermal post-processing.

In comparison the amount of Oxygen (O 1s) is increased with the thermal process on all the surface structures. The amount of Titanium (Ti 2p) on the surface is relatively similar between the two sets of samples with the exception of the polished surface, where the amount of Ti 2p has increased with thermal post-processing. This could be due to the amount of carbon (C 1s) presented on the surface of the sample with no thermal-process, indicating a higher amount of ambient contaminants present on the surface, affecting the element characterisation.

Figure 6.8(a) describes the atomic concentration % of samples with no thermal post-process. The main trend that can be observed is the increase in Oxygen (O 1s) with all the laser surface texturing processes compared with the polished sample. This is as expected as the thermal component of the laser beam during laser processing in air affects the surface and thus oxidising the material. However, the amount of carbon concentration (C 1s) decreases in different ratios depending of the type of surface structure. The combination of micro-pillar and LIPSS have the lowest concentration of carbon perhaps due to the two laser surface process removing surface contamination more effectively. The inverse trend is observed for the concentration of oxygen (O 1s) where the highest accumulation is observed for the hierarchical surface structure induced by the two laser surface texturing processes.

The XPS analysis of the samples with thermal post-processing (Figure 6.8 (b)) show a similar trend for surface oxidation as described in Chapter 5. The amount of carbon (C 1s) decreases and the oxygen concentration increases (O 1s) for all the surface structures with thermal post-processing compared with the samples without this post-process.

A similar trend as with the samples with no thermal post-processing is observed in the carbon and oxygen concentrations (C 1s and O 1s) with the different surface textures. Carbon concentration decreases with the number of surface texturing processes. The highest amount of carbon concentration is observed on the surface with nanoscale structure (LIPSS) and decreases as with the hierarchical surface structure (micro-pillar and LIPSS).

However, there is a big difference on the polished surface where the carbon concentration is significantly reduced compared with all the other surfaces (with thermal and without thermal post-processing). This is likely attributed to a decrease in surface contamination due to the thermal treatment and the lack of surface structure.

As can be observed from the XPS analysis, change in surface chemistry can play a fundamental role in the wettability properties of Ti-6Al-4V, however, the presence of an oxide layer alone on the titanium alloy does not create a super-hydrophobic surface. A combination of surface structure (micro, or hierarchical structure) with the oxide layer is required for a super-hydrophobic behaviour of the surface. This can be observed with the oxygen and carbon concentrations (O 1s and C 1s) compared between the polished sample with thermal post-processing and the hierarchical structure (Micro-structure + LIPSS) and it has been suggested in recent investigations[140]. The hierarchical structure with thermal post-processing presents a super-hydrophobic behaviour compared with the normal wettability behaviour presented on the polished surface as shown in Figures 6.9 and 6.10 below.

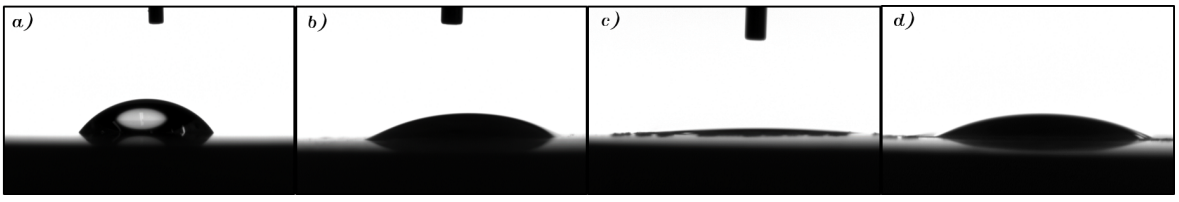

Figure 6.9: *Static contact angle of Ti-6Al-4V samples with* ***no thermal post-processing*** *one day after laser surface texturing and different surface textures, a) Polished sample, b) Laser induced periodic surface texture (LIPSS), c) Micro-pillar structure and d) Hierarchical surface structure.*

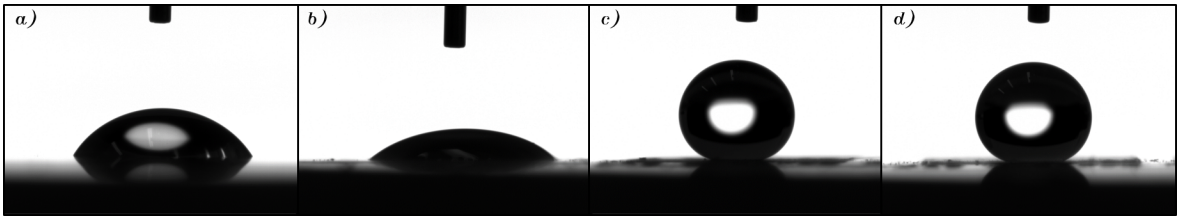

Figure 6.10: *Static contact angle of Ti-6Al-4V samples with* ***thermal post-processing*** *one day after laser surface texturing and different surface textures, a) Polished sample, b) Laser induced periodic surface texture (LIPSS), c) Micro-pillar structure and d) Hierarchical surface structure.*

Figures 6.9 and 6.10 shows how the static contact depends on the combination of surface structure and oxidation state of the material one day after the laser surface texturing process. Samples with no thermal post-processing follow the same effects discussed in Chapter 5 with a decrease in the static contact angle after laser surface texturing and slowly improving over time (Figure 6.9).

In comparison, samples with a micro-pillar and hierarchical surface structures and thermal post-processing clearly display a super-hydrophobic behaviour on the first day as can be observed in Figure 6.10 (c) and (d). This is not the case for the polished material and the laser induced periodic surface structure (LIPSS). These two samples show a low static contact angle nowhere near the super-hydrophobic regime(Figure 6.10 a) and b)).

Static contact angle measurements show an improvement in the wettability propiertes of hierarchically surface structured Ti-6Al-4V in comparison with the micro-pillar structure both of them with thermal post-processing as shown in Figure 6.7. The improvement is not only observed on the static contact angle measurements but also on the sliding angle (SA) and contact angle hysteresis (CAH) compared on Table 6.4. It is clear that the hierarchically surface structure provides benefits for the development of super-hydrophobic surfaces, however, in order to create this hierarchical surface structure two laser systems were used. The use of the picosecond laser system limits the capacity and increases the equipment complexity required for the production of this type of surfaces.

Laser induced periodic surface structures (LIPSS) are typically created with ultra-short pulsed lasers only[47, 50], however, an alternative for these type of surface features is explored in the next section for improving the wettability properties of Ti-6Al-4V using only the nanosecond pulsed laser.

6.4 Alternative enhanced single laser technique for the generation of hierarchical surface structures

The creation of hierarchical surface structures for the improvement of the wettablity properties of Ti-6Al-4V was explored in the previous section, displaying an enhancement on the contact angle hysteresis (CAH) and sliding angle (SA) for a stable superhydrophobic behaviour of the surface. However this required the use of two different laser systems increasing the time and needed equipment. In order to avoid this, an alternative scanning technique for the creation of micro-pillar surface structure using only the nanosecond laser is proposed in this section. This scanning technique is based on the preliminary scanning technique presented in Chapter 5 and shown in Figure 6.12 below.

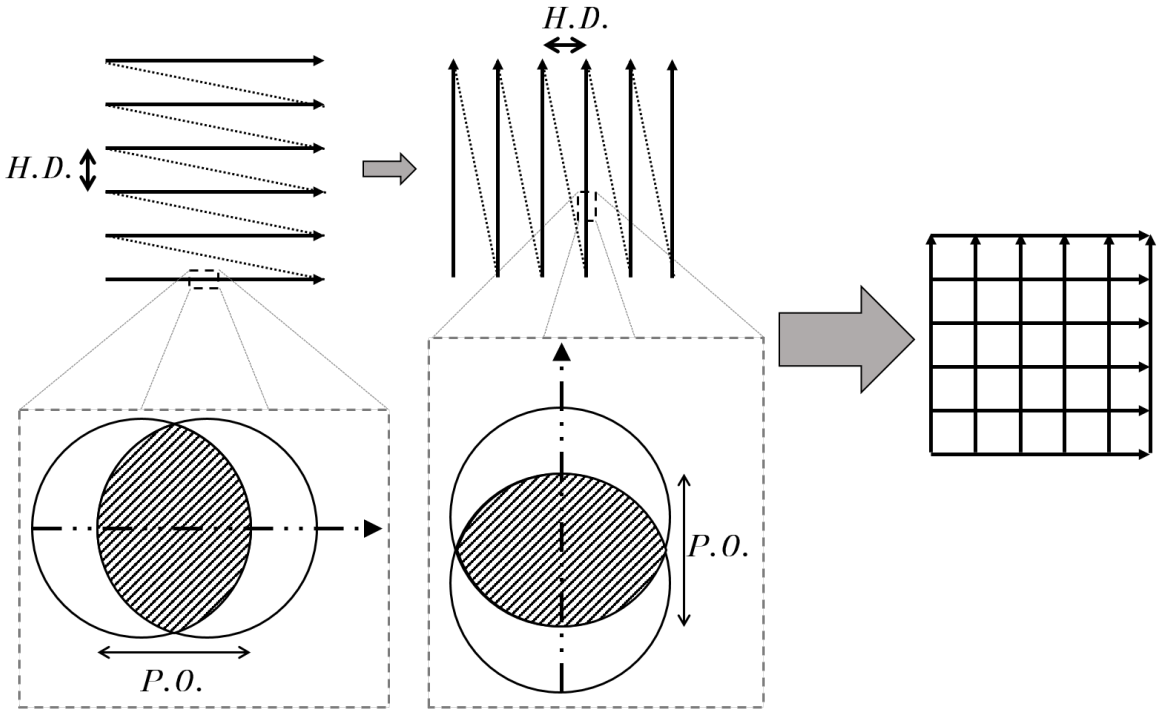

Figure 6.11: *Alternative scanning technique for the creation of micro-pillar structure with nanosecond pulsed laser.*

Figure 6.11 shows the scanning technique for generating a hierarchical type surface structure with the nanosecond pulsed laser on as-received Ti-6Al-4V in order to compare the processing capabilities of the laser system.

The aim of the alternative enhanced scanning technique is to generate a micro-pillar shaped surface structure with surface roughness in the centre area between the micro-pillars. The main goal is to emulate the surface roughness induced by the Laser Induced Periodic Surface Structures(LIPSS) produced by the picosecond laser in the previous section and improve the wettability behaviour of the material surface. For this, the scanning technique relies on a high Pulse Overlap (P.O.) for the creation of a grid based surface structure with the parameters presented in Table 6.5.

Table 6.5: *Laser processing parameters for as-received Ti-6Al-4V surface texturing for square-shaped scanning technique*

Laser parameter	**Value**
Laser fluence, [J/cm²]	5.10 - 7.94
Repetition frequency, [kHz]	25 - 65
Pulse duration, [ns]	65 - 200
Scan speed, [mm/s]	100 - 260
Hatch Distance, [H.D. (μm)]	50
Pulse Overlap, [P.O. (%)]	91.95

Table 6.5 show the range of parameters used for laser surface texturing of a square-grid based technique. The range in laser fluence follows the calculated values for an ablated crater $\approx D_{min}$. Pulse repetition frequency selection is according to the operation parameters of the SPI G4 fibre laser for different pulse durations. Finally the scanning speed is calculated in order to maintain the Pulse Overlap (P.O.) according to the pulse repetition frequency. It was decided to use as-received, unpolished material for this study to demonstrate industrial applicability with the nanosecond pulsed fibre laser.

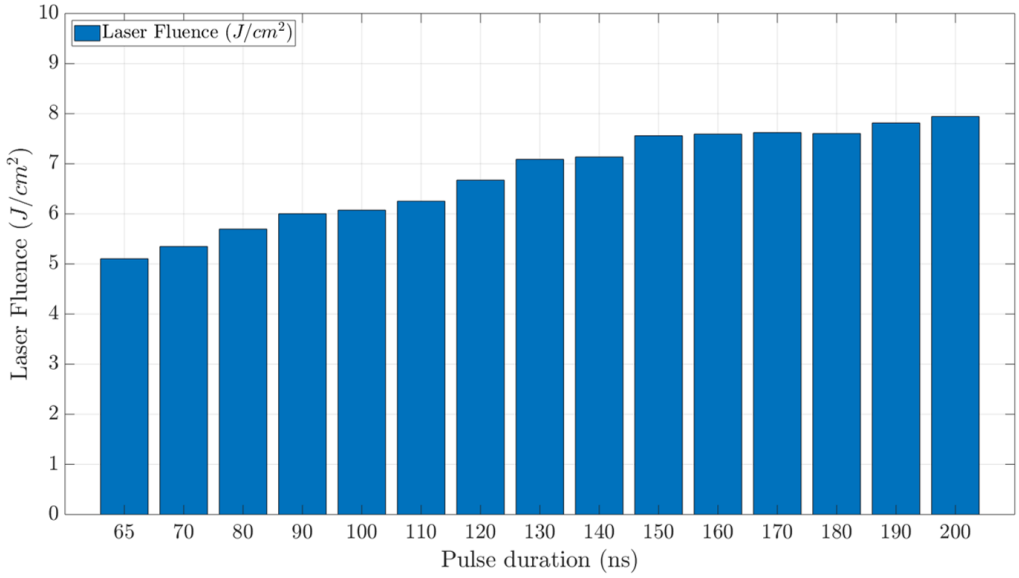

Figure 6.12: *Calculated laser fluence for an ablated crater* $\approx D_{min}$ *with different pulse durations.*

Figure 6.12 shows how the required laser fluence for an ablated crater $\approx D_{min}$ increases as the pulse duration increases as shown in Chapter 4, according to the temporal shape of the SPI G4 pulse. The use of this level of laser fluence is in order to create an ablated crater with a near-circular shape, thus maintaining the shape of the ablated channel in both directions (horizontal and vertical).

A thermal post-process has been applied directly after the laser surface texturing process. The samples were placed in an electrical oven (MEMMERT SM 100) for 20 hours at a pre-heated temperature of 200 $°C$.

6.5 Experimental results for enhanced single laser generation of hierarchical surface structures

6.5.1 Surface topography

Created micro-structures through laser surface texturing ablation were analysed using the white light interferometer (WYKO) to characterise the created features. In this case only the nanosecond pulsed laser has been used. Figure 6.13 displays an example of the created surface below.

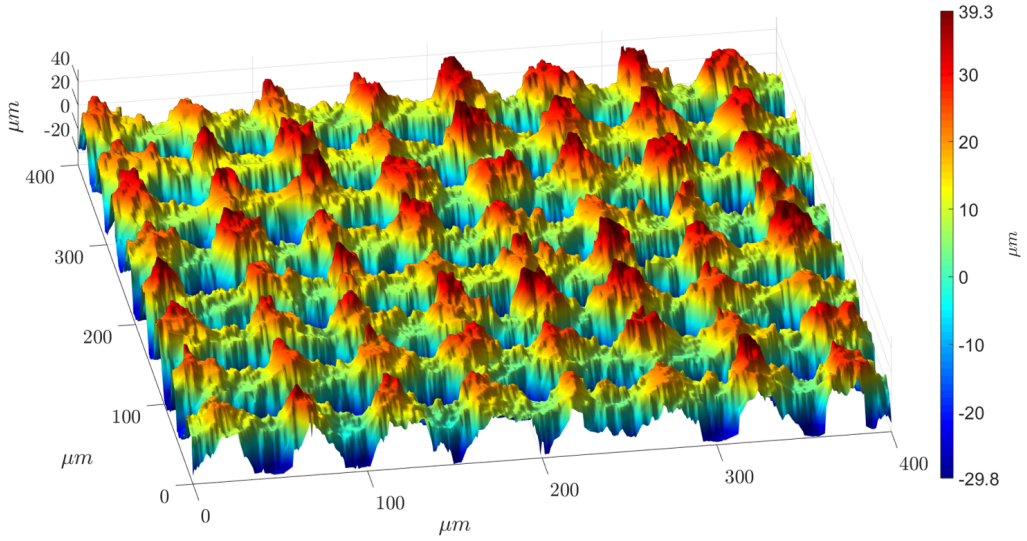

Figure 6.13: *Laser textured surfaces on* ***unpolished as-received*** *Ti-6Al-4V, the micro-structure is created with nanosecond pulsed laser 7.09 J/cm^2 fluence, 130 ns pulse duration, 30 kHz of pulse frequency, 132 mm/s of scanning speed.*

Figure 6.13 shows the surface micro-structure created with a pulse duration of 130 ns. It can be seen that a micro-pillar topography has been generated as before. However, horizontal micro-channels can now be observed on the surface compared to the results in Figure 6.3. This is due to the revised scanning technique and the amount of molten material accumulation in the first step of laser surface texturing. As described in Figure 6.11, the first step in the scanning technique is to created horizontal lines of ablation, this produces molten material accumulation on the edges parallel to the scanning direction.

The second step in the scanning technique creates vertical ablated lines on top of the first created surface structure, thus re-scanning the molten material deposited on the edges of the first micro-structure with the ultimate goal of generating more surface roughness at the right scale.

The main objective of this scanning technique is to mimic the nano-structures created through laser induced periodic surface structures (LIPSS) using the High-Q picosecond laser presented earlier. For this, a high pulse overlap for the ablated channel is required in order to leave molten material behind in each one of the ablated craters. Thus, creating a micro-structure inside of the valleys between the micro-pillars.

For the creation of these types of micro-structures a sensible spot separation is required in order to allow the molten material deposition between the ablated craters. For this technique a constant spot separation of 4 μm was selected in order to allow this molten material deposition. These features can be observed in Figure 6.14.

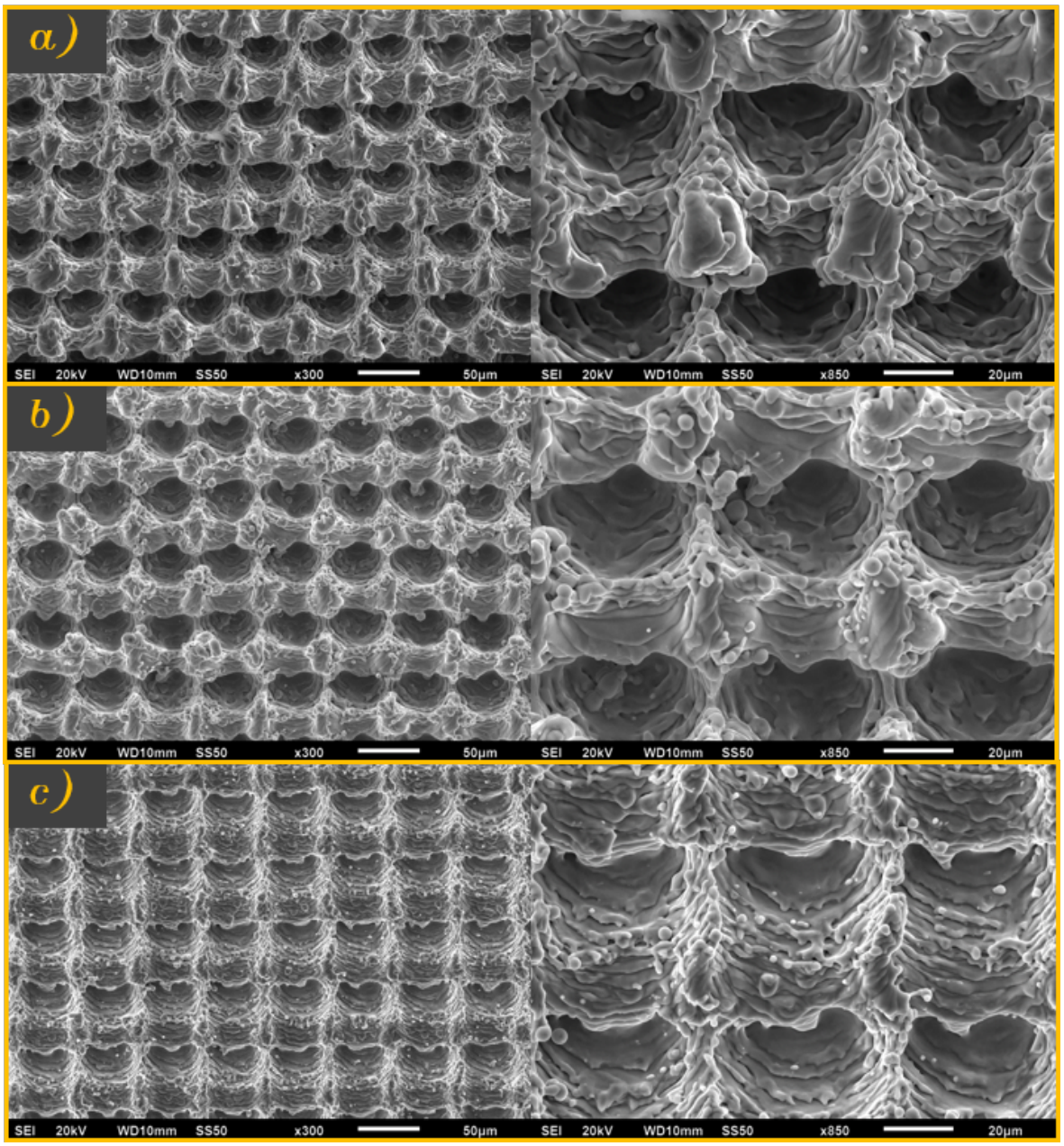

Figure 6.14: *SEM images of laser textured surfaces on* ***unpolished as-received*** *Ti-6Al-4V, with proposed scanning technique, a) 7.94 J/cm^2 fluence, 25 kHz pulse repetition and 200 ns pulse duration, b) 7.09 J/cm^2 fluence, 33 kHz pulse repetition and 130 ns pulse duration, c) 5.10 J/cm^2 fluence, 65 kHz pulse repetition and 65 ns pulse duration.*

Figure 6.14 shows the created micro-structures with three different pulse durations, 200 (a), 130 (b) and 65 (c) ns. As can be observed all the surface micro-strucutres show the additional structure between the micro-pillars. However, the quality and shape of the micro-pillars has been affected with the longer pulse duration (200 ns) due to the amount of molten material deposited by each of the pulses.

The amount of molten material produced by a single pulse increases with longer pulse durations as demonstrated in Chapter 4. The pulse duration has an effect on the amount of material removed by ablation as well as the amount of molten material deposited on the surface by the thermal component of the nanosecond laser system. This has effects on the characteristics of the created surfaces as shown in Figure 6.15 below.

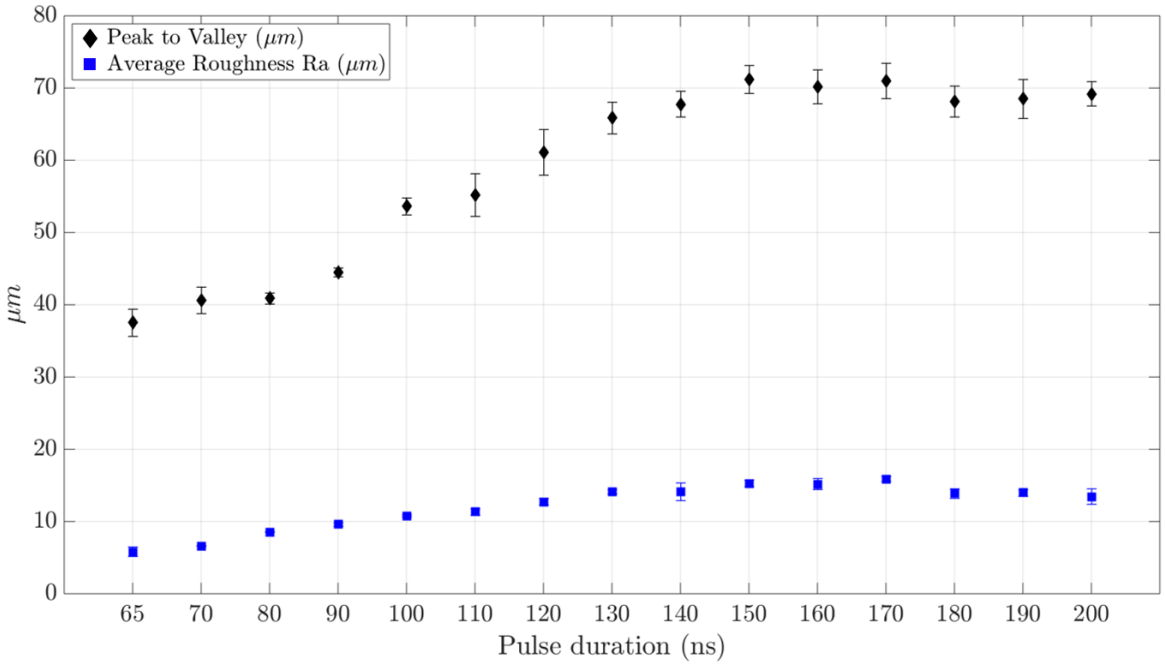

Figure 6.15: *Average Roughness (Ra) and Peak to Valley measurements for surface microstructures created with scanning technique for replacement of hierarchical surface structure with different pulse durations and a calculated fluence to give an ablated crater size* $\approx D_{min}$.

Figure 6.15 shows the average roughness (Ra) and peak to valley measured in three areas of the generated micro-pillar structure. It can be observed that the average roughness (Ra) increases as the pulse duration increases due to the amount of material removed. However, a slight decrease can be observed with pulse durations above 160 ns for both average roughness and peak to valley distance. This is likely due to the increase of molten material deposition with longer pulse durations and the way this material has deposited on top of the surface. Figure 6.14 (a) shows how the molten material appears to have been trapped inside of the created microstructure. These type of effects were observed in Chapter 4 of this thesis.

Despite the effects of molten material deposition with long pulse durations, the surface still remains in a micro-pillar like structure with the additional structures in-between, induced by the molten material deposition itself.

6.5.2 Contact angle

Static contact angle measurements were obtained with the use of the DropShape analysis system for each one of the created micro-structures with different pulse durations in order to characterise the wettability modifications capabilities on unpolished as-received Ti-6Al-4V. These are presented in Figure 6.16 showing the static contact angle measurements over 31 days for the surface micro-structures created with different pulse durations and calculated fluence to give an ablated crater $\approx D_{min}$.

It can be seen that the use of this scanning technique on as-received Ti-6Al-4V has shown a significant improvement on the static contact angle for the micro-structures created with different pulse durations. All the surfaces displayed a contact angle superior to 150 ° on day one after laser processing and subsequent thermal post-processing.

A good stabilisation of the static contact angle over time was also achieved maintaining similar level from day one until day 31, indicating that a stable hydrophobicity has been achieved in the structured surface. However, samples with longer pulse durations (180 to 200 ns) showed a slight increased variability for the static contact angle measurements over time. This is likely due to the shape of the surface structure and the high amount of molten material deposited on the surface creating an uneven pattern on the micro-pillars shape as shown in Figure 6.14.

It is important to mention that all of the samples displayed a static contact angle of around 160 °. This is clearly in the hydrophobic regime of the surface, however, measurements of contact angle hysteresis (CAH) and sliding angle (Figure 6.17) demonstrated that even when the static contact angle is in the super-hydrophobic regime, the liquid droplet cannot be easily removed from the surface by tilting of the sample.

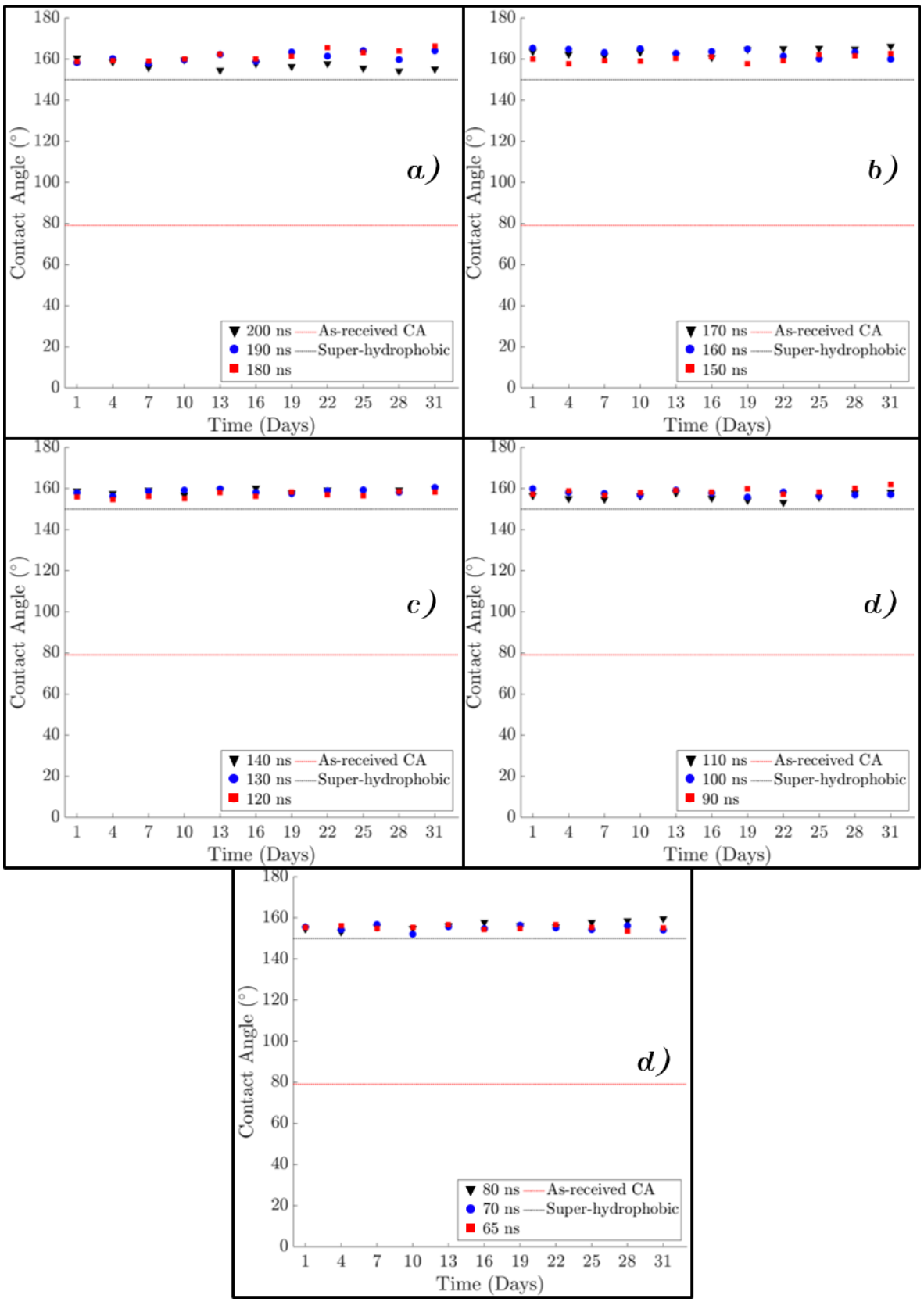

Figure 6.16: *Static contact angle measurements for surface micro-structures created with scanning technique for replacement of hierarchical surface structure with different pulse durations and calculated fluence for ablated crater size ≈ D_{min}., a) 180 to 200 ns pulse duration, b) 150 to 170 ns pulse duration, c) 120 to 140 ns pulse duration, d) 90 to 110 ns pulse duration, and e) 65 to 80 ns pulse duration.*

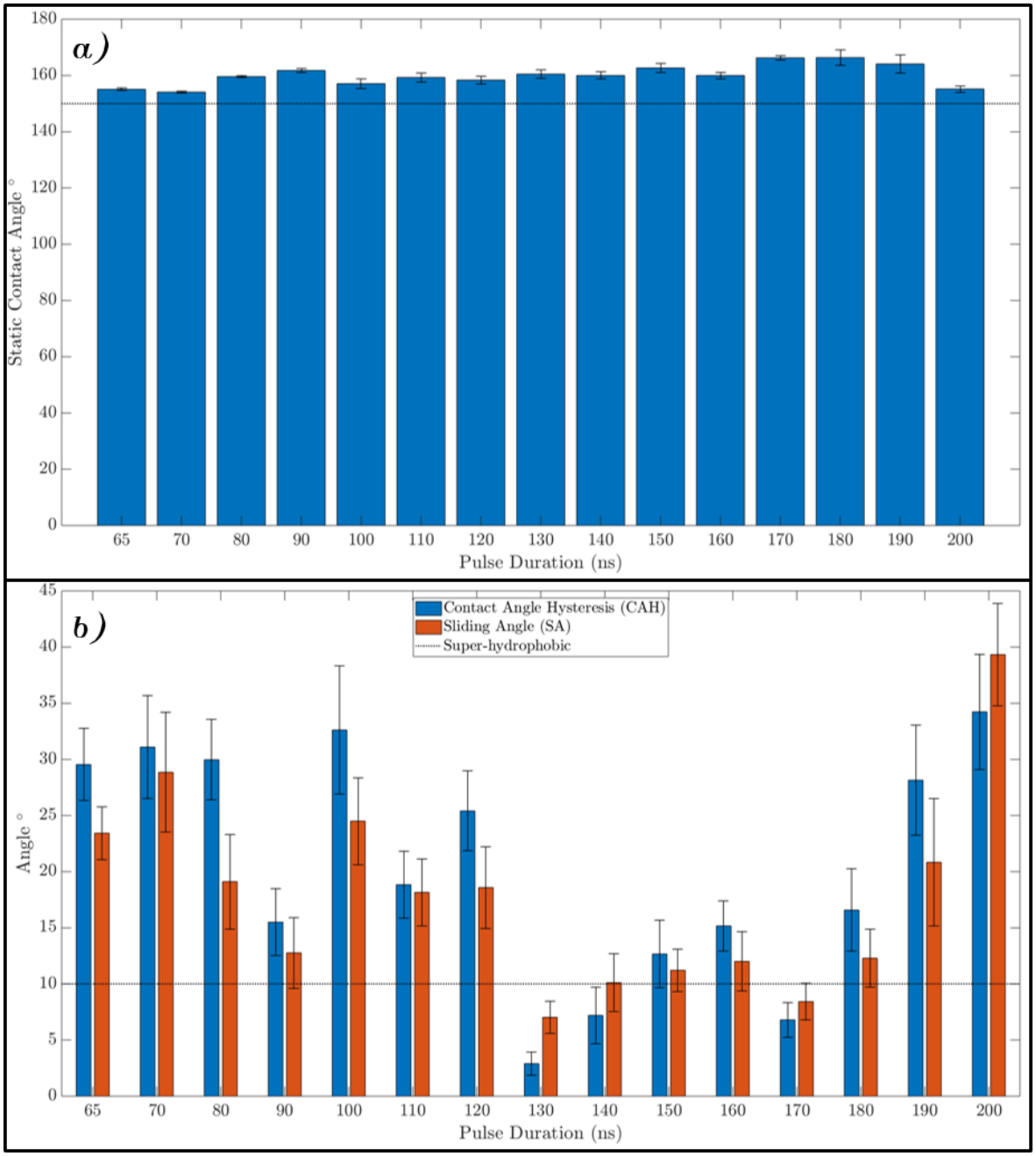

Figure 6.17: *a) Static Contact Angle measured at day number 31 for surface micro-structures created with scanning technique for replacement of hierarchical surface structure with different pulse durations and calculated fluence for ablated crater size ≈ D_{min}., b) Contact angle hysteresis (CAH) and Sliding Angle (SA) measured using tilting method for the characterisation of the hydrophobicity of created micro-structures with different pulse durations at day number 31. The dotted line indicates the required angle for super-hydrophobic behaviour.*

As can be observed from Figures 6.16 and 6.17(a), a high static contact angle does not necessary mean a super-hydrophobic state of the surface. Figure 6.17(b) shows how the sliding angle(SA) and contact angle hysteresis(CAH) are closely related to each other.

A small contact angle hysteresis(CAH) means that the interaction between the liquid droplet and the surface follows the Cassie-Baxter model where the liquid only touches the micro-pillars on the surface creating pockets air within the rest of the surface structure, thus reducing the sliding angle(SA).

However with a high sliding angle the liquid droplet is likely touching the inside of the valleys of the created micro-structure, however due to the micro-dimples created inside of these valleys, the static contact angle is still above 150 ° and the liquid droplet is able to be removed with high angle of tilt.

Small sliding angle(SA) and contact angle hysteresis (CAH), below 10°, creates a highly super-hydrophobic surface capable of repelling the liquid droplet at small tilt angles, as observed in Figure 6.18 below.

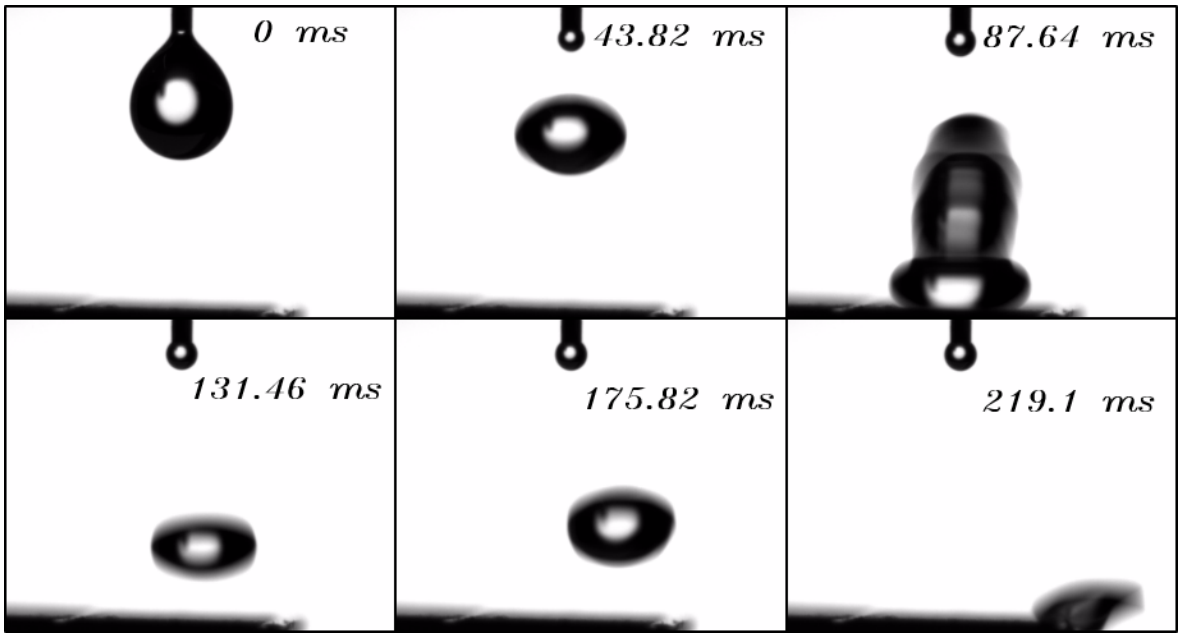

Figure 6.18: *Super-hydrophobic effect of micro-structure created with alternative enhanced single laser technique with 170 ns pulse duration, 7.62 J/cm^2 fluence for ablated crater size $\approx D_{min}$, 28 kHz pulse repetition frequency and 112 mm/s of scanning speed.*

The implementation of the alternative enhanced single laser technique has proven capable of producing super-hydrophobic surfaces with a wide range of pulse durations. With this technique the use of ultra-short pulsed lasers for the creation of super-hydrophobic surfaces on titanium alloy can be replaced with a robust state of the art nanosecond pulsed fibre laser.

6.6 Summary

The use of two laser systems in order to create a hierarchical surface structure has shown important potential benefits for the creation of stable super-hydrophobic surfaces on Ti-6Al-4V. The first study showed how a micro-structure created with a nanosecond pulsed laser can be modified with a secondary laser processing step using a picosecond pulsed laser for the creation of nano-structures on top. These nano-structures (LIPSS) have shown to be beneficial for the contact angle development and the increased hydrophobicity of the hierarchical structure created.

XPS analysis of the samples revealed a modification in the surface chemical composition due to the secondary laser processing. Carbon content (C 1s) is diminished with this secondary laser processing as the Oxygen content (O 1s) is increased, likely increasing the oxidation elements on the surface of the material and thus the hydrophobicity of the created hierarchical surface structure.

However, the use of both laser systems increases the complexity and cost of operation for the creation of such surfaces. Picosecond pulsed lasers tend to be used for research environments due to the high equipment complexity and reduced manufacturing throughput as described in this chapter.

In order to avoid the use of two laser systems, a scanning technique was proposed for the creation of a similar surface structure with the use of only the nanosecond pulsed fibre laser, making use of the thermal component and molten material deposition for mimicking a hierarchical surface structure.

The use of this alternative enhanced scanning technique showed excellent results on the static contact angle measurements for surface structures created within a pulse duration range between 65 and 200 ns. Ablated crater size estimations and pulse duration was taken into account for the parameters selection and the creation of such surfaces.

Capabilities for creating super-hydrophobic surfaces with different pulse durations was also explored. The use of this alternative single laser scanning technique to replace the hierarchical surface structure did show benefits for the static contact angle but to limitations on the structure itself due to the molten material accumulation, especially with longer laser pulses (above 180 ns).

Capabilities for creating stable super-hydrophobic surfaces with the use of a robust state of the art nanosecond pulsed fibre laser has been demonstrated for the manufacturing of such surfaces even on unpolished as-received substrates.

Chapter 7

Discussion

7.1 Chapter 4 Nanosecond pulsed laser ablation of Ti-6Al-4V

Chapter 4 presented the analysis of single pulse ablated craters on Ti-6Al-4V using the nanosecond pulsed fibre laser with different pulse durations and E_{Pulse}. The ablation threshold for pulse duration between 65 and 200 ns on polished and unpolished as-received titanium alloy(Ti-6Al-4V) was carried out in order to identify the required E_{Pulse} for removing material from the surface through the ablation process. The calculated values of the ablation threshold with a single pulse ablation were calculated within a ranges shown in table 7.1 below.

Table 7.1: *Static contact angle measurements after 31 days on Ti-6Al-4V surface structured with nanosecond pulsed laser and picosecond pulsed laser*

Material	**Required Peak Fluence for ablation**	
	65 ns	**200 ns**
Polished Ti-6Al-4V	$5.34 \pm 0.05\ J/cm^2$	$10.25 \pm 0.09\ J/cm^2$
As-received Ti-6Al-4V	$4.53 \pm 0.06\ J/cm^2$	$10.42 \pm 0.15\ J/cm^2$

Table 7.1 shows minimum laser peak fluence required ablation initiation of the material. These values serves as the basis for the energy selection for laser surface texturing with the SPI G4 system with different pulse durations.

At the same time, the calculation the ablation tendencies serves as guidance for predicting the ablated crater size with a given E_{Pulse}. Several previous investigations have used the same calculation method for the ablation threshold and therefore providing reliable results for the ablated crater sizes[39, 46, 145–147]. As can be seen from the values presented in Table 7.1, the ablation threshold is reduced as the pulse duration is reduced, this is likely due to the temporal shape characteristics of the SPI G4 system, as discussed in Chapter 4 section 4.3.1 of this thesis.

After the ablation threshold calculation, the surface topography analysis of single pulse ablation was carried out in order to characterise the amount of material removed with pulse durations in the range of 65 to 200 ns. Through this analysis a window of depth of ablation per single pulse of $0.84 \pm 0.11\,\mu m$ for 65 ns pulse duration to $1.79 \pm 0.07\,\mu m$ for 200 ns pulse duration is defined when E_{Pulse} is calculated for an ablated crater size $\approx D_{min}$. A similar behaviour as the ablation threshold is observed in the measurements of depth of ablation per single pulse. The ablated depth is reduced as the pulse duration is reduced, this is due to the same effect of the pulse temporal shape as a fast ascending and descending peak of the power followed by a long low-power tail of longer pulse durations, between 100 and 200 ns, is beneficial for an increased material removal as proposed by *Ali Gokhan Demir et al* (2015)[127].

Multi-pulse ablated craters are measured in order to verify the capabilities of the system to create craters in increased depth of ablation through this method. Measurements of the ablated depth with multiple pulses indicated that the depth of ablation per pulse remains virtually the same from 1 to 32 pulses. This is an advantage in comparison with multi-pulse ablation depth reached with ultra-short pulsed lasers, as observed by *B. Zheng et al*(2014) where a depth of ablation on Ti-6Al-4V of $\approx 25\,\mu m$ is achieved with 2000 pulses by a ultra-short picosecond laser[146]. In comparison the same depth of ablation is achieved with just 16 pulses with the SPI G4 system using a E_{Pulse} calculated for a crater size $\approx D_{min}$ and 140 ns of pulse duration.

However, the increase in the number of pulses for a single spot ablation increases the amount of molten material deposited on the surface. This increase follows the same behaviour than the ablation threshold and depth of ablation per pulse and it can be explained by same previous reason, the temporal shape of the pulse. As presented on Chapter 2 section 2.3.1 "Laser ablation", the ablation with pulsed lasers working in the nanosecond regime induce a thermal component in the surface of the material. This effect is likely magnified by long low-power tail of the temporal shape with long pulse durations(between 100 and 200 ns).This effect explains the increase on molten material deposition with long pulse durations as observed in Figure 7.1.

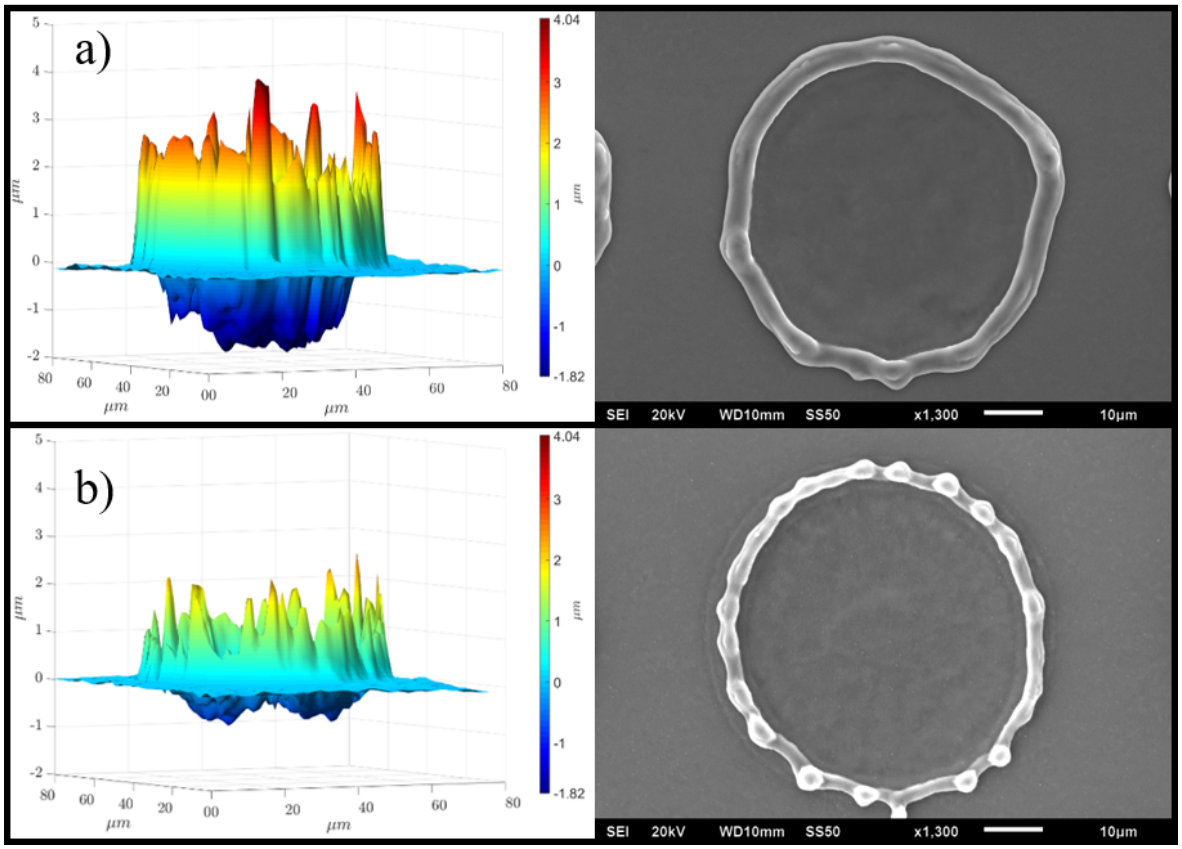

Figure 7.1: *3D representation and SEM image of ablated crater and molten material with a single pulse of the nanosecond pulsed laser on polished Ti-6Al-4VLaser textured surfaces on Ti-6Al-4V, a) 200 ns pulse duration* $E_{Pulse} \approx 148\mu J$*, b) 65 ns pulse duration* $E_{Pulse} \approx 113\mu J$*.*

Figure 7.1 highlights the effects of reducing the pulse duration of the SPI G4 system in the ablation crater and molten material deposition as previously discussed. The scrutiny of these effects will help for the correct analysis of the micro-structures created in Chapters 5 and 6.

7.2 Chapter 5 Surface structuring for wettability modification

The wettability behaviour exhibited by the preliminary scanning technique shows a clear benefit with the thermal post-processing right after the laser surface texturing process. Static contact angle of the samples with the thermal post-processing show a clear improvement over the measurements taken of the samples with laser surface texturing but no thermal post-processing. Previous investigation have demonstrated that the wettability behaviour of a metallic surface processed with a laser changes over time and it is attributed to the change in the oxidation state of the surface[89–93]. In this case the use of the thermal post-processing increases the static contact angle since the first day after the laser surface texturing.

However, the oxidation state of the surface is just one of the required parameters for the creation of a super-hydrophobic state on a metallic surface. The second parameter is an adequate surface micro-structure, for this the analysis of the preliminary scanning technique shows a clear difference in static contact angle measurements with different hatch distance(H.D.) as shown in Figure 7.2 below.

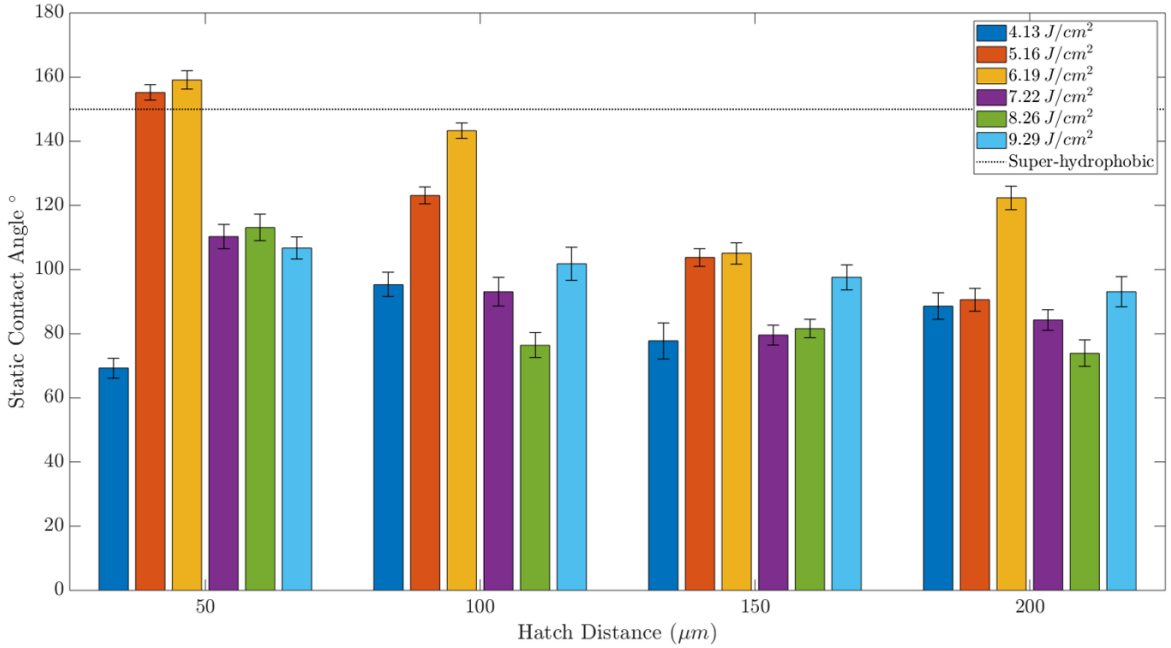

Figure 7.2: *Hatch distance vs static contact angle values after 31 days for squared-grid shaped nanosecond laser structured surface on Ti-6Al-4V,* ***with thermal post-processing****, for six different laser fluence.*

Figure 7.2 shows the static contact angle measurements at day 31 after the laser surface texturing and thermal post-processing. As can be observed from the graph, the laser fluence and hatch distance(H.D.) have an effect on the wettability behaviour of the surface. In this case the only surface structures capable of displaying a super-hydrophobic behaviour(above 150°), are the ones processed with 5.16 J/cm^2 and 6.19 J/cm^2 with a H.D. of 50 μm. These two surfaces display a clearly defined micro-pillar like structure. This type of micro-structure has been observed in nature and proven beneficial for the super-hydrophobic behaviour of a surface[73]. However, as the laser fluence is increased above 6.19 J/cm^2, the static contact angle is reduced again, this is due to the increase on the ablated crater size as mentioned on Chapter 4 of this thesis as the ablated crater size is increased above the H.D. and therefore having an impact of the generation of suitable micro-pillars. Opposite effect is observed with a laser fluence of 4.13 J/cm^2 due to a calculated crater size of $37.53 \pm 0.14\,\mu m$ being $\approx 12\,\mu m$ inferior to the H.D. These effect are highlighted on Figure 5.6 in Chapter 5 of this thesis.

The increase in the H.D. above 50 μm has a detrimental effect on the wettability behaviour, this is due to the increase of untreated areas in the surface of the material and the limited height of molten material features. This type of surface structure has been previously observed to create super-hydrophobic surfaces, however, a molten material height of $\approx 40\mu m$ for H.D. of $=> 100\mu m$ with virtually no ablated channel is developed in the surface of stainless steel by *Ngo C et al*(2017) achieving static contact angles $> 160°$[120].

In comparison, the maximum molten material height achieved by the presented surfaces reaches a maximum of $10.59 \pm 3.29\,\mu m$ and ablated channel width of $63.36 \pm 3.27\,\mu m$ on Ti-6Al-4V, clearly limiting the capabilities to achieve a super-hydrophobic state of the surface with this type of micro-structures according to *Marmur*(2004) who explains how an increase on the surface features is required when the distance between such features is increased for a super-hydrophobic effect[69].

Due to these limitations, an improved laser scanning technique is presented for the creation of micro-pillar like surface structures with a low Pulse Overlap (P.O.) and 10 overscans. The low pulse overlap is designed to provide small untreated areas between the ablated craters for the creation of micro-pillars. This basically creates a surface with two methods, ablation to remove material from the surface and molten material deposition on the untreated surface areas for the creation of micro-pillars.

The creation of micro-pillar like surface structure is carried out with different pulse durations in a range of 90 to 200 ns and 130 μJ of E_{Pulse} in order to compare the effects of pulse duration on the created surface features and wettability behaviour. As shown in Figure 5.20(a) in Chapter 5 of this thesis, most of the created surface micro-structures display a static contact angle superior to 150° with the exception of surfaces created with 200 and 190 ns of pulse duration. An analysis of the surface topography(Figure 7.3) shows a main difference on the micro-structure, with long pulse duration such as 190 ns the micro-structure created is similar to a micro-channel like structure(Figure 7.3a), different to the clear micro-pillar like surface structure(Figure 7.3b).

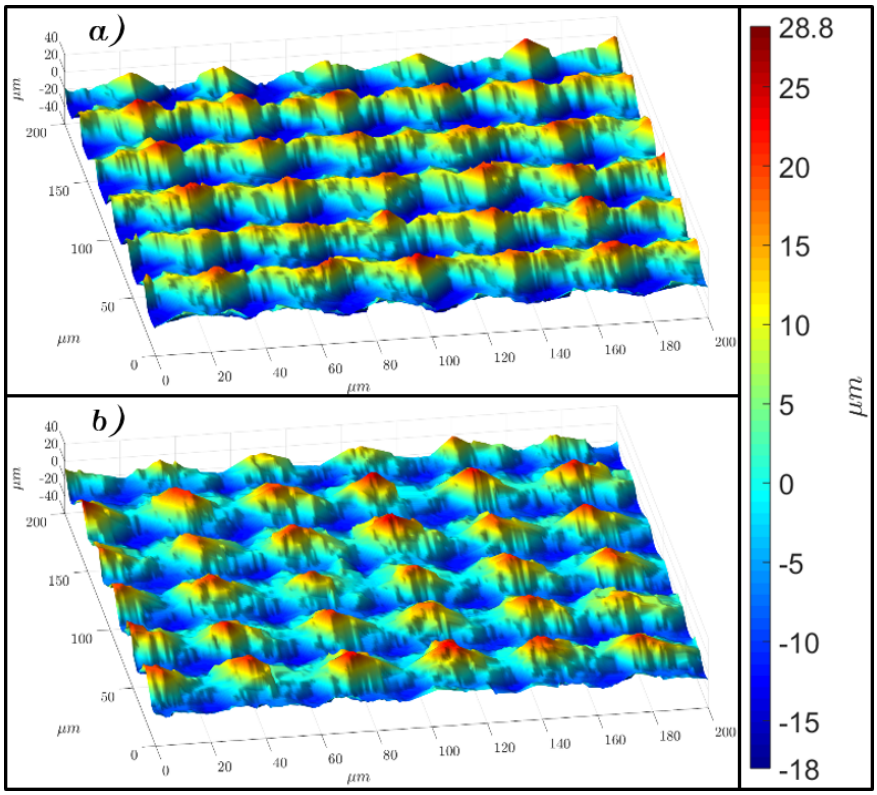

Figure 7.3: *Laser textured surfaces on Ti-6Al-4V with 6.71 J/cm^2 low pulse overlap, 10 overscans and different pulse duration, a) 190 ns pulse duration and b) 110 ns pulse duration.*

Figure 7.3 shows the main difference between the micro-channel like structure created with 190 ns of pulse duration and the micro-pillar like structure with 110 ns of pulse duration. Differences between the ablated crater size with the same laser fluence(6.71 J/cm^2) and different pulse durations can be observed in Figure 5.22 in Chapter 5 of this thesis. This disparity partly explains the difference in surface structures as the H.D. and the distance between pulses remains constant(36 μm). The quality mode of the SPI G4 laser ($M^2 = 1.83$) helps to explain these effects due to the elliptical shape tendency particularly with laser fluence $< D_{min}$, which is the case with 6.71 J/cm^2 for the long pulse durations. Surface features became more adequate as the pulse duration decreases due to the increase in the ablated crater size with smaller pulse durations. However, the reduction of pulse duration has the detrimental effect of reducing the depth of ablation per pulse from $1.36 \pm 0.03\,\mu m$ of for 200 ns to $0.86 \pm 0.26\,\mu m$ for a 90 ns of pulse duration.

Due to the reduction of ablated depth and the increase of ablated crater size per pulse as the pulse duration is reduced, a balance between both can be found at surface structures created with 140 ns. This surface displays a static contact angle of $\approx 162°$ with Contact Angle Hysteresis (CAH) of $\approx 6°$ and Sliding Angle (SA) of $\approx 8°$ effectively presenting a super-hydrophobic behaviour. Similar micro-pillar like surface structures have been investigated specially with ultra-shorty pulsed lasers reaching static contact angles of 160° after 12 days with a femtosecond pulsed laser[90] and 151° after 4 days with a picosecond laser[92]. It is important to notice that the static contact angle of these investigations is reached without the use of a thermal post-processing.

The surface chemistry analysis shows that the use of a thermal post-processing is beneficial for the stabilisation of the oxidation layer increasing the hydrophobic nature of the surface due to higher accumulation of TiO_2 in comparison with samples without thermal post-processing. The increase and stabilisation of the oxides on the surface has been proven to be beneficial for the hydrophobicity of metallic surfaces patterned with laser surface texturing[90, 91, 120].

7.3 Chapter 6 Hierarchical surface structures

Super-hydrophobic surfaces generally present a hierarchical surface structure(nano and micro scale features). The creation of a hierarchical surface structure is produced with the nanosecond pulsed fibre laser for the micro-pillar like structure and followed by the picosecond laser processing to induce LIPSS(Laser Induced Periodic Surface Structures) on top of the micro-pillars. The addition of the nano-structure proves to be beneficial for the wettability behaviour of the surface as shown in Table 6.4 in Chapter 6 of this thesis. Static contact angle is improved $\approx 10°$(from 157.90° to 167.60°), and values for contact angle hysteresis(CAH) and sliding angle(SA) are reduced $\approx 5°$ (from 10.34° to 5.18°) with the addition of the LIPSS on top of the micro-pillar like structure for samples with thermal post-processing after both laser surface texturing techniques.

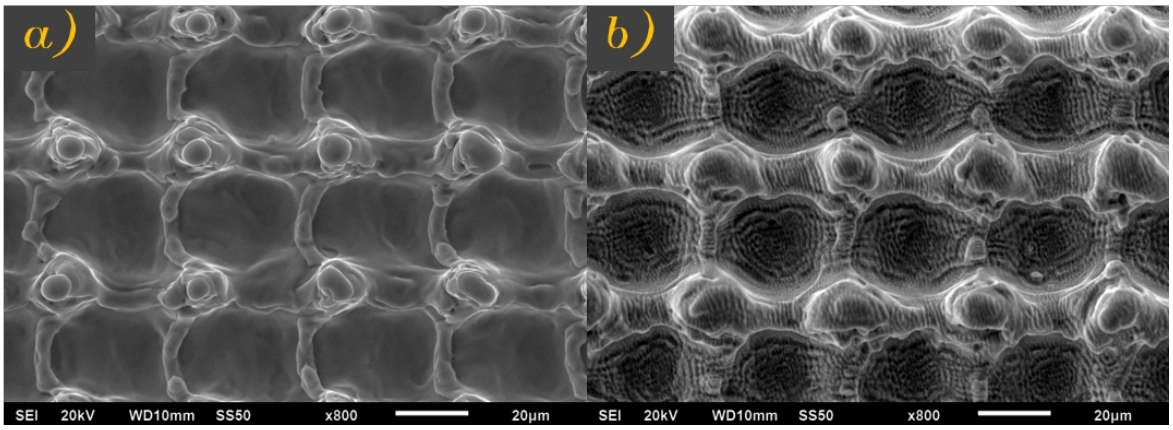

Figure 7.4: *SEM images of surface structures created with nanosecond and picosecond pulsed laser a) SEM image of micro-pillar like surface micro-structure with nanosecond pulsed laser, b) SEM image of hierarchical surface structure created with nanosecond and picosecond pulsed laser.*

Figure 7.4 (b) shows the hierarchical surface structure processed with both laser systems. As can be observed there is no difference in the micro pillars and the only difference is the ripple-like surface observed in the hierarchical structure in comparison with the lack of this effect observed in Figure 7.4 (a).

The use of multiple lasers for inducing two types of surface structures on Ti-6Al-4V has been recently observed in a previous investigation were a square-grid micro-structure is created with a nanosecond pulsed laser and LIPSS are induced on top of this structure with a femtosecond pulsed laser. The same effect is observed as the SCA is improved from 150° for a purely micro-structure to 160° for the hierarchical surface structure one month after laser processing[140].

Chemical analysis of the hierarchical surface structures presented in Chapter 6 shows how the thermal post-processing is beneficial for the wettability behaviour due to the oxidation state of the surface structure. The thermal post-processing increases the amount Oxygen (O 1s) in the surface structure thus increasing the oxidation of the material. The highest accumulation Oxygen (O 1s) accumulation is observed in the hierarchical surface structure likely due to the two laser surface texturing processes to which is subjected. This effect is corroborated by the results presented by *Huerta D et al*(2019) were the increase in oxidation increases the static contact angle of the samples with hierarchical surface structures[140].

With the improved results on wettability behaviour observed by the hierarchical structures particular interest is taken into the possibility to emulate the nanoscale features(LIPSS) with the nanosecond pulsed fibre laser. A feature observed in the micro-channels created with the squared-grid surface structures shown in Chapter 5 of this thesis seems like an appropriate candidate for the emulation of LIPSS, as shown in Figure 7.5.

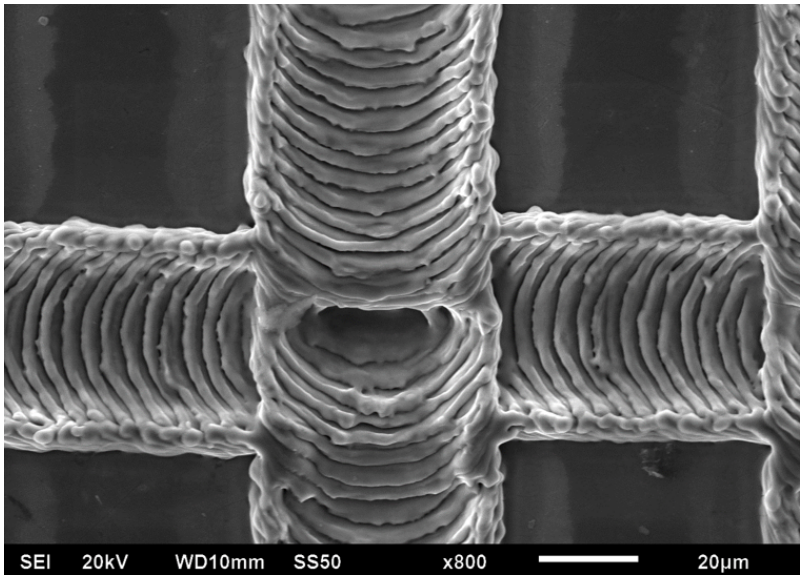

Figure 7.5: *SEM image of ablated micro-channel with* 4.13 J/cm^2 *and 65 ns of pulse duration.*

As can be observed in Figure 7.5 the high pulse overlap for the ablation of the micro channel leaves a trail of micro-dimples in the ablated channel. This is due to the molten material left behind by the thermal component of each pulse generated by the nanosecond pulsed laser as previously discussed in Chapter 4 of this thesis. The generation of these micro-dimples like features are taken into the consideration for the development of an alternative scanning technique.

The alternative enhanced single laser technique is based on the square-grid technique generated with high Pulse Overlap (P.O.) in order to create micro-dimples with a separation of $\approx 4\ \mu m$ to enhance the surface roughness, particularly between the created micro-pillars. In order to demonstrate the manufacturing capabilities this alternative technique is created on unpolished as-received Ti-6Al-4V. The calculated ablation threshold values for as-received Ti-6Al-4V presented in Chapter 4 are used for the calculation of the required E_{Pulse} for and ablated crater size $\approx D_{min}$ in order to create a near circular ablated crater.

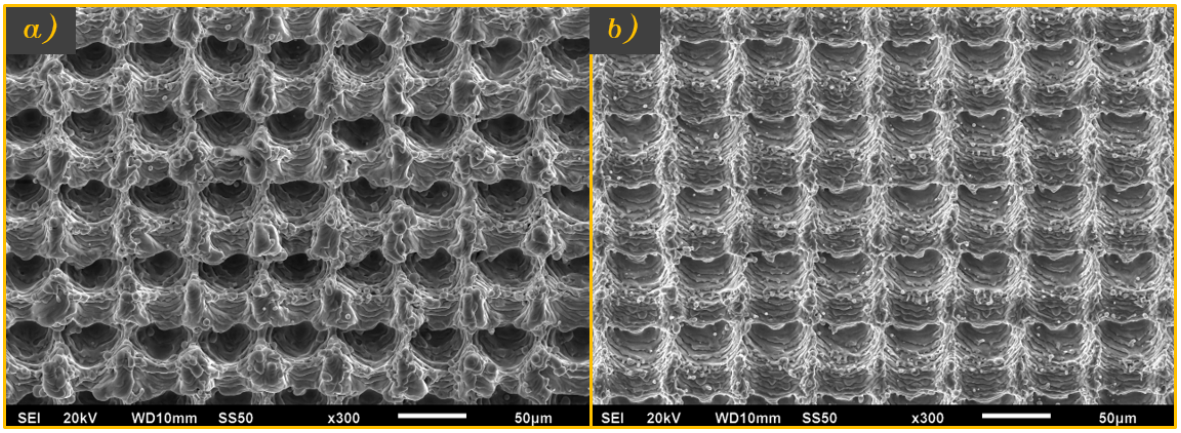

Figure 7.6: *SEM images of laser textured surfaces with proposed scanning technique on unpolished as-received Ti-6Al-4V with different laser fluence and pulse durations a)* $7.94 J/cm^2$ *and 200 ns of pulse duration, b)* $5.10\ J/cm^2$ *and 65 ns of pulse duration.*

Figure 7.6 (a) shows features created with 200 ns pulse duration, as can be observed the amount of molten material accumulated in the micro-pillars is noticeable due to the long pulse duration and the effect of the temporal pulse shape of the SPI G4 system with long pulses as discussed in detail in Chapter 4 of this thesis. Nonetheless, the general micro-pillar like surface structure is still created and notable micro-dimples are created between the micro-pillar features.

Figure 7.6 (b) displays the same scanning technique using a 65 ns pulse duration, as the pulse duration decreases the amount of molten material and depth of ablation decreases and this is noticeable between 65 (b) and 200 ns (a). The main micro-pillar surface structure remains the same, however, the features sizes are reduced due to the reducing molten material with shorter pulse duration. As can be observed the distance between the micro-dimples remains virtually the same, instead the thickness of such features is reduced as the molten material left behind by each pulse is reduced. These effects are fully measured in Figure 6.15 in Chapter 6 of this thesis.

Static contact angle measurements of the created samples with thermal post-processing displayed a super-hydrophobic behaviour for all the pulse duration(65 to 200 ns), exhibiting a clear improvement over the previous scanning technique(low Pulse Overlap) for the creation of micro-pillars shown in Chapter 5 of this thesis.

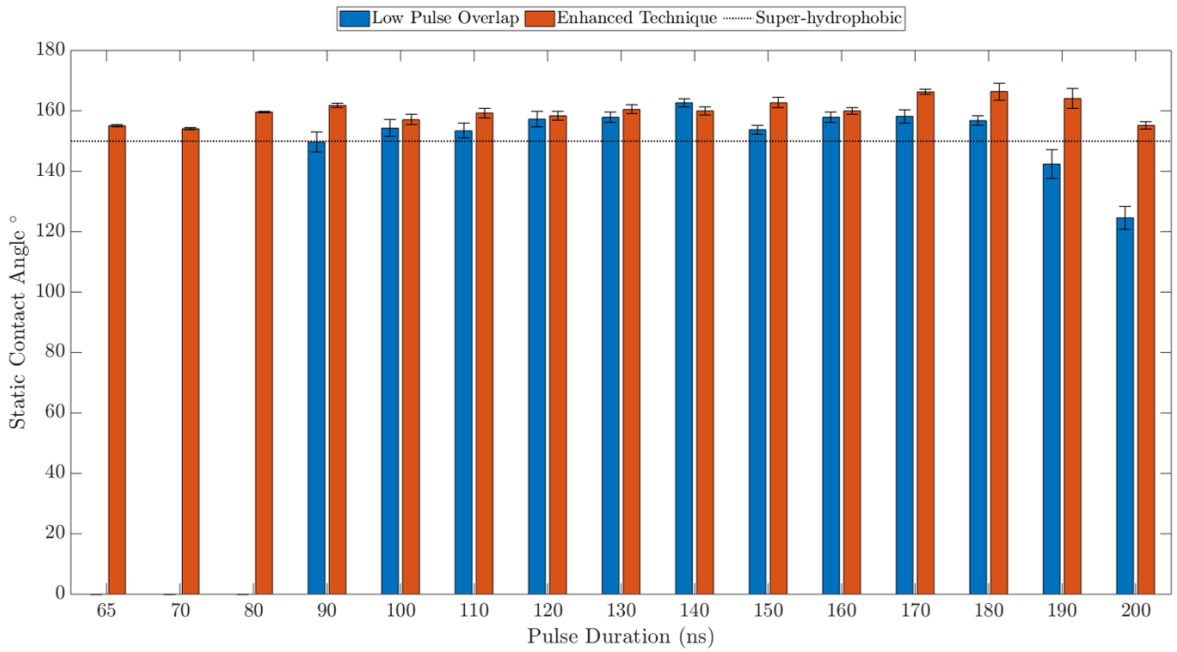

Figure 7.7: *Static contact angle measurements comparison at day 31 for micro-pillar surface structures created with two different scanning techniques, Blue series represents measurements for Low Pulse Overlap technique and Red series represents measurements for Enhanced Technique.*

Figure 7.7 shows a static contact angle comparison between samples processed with the technique discussed in the second part of Chapter 5 (Low Pulse Overlap) and the enhanced technique proposed for the micro-dimples production between the micro-pillars features. As can be observed, the static contact angle is generally improved with the micro-dimples between the micro-pillars features. Contact angle hysteresis (CAH) and Sliding Angle (SA) are also as these values are decreased to values of $\approx 7°$ of SA and $\approx 3°$ of CAH for the surface structure processed with 130 ns of pulse duration and 7.09 J/cm^2 of laser fluence.

Nonetheless, the creation of the surface structure with micro-dimples implies a higher molten material accumulation within the whole surface. Due to this a more fine and careful balance between the required laser fluence and pulse overlap should be investigated to improve the development super-hydrophobic surfaces.

Chapter 8

Conclusions and future work

8.1 Conclusions

This thesis carried out the surface structuring process of Ti-6Al-4V using a robust state of art nanosecond pulsed fibre laser for the modification of the wettability properties. Investigations into the effects induced on the titanium alloy surface through the laser ablation process were carried out using different pulse durations in a range of 65 to 200 ns on polished and unpolished as-received Ti-6Al-4V. Super-hydrophobic surface structures with high water repellence behaviour were achieved. The key finding of this research are presented below.

Analysis of the SPI G4 nanosecond pulsed fibre laser capabilities for the ablation of Ti-6Al-4V was explored in Chapter 4 of this thesis. Single pulse ablation threshold values were calculated for polished and unpolished as-received samples with a pulse duration range within 65 to 200 ns. The obtained results provided windows of parameters of 5.34 $J/cm^2 \pm 0.05$ for 65 ns pulse duration to 10.25 $J/cm^2 \pm 0.09$ for 200 ns pulse duration on polished Ti-6Al-4V, and 4.53 $J/cm^2 \pm 0.06$ for 65 ns pulse duration to 10.41 $J/cm^2 \pm 0.0.15$ for 200 ns pulse duration on unpolished as-received Ti-6Al-4V. The calculation of the ablation threshold gave trending equations for calculating the ablated crater size at a give E_{Pulse} and pulse duration.

Rate of single pulse material removal was quantified through depth of ablation with different pulse durations providing a range of $0.84 \pm 0.11\,\mu m$, for 65 ns pulse duration, to $1.77 \pm 0.06\,\mu m$, for 200 ns pulse duration, using a calculated $E_{Pulse} \approx D_{min}$ for a proper comparison. The correlation between decrease in the amount of material removed per pulse and the decrease in pulse duration was linked to the temporal pulse shape of the different pulse durations of the SPI G4 system, which shows a rapid energy rise followed by a low energy long coupling time increasing the heating of the material and thus the depth of ablation per single pulse, especially when pulse duration is above 100 ns. Nevertheless, when the pulse duration is below 100 ns, this low energy coupling time is significantly reduced and thus reducing the depth of ablation per single pulse.

Molten material accumulation as observed to follow the same trend as the depth of ablation per single pulse with different pulse durations, increasing the amount of molten material as the pulse duration is increased.

Two main scanning techniques were investigated for the creation of super-hydrophobic surface in Chapter 5, a square-grid shape and a low pulse overlap shape technique. From the square-grid shape technique a small hatch distance(H.D.) of 50 μm as concluded to achieve a super-hydrophobic behaviour achieving a static contact angle of $\approx 159^{\circ}$ and a contact angle hysteresis of $\approx 16^{\circ}$ when samples are put through a thermal post-processing after the laser surface texturing process. Surface topography analysis of this particular micro-structure showed the creation of a micro-pillar like structure due to molten material deposition and the similarity between H.D. and D_{min} and thus displaying a micro-pillar like surface structure which has been previously explored as beneficial for super-hydrophobic behaviour on the nature.

The second scanning technique explored in Chapter 5 is the low ulse overlap shape technique. This technique was developed for the creation of micro-pillar like surface structures with a low Pulse Overlap (P.O.) and 10 overscans.

The improved laser scanning technique was developed for the creation of micro-pillar like surface structures with a low Pulse Overlap (P.O.) and 10 overscans. The low pulse overlap was designed to provide small untreated areas between the ablated craters for the creation of micro-pillars. This basically creates a surface with two methods, ablation to remove material from the surface and molten material deposition for the creation of micro-pillars. Creation of the micro-pillar like surface structure was carried out with different pulse durations within a range of 90 to 200 ns and 130 μJ of E_{Pulse} in order to compare the effects of pulse duration on the micro-structure. Surface structures created with 140 ns displayed a static contact angle of $\approx 162°$ effectively presenting a great super-hydrophobic behaviour with a contact angle hysteresis of $\approx 6°$ and a Sliding Angle (SA) of $\approx 8°$. Surface topography and SEM imaging showed that in order to achieve super-hydrophobic behaviour, a constant and well defined micro-pillar surface structure needs to be produced, in comparison with surfaces created with longer pulse duration(200 ns) that presented a micro-channels like surface which presented static contact angles below the super-hydrophobic behaviour.

Surface chemistry analysis and static contact angle measurements showed that the use of the thermal post-processing is beneficial for the increase and stabilisation of the oxidation state of the material. This oxidation is activated with the laser surface texturing process an is developed over time under ambient air conditions storage. The use of the thermal post-processing has proven helpful for the reduction of the required time and increase of TiO_2 on the structured surface which helps to the hydrophobicity behaviour. It is important to mention that a combination of a suitable micro-structure and the oxides is required for a super-hydrophobic behaviour on the material. Surface structures created with the same scanning technique but no thermal post-processing displayed a hydrophilic behaviour in the first few days after the laser surface texturing process and slowly improving the static contact angle over time without reaching super-hydrophobic levels.

A hierarchical surface micro-structure was created with the use of two laser systems, the nanosecond pulsed fibre laser for the creation of micro-pillars followed by a picosecond laser to induce LIPSS(Laser Induced Periodic Surface Structures) on top of the micro-pillars. The creation of this hierarchical structure proven beneficial for the super-hydrophobic behaviour presenting a static contact angle $\approx 167°$ and contact angle hysteresis $\approx 5°$ when the surface is subjected to a thermal post-processing. The use of LIPSS on the surface structure created nanoscale surface structure covering the entirety of the micro-pillars emulating super-hydrophobic natural surfaces such as the Lotus leaf.

An alternative enhanced single laser technique was carried out with the nanosecond pulsed fibre laser in order to emulate the creation of the nano-structures created with the picosecond laser. This square-grid technique was generated with high Pulse Overlap (P.O.) in order to create micro-dimples with a separation of $\approx 4\ \mu m$ to enhance the surface roughness. This technique proved to be highly successful in the improvement of the static contact angle of surfaces processed with pulse durations in the range of 65 to 200 ns. These surface structures were created on unpolished as-received Ti-6Al-4V in order to demonstrate manufacturing capabilities. This alternative technique proved to create surface structures capable of excellent results on the static contact angle (above 160°) and relatively small contact angle hysteresis $\approx 3°$ and sliding angle $\approx 7°$ for a surface processed with 130 ns of pulse duration and 7.09 J/cm^2 of laser fluence.

It is believed that the novel approach presented in this thesis using a robust state of the art nanosecond pulsed fibre laser can work as a reference for the creation of super-hydrophobic surfaces in industrial mass production environments with a reduced numbers of required tools and the flexibility provided by the fibre laser system.

The manufacturing of suitable super-hydrophobic surfaces can be achieved with the proposed scanning techniques and due to the maintenance free characteristics of the SPI G4 system a cost of £1 per every $10 cm^2$ of processed area can be roughly estimated from the power consumptions characteristics of the laser system including the auxiliary equipment such as computer, controller, galvo-scanning and positioning system.

8.2 Recommendations for future work

The work carried out during this research project shown potential applications for robust state of the art fibre laser systems in the manufacturing industry. In order to increase the viability of the work presented in this thesis on the manufacturing environment, further recommendations are given below.

Due to the operation parameter of the SPI G4 system, the manufacturing speed was governed by the pulse duration selection, defining the pulse frequency and thus, the required scanning speeds. This creates a limitation on the processing speed for big surface areas increasing the required time for the laser surface texturing process and limiting the manufacturing volume capabilities. In order to improve this, a diffractive optical beam splitter can be implemented before the galvo-scanning system producing multiple beams for the laser surface texturing process. This can increase the manufacturing speeds with the correct parameters selection. Multiple beam processing has been proven beneficial with ultra-short pulsed lasers, and the implementation on the nanosecond fibre laser system could improve the processing times allowing a high volume manufacturing system.

As demonstrated during this work, the oxidation state of the surface plays a significant role in the creation of super-hydrophobic surfaces on metallic materials. During this work this was improved with a low-temperature thermal post-processing, however, this required the use of additional equipment and increased the manufacturing time. Although thermal processes are a common practice in the manufacturing industry, especially with metallic alloys, these can also be improved. The nanosecond pulsed

fibre system is capable of providing different thermal processes due to the laser beam irradiation as demonstrated in this work. In this case, an opportunity for emulating the thermal post-processing with the nanosecond pulsed fibre laser instead of using a conventional oven can create a single system manufacturing process. Further investigations are required in order to induce the required oxidation via laser irradiation avoiding melting regions in order to evade the modification of the created micro-pillar structures.

As demonstrated in chapter 6 of this work the creation of nano-structures induced by an ultra-short pulsed laser proven to be beneficial for the development of super-hydrophobic surfaces with small sliding angle (SA) and contact angle hysteresis (CAH). More experiments for the creation of this type of surface structures using a nanosecond pulsed fibre laser could improve the surface texturing technique improving the surface structure proposed in this thesis.

References

1. W. M. Steen, J. Mazumder, *Laser Material Processing* (Springer, London, 2010), p. 558, ISBN: 978-1-84996-061-8.
2. T. Darmanin, F. Guittard, *Journal of Materials Chemistry A* **2**, 16319–16359, ISSN: 2050-7488, (http://dx.doi.org/10.1039/C4TA02071E) (2014).
3. K. Liu, L. Jiang, *Nanoscale* **3**, 825–838, ISSN: 2040-3364, (http://dx.doi.org/10.1039/C0NR00642D) (2011).
4. J. T. Simpson, S. R. Hunter, T. Aytug, *Reports on Progress in Physics* **78**, 086501, ISSN: 0034-4885 1361-6633, (http://dx.doi.org/10.1088/0034-4885/78/8/086501) (2015).
5. X. Yao, Y. Song, L. Jiang, *Advanced Materials* **23**, 719–734, ISSN: 0935-9648, (https://doi.org/10.1002/adma.201002689) (2011).
6. C. Chen *et al.*, *Chemical Communications* **47**, 1336–1338, ISSN: 1359-7345, (http://dx.doi.org/10.1039/C0CC03926H) (2011).
7. M. Zervas, *Laser Systems Europe*, 12+, ISSN: 17590752 (2018).
8. S. Woods, *Laser Technik Journal* **6**, 23–26, ISSN: 1613-7728, (https://doi.org/10.1002/latj.200990070) (2009).
9. J. Jeevahan, M. Chandrasekaran, G. Britto Joseph, R. B. Durairaj, G. Mageshwaran, *Journal of Coatings Technology and Research* **15**, 231–250, ISSN: 19459645 (2018).
10. G. Lütjering, J. C. Williams, *Titanium* (Springer, Berlin, Second, 2007), ISBN: 1619-0181.
11. B. Tan, *Laser Material Processing for Aerospace Applications*, vol. 02.
12. I. Upadhyay, *International Journal of Engineering Development and Research* **4**, 231–241 (2016).
13. I. Hutchings, P. Shipway, in *Tribology (Second Edition)*, ed. by I. Hutchings, P. Shipway (Butterworth-Heinemann, 2017), pp. 237–281, ISBN: 978-0-08-100910-9.
14. A. M. Kovalchenko, *Problems of Friction and Wear* (2011).
15. N. Lin *et al.*, *Materials* **9**, 875–1 (2016).
16. W. Wu, T. Shao, G. Chen, *Science China Technological Sciences* **59**, 183–190, ISSN: 1869-1900, (https://doi.org/10.1007/s11431-015-5920-2) (2016).

17. D. Coblas, A. Fatu, A. Maoui, M. Hajjam, *Proceedings of the Institution of Mechanical Engineers, Part J: Journal of Engineering Tribology* **229** (2014).

18. A. Stankiewicz, in *Nanotechnology in Eco-efficient Construction (Second Edition)*, ed. by F. Pacheco-Torgal *et al.* (Woodhead Publishing, 2019), pp. 303–335, ISBN: 978-0-08-102641-0, (http://www.sciencedirect.com/science/article/pii/B9780081026410000141).

19. J.-H. Park, T. S. Sudarshan, *Chemical Vapor Deposition* (A S M International, Materials Park, UNITED STATES, 2001), ISBN: 9781615032242.

20. C. A. D. Rodriguez, G. Tremiliosi-Filho, in *Encyclopedia of Tribology*, ed. by Q. J. Wang, Y.-W. Chung (Springer US, Boston, MA, 2013), pp. 918–922, ISBN: 978-0-387-92897-5, (https://doi.org/10.1007/978-0-387-92897-5_700).

21. K. Reichelt, X. Jiang, *Thin Solid Films* **191**, 91–126, ISSN: 0040-6090, (http://www.sciencedirect.com/science/article/pii/004060909090277K) (1990).

22. N. C. Raut, K. Al-Shamery, *Journal of Materials Chemistry C* **6**, 1618–1641, ISSN: 2050-7526, (http://dx.doi.org/10.1039/C7TC04804A) (2018).

23. A. Soleimani-Gorgani, in *Printing on Polymers*, ed. by J. Izdebska, S. Thomas (William Andrew Publishing, 2016), pp. 231–246, ISBN: 978-0-323-37468-2, (http://www.sciencedirect.com/science/article/pii/B9780323374682000142).

24. L. Sexton, S. Lavin, G. Byrne, A. Kennedy, *Journal of Materials Processing Technology* **122**, 63–68, ISSN: 0924-0136, (http://www.sciencedirect.com/science/article/pii/S0924013601011219) (2002).

25. L. Quintino, in *Surface Modification by Solid State Processing*, ed. by R. Miranda (Woodhead Publishing, 2014), pp. 1–24, ISBN: 978-0-85709-468-1, (http://www.sciencedirect.com/science/article/pii/B9780857094681500013).

26. N. Bowden, S. Brittain, A. G. Evans, J. W. Hutchinson, G. M. Whitesides, *Nature* **393**, 146–149, ISSN: 1476-4687, (https://doi.org/10.1038/30193) (1998).

27. C. S. Montross, T. Wei, L. Ye, G. Clark, Y.-W. Mai, *International Journal of Fatigue* **24**, 1021–1036, ISSN: 0142-1123, (http://www.sciencedirect.com/science/article/pii/S0142112302000221) (2002).

28. N.-T. Nguyen, in *Micromixers (Second Edition)*, ed. by N.-T. Nguyen (William Andrew Publishing, Oxford, 2012), pp. 113–161, ISBN: 978-1-4377-3520-8, (http://www.sciencedirect.com/science/article/pii/B9781437735208000048).

29. B. Zhang, T. D. Howes, *CIRP Annals* **43**, 305–308, ISSN: 0007-8506 (1994).

30. M. Günay, M. E. Korkmaz, **30**, 111–119 (2017).

31. T. B. Thoe, D. K. Aspinwall, M. L. H. Wise, *International Journal of Machine Tools and Manufacture* **38**, 239–255, ISSN: 0890-6955, (http://www.sciencedirect.com/science/article/pii/S0890695597000369) (1998).

32. V. Jain (2008).

33. Q. J. Wang, A. Greco, K. Ehmann, in *Encyclopedia of Tribology*, ed. by Q. J. Wang, Y.-W. Chung (Springer US, Boston, MA, 2013), pp. 3505–3509, ISBN: 978-0-387-92897-5, (https://doi.org/10.1007/978-0-387-92897-5_11).

34. S. Jithin *et al.*, *Advances in Materials and Processing Technologies* **4**, 466–479, ISSN: 2374-068X, (https://doi.org/10.1080/2374068X.2018.1457350) (2018).

35. N. Parkansky *et al.*, *Surface and Coatings Technology* **205**, 287–293, ISSN: 0257-8972 (2010).

36. R. M. André, M. J. B. Marques, O. Frazão, presented at the Photoptics 2015, ed. by P. Ribeiro, M. Raposo, pp. 3–15, ISBN: 978-3-319-30137-2.

37. L. V. Zhigilei, P. B. S. Kodali, B. J. Garrison, *The Journal of Physical Chemistry B* **102**, 2845–2853, ISSN: 1520-6106, (https://doi.org/10.1021/jp9733781) (1998).

38. C. F. Dowding, J. Lawrence, *Optics and Lasers in Engineering* **47**, 1169–1176, ISSN: 0143-8166, (http://www.sciencedirect.com/science/article/pii/S0143816609001523) (2009).

39. X. Liu, D. Du, G. Mourou, *IEEE Journal of Quantum Electronics* **33**, 1706–1716 (1997).

40. C. Dowding, A. Borman, in *Laser Surface Engineering*, ed. by J. Lawrence, D. G. Waugh (Woodhead Publishing, 2015), pp. 523–546, ISBN: 978-1-78242-074-3.

41. G. W. Yang, *Progress in Materials Science* **52**, 648–698, ISSN: 0079-6425, (http://www.sciencedirect.com/science/article/pii/S0079642506000788) (2007).

42. P. P. Pronko *et al.*, *Optics Communications* **114**, 106–110, ISSN: 0030-4018, (http://www.sciencedirect.com/science/article/pii/003040189400585I) (1995).

43. P. V. Petkov, S. S. Dimov, R. M. Minev, D. T. Pham, *Proceedings of the Institution of Mechanical Engineers, Part B: Journal of Engineering Manufacture* **222**, 35–45, ISSN: 0954-4054, (https://doi.org/10.1243/09544054JEM840) (2008).

44. D. von der Linde, K. Sokolowski-Tinten, *Applied Surface Science* **154-155**, 1–10, ISSN: 0169-4332, (http://www.sciencedirect.com/science/article/pii/S0169433299004407) (2000).

45. D. Breitling, A. Ruf, F. Dausinger, *Fundamental aspects in machining of metals with short and ultrashort laser pulses* (SPIE, 2004), vol. 5339, (https://doi.org/10.1117/12.541434).

46. K.-H. Leitz, B. Redlingshöfer, Y. Reg, A. Otto, M. Schmidt, *Physics Procedia* **12**, 230–238, ISSN: 1875-3892, (http://www.sciencedirect.com/science/article/pii/S1875389211002070) (2011).

47. H. M. van Driel, J. E. Sipe, J. F. Young, *Physical Review Letters* **49**, 1955–1958, (https://link.aps.org/doi/10.1103/PhysRevLett.49.1955) (1982).

48. J. Bonse, J. Krüger, S. Höhm, A. Rosenfeld, *Journal of Laser Applications* **24**, 042006, ISSN: 1042-346X, (https://doi.org/10.2351/1.4712658) (2012).

49. F. Keilmann, Y. H. Bai, *Applied Physics A* **29**, 9–18, ISSN: 1432-0630, (https://doi.org/10.1007/BF00618110) (1982).

50. J. Bonse, S. Höhm, S. V. Kirner, A. Rosenfeld, J. Krüger, *IEEE Journal of Selected Topics in Quantum Electronics* **23**, 1 (2017).

51. A. Borowiec, H. K. Haugen, *Applied Physics Letters* **82**, 4462–4464, ISSN: 0003-6951, (https://doi.org/10.1063/1.1586457) (2003).

52. R. Wagner, J. Gottmann, A. Horn, E. W. Kreutz, *Applied Surface Science* **252**, 8576–8579, ISSN: 0169-4332, (http://www.sciencedirect.com/science/article/pii/S0169433205016417) (2006).

53. M. Huang, F. Zhao, Y. Cheng, N. Xu, Z. Xu, *ACS Nano* **3**, 4062–4070, ISSN: 1936-0851, (https://doi.org/10.1021/nn900654v) (2009).

54. H. J. Eichler, J. Eichler, O. Lux, in *Lasers: Basics, Advances and Applications*, ed. by H. J. Eichler, J. Eichler, O. Lux (Springer International Publishing, Cham, 2018), pp. 51–62, ISBN: 978-3-319-99895-4, (https://doi.org/10.1007/978-3-319-99895-4_3).

55. H. Jeff, in *Understanding Lasers: An Entry-Level Guide* (IEEE, 1994), pp. 60–92, (http://ieeexplore.ieee.org/document/5264117).

56. Web Page, (http://electrons.wikidot.com/principle-and-application-of-laser).

57. Audiovisual Material, 2016.

58. B. S. Nufern, L. Dong, in *Handbook of Solid-State Lasers*, ed. by B. Denker, E. Shklovsky (Woodhead Publishing, 2013), pp. 403–462, ISBN: 978-0-85709-272-4.

59. H. J. Eichler, J. Eichler, O. Lux, in *Lasers: Basics, Advances and Applications*, ed. by H. J. Eichler, J. Eichler, O. Lux (Springer International Publishing, Cham, 2018), pp. 315–334, ISBN: 978-3-319-99895-4, (https://doi.org/10.1007/978-3-319-99895-4_17).

60. W. Koechner, in *Solid-State Laser Engineering*, ed. by W. Koechner (Springer New York, New York, NY, 2006), pp. 534–586, ISBN: 978-0-387-29338-7, (https://doi.org/10.1007/0-387-29338-8_10).

61. E. Tarek, A. Rabah, (https://doi.org/10.5772/52214) (2013).

62. Figure, 2004 2004, (https://spie.org/news/getting-practical).

63. N. S. Kim, *The Review of Laser Engineering* **36**, 1115–1118 (2008).

64. A. Othonos, K. Kalli, D. Pureur, A. Mugnier, in *Wavelength Filters in Fibre Optics*, ed. by H. Venghaus (Springer Berlin Heidelberg, Berlin, Heidelberg, 2006), pp. 189–269, ISBN: 978-3-540-31770-8, (https://doi.org/10.1007/3-540-31770-8_6).

65. G. n. Steinmeyer, *Journal of Optics A: Pure and Applied Optics* **5**, R1–R15, ISSN: 1464-4258, (http://dx.doi.org/10.1088/1464-4258/5/1/201) (2002).

66. P. G. Laboratory, (https://www.plymouthgrating.com/applications/chirped-pulse-amplification-cpa/) (2019).

67. Z. Yoshimitsu, A. Nakajima, T. Watanabe, K. Hashimoto, *Langmuir* **18**, 5818–5822, ISSN: 0743-7463, (https://doi.org/10.1021/la020088p) (2002).

68. M. Nosonovsky, B. Bhushan, *Microsystem Technologies* **11**, 535–549, ISSN: 1432-1858, (https://doi.org/10.1007/s00542-005-0602-9) (2005).

69. A. Marmur, *Langmuir* **20**, 3517–3519, ISSN: 0743-7463, (https://doi.org/10.1021/la036369u) (2004).

70. C. W. Extrand, *Langmuir* **18**, 7991–7999, ISSN: 0743-7463, (https://doi.org/10.1021/la025769z) (2002).

71. B. Bhushan, M. Nosonovsky, in *Encyclopedia of Nanotechnology*, ed. by B. Bhushan (Springer Netherlands, Dordrecht, 2012), pp. 1224–1233, ISBN: 978-90-481-9751-4, (https://doi.org/10.1007/978-90-481-9751-4_158).

72. B. Bhushan, M. Nosonovsky, Y. C. Jung, in *Nanotribology and Nanomechanics: An Introduction*, ed. by B. Bhushan (Springer Berlin Heidelberg, Berlin, Heidelberg, 2008), pp. 995–1072, ISBN: 978-3-540-77608-6, (https://doi.org/10.1007/978-3-540-77608-6_19).

73. K. Koch, B. Bhushan, W. Barthlott, *Progress in Materials Science* **54**, 137–178, ISSN: 0079-6425, (http://www.sciencedirect.com/science/article/pii/S0079642508000704) (2009).

74. W. Li, A. Amirfazli, *Soft Matter* **4**, 462–466, ISSN: 1744-683X, (http://dx.doi.org/10.1039/B715731B) (2008).

75. B. Bhushan, Y. C. Jung, K. Koch, *Philosophical Transactions of the Royal Society A: Mathematical, Physical and Engineering Sciences* **367**, 1631–1672, (https://doi.org/10.1098/rsta.2009.0014) (2009).

76. Y. Y. Yan, N. Gao, W. Barthlott, *Advances in Colloid and Interface Science* **169**, 80–105, ISSN: 0001-8686, (http://www.sciencedirect.com/science/article/pii/S0001868611001552) (2011).

77. R. N. Wenzel, *Industrial and Engineering Chemistry* **28**, 988–994, ISSN: 0019-7866, (https://doi.org/10.1021/ie50320a024) (1936).

78. R. N. Wenzel, *The Journal of Physical and Colloid Chemistry* **53**, 1466–1467, ISSN: 0092-7023, (https://doi.org/10.1021/j150474a015) (1949).

79. A. B. D. Cassie, S. Baxter, *Transactions of the Faraday Society* **40**, 546–551, ISSN: 0014-7672, (http://dx.doi.org/10.1039/TF9444000546) (1944).

80. Y. Gu *et al.*, *Advances in Mechanical Engineering* **9**, 168781401774685 (2017).

81. J. Kim, S. O. Choi, in *Waterproof and Water Repellent Textiles and Clothing*, ed. by J. Williams (Woodhead Publishing, 2018), pp. 267–297, ISBN: 978-0-08-101212-3, (http://www.sciencedirect.com/science/article/pii/B9780081012123000101).

82. A. K. Kota, W. Choi, A. Tuteja, *MRS Bulletin* **38**, 383–390, ISSN: 0883-7694, (https://www.cambridge.org/core/article/superomniphobic-surfaces-design-and-durability/33F1E0343461F69C74E6B85B9E3E349E) (2013).

83. T.-S. Wong, T. Sun, L. Feng, J. Aizenberg, *MRS Bulletin* **38**, 366–371, ISSN: 0883-7694, (https://www.cambridge.org/core/article/interfacial-materials-with-special-wettability/D0E7D6EE5FC8930798D0206C87492E8E) (2013).

84. A. M. Emelyanenko, F. M. Shagieva, A. G. Domantovsky, L. B. Boinovich, *Applied Surface Science* **332**, 513–517, ISSN: 0169-4332, (http://www.sciencedirect.com/science/article/pii/S0169433215002445) (2015).

85. Generic, 2011, (https://liverpool.idm.oclc.org/login?url=https://search.ebscohost.com/login.aspx?direct=true&db=edseee&AN=edseee.6013188&site=eds-live&scope=site).

86. D. H. Kam, S. Bhattacharya, J. Mazumder, *Journal of Micromechanics and Microengineering* **22**, 105019, ISSN: 0960-1317 1361-6439, (http://dx.doi.org/10.1088/0960-1317/22/10/105019) (2012).

87. J. Lu, T. Huang, Z. Liu, X. Zhang, R. Xiao, *Applied Surface Science* **459**, 257–262, ISSN: 0169-4332, (http://www.sciencedirect.com/science/article/pii/S0169433218321238) (2018).

88. H. Exir, A. Weck, *Surface and Coatings Technology* **378**, 124931, ISSN: 0257-8972 (2019).

89. A.-M. Kietzig, S. G. Hatzikiriakos, P. Englezos, *Langmuir* **25**, 4821–4827, ISSN: 0743-7463, (https://doi.org/10.1021/la8037582) (2009).

90. S. S. Sinha, S. Kedia, D. Singh, M. Subramanian, Sucharita, *physics.med-ph* (2018).

91. P. Bizi-bandoki, S. Valette, E. Audouard, S. Benayoun, *Applied Surface Science* **273**, 399–407, ISSN: 0169-4332, (http://www.sciencedirect.com/science/article/pii/S0169433213003620) (2013).

92. R. Jagdheesh, *Langmuir* **30**, 12067–12073, ISSN: 0743-7463, (https://doi.org/10.1021/la5033527) (2014).

93. J. Long, M. Zhong, H. Zhang, P. Fan, *Journal of Colloid and Interface Science* **441**, 1–9, ISSN: 0021-9797, (http://www.sciencedirect.com/science/article/pii/S0021979714008637) (2015).

94. Q. Pan, Y. Cao, W. Xue, D. Zhu, W. Liu, *Langmuir* **35**, 11414–11421, ISSN: 0743-7463, (https://doi.org/10.1021/acs.langmuir.9b01333) (2019).

95. F. H. Rajab, Z. Liu, L. Li, *Applied Surface Science* **466**, 808–821, ISSN: 0169-4332 (2019).

96. M. H. Kwon, H. S. Shin, C. N. Chu, *Applied Surface Science* **288**, 222–228, ISSN: 0169-4332, (http://www.sciencedirect.com/science/article/pii/S0169433213018588) (2014).

97. Y. Li, Y. Tian, C. Yang, D. Zhang, X. Liu, presented at the 2015 International Conference on Manipulation, Manufacturing and Measurement on the Nanoscale (3M-NANO), pp. 153–158.

98. D. S. Patel, A. Singh, K. Balani, J. Ramkumar, *Surface and Coatings Technology* **349**, 816–829, ISSN: 0257-8972, (http://www.sciencedirect.com/science/article/pii/S0257897218305073) (2018).

99. C.-j. Yang *et al.*, *The International Journal of Advanced Manufacturing Technology* **87**, 1663–1670, ISSN: 1433-3015, (https://doi.org/10.1007/s00170-016-8601-9) (2016).

100. S. L. U. Ltd, *G4 Pulsed Fibre Laser Product Manual* (SPI Lasers UK Ltd., 2012).

101. N. Technology, *Pipeline-1 and 2 Scan Controller User Manual* (Nutfiel Technology, Hudson Nh 03051 USA, 2016).

102. N. Technology, *Surfboard USB Users Manual* (Nutfield Technology, Hudson NH 03051 USA).

103. Catalog, (https://nutfieldtech.com/wp-content/uploads/2018/05/Nufield-Techs-XLR8-and-Xtreme-Scan-Heads-Data-Sheet.pdf).

104. N. Techology, *XLR8 2-Axis Scan head Hardware Manual Digital and Analog Interface* (Nutfield Technology, Hudson NH 03051 USA, 2013), (https://nutfieldtech.com/nutfield-technology-product-manuals/).

105. N. Technology, *WaveRunner V2.6 Users Manual* (Nutfield Technology, Hudson NH 03051 USA, 2003), (https://nutfieldtech.com/nutfield-technology-product-manuals/).

106. S. GmbH, *SAMLight Manual* (SCAPS GmbH, Cambridge UK, 2019), (http://download.scaps.com/downloads/manuals/sc_manual_sl_English.pdf).

107. S. GmbH, *SAMLight Manual*.

108. THORLABS, *LST150 and LTS300 Long Travel Stages User Guide* (THORLABS, Cambridgeshire UK, 2018), (https://www.thorlabs.com/drawings/300d325abd4a2863-84D101C1-B023-5BD0-E5C1E3048FBF5BF3/LTS150_M-APTManual.pdf).

109. THORLABS, *L490MZ Motorized Lab Jack User Guide* (THORLABS, Cambridgeshire UK, 2014).

110. Catalog, 2019, (https://www.nikonmetrology.com//images/brochures/lv-n-en.pdf).

111. THORLABS, *DCx Camera Functional Description and SDK Manual* (THORLABS, 2018), (https://www.thorlabs.com/drawings/300d325abd4a2863-84D101C1-B023-5BD0-E5C1E3048FBF5BF3/DCC1645C-Manual.pdf).

112. V. I. Inc., *WYKO NT9100 Surface Profiler Setup and Operation Guide* (Veeco Instruments inc., USA, 2008).

113. K. GmbH, *EasyDrop standard Drop Shape Analysis System* (Kruss GmbH, 2008).

114. Catalog, 2014, (https://m.neyco.fr/uploads/media/product/0001/04/FT-KRATOS-AXIS-Supra-NEYCO.pdf).

115. G. Eberle, C. Dold, K. Wegener, *IJMIC* **20**, 199–207 (2013).

116. Catalog, 2019, (https://www.qioptiq-shop.com/out/Graphics/en/00127002_0.pdf).

117. Q. Photonics, *F-Theta-Ronar F=160 mm, Wavelength = 1064 nm* (QIOPTIQ Photonics, 2003), (https://www.qioptiq-shop.com/out/Graphics/en/00124916_0.pdf).

118. J. Chen, S.-w. Lin, X. Zhou, Y.-l. Tu, *Precision Engineering* **47**, 239–248 (2017).

119. Q. Photonics, *LINOS F-Theta-Ronar Lens f=100mm, 1064nm. telecentric* (QIOPTIQ Photonics, 2019), (https://www.qioptiq-shop.com/out/Graphics/en/00126981_0.pdf).

120. C.-V. Ngo, D.-M. Chun, *Applied Surface Science* **409**, 232–240, ISSN: 0169-4332 (2017).

121. D. V. Ta *et al.*, *Applied Surface Science* **357**, 248–254, ISSN: 0169-4332, (http://www.sciencedirect.com/science/article/pii/S0169433215021182) (2015).

122. D.-M. Chun, C.-V. Ngo, K.-M. Lee, *CIRP Annals* **65**, 519–522, ISSN: 0007-8506 (2016).

123. A. He, W. Liu, W. Xue, H. Yang, Y. Cao, *Applied Surface Science* **434**, 120–125, ISSN: 0169-4332, (http://www.sciencedirect.com/science/article/pii/S0169433217330945) (2018).

124. F.-M. Chang, S.-L. Cheng, S.-J. Hong, Y.-J. Sheng, H.-K. Tsao, *Applied Physics Letters* **96**, 114101, ISSN: 0003-6951, (https://doi.org/10.1063/1.3360847) (2010).

125. J. Bonse, J. M. Wrobel, J. Krüger, W. Kautek, *Applied Physics A: Materials Science and Processing* **72**, 89, ISSN: 09478396, (https://liverpool.idm.oclc.org/login?url=https://search.ebscohost.com/login.aspx?direct=true&db=a9h&AN=4720340&site=eds-live&scope=site) (2001).

126. J. M. Liu, *Optics Letters* **7**, 196–198, ISSN: 01469592 15394794, (https://liverpool.idm.oclc.org/login?url=https://search.ebscohost.com/login.aspx?direct=true&db=edo&AN=ejs20954963&site=eds-live&scope=site) (1982).

127. A. G. Demir, K. Pangovski, W. O'Neill, B. Previtali, *Journal of Physics D: Applied Physics* **48**, 235202, ISSN: 0022-3727 1361-6463, (http://dx.doi.org/10.1088/0022-3727/48/23/235202) (2015).

128. A. G. Demir, K. Pangovski, W. O'Neill, B. Previtali, *Surface and Coatings Technology* **258**, 240–248, ISSN: 0257-8972 (2014).

129. M. S. Trtica *et al.*, *Applied Surface Science* **225**, 362–371, ISSN: 0169-4332, (http://www.sciencedirect.com/science/article/pii/S0169433203012364) (2004).

130. J. Blackburn, in *Welding and Joining of Aerospace Materials*, ed. by M. C. Chaturvedi (Woodhead Publishing, 2012), pp. 75–108, ISBN: 978-1-84569-532-3, (http://www.sciencedirect.com/science/article/pii/B9781845695323500034).

131. L. Feng *et al.*, *Advanced Materials* **14**, 1857–1860, ISSN: 0935-9648, (https://doi.org/10.1002/adma.200290020) (2002).

132. M. Kagerer, F. Irlinger, T. C. Lueth, presented at the 2012 IEEE/ASME International Conference on Advanced Intelligent Mechatronics (AIM), pp. 135–140, ISBN: 2159-6255.

133. G. Callies, P. Berger, H. Hugel, *Journal of Physics D: Applied Physics* **28**, 794–806, ISSN: 0022-3727 1361-6463, (http://dx.doi.org/10.1088/0022-3727/28/4/026) (1995).

134. J. E. Sipe, J. F. Young, J. S. Preston, H. M. van Driel, *Physical Review B* **27**, 1141–1154, (https://link.aps.org/doi/10.1103/PhysRevB.27.1141) (1983).

135. G. Miyaji, K. Miyazaki, *Optics Express* **16**, 16265–16271 (2008).

136. D. Dufft, A. Rosenfeld, S. K. Das, R. Grunwald, J. Bonse, *Journal of Applied Physics* **105**, 034908, ISSN: 0021-8979, (https://doi.org/10.1063/1.3074106) (2009).

137. S. Moradi, S. Kamal, P. Englezos, S. G. Hatzikiriakos, *Nanotechnology* **24**, 415302, ISSN: 0957-4484 1361-6528, (http://dx.doi.org/10.1088/0957-4484/24/41/415302) (2013).

138. J. Yong *et al.*, *Applied Surface Science* **389**, 1148–1155, ISSN: 0169-4332, (http://www.sciencedirect.com/science/article/pii/S0169433216315112) (2016).

139. A. Y. Vorobyev, C. Guo, *Journal of Applied Physics* **117**, 033103, ISSN: 0021-8979, (https://doi.org/10.1063/1.4905616) (2015).

140. D. Huerta-Murillo *et al.*, *Applied Surface Science* **463**, 838–846, ISSN: 0169-4332, (http://www.sciencedirect.com/science/article/pii/S0169433218324243) (2019).

141. L. Gao, T. J. McCarthy, *Langmuir* **22**, 6234–6237, ISSN: 0743-7463, (https://doi.org/10.1021/la060254j) (2006).

142. L. Yao, J. He, *Progress in Materials Science* **61**, 94–143, ISSN: 0079-6425, (http://www.sciencedirect.com/science/article/pii/S0079642513000881) (2014).

143. E. Pierce, F. J. Carmona, A. Amirfazli, *Colloids and Surfaces A: Physicochemical and Engineering Aspects* **323**, 73–82, ISSN: 0927-7757, (http://www.sciencedirect.com/science/article/pii/S0927775707008801) (2008).

144. T. Y. Yang, C. C. Li, P. H. Huang, S. J. Chang, *Journal of the American Ceramic Society* **100**, 56–64, ISSN: 15512916 00027820, (https://liverpool.idm.oclc.org/login?url=https://search.ebscohost.com/login.aspx?direct=true&db=edselc&AN=edselc.2-52.0-84990842412&site=eds-live&scope=site) (2017).

145. M. Paul, M. Jonathan, C. Edward, M. O. Gerard, presented at the Proc.SPIE, vol. 4876, (https://doi.org/10.1117/12.463744).

146. B. Zheng, G. Jiang, W. Wang, K. Wang, X. Mei, *AIP Advances* **4**, 031310, (https://doi.org/10.1063/1.4867088) (2014).

147. K. Kiran Kumar, G. L. Samuel, M. S. Shunmugam, *Journal of Materials Processing Technology* **263**, 266–275, ISSN: 0924-0136, (http://www.sciencedirect.com/science/article/pii/S0924013618303704) (2019).

Appendices

Appendix A

SPI G4 Test Report

SPI® Lasers | inspiring your products & manufacturing

redENERGY™

TEST REPORT

PART NUMBER: SP-020P-A-HS-L-A-Y(01)
SERIAL NUMBER: 368742

TEST DATE: 2013-01-10 14:02
PASS / FAIL: PASS
APPROVED BY: AmberJo

Output Beam Parameters		spec limits		test data	
parameter	unit	min	max	value	pass/fail
M2		1.60	2.00	1.83	PASS
Divergence	mrad	95.0	115.0	100.4	PASS
Circularity		0.9	1.1	0.93	PASS

Spectral Characteristics		spec limits		test data	
parameter	unit	min	max	value	pass/fail
Central Emission Wavelength (λ0)	nm	1059.0	1065.0	1061.7	PASS
Emission Bandwidth	nm	1.0	10.0	5.4	PASS
Power within +/- 20nm of λ0	%	70.0	100.0	94.4	PASS

Laser Output Pulse Characteristics		spec limits		test data	
parameter	unit	min	max	value	pass/fail
Maximum Average Power	W	20.70	22.00	20.90	PASS
Output Power Variation	%	0.0	8.0	2.5	PASS
Maximum Pulse Energy	mJ	0.82	0.89	0.84	PASS
Pulse Energy Stability	% RMS	0.0	3.0	0.4	PASS
Maximum Peak Power	kW	12.0	21.0	14.9	PASS
Pulse Duration (FWHM)	ns	17.0	35.0	28.7	PASS
Pulse Width Stability	%RMS	0.0	6.0	1.1	PASS

11/01/13
Passed

9816:368742:SP-020P-A-HS-L-A-Y(01)

date printed: 10/01/2013 EP-S00085(A) (C) 2011 SPI Lasers UK Ltd

Appendix B

Table of waveforms

14.3 Waveform Reference Tables - HS variants

G4 HS Variants have a variety of pre-defined waveforms. Users can select different waveforms which, in combination with their chosen pulse repetition rate, can be used to optimize the pulse characteristics and processing speed for their target application. See section 15 for waveform examples.

Wavefomm Number	Approx. Electrical Duration (ns)	12W L type		20W L type		30W H type		Approx. Electrical Duration (ns)	40W H type		Approx. Electrical Duration (ns)	20W S type		30W S type	
		PRF_0 (kHz)	E_{MAX} (mJ)	PRF_0 (kHz)	E_{MAX} (mJ)	PRF_0 (kHz)	E_{MAX} (mJ)		PRF_0 (kHz)	E_{MAX} (mJ)		PRF_0 (kHz)	E_{MAX} (mJ)	PRF_0 (kHz)	E_{MAX} (mJ)
0	200	20	0.6	25	0.8	30	1.0	250	30	1.33	220	35	0.57	45	0.67
1	65	50	0.24	65	0.31	75	0.4	130	47	0.85	120	55	0.36	70	0.43
2	30	100	0.12	125	0.16	150	0.2	60	76	0.53	55	90	0.22	115	0.26
3	15	200	0.06	250	0.08	300	0.1	30	145	0.28	25	170	0.12	220	0.14
4	12	300	0.04	375	0.053	450	0.067	20	230	0.17	18	270	0.074	350	0.09
5	9	400	0.03	500	0.04	500	0.06	9	250	0.16	15	290	0.068	375	0.08
6	Duplicate of waveform 5														
7															
8															
9															
10															
11	200	20	0.6	25	0.8	30	1.0	250	30	1.33	220	35	0.57	45	0.67
12	190	20.8	0.58	26	0.77	31	0.97	230	32	1.25	205	37	0.54	48	0.63
13	180	21.6	0.56	27	0.74	32	0.94	220	34	1.18	200	39	0.51	50	0.60
14	170	22.4	0.54	28	0.71	33	0.91	200	38	1.05	190	44	0.45	57	0.53
15	160	23.2	0.52	29	0.69	34	0.88	170	41	0.98	160	48	0.42	62	0.48
16	150	24.4	0.49	30.5	0.66	36	0.83	150	43.5	0.92	140	51	0.39	66	0.45
17	140	25.6	0.47	32	0.63	38	0.79	130	47	0.85	120	55	0.36	71	0.42
18	130	26.8	0.45	33.5	0.6	40	0.75	110	51	0.78	100	60	0.33	77	0.39
19	120	28.4	0.42	35.5	0.56	42.5	0.71	100	54	0.74	95	63	0.32	81	0.37
20	110	30.4	0.4	38	0.53	45.5	0.66	90	58	0.69	85	68	0.29	87	0.34
21	100	32.8	0.37	41	0.49	49	0.61	80	62	0.65	75	72	0.28	93	0.32
22	90	36	0.33	45	0.44	54	0.56	70	69	0.58	65	80	0.25	103	0.29
23	80	40	0.3	50	0.4	60	0.5	60	76	0.53	55	90	0.22	116	0.26
24	70	45.6	0.26	57	0.35	68	0.44	50	89	0.45	45	105	0.19	135	0.22
25	60	52.8	0.23	66	0.3	79	0.38	40	108	0.37	35	125	0.16	160	0.19
26	50	62.4	0.19	78	0.26	93	0.32	30	145	0.28	25	170	0.12	220	0.14
27	40	77.6	0.15	97	0.21	116	0.26	20	230	0.17	18	270	0.074	350	0.09
28	30	108	0.11	135	0.15	162	0.19	9	250	0.16	15	290	0.068	375	0.08
29	20	200	0.06	250	0.08	300	0.1	Duplicate of waveform 28							
30 - 63	Duplicate of waveform 29														

Appendix C

L-type optical pulse shape

15.2 20W L-type Optical Pulse Shape Examples

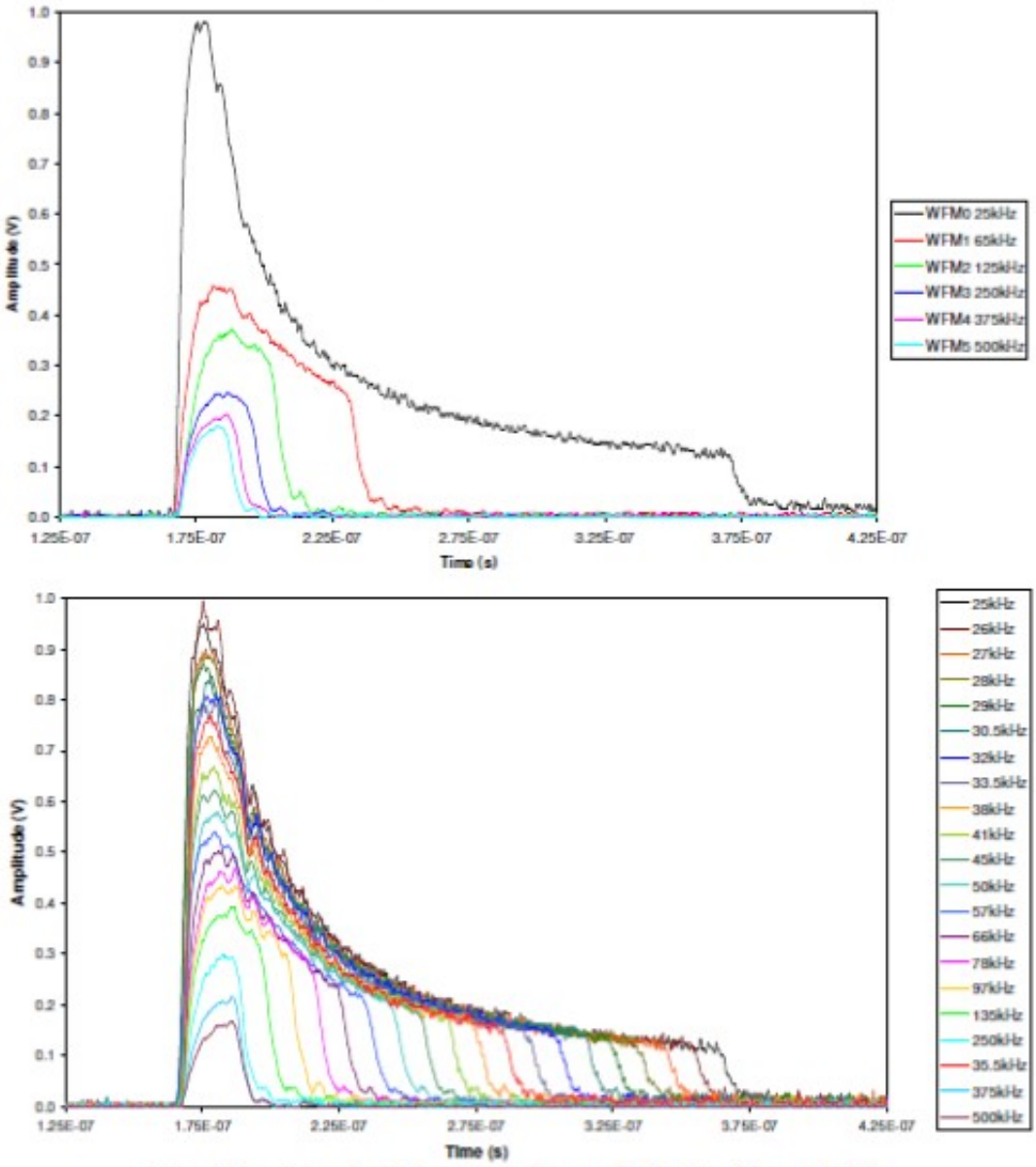

Figure 48. **Example Pulse Shapes from a 20W Pulsed Laser Module**
(*top*) waveforms 0 – 5 at PRF_0 for each waveform
(*bottom*) waveforms 11 – 29 at PRF_0 for each waveform